ASME
SETTING THE STANDARD

Transactions of the ASME, Journal of Fluids Engineering (ISSN 0098-2202) is published monthly by The American Society of Mechanical Engineers, Three Park Avenue, New York, NY 10016. Periodicals postage paid at New York, NY and additional mailing offices.
POSTMASTER: Send address changes to Transactions of the ASME, Journal of Fluids Engineering, c/o THE AMERICAN SOCIETY OF MECHANICAL ENGINEERS, 22 Law Drive, Box 2300, Fairfield, NJ 07007-2300.
CHANGES OF ADDRESS must be received at Society headquarters seven weeks before they are to be effective. Please send old label and new address.
STATEMENT from By-Laws. The Society shall not be responsible for statements or opinions advanced in papers or ... printed in its publications (B7.1, Par. 3).

Journal of Fluids Engineering

Published Monthly by ASME

VOLUME 131 • NUMBER 2 • FEBRUARY 2009

RESEARCH PAPERS

Flows in Complex Systems

021101 Characteristics and Control of the Draft-Tube Flow in Part-Load Francis Turbine
Ri-kui Zhang, Feng Mao, Jie-Zhi Wu, Shi-Yi Chen, Yu-Lin Wu, and Shu-Hong Liu

021102 Simulation of Turbine Blade Trailing Edge Cooling
Jongwook Joo and Paul Durbin

021103 Efficiency Improvement of Centrifugal Reverse Pumps
Shahram Derakhshan, Bijan Mohammadi, and Ahmad Nourbakhsh

021104 Effect of Side Wind on a Simplified Car Model: Experimental and Numerical Analysis
Emmanuel Guilmineau and Francis Chometon

Fundamental Issues and Canonical Flows

021201 Passive Manipulation of Separation-Bubble Transition Using Surface Modifications
Brian R. McAuliffe and Metin I. Yaras

021202 PIV-POD Investigation of the Wake of a Sharp-Edged Flat Bluff Body Immersed in a Shallow Channel Flow
Arindam Singha, A.-M. Shinneeb, and Ram Balachandar

021203 Quasi-1D Unsteady Conjugate Module for Rocket Engine and Propulsion System Simulations
Bryan T. Campbell and Roger L. Davis

Multiphase Flows

021301 Motion of a Single Newtonian Liquid Drop Through Quiescent Immiscible Visco-Elastic Liquid: Shape and Eccentricity
Ritu Gupta and R. K. Wanchoo

021302 Axial Development of Flow Regime in Adiabatic Upward Two-Phase Flow in a Vertical Annulus
J. Enrique Julia, Basar Ozar, Abhinav Dixit, Jae-Jun Jeong, Takashi Hibiki, and Mamoru Ishii

021303 Incubation Time and Cavitation Erosion Rate of Work-Hardening Materials
Jean-Pierre Franc

(Contents continued on inside back cover)

This journal is printed on acid-free paper, which exceeds the ANSI Z39.48-1992 specification for permanence of paper and library materials. ♾™
♻ 85% recycled content, including 10% post-consumer fibers.

(**Contents continued**)

Journal of Fluids Engineering **Volume 131, Number 2** **FEBRUARY 2009**

TECHNICAL BRIEFS

024501 Thermal Effect at the Incipient Stage of Cavitation Erosion on a Stainless Steel in Ultrasonic Vibration Cavitation
Chen Haosheng, Li Jiang, and Liu Shihan

The ASME Journal of Fluids Engineering is abstracted and indexed in the following:

Applied Science & Technology Index, Chemical Abstracts, Chemical Engineering and Biotechnology Abstracts (Electronic equivalent of Process and Chemical Engineering), Civil Engineering Abstracts, Computer & Information Systems Abstracts, Corrosion Abstracts, Current Contents, Ei EncompassLit, Electronics & Communications Abstracts, Engineered Materials Abstracts, Engineering Index, Environmental Engineering Abstracts, Environmental Science and Pollution Management, Excerpta Medica, Fluidex, Index to Scientific Reviews, INSPEC, International Building Services Abstracts, Mechanical & Transportation Engineering Abstracts, Mechanical Engineering Abstracts, METADEX (The electronic equivalent of Metals Abstracts and Alloys Index), Petroleum Abstracts, Process and Chemical Engineering, Referativnyi Zhurnal, Science Citation Index, SciSearch (The electronic equivalent of Science Citation Index), Shock and Vibration Digest, Solid State and Superconductivity Abstracts, Theoretical Chemical Engineering

Ri-kui Zhang

Feng Mao

State Key Laboratory for Turbulence and Complex Systems,
College of Engineering,
Peking University,
Beijing 100871, China

Jie-Zhi Wu[1]

State Key Laboratory for Turbulence and Complex Systems,
College of Engineering,
Peking University,
Beijing 100871, China;
University of Tennessee Space Institute,
Tullahoma, TN 37388
e-mail: jzwu@mech.pku.edu.cn

Shi-Yi Chen

State Key Laboratory for Turbulence and Complex Systems,
College of Engineering,
Peking University,
Beijing, 100871, China;
Department of Mechanical Engineering,
Johns Hopkins University,
Baltimore, MD 21218

Yu-Lin Wu

Shu-Hong Liu

State Key laboratory of Hydroscience and Engineering,
Department of Thermal Engineering,
Tsinghua University,
Beijing 100084, China

Characteristics and Control of the Draft-Tube Flow in Part-Load Francis Turbine

Under part-load conditions, a Francis turbine often suffers from very severe low-frequency and large-amplitude pressure fluctuation, which is caused by the unsteady motion of vortices (known as "vortex ropes") in the draft tube. This paper first reports our numerical investigation of relevant complex flow phenomena in the entire draft tube, based on the Reynolds-averaged Navier–Stokes (RANS) equations. We then focus on the physical mechanisms underlying these complex and somewhat chaotic flow phenomena of the draft-tube flow under a part-load condition. The flow stability and robustness are our special concern, since they determine what kind of control methodology will be effective for eliminating or alleviating those adverse phenomena. Our main findings about the flow behavior in the three segments of the draft tube, i.e., the cone inlet, the elbow segment, and the outlet segment with three exits, are as follows. (1) In the cone segment, we reconfirmed a previous finding of our research group based on the turbine's whole-flow RANS computation that the harmful vortex rope is an inevitable consequence of the global instability of the swirling flow. We further identified that this instability is caused crucially by the reversed axial flow at the inlet of the draft tube. (2) In the elbow segment, we found a reversed flow continued from the inlet cone, which evolves to slow and chaotic motion. There is also a fast forward stream driven by a localized favorable axial pressure gradient, which carries the whole mass flux downstream. The forward stream and reversed flow coexist side-by-side in the elbow, with a complex and unstable shear layer in between. (3) In the outlet segment with three exits, the forward stream always goes through a fixed exit, leaving the other two exits with a chaotic and low-speed fluid motion. Based on these findings, we propose a few control principles to suppress the reversed flow and to eliminate the harmful helical vortex ropes. Of the methods we tested numerically, a simple jet injection in the inlet is proven successful.
[DOI: 10.1115/1.3002318]

1 Introduction

The Francis turbine is a standard facility of large hydraulic power stations. The water enters a spiral case toward the turbine's center, as shown in Fig. 1. After guided by stay vanes and guide vanes, the water pushes the runner to rotate. Then the water runs through a draft tube consisting of three segments: a cone, an elbow, and nearly horizontal outlets.

It is well-known that, at certain off-design conditions, strong unsteady vortices (often called vortex ropes) may occur in the draft tube of a Francis turbine. Figure 2 shows two kinds of observed vortex ropes. The spiral-type vortex rope (Fig. 2(*a*)) occurs typically at the "part-load condition" (below 60% of the full load or so), whose strong unsteady motion is associated with severe low-frequency pressure fluctuations that may damage the turbine's normal operation and even the safety of the whole power station. The bubble-type vortex rope (Fig. 2(*b*)) occurs typically at the so-called "higher part-load condition" (at 60–85% of the full load), whose spiral tails also cause pressure fluctuations of smaller amplitude. Although some engineering practices, such as air admission at the runner outlet, have been proven to be somewhat useful in alleviating the pressure fluctuation caused by either kind of vortex rope, more effective control methodologies and/or improved turbine design are still highly desired. Any essential progress toward this goal will rely on a better understanding of the physical mechanisms for the formation of the vortex ropes and the flow conditions in the entire draft tube.

After several decades' effort, the vortex-rope phenomenon has recently been well understood, owing to their close similarity with the well-known vortex breakdown patterns, say, Fig. 3 [1], observed above a delta wing at a large angle of attack. The only difference is that, while the vortex breakdown happens suddenly downstream of a well-developed thin vortex, the draft-tube vortex rope directly follows a swirling flow at the runner's outlet.

This observation strongly suggests that the physical root of draft-tube vortex ropes is the swirling flow instability (e.g., Ref. [2]) that inevitably appears in the cone segment under part-load

[1]Corresponding author.

Contributed by the Fluids Engineering Division of ASME for publication in the JOURNAL OF FLUIDS ENGINEERING. Manuscript received December 10, 2006; final manuscript received May 15, 2008; published online January 7, 2009. Assoc. Editor: Yu-Tai Lee.

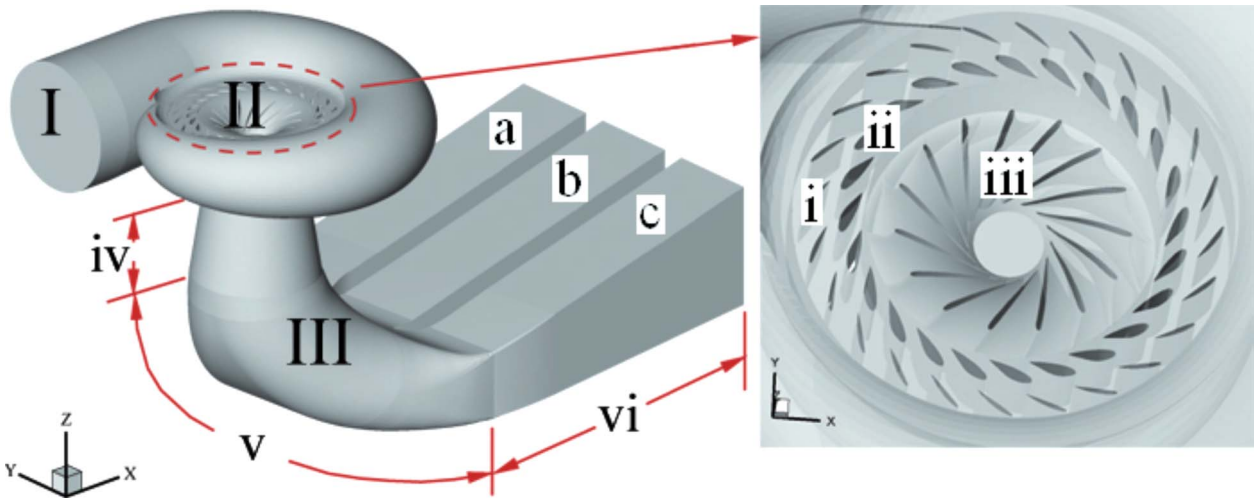

Fig. 1 A Francis turbine. (I) spiral case; (II) vanes and runner, with (i) stay vanes, (ii) guide vanes, and (iii) runner; (III) draft tube, with (iv) cone, (v) elbow, and (vi) outlet segments. The outlets (*a*), (*b*), and (*c*) will be referred to as the left, middle, and right outlets, respectively.

conditions. Following this clue, Susan-Resiga and co-workers [3–5] applied an early theory of Benjamin [6] on vortex breakdown to analyze their experimentally measured mean velocity profiles in cone segment. The theory is based on the Bragg–Hawthorne equation governing inviscid, steady, and axisymmetric swirling flow. The axial-disturbance eigenvalues of the flow are used to judge whether it can sustain standing waves (subcritical) or not (supercritical). Susan-Resiga and co-worker have found that the critical state of the swirl configuration is in agreement with experimental observations.

In a different approach, Zhang et al. [7] analyzed the axial development of the local absolute instability/convective instability (AI/CI) (e.g., Ref. [2]; see also Sec. 3.2) behavior of the mean velocity profiles in the inlet cone, based on their unsteady Reynolds-averaged Navier–Stokes (URANS) simulation of the *whole-turbine flow* (WTF) (i.e., the flow in the entire Francis turbine). They found that under part-load condition, the swirling cone flow is absolutely unstable with a dominating helical mode, which leads to a spiral vortex rope and severe pressure fluctuation; under higher part-load condition, the swirling flow is also absolutely unstable but with a dominating axisymmetric mode, leading to a bubble-type vortex rope with small-amplitude pressure fluctuation; and under full-load condition, the flow has only a very weak swirl and is convectively unstable with almost no pressure fluctuation.

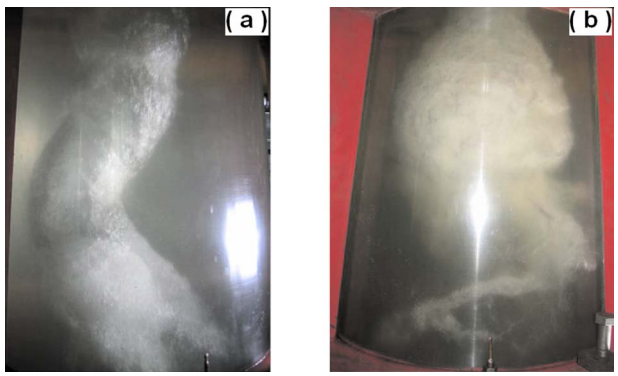

Fig. 2 Typical vortex ropes in the draft-tube cone of a Francis turbine model (photos taken at Harbin Electric Machinery Co. by Q. D. Cai): (*a*) spiral-type vortex rope and a (*b*) bubble-type vortex rope

Having had these new developments [3–5,7], it is natural to further investigate the *basic control* strategy for ultimately eliminating these vortex ropes in practical applications. To this end, one should also clarify how the swirling vortex instability is affected by the flow condition at both upstream and downstream ends of the inlet cone. This issue amounts to the *stability and robustness of the entire draft-tube flow* under part-load conditions, which are the focus of the present numerical study.

Fig. 3 Vortex breakdown above a delta wing, spiral-type on the left and bubble-type on the right [1]

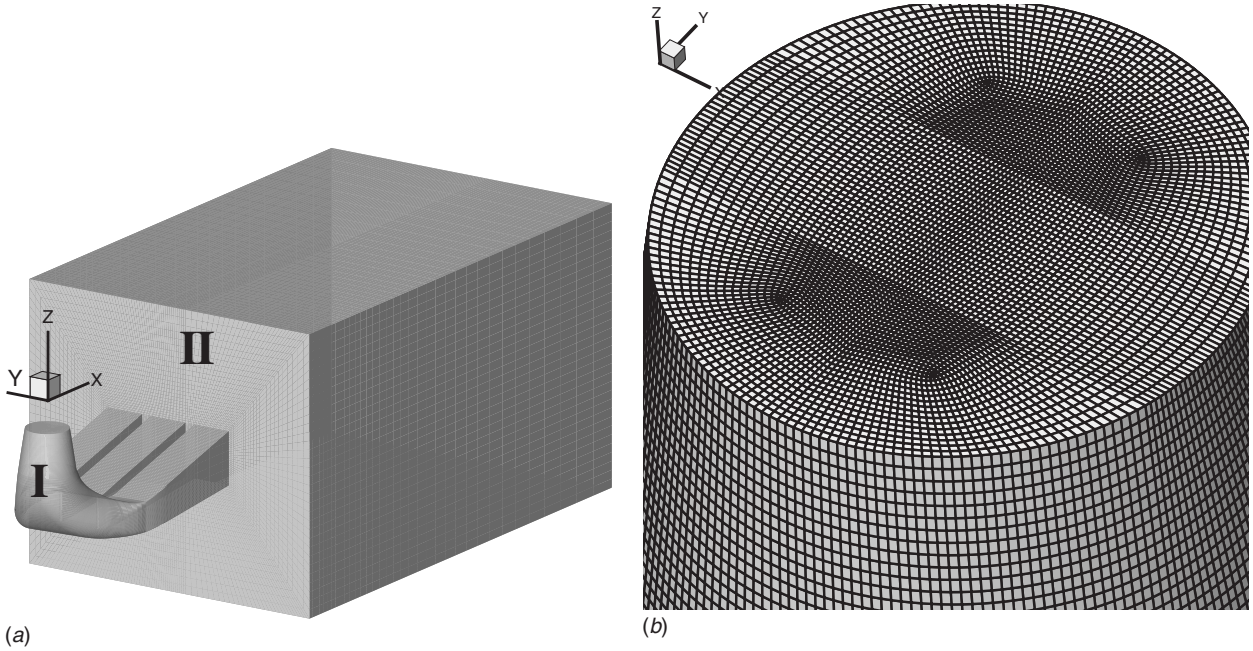

Fig. 4 (*a*) Sole draft-tube Model: (I) draft tube and (II) river; and (*b*) a part of the cone surface grid

Section 2 presents the methodology of our numerical simulation. In Sec. 3 we identify the dominant factor leading to the formation of the vortex rope. In Sec. 4 we investigate the characteristics and underlying physics of the complex unsteady flow in the elbow and outlets. These studies lead to an assessment of the global robustness of the entire draft-tube flow and a few guiding principles for controlling the vortex rope to be reported in Sec. 5, along with a couple of numerical control tests. In Sec. 6 we make some conclusions.

2 Formulation of Numerical Simulation

2.1 Computational Strategy and Numerical Method. In reality, the highly unsteady interactions of the flows in all components of a Francis turbine produce many disturbance modes with various scales in space and time. These modes may all enter the draft tube. Resolving all these modes by RANS or large eddy simulation (LES) requires a formidably large grid number and small time steps, which are currently impractical for engineering simulation. Thus, the aforementioned WTF simulations of Zhang et al. [7] had to be done with quite coarse grids and a simplified outflow condition.

Fortunately, the upstream disturbances to the draft-tube flow are on much smaller time scales (higher frequencies) and do not resonate with the low-frequency AI modes of vortex ropes [8]. Therefore, in studying the draft-tube flow one often ignores the upstream disturbances and works on the much simpler *sole draft-tube flow* (SDTF), either experimentally (e.g., Refs. [9,10]) or numerically (e.g., Refs. [11,12]). This kind of SDTF model is also adopted in the present numerical study. Even for this SDTF simulation, in order to cover all relevant flow structures with a reasonable grid number, we still had to confine our computation to a moderate Reynolds number. Thus, a one-twentieth model draft tube was used, for which the computational domain and a part of the grid are shown in Fig. 4, where the coordinate system xyz is also located with the origin at $1.5D^*$ above the center of the cone inlet. Since usually at the draft-tube exits the pressure is still under the influence of the upstream flow, we postponed the prescription of the downstream pressure condition to the exit of a "river" connecting to the draft-tube exits, with a length of about 12 times the diameter D^* of the cone inlet.

Our numerical results will be presented in a dimensionless form, scaled by the cone inlet diameter D^*, the water density ρ, and the volume flux Q^* at the full-load condition. Thus, denoting the dimensional quantities by an asterisk and the mean flow quantity by capital letters, the velocity scale V_0^* and time scale T_0^* are

$$V_0^* = \frac{4Q^*}{\pi D^{*2}}, \quad T_0^* = \frac{D^*}{V_0^*} = \frac{\pi D^{*3}}{4Q^*} \tag{1}$$

and the pressure coefficient is defined by

$$C_p = \frac{2(P - P_{\text{ref}})}{\rho V_0^{*2}} \tag{2}$$

where p_{ref} is the reference pressure at the center of the exit of the river.

The computation was conducted at the Reynolds number $\text{Re} = V_0^* D^* / \nu = 1.80 \times 10^6$, using the commercial code FLUENT 6.1.22. The three-dimensional incompressible and unsteady turbulent flow was solved by URANS simulation, along with the renormalization-group (RNG) k-ε turbulence model and logarithmic wall function. We chose the RNG-based model because it is claimed to be more responsive to the effects of rapid strain and streamline curvature than the standard k-ε model [13]. The flow field was discretized with a structured mesh (Fig. 4(*b*)). The grid contains about 1.0×10^6 nodes for the draft tube alone and 4×10^5 for the river. The discretization uses a second-order implicit scheme in time and the quadratic upstream interpolation for convective kinetics (QUICK) scheme in space. We will report our tests on the sensitivity of the computed flow properties to the grid number and time step in Sec. 3.1.

2.2 Boundary Conditions. The adherence (no-slip and no-through) condition $\boldsymbol{u}^* = 0$ was imposed on the draft-tube wall. A linear static pressure distribution was assumed at the exit of the river.

The results of SDTF simulation strongly depend on the choice of the inflow conditions. Ruprecht et al. [11] and Buntic et al. [12] used the data at the runner's exit, taken from WTF simulation or laboratory measurements, to construct the inflow condition. The RANS simulation of WTF by Zhang et al. [7] has shown that except the near-wall shear layer the averaged velocity profiles in the cone can be approximated by the Batchelor vortex family.

Table 1 Dimensionless parameters for Cases I and II

		Case I	Case II
Volume flux		0.555	1.0
Time step ($\Delta t^*/T_0^*$)		0.072	0.072
Calculated time (t^*/T_0^*)		14.4	14.4
Batchelor vortex	Swirling parameter (q)	−1.0	−1.0
	Axial parameter (a)	−0.5	2.0

Thus, we simply define the inflow condition by this vortex family.

In the cylindrical coordinates (r^*, θ, z^*) (positive z^* is upward) for the cone flow, the dimensional radial, azimuthal, and axial velocity components (U^*, V^*, W^*) of a Batchelor vortex are [14]

$$U^*(r^*) = 0$$

$$V^*(r^*) = \frac{\Omega_c^* R^*}{r^*/R^*}\left[1 - e^{-(r^*/R^*)^2}\right] \tag{3}$$

$$W^*(r^*) = W_\infty^* + (W_c^* - W_\infty^*)e^{-(r^*/R^*)^2}$$

where W_∞^* is the freestream axial velocity, W_c^* is the centerline axial velocity, Ω_c is the rotation rate at the axis, and R^* is a measure of the vortex core radius. Equation (3) should be nondimensionalized by the *intrinsic scales* of each specific Batchelor vortex. Following Ref. [14], we use R^* and $\Delta W^* = W_c^* - W_\infty^*$ to scale the length and velocity. Then Eq. (3) yields a two-parameter family of vortices

$$U(r) = 0, \quad V(r) = \frac{q}{r}(1 - e^{-r^2}), \quad W(r) = a + e^{-r^2} \tag{4}$$

where $r = r^*/R$ and

$$q = \frac{\Omega_c^* R^*}{\Delta W^*}, \quad a = \frac{W_\infty^*}{\Delta W^*} \tag{5}$$

are the *swirl ratio* and *external axial velocity parameter*, respectively. The sign and range of a deserve special attention. We have a coflowing jet if $a > 0$, a coflowing wake if $a < -1$, and a counterflowing jet or wake if $-1 < a < 0$. It will be seen that the value of a dominates the appearance of the AI zone and hence the existence of a vortex rope under part-load conditions.

We chose two Batchelor vortices as the inflow conditions to mimic the flows under a part-load condition (referred to as Case I) and a full-load condition (Case II). The two sets of dimensionless parameters and computational time steps are listed in Table 1. The velocity and axial vorticity profiles are plotted in Fig. 5, where the Batchelor vortices are smoothly connected with a quadratic shear layer to satisfy the no-slip condition on the wall. Note that the dimensionless axial vorticity ω_z inside the Batchelor vortex is

$$\omega_z = \frac{2\Omega_c^* D^*}{V_0^*} e^{-r^2} = \frac{2q\Delta W^* D^*}{R^* V_0^*} e^{-r^2} \tag{6}$$

As shown in Fig. 5, although the swirling parameter q in both cases remains the same, the axial vorticity ω_z at the vortex center in Case I is much stronger than that in Case II due to a larger ΔW^* in the former. The sign of ΔW^* in the two cases are different, and hence so are the rotating directions of the swirling flows; also, we have a strong adverse flow in Case I versus a coflowing jet in Case II.

3 Cone Flow: Characteristics and Stability

3.1 Flow Patterns and Discussion on Numerical Resolution. For Case I, our SDTF computation did capture a strong spiral vortex rope in the cone as expected, which is visualized in Fig. 6 at two instants by using the rational Δ-criterion [15]. This criterion defines a vortex as a connected flow region where the rotation is stronger than the strain rate. A quantification of this requirement stems from the characteristic equation of the velocity gradient tensor $\nabla \boldsymbol{u}$

$$\sigma^3 + Q\sigma - R = 0 \tag{7}$$

derived from $|\sigma \mathbf{I} - \nabla \boldsymbol{u}| = 0$ where $\mathbf{I}$ is the unit matrix. The roots σ_i $(i = 1, 2, 3)$ of Eq. (7) are the eigenvalues of $\nabla \boldsymbol{u}$, and the coefficients $Q = \sigma_1\sigma_2 + \sigma_2\sigma_3 + \sigma_3\sigma_1$ and $R = \sigma_1\sigma_2\sigma_3$ are invariant. Then the Δ-criterion defined thereby is also invariant, without any artificial adjustment parameter; by which a flow region is a vortex if the inequality (8) holds therein

$$\Delta = \left(\frac{Q}{3}\right)^3 + \left(\frac{R}{2}\right)^2 > 0 \tag{8}$$

The vortex pattern identified by Eq. (8) may not be the same as those by other simpler but irrational criteria such as isopressure surfaces.

Associated with this spiral vortex rope is a low-frequency and large-amplitude pressure fluctuation, as plotted in Fig. 7(*a*) for three check points marked in Fig. 6(*b*). The power spectra at these points are plotted in Fig. 7(*b*). The dimensionless dominating fre-

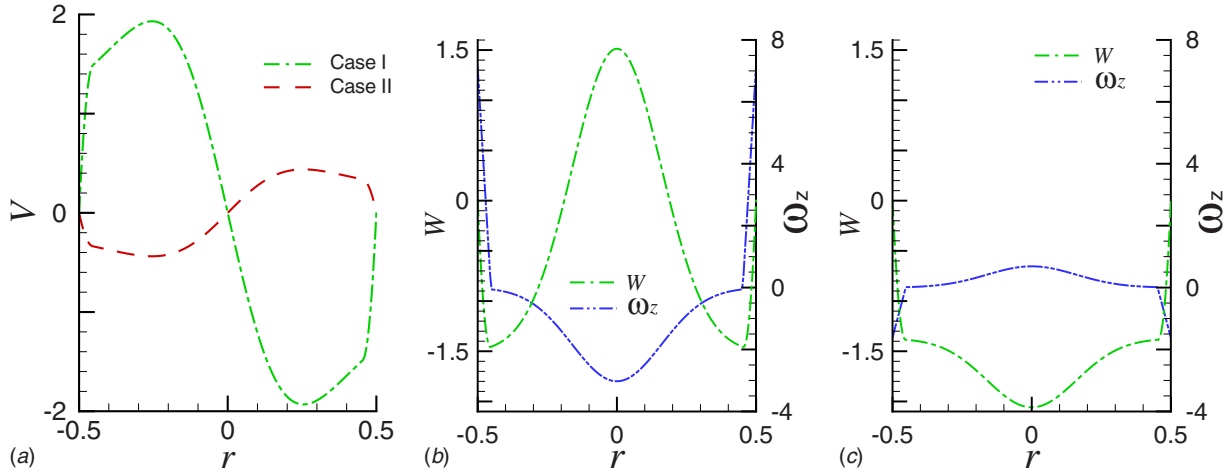

Fig. 5 Velocity and axial vorticity profiles of the Batchelor vortex. Quantities are nondimensionalized by the global scales D^* and V_0^*. (*a*) is the azimuthal velocity profile and (*b*) and (*c*) are the axial velocity (W) and vorticity (ω_z) profiles of Cases I and II, respectively.

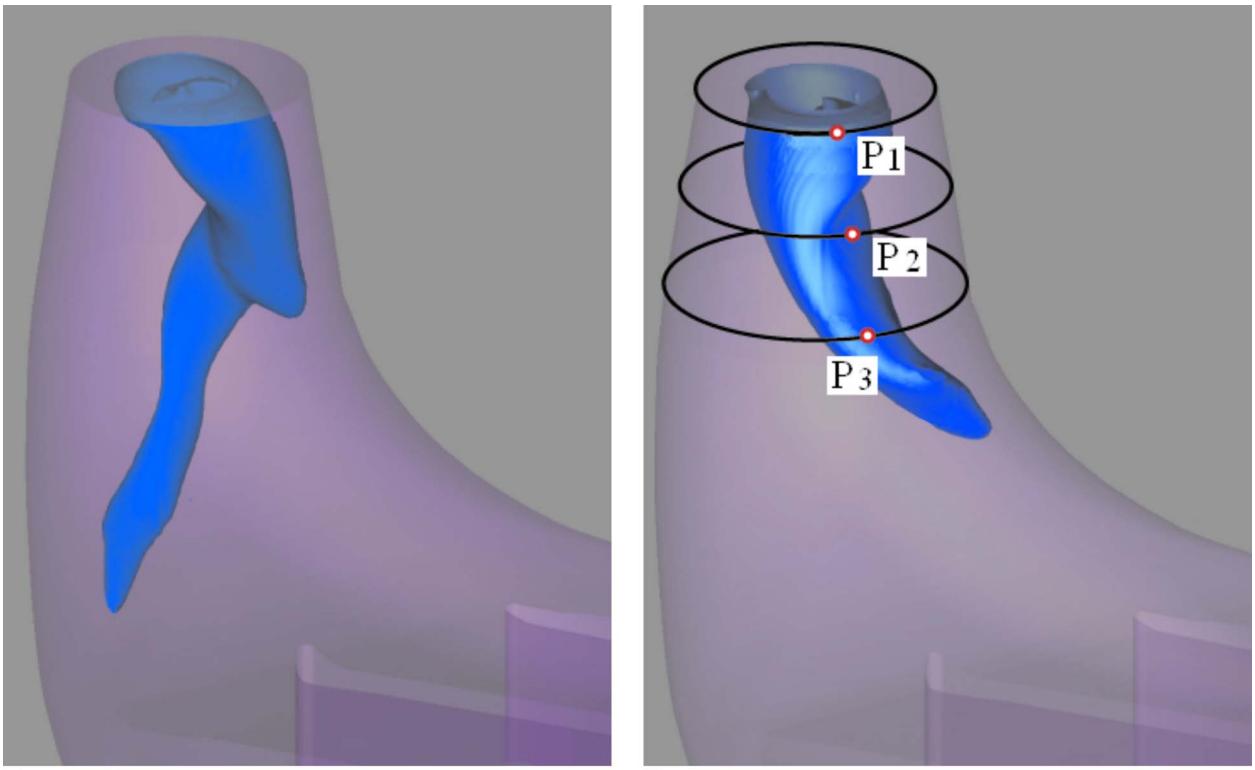

(*a*) (*b*)

Fig. 6 Vortex rope in Case I by using isosurfaces of Δ ($\Delta/\Delta_{max}=6\times10^{-6}$, where Δ_{max} is the maximum of Δ in the draft tube): (*a*) $t=11.52$ and (*b*) $t=13.39$, where *P*1, *P*2, and *P*3 are test points

quency or Strouhal number $St=f^*D^*/V_0^*$ (f^* is the frequency) of the vortex rope is 0.271. In Fig. 7(*b*), the third sample point *P*3 experiences strong harmonics of the fundamental frequency. This is likely due to the receptivity of the unsteady shear layer between the forward and reversed streams in the elbow segment (see Sec. 5.1) to the quasiperiodic disturbance imposed by the vortex-rope motion.

A series of numerical tests were performed to examine the influence of the time step and grid size on the computed flow field. We found that a $\Delta t=0.108$ still yielded a dominant St=0.271 and the same pressure fluctuation patterns on the same sample points. So did a coarse mesh of the same topology with 5.6×10^5 nodes. But a further coarse mesh of 3.1×10^5 nodes yielded St=0.191 incorrectly. Thus, our chosen $\Delta t=0.072$ (Table 1) and the mesh with $O(10^6)$ nodes are sufficiently dense to capture global performances and dominant flow structures.

The above URANS result is in good qualitative agreement with the actual measurements of prototype hydraulic turbines [16], which gives St=0.243 for the dominant pressure fluctuations under two part-load conditions. The corresponding numerical simulations predicted St=0.243–0.302 (e.g., Refs. [8,16]). Therefore, in search of physical mechanisms and control strategy, the unsteady swirling flow in the draft tube of a Francis turbine can indeed be simulated and analyzed using an SDTF model, with a Batchelor vortex as the inflow condition.

Although the present 10^6 grid can predict correct global perfor-

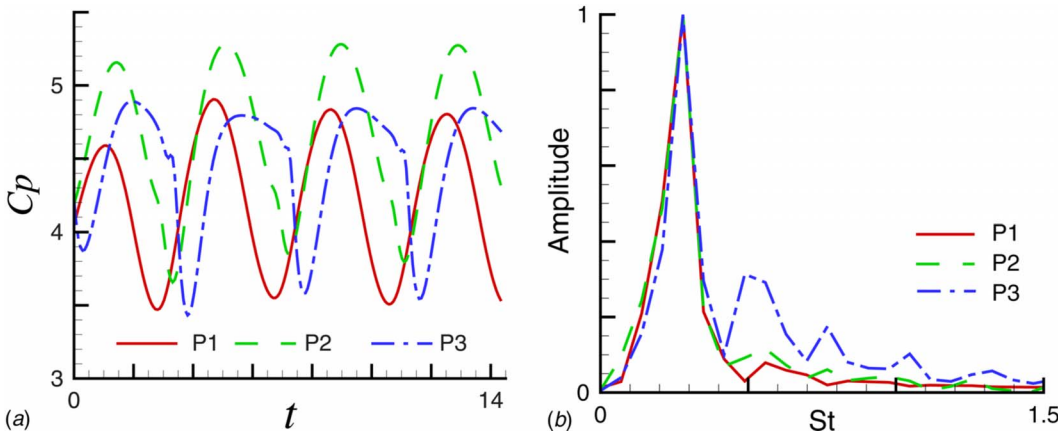

Fig. 7 Pressure fluctuations on test points (as shown in Fig. 6(*b*)) and their amplitude spectra in Case I: (*a*) pressure fluctuations and (*b*) power spectra of amplitude

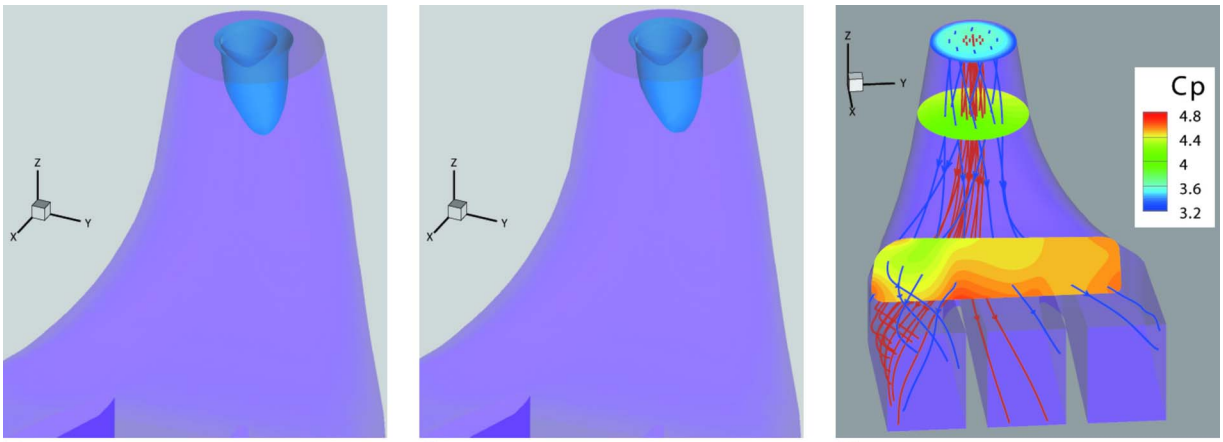

Fig. 8 Isosurfaces of Δ ($\Delta/\Delta_{max}=2\times10^{-6}$) in Case II at (*a*) *t*=2.13 and (*b*) *t*=2.66. (*c*) Shows instantaneous streamlines at *t*=2.13.

mances, however, it is too coarse to fully resolve the turbulent boundary layers and their separation (in the URANS sense). For the standard wall function, each wall-adjacent cell's centroid in a RANS simulation should be located within the log-law layer with $30<y^+<300$, preferably with y^+ close to its lower bound 30 [13]. This requirement was not well satisfied in the present Case I simulation.

To examine how the boundary layer behavior influences the global draft-tube flow, we performed a numerical test on a grid with 3.7×10^6 nodes and 3.2×10^6 cells. This denser grid yielded $y^+<50$ at 98.6% wall-adjacent nodes and $y^+_{max}=60.1$ ($y^+>50$ only occurred sparsely in space and time as the vortex rope swept a nearby cone boundary node). The computed spiral vortex shape, pressure fluctuations at check points marked in Fig. 6(*b*) and their dominant frequencies were almost the same as those given in Figs. 6 and 7, though the new simulation displays stronger harmonics at the third test point (figure not shown). Namely, the denser grid can capture more relatively small-scale URANS behavior of turbulent boundary layers, which however does not alter the basic features of large-scale structures captured by the coarse grid. Since our focus is on the part-load flow physics in the entire draft tube and control strategy, we will be satisfied with using the flow data generated by our URANS simulation with the 10^6 grid (which can save more than two-thirds of the computing time compared with the denser grid). However, for accurate prediction of the frequency, amplitude, and spectra of the pressure fluctuations, our grid-dependence test strongly suggests that a grid with y^+ close to 30 is necessary.

Contrary to Case I, the Case II flow does not have a spiral vortex rope but a weak and nearly steady vortex (Figs. 8(*a*) and 8(*b*)). The flow quasisteadiness is confirmed by the instantaneous streamlines shown in Fig. 8(*c*), as well as the nearly constant pressure signals (figure not shown) at similar check points as in Case I.

3.2 The Absolute Instability of Case-I Flow. Conventionally, hydrodynamic stability theories start from a laminar basic flow, either steady or periodic, which itself is an exact solution of the governing equations. However, turbulent flow also has stability problems. A disturbance may bring a flow from one turbulent state (e.g., attached turbulent boundary layer) to another (e.g., separated turbulent shear layer). Many worked out examples have convinced that the hydrodynamic stability theories for laminar flows can be carried over to study the stability of a turbulent mean (Reynolds-averaged) flow in an approximate sense. Along with a specific model for the closure of the URANS equations, one might conceive the stability problem of a mean turbulent flow as that of a laminar flow of a non-Newtonian fluid, of which the constitutive equation is defined by that closure model.

Having said this, we take the temporal and azimuthal average

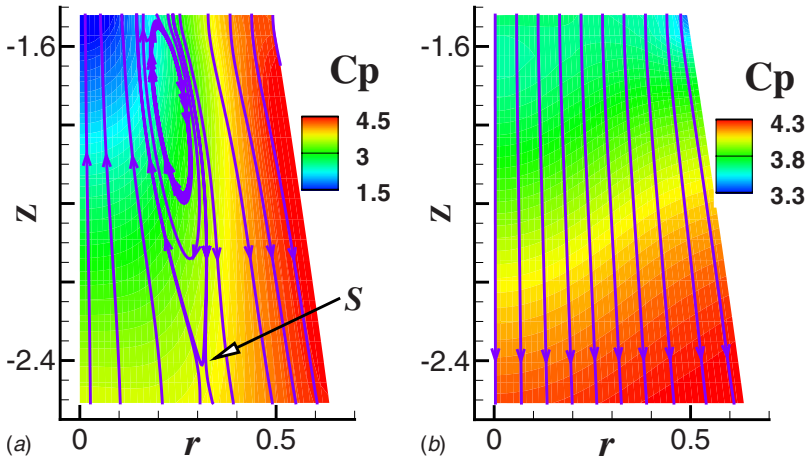

Fig. 9 Temporal-averaged streamlines and pressure distribution on the meridian plane of the cone: (*a*) Case I, where *S* is a saddle point and (*b*) Case II

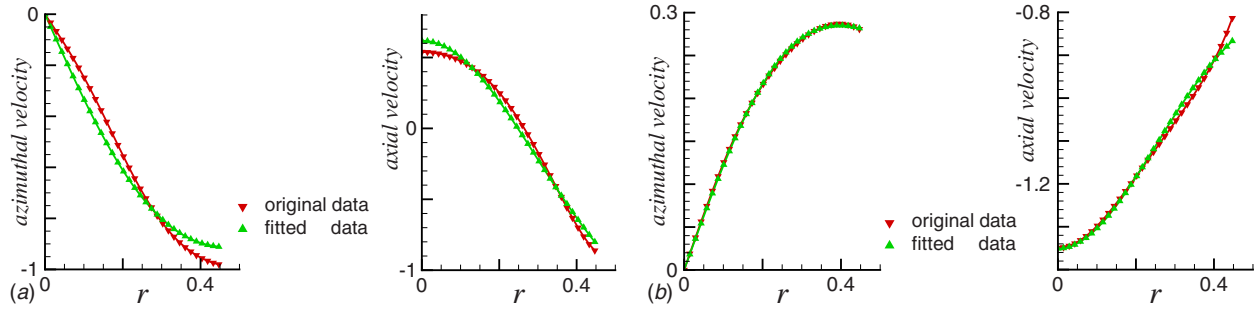

Fig. 10 Azimuthal and axial velocity profiles of the basic flow and the fitted Batchelor vortex on a cross section ($z=-2.0$), where the data are made dimensionless by the velocity scale V_0^* defined by Eq. (1) and the cone inlet diameter D^*: (*a*) Case I and (*b*) Case II

of our URANS solutions at the cone as the axisymmetric basic flows for Cases I and II and analyze their stability characteristics. Their streamlines and pressure distribution on a (r,z)-plane are shown in Fig. 9. When a local disturbance grows, the flow can be either absolutely unstable or convectively unstable, depending on whether the disturbance propagates both upstream and downstream so that the flow is gradually contaminated everywhere by a point-source input, or develops only in downstream direction so that the flow eventually recovers its undisturbed state at the location where the disturbance was initially introduced. In terms of the linear spatial-temporal normal-mode approach and in cylindrical coordinates (r,θ,z), for analyzing the AI/CI characteristics of a steady axisymmetric flow one writes the disturbance mode as

$$\boldsymbol{u}' = A(r)e^{i(kz+n\theta-\omega t)} \tag{9}$$

where $A(r)$ is the amplitude, n is the integer azimuthal wave number, and $k=k_r+ik_i$ and $\omega=\omega_r+i\omega_i$ are the complex axial wave number and frequency, respectively. If the basic swirling flow is absolutely unstable, one of the azimuthal disturbance modes ($n=0,\pm1,\pm2,\pm3,\ldots$) will grow to form a new dominating flow pattern. When the mode $n=0$ dominates, the flow evolves to a bubble-type axisymmetric structure (Fig. 2(*b*)); when the modes $n=\pm1$ or ±2 dominate, the flow evolves into a single (Fig. 2(*a*)) or double righthand/lefthand helix, respectively.

For the cone swirling flow, a sufficiently large AI zone causes the above dominant disturbance modes to fully evolve into quite strong vortical structures and hence implies the *global instability* of the basic flow [17], which completely alters the flow pattern and causes significant spontaneous unsteadiness. In principle, to identify an AI zone in the flow field one could substitute Eq. (9) into the URANS equations and then solve a linearized complex eigenvalue problem (for details see Refs. [17,18]). However, in order to see clearly the key physical mechanisms behind the AI/CI characteristics of the cone flow and to save labor, we follow Ruith et al. [19] and Zhang et al. [7] to take a much simpler approach: we fit the mean velocity profiles at many z-sections by those of the Batchelor vortex family (Eq. (4)) with only two parameters (a,q), and fully utilize the known AI/CI boundaries on the (a,q) plane. An example of such a velocity profile fitting is shown in Fig. 10, which determines the (a,q) values of the Batchelor vortex used to replace the mean RANS swirling flow at $z=-2.0$. As the z-location of the section moves downstream from the cone inlet, we obtain a "trajectory line" on the (a,q) plane to characterize the evolution of the vortex including its stability.

The AI/CI boundaries of the Batchelor vortex family on the (a,q) plane have been investigated by several authors for small Reynolds numbers $\mathrm{Re}_B=\Delta W^* R^*/\nu$. Olendradu and Sellier [20] found that the viscous instability modes decay very fast as Re_B increases, and at the largest Reynolds number, $\mathrm{Re}_B=667$, for which the AI/CI boundaries of the Batchelor vortex family have been calculated, the instability characteristics are dominated by inviscid modes. In Fig. 11 we reproduce the inviscid AI/CI boundaries at $\mathrm{Re}_B=667$ calculated by Delbende et al. [14] for different azimuthal wave numbers n, on which we plot the trajectory lines of the mean flows for Cases I and II. For comparison, Fig. 11 also reproduces the trajectory lines for the mean flows at a part-load, and the full-load conditions obtained by Zhang et al. [7] for a prototype turbine using the WTF simulation. The main difference of the WTF and SDTF's AI/CI trajectories is not caused by the computational models but the arbitrariness in choosing the (a,q) values of the Batchelor vortex as the inflow condition in SDTF computation. As far as the AI/CI characteristics are concerned, the present SDTF results are in good agreement with those obtained by the WTF computation.

Note that Fig. 11 is not yet the direct answer of the AI/CI behavior of Cases I and II flows. Our URANS simulation was made at $\mathrm{Re}=V_0^* D^*/\nu=(V_0^* D^*/\Delta W R^*)\mathrm{Re}_B \sim 1.8\times10^6$ or at an Re_B larger than 667 by two orders, for which the AI/CI boundary diagram of the Batchelor vortex family is still unknown and must differ significantly from the one shown in Fig. 11. However, one knows that [20] as Re_B increases, the AI zone on the (a,q) plane expands monotonically but in a limited manner; when $\mathrm{Re}_B \gg 1$, the swirl ratio q of the AI zone is always bounded by, roughly, $0 \le |q| \le 1.5$ for any Re_B. The zone expands mainly toward the more negative side of the external axial velocity parameter a. Therefore, we may conclude that, if a Batchelor vortex falls in the AI zone in Fig. 11, it must still do so at a Re as high as $O(10^6)$; but if the vortex falls in the CI zone in Fig. 11, it could become absolutely unstable at $\mathrm{Re}=O(10^6)$. A swirling vortex can remain convectively unstable at any Re only if its (a,q) trajectory keeps

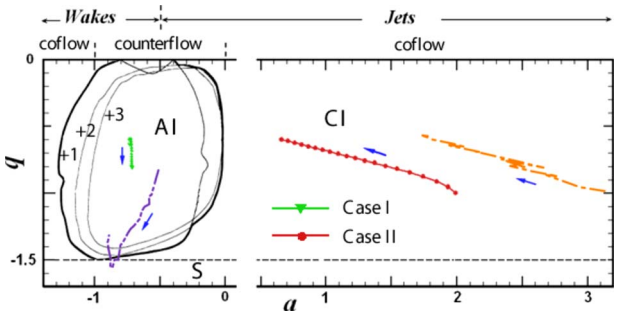

Fig. 11 AI/CI trajectory lines of the Batchelor vortex on the (a,q) plane for Cases I and II, compared with a WTF simulation result (the dashed-dot-dotted line and the dashed-dotted line are the results under part-load and full-load conditions, respectively). The arrows point to the downstream direction. Thin lines are the AI/CI boundaries for azimuthal modes $n=+1$, +2, +3 and the bold line is the outermost boundary of the AI zone, taken from Ref. [14].

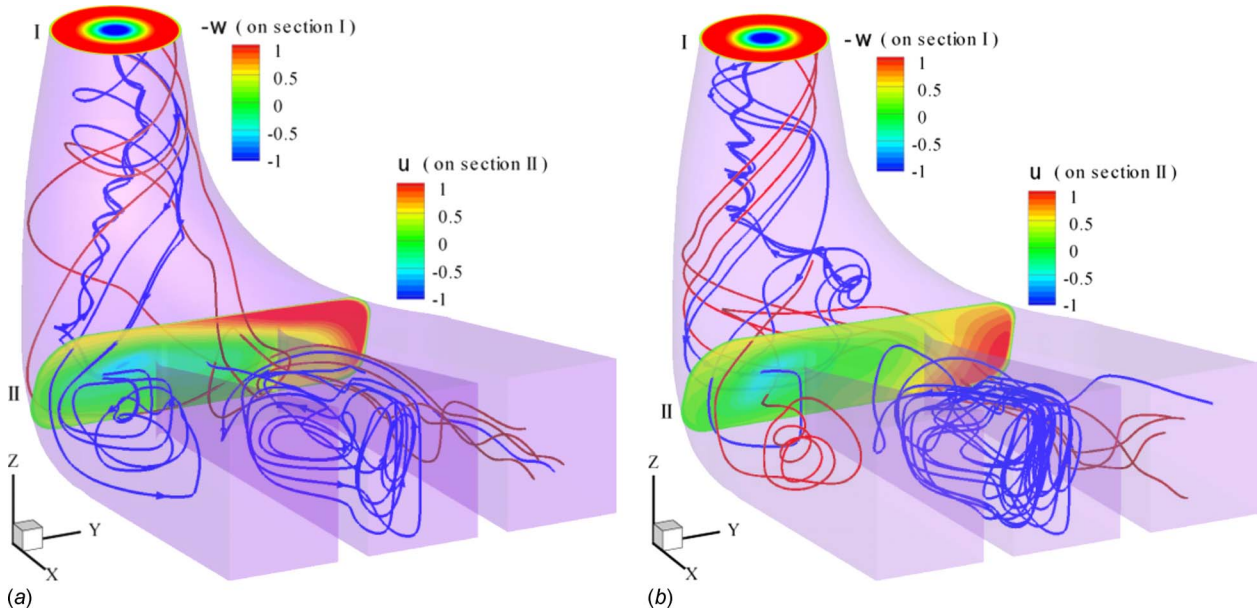

Fig. 12 Instantaneous streamlines, the $-z$-velocity contours at the inlet, and the x-velocity contours on a cross section near the exit of the elbow for Case I. Red and blue lines are in the forward and reversed streams, respectively. (*a*) $t=11.52$ and (*b*) $t=13.39$ (color online).

far from the AI zone in Fig. 11, which is the case for both mean flows of Case II (SDTF) and at full-load condition (WTF). In this way, the AI/CI characteristics of the mean flows for Cases I and II at $\mathrm{Re}=O(10^6)$ are approximately determined, with good qualitative trustworthiness.

3.3 Discussions. We now make a few discussions on the above analysis of the cone flow. First, in the WTF computation it is difficult to pinpoint the key mechanism responsible for the flow's AI behavior, e.g., whether it is the disturbances from upstream or downstream, or from the operating conditions themselves. But we now see that the latter is the major cause. This identification is of significance in establishing the physical basis for suppressing the spiral vortex rope. One has to modify the velocity profiles of the basic flow at the draft-tube inlet (the runner's exit) to prevent the flow from entering the AI zone.

Second, the runner blades are so designed that at the optimal operating condition the blades can rectify the rotating fluid toward the axial direction (along $-z$), i.e., to make it swirl-free in the cone. But in off-design conditions, as the azimuthal velocity of the flow at the guide vanes (see Fig. 1) reduces, the runner's rotational speed still remains the same. Thus, the fluid downstream the runner gains inevitably an azimuthal velocity to form a $|q|>0$ swirl in the cone. Therefore, while the above analysis has attributed the control problem to controlling the (a,q) variation along z, only the *axial velocity profile parameter* a, but not q, can be effectively monitored by some additional means.

Third, compared with the part-load and higher part-load conditions found in the WTF computation of Zhang et al. [7] (see Figs. 6(*a*) and 6(*b*) therein), the assumed part-load condition (through the choice of (a,q) at the inlet) for the present Case I leads to a more extended reversed flow from inlet to exit of the cone. This implies a larger reversed flow region and stronger global instability. Therefore, if the control strategy is found for this Case-I flow, those cases with smaller AI zones should be trackable without difficulty.

The main conclusion of this subsection is: for understanding the physical mechanism of the vortex-rope formation, it is necessary to consider a swirling flow with a radially varying axial velocity and to employ a stability theory able to handle azimuthal disturbance modes.

4 Flows in Elbow and Outlets: From Unsteady to Quasisteady

Although the preceding cone flow analysis has excluded the upstream disturbance from the key mechanisms causing the global instability of the swirling vortex, the flow downstream the cone could still affect the cone flow. This influence could be very complicated because unsteadiness, instability, flow separation, and locally reversed flow may all happen in the elbow at off-design conditions. In order to explore the axial flow control strategy, it is still necessary to continue our analysis to the flows in the elbow and three outlets. The flow control guidelines can be well established only after the entire draft-tube flow characteristics have been clarified.

4.1 Instantaneous Flow Pattern of Case I. Figure 12 shows some selected instantaneous streamlines in the entire draft tube for Case I at two instants, along with the contours of velocity components normal to two sectional planes. Recall that the cone reversed flow occurs in the core region of the swirling vortex, and the forward streams go through the outer region (Fig. 9(*a*)). We thus mark the streamlines going through these distinct regions by blue and red, respectively. From the figure one may feel how complicated the elbow flow is.

Roughly speaking, about two-thirds of the elbow space in the middle and on the right part (see the caption of Fig. 1 for "left" and "right") is full of the low-speed, reversed, and somewhat chaotic flow. On the other hand, the forward stream is always concentrated on the left part of the elbow, rather than switching back and forth among the three outlets as the vortex-rope spirals. Consequently, as shown in Fig. 13(*a*), almost the entire mass flux runs only through the left outlet at high speed, which in the transient process after the start is even larger than the total flux Q at the tube inlet. When the flow becomes stationary, the fluxes through the middle and right outlets are negative and slightly positive, respectively.

A similar uneven partition of the mass flux has been found experimentally and numerically as reported by Sabourin [21]. The underlying physics is that the left outlet is the only exit for the rotating fluid to run away tangentially as if the centripetal force provided by the tube wall is suddenly removed. A numerical test

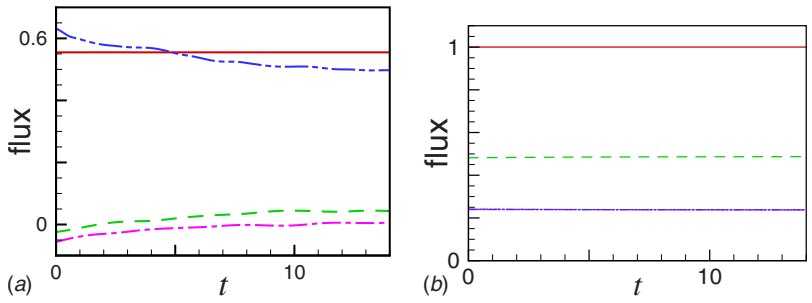

Fig. 13 Mass flux partition. Solid, dashed, dashed-dotted, and dashed-dot-dotted lines denote the fluxes through the cone inlet and right, middle, and left outlets, respectively. (*a*) Case I and (*b*) Case II.

of ours indicates that reversing the runner's rotating direction (set q to $-q$) switches the forward stream to the right exit at once. Such a high-swirl flow phenomenon forms a sharp contrast to the pretty uniformly-spread quasisteady instantaneous streamline pattern of Case II, Fig. 8(*c*). Even the flux partition of Case II exhibits a certain uneven feature. Note that the major portion of the flow for Case II gets through the right outlet because the rotating directions of the cone flows in Cases I and II are opposite.

The uneven partition of Q among the tube outlets has a correlation with the uneven distribution of the flow unsteadiness. Figure 14 displays the time variation of kinetic energy and pressure at a few points on a sectional plane (Section II in Fig. 12). The strong fluctuation on the left and front parts of the plane is governed by the periodic spiral motion of the vortex rope, but the wave pattern of the weaker fluctuation on the right and rear parts is more irregular.

For Case I, the pressure distribution at the exits of three outlets is nearly uniform (figure not shown), with variation $\max|\Delta C_p| \sim 0.3$. Although this value is just about 25% of the pressure fluctuation amplitudes in the cone (Fig. 7(*a*)), it is of the same order as that in the elbow (Fig. 14, which is about 0.5). Therefore, for revealing the fluctuating feature in the latter, it is necessary to add a river at the draft-tube outlet to impose a better outflow condition.

4.2 Pseudo-Reynolds Stress and Time-Averaged Flow. The complex elbow-outlet flow may also be examined by splitting the incompressible Navier–Stokes equation

$$\frac{\partial \boldsymbol{u}}{\partial t} + \boldsymbol{u} \cdot \nabla \boldsymbol{u} = -\frac{1}{\rho} \nabla p - \nu \nabla \times \omega \tag{10}$$

into a time-averaged part and a fluctuating part, where the gravitational potential $\rho g z$ has been absorbed into pressure p. Away from thin boundary layers, the internal vortical flow of $\mathrm{Re} = O(10^6)$ can be treated as inviscid. Denoting the time-averaged quantities by capital letters as before, the time-averaged products by an overbar, and time-fluctuating ones by a prime, we have $\boldsymbol{u} = \boldsymbol{U} + \boldsymbol{u}'$ and $p = P + p'$. The time-averaged inviscid version of Eq. (10) then yields

$$\boldsymbol{U} \cdot \nabla \boldsymbol{U} = -\frac{1}{\rho} \nabla P - \nabla \cdot (\overline{\boldsymbol{u}'\boldsymbol{u}'}) \tag{11}$$

Here, $-\nabla \cdot (\overline{\boldsymbol{u}'\boldsymbol{u}'})$ is the "pseudo-Reynolds stress," whose distribution is shown in Fig. 15. Strong fluctuations in the cone become much smaller as the flow enters the outlets. Therefore, for the flow in the lower portion of the draft tube we may drop the residual pseudo-Reynolds stress from Eq. (11). Figure 16 displays some streamlines in the time-averaged velocity field $\boldsymbol{U}(\boldsymbol{x})$ and contours of the mean pressure gradient $\partial P/\partial x$ on the three vertical planes, from which we may gain some further insights.

First, the forward and reversed mean streams are strongly correlated with the favorable and adverse $\partial P/\partial x$, respectively.

Second, the absence of mean streamlines in the left and right outlets indicates that the flow speed there is only of the order of the speed in the pseudo-Reynolds stress and hence completely filtered out. This confirms the preceding observation on the slowness of the chaotic reversed flow.

Third, while the spiral of blue streamlines in the cone segment is induced by the strong vortex rope, the vorticity in the elbow is no longer concentrated in a strong vortex, and the blue-streamline turning back toward the upstream direction is caused mainly by the adverse axial pressure gradient. This is seen most clearly from decomposing Eq. (11) in terms of intrinsic streamline coordinates (s,n,b), with orthonormal unit vectors $(\boldsymbol{t},\boldsymbol{n},\boldsymbol{b})$ along the tangential, normal, and binormal directions of a steady streamline, respectively [2]

$$-\frac{1}{\rho}\frac{\partial P}{\partial s} \simeq \frac{1}{2}\frac{\partial |\boldsymbol{U}|^2}{\partial s}, \quad -\frac{1}{\rho}\frac{\partial P}{\partial n} \simeq |\boldsymbol{U}|^2 \kappa, \quad -\frac{1}{\rho}\frac{\partial P}{\partial b} \simeq 0 \tag{12}$$

where κ is the curvature of the mean streamline. Thus, when a streamline hits an isosurface of $\partial P/\partial x$ in an inclined angle so that

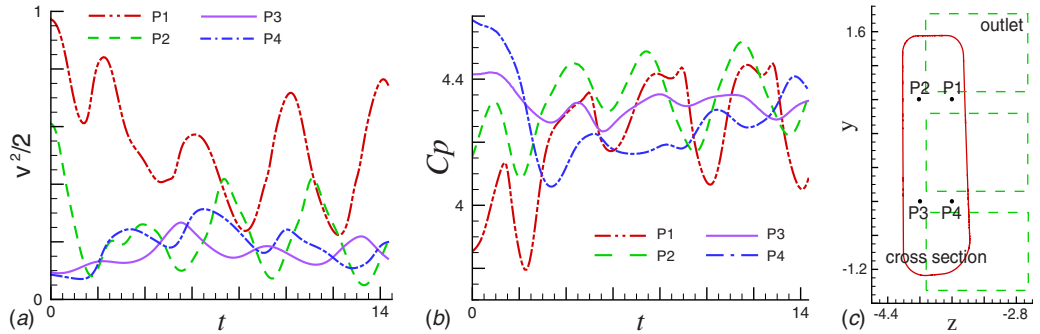

Fig. 14 Variations of kinetic energy (*a*) and pressure (*b*) versus time at four points on a sectional plane (Section II in Fig. 12); the locations of the plane and date-extracted points are defined in (*c*)

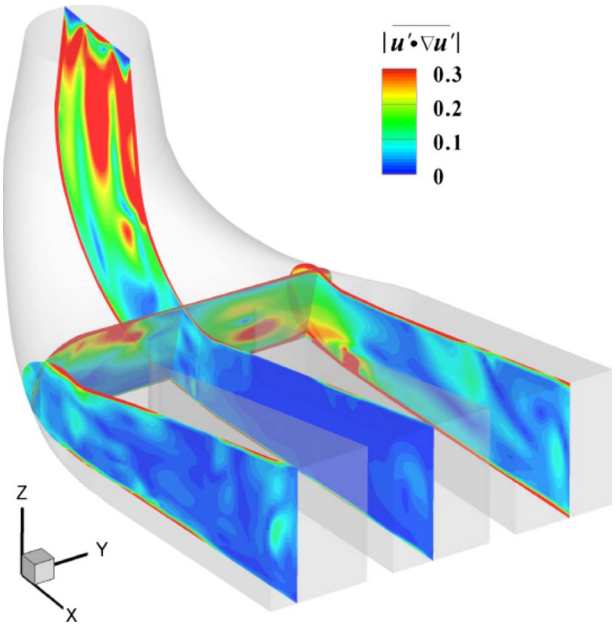

Fig. 15 Distribution of $|\overline{u' \cdot \nabla u'}|$ in the elbow and outlets

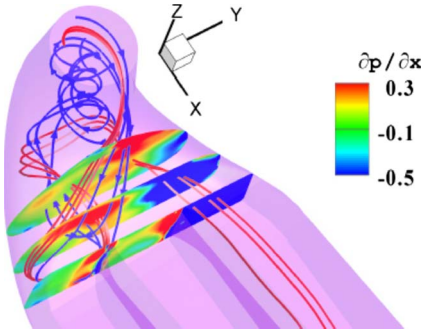

Fig. 16 Time-averaged streamlines and $\partial P/\partial x$ contours on three (y,z) planes at $x=0.7$, 1.1, and 1.5 in the draft tube for Case I. Red lines describe the forward flow, and blue lines indicate the reversed flow initiated at the center of vortex rope (color online).

there is a pressure gradient normal to the line, the streamline will make a turn; and for a given $\partial P/\partial x$, the curvature is inversely proportional to $|U|^2$, such that sharp turns occur in the lower-speed flow region. This mechanism can indeed be identified from Fig. 16.

4.3 Opposite Streams, Flow Instability, and Chaos. One more important behavior of the elbow flow suggested by Fig. 16 is the *side-by-side coexistence* of the forward and reversed streams. Driven by a local favorable pressure gradient, the high-speed forward stream carrying the entire mass flux of the draft tube tends naturally to enter the left outlet, and hence squeezing the reversed stream to the right side. This was already seen from the uneven mass-flux partition in Fig. 13, and is further confirmed by Fig. 17, which plots the mean pressure contours on an (x,y)-plane cutting the bottom of the elbow and three outlets. The high pressure at the back of elbow ($x<0$ side, see Fig. 4(a) for the location of the coordinate axes) is for balancing the centrifugal force as the fluid elements make a turn from the $-z$-direction to the nearly x-direction, and the left outlet has a much lower P and $\partial P/\partial x$ than the others. The forward stream on the left elbow and outlet forms a "mass-flux channel" of an irregular cross-sectional shape. At the upstream end of the elbow, this channel obviously links up with the annular downward jet flow at $r>0.8$, near the cone wall; while at the downstream end it runs into the left outlet and becomes quasisteady.

Note that the side-by-side forward and reversed streams must have an unstable free shear layer in between. It is sensitive to the vortex-rope sweeping disturbance and may easily evolve to a complex array of discrete vortices. This shear layer instability should be responsible for most of the chaotic behavior in the slow reversed flow region, as seen from the instantaneous streamline patterns (blue lines in Fig. 12), the magnitude of the pseudo-Reynolds stress (Fig. 15), and pressure signals (Fig. 14(b)). In contrast, the flow in the mass-flux channel (Fig. 12) is relatively more regular due to a much faster forward speed.

5 Vortex-Rope Control: Principles and Results

Ideally, for suppressing the severe pressure fluctuations, one could develop new optimal integrated design methods in a wide range of operating conditions, to produce innovative configurations for the entire turbine rather than its runner alone. But in the present study we assume that the draft-tube configuration is already fixed, and only consider possible control principles and test some control means.

5.1 Case-I Flow Robustness and Control Principles. It is well-known that the best flow control means would be using a

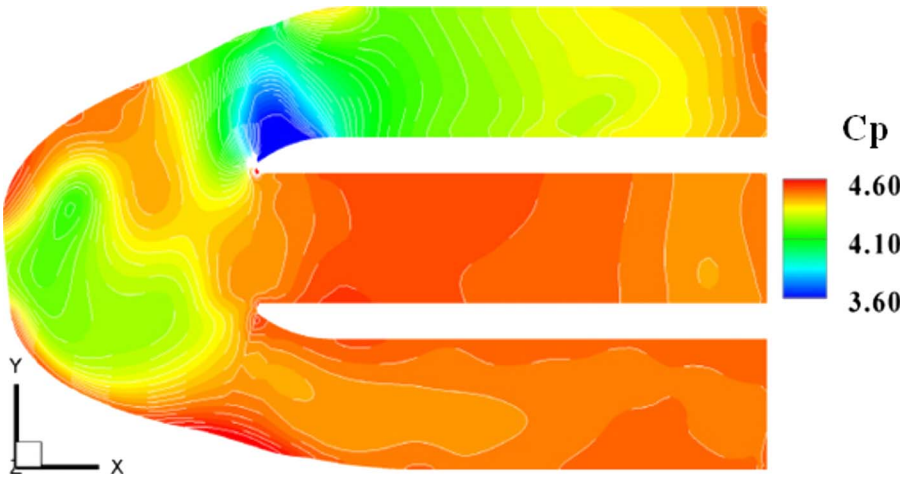

Fig. 17 Mean-pressure partition along the outlets at a horizontal sectional plane with $z=-3.6$

small power input to alter the entire flow pattern. But this principle only works at certain sensitive locations where the flow to be controlled is near its stability boundary. Now the correct control strategy has to follow from the specific stability and robustness nature of the part-load draft-tube flow. Although the rigorous stability analysis of such a complex flow is impossible, we may at least make some qualitative assessments based on our preceding results.

We have seen that the steady basic cone flow (a Batchelor vortex with wakelike counterflow) is absolutely unstable. Once the dominant disturbance mode is excited, it will evolve into the corresponding vortex-rope flow. Then the latter can hardly be altered any more by other disturbances. Namely, the periodic vortex-rope flow itself is quite robust. Here and below the word "robust" is used in a broader and more flexible sense than "stable" to describe certain flow patterns, either steady or unsteady, laminar or turbulent, which are strong existence able to withstand disturbances and maintain their *qualitative* characteristics.

We have also seen that the local stability status of the flow in the elbow and outlets is more involved than the cone flow. Putting this complexity aside, however, a critical fact is that the side-by-side coexistence of the high-speed forward stream and the disordered slow reversed flow in the elbow is even not influenced at all by the very strong upstream disturbances from the spiral vortex rope. It is actually the most robust and dominant overall pattern of the Case-I flow.

Interestingly, even the chaos in the reversed flow region may have a certain favorable effect. The chaos may block any disturbances of mild amplitude from propagation upstream and downstream. Thus, the low-frequency fluctuation caused by the vortex rope cannot penetrate the right part of the elbow down to the middle and right outlets, but can only be advected into a portion of the left outlet. This could be another possible mechanism responsible for the outlet flow steadiness. On the other hand, the stability (or convective instability) of the mass-flux channel also blocks the two-way propagation of disturbances from entering either the inlet or the exit of outlets. This fact was verified by a numerical simulation, in which we shut off the entire left exit. Except to a repartition of the mass flux between the middle and right outlets, we found that (figure not shown) the vortex rope in the cone segment was completely unaffected, and the pressure fluctuation was the same as the three-outlet case.

In summary, although the runner has been optimally designed to yield a very high energy conversion efficiency, as it is done in modern Francis turbines, the draft-tube flow still has very undesirable properties at part-load conditions. In the cone segment, the robust spiral vortex rope rules the flow and causes severe pressure fluctuation. But this strong disturbance is suppressed in the elbow and outlets by the even more robust coexistence of the quasisteady high-speed mass-flux channel and the low-speed chaotic reversed flow.

From this overall assessment, we naturally obtain a few guiding principles for effective control of Case-I flow as follows.

1. The control should be imposed at the inlet of the draft tube (exit of the runner) rather than anywhere downstream the cone segment.
2. The control should focus on dealing with the reversed axial flow at the cone inlet.
3. The control cannot be achieved by small forcing disturbances; rather, a sufficiently strong interference by either solid or fluid means is necessary.

5.2 Flux Injection at Inlet. The above control principles can explain one of the existing control means: adding a cylindrical runner-hub at the bottom of the runner center [22]. It is a passive flow control by solid means, where the runner-hub displaces a portion of the reversed flow in the cone. This simple control method leads to a favorable effect. Since the possible size of the runner-hub is limited, it can only alleviate but not fully eliminate the strong low-frequency pressure fluctuation.

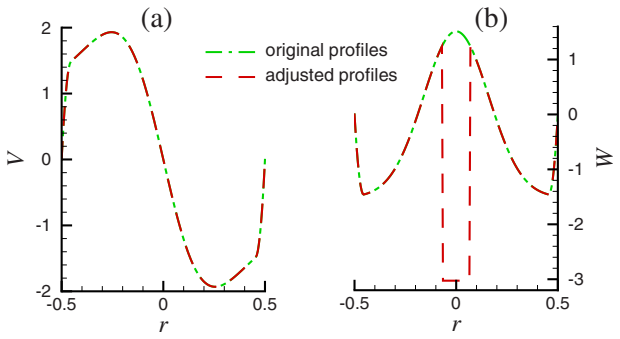

Fig. 18 Azimuthal (V) and axial (W) velocity profiles at the cone inlet for the water-injection control simulation quantities are nondimensionalized by global scales

Alternative to solid means, one may introduce a fluid flow into the cone inlet to directly counteract the reversed flow there (fluid means). The familiar air admission through the runner's center is actually a weak form of this kind of control, but "water admission" or water flux injection should be far more effective. This active control method has been studied by Blommaert [23] and Susan-Resiga et al. [24]. The latter group investigated the water-jet control to mitigate the vortex ropes at 70% best-efficiency-point discharge of a Francis turbine by three-dimensional unsteady numerical simulation. They numerically tested the water-jet flow flux Q_j ranging from 1% to 28% of the total flux Q. Although for power generation the flux used for injection is a loss, the authors claimed that the jet at part-load improves the flow in both the draft tube and the runner, and hence the overall efficiency losses due to jet operation were only in the order of 0.2%.

To test the idea of water-injection at the fundamental level, we superposed a strong axial jet within a thin cylindrical region in the neighborhood of the axis to the uncontrolled axial velocity profile of Case I, see Fig. 18. The jet adds a mass flux Q_j to the draft-tube flow with $Q_j/Q \simeq 10.2\%$. The azimuthal velocity profile remains unchanged. The Case-I flow with an already fully developed vortex rope (Fig. 6) was used as the initial flow field of the control simulation (set as $t=0$). Note that this jet flux was chosen quite arbitrarily as a preliminary test, not yet optimized.

The control effect on the vortex rope is visualized in Fig. 19 by using the Δ-criterion. Shortly after the onset of control, the jet causes the spiral vortex rope to split into two branches of different lengths (Fig. 19(*b*)). Then the shorter branch continuously splits into several little ones, and the longer branch gradually shrinks (Figs. 19(*c*) and 19(*d*)). At last, the spiral vortex rope is converted into a highly localized "mushroom" near the cone segment inlet (Figs. 19(*e*) and 19(*f*)). The vorticity is mainly concentrated in this region.

The nearly axisymmetric mushroom also indicates that the pressure fluctuation originally induced by the spiral vortex rope has now been significantly alleviated. Indeed, once the transient process is over, the flow in the entire draft tube approaches a quasi-steady state, as shown in Fig. 20, which is what is ultimately desired. Moreover, due to the water-injection, the averaged pressure at the six sample points is reduced by 1.6–8.7%, and the pressure recovery coefficient in the draft tube is increased from 63.2% to 65.6%. Therefore, the control is effective.

The instantaneous streamline pattern of the controlled draft-tube flow, at the same time of Fig. 19(*f*), is shown in Fig. 21. Remarkably, its difference from the uncontrolled pattern (Fig. 12) is quite insignificant, only a closer inspection indicates that the spirals of the controlled streamlines in the cone are much looser. The jet remains nearly straight only for a short distance (not seen in the figure), and its effect cannot reach the elbow and outlet. This fact reconfirms the preceding observation that the natural

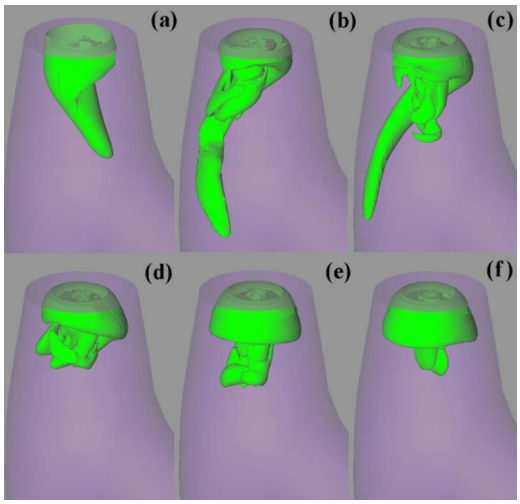

Fig. 19 Isosurfaces of Δ ($\Delta/\Delta_{max}=6\times10^{-6}$) of the controlled flow by jet injection. Starting from the onset of control, the dimensionless times in (*a*)–(*f*) are *t*=0, 3.60, 5.04, 7.92, 12.25, and 32.4, respectively.

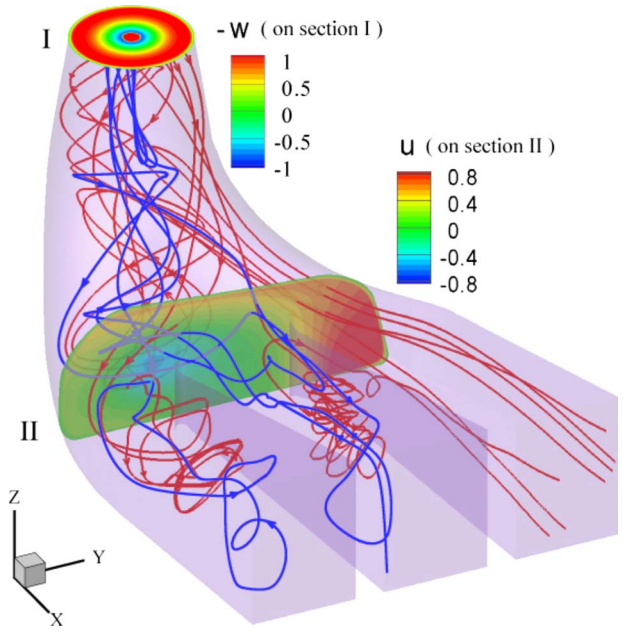

Fig. 21 Instantaneous streamlines of the controlled flow in the draft tube at *t*=32.4

tendency for the swirling flow at part-load condition to discharge from the left outlet is a very robust mechanism to calm down upstream disturbances and unsteadiness. Consequently, the mass-flux partition under the control also remains nearly the same as Fig. 13 at large *t*.

According to Susan-Resiga et al. [24], the suppression of the vortex rope and pressure fluctuation by water-injection control could reach higher energy conversion efficiency as well as hydraulic stability compared with uncontrolled flow. The gain of these performances could compensate at least part of the energy loss consumed in introducing the jet. But whether the control can bring an overall benefit in engineering applications cannot be studied by an SDTF model; one has to return to WTF simulation and experiment.

6 Conclusions

In this paper, we have investigated the physical characteristics and control strategy of the complex unsteady vortical flow in a Francis turbine draft tube, based on our RANS simulation of the SDTF under a part-load condition. The main features of the flow are found to be as follows.

- In the cone, the swirling flow is absolutely unstable, leading to a strong and robust spiraling vortex rope as the source of severe low-frequency pressure fluctuation. Since under part-load condition the fluid rotation is inevitable, the key to eliminating the vortex rope is to suppress the reversed axial flow.
- In the elbow, the forward stream with high momentum carries almost the entire mass flux of the draft tube downstream. It always goes through the left outlet due to the centrifugal force in the rotating fluid. This natural tendency pushes the reversed flow to the right portion of the elbow, which coexists with the forward stream side-by-side. The reversed fluid motion is slow but more fluctuating and chaotic, due in part to the unsteady and unstable shear layer between the two opposite streams. This complex flow pattern itself is the most robust existence in the draft-tube flow under part-load conditions.
- In three outlets, owing to the strong stabilizing effect of the natural choice of the left outlet as the mass-flux channel, the flow has a very uneven mass-flux partition but is steady. The middle and right outlets only have very small negative and positive fluxes, respectively.

Guided by the above discovery, especially by the global robustness of the entire draft-tube flow, in order to fully eliminate the harmful spiral vortex ropes under part-load conditions for a given

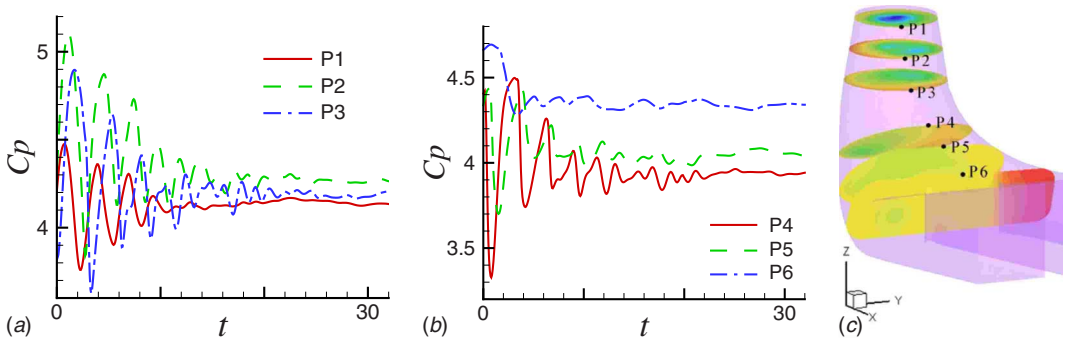

Fig. 20 Pressure fluctuations of the controlled flow by jet injection: (*a*) and (*b*) are the pressure fluctuations on six check points, whose locations are marked in (*c*)

set of runner and draft tube, one should produce a sufficiently strong interference at the draft-tube inlet to suppress the reversed axial flow. The existing air admission method is of this type but is too weak for fully eliminating the spiral vortex ropes. In contrast, as one of possible control means, a water-injection with a stronger forward mass flux is shown to be powerful and successful.

Acknowledgment

The authors are very grateful to Professors Roy Schulz, Cun-Biao Lee, Qing-Dong Cai, Wei-Dong Su, Jian-Jun Tao, Xian-Wu Luo, Le-Fu Zhang, and Mr. Yan-Tao Yang for valuable discussions. Our thanks also go to the referees for useful comments, and especially to the associate journal editor for very detailed and constructive advices that have led to the significant improvement of this paper. This work was supported in part by the National Natural Science Foundation of China (Key Project Nos. 10532010 and 90410019), and the computational work was performed on the HP cluster at the Center of Computational Science and Engineering, Peking University.

Nomenclature

- $*$ = a superscript denoting dimensional quantities; quantities without the asterisk are dimensionless
- D^* = inlet diameter of the draft tube
- ρ = density
- V_0^* = velocity scale
- T_0^* = time scale
- Q^* = volume flux
- C_p = pressure coefficient
- p = pressure
- p_{ref} = reference pressure
- (r,θ,z) = radial, azimuthal, and axial coordinates of the cylindrical system; when used as subscripts, denote the corresponding components of a vector
- (U,V,W) = radial, azimuthal, and axial components of velocity
- a = external axial velocity parameter of a Batchelor vortex
- q = swirl ratio of a Batchelor vortex
- R^* = core size of a Batchelor vortex
- W_∞^* = freestream axial velocity of a Batchelor vortex
- W_c^* = centerline axial velocity of a Batchelor vortex
- Ω_c^* = rotation rate on the axis of a Batchelor vortex
- ΔW^* = axial velocity difference of a Batchelor vortex
- Re = Reynolds number based on V_0^* and D^*
- Re_B = Reynolds number for Batchelor vortices, based on ΔW^* and R^*
- St = Strouhal number
- $(\boldsymbol{t},\boldsymbol{n},\boldsymbol{b})$ = tangential, normal, and binormal unit vectors of streamline coordinates

References

[1] Lambourne, N. C., and Bryer, D. W., 1961, "The Bursting of Leading Edge Vortices—Some Observation and Discussion of the Phenomenon," Aeronautical Research Council, Report No. 3282.
[2] Wu, J. Z., Ma, H. Y., and Zhou, M. D., 2006, *Vorticity and Vortex Dynamics*, Springer-Verlag, Berlin.
[3] Susan-Resiga, R., Ciocan, G. D., and Avellan, F., 2004, "Swirling Flow Downstream a Francis Turbine Runner," The Sixth International Conference on Hydraulic Machinery and Hydrodynamics, Romania.
[4] Susan-Resiga, R., Avellan, F., Ciocan, G. D., Muntean, S., and Anton, I., 2005, "Mathematical and Numerical Modeling of Swirling Flow in Francis Turbine Draft Tube Cone," Workshop on Vortex Dominated Flows—Achievements and Open Problems, Timisoara, Romania.
[5] Susan-Resiga, R., Ciocan, G. D., Anton, I., and Avellan, F., 2006, "Analysis of the Swirling Flow Downstream a Francis Turbine Runner," ASME J. Fluids Eng., **128**, pp. 177–189.
[6] Benjamin, T. J., 1962, "Theory of the Vortex Breakdown Phenomenon," J. Fluid Mech., **14**, pp. 593–629.
[7] Zhang, R. K., Cai, Q. D., Wu, J. Z., Wu, Y. L., Liu, S. H., and Zhang, L., 2005, "The Physical Origin of Severe Low-Frequency Pressure Fluctuations in Giant Francis Turbines," Mod. Phys. Lett. B, **19**(28–29), pp. 1527–1530.
[8] Liu, S. H., Shao, Q., Yang, J. M., Wu, Y. L., and Dai, J., 2005, "Unsteady Turbulent Simulation of Prototype Hydraulic Turbine and Analysis of Pressure Fluctuation in Draft Tube," J. Hydraul. Eng., **24**(1), pp. 75–78 (in Chinese).
[9] Nishi, M., Yoshida, K., Ma, Z., and Fujii, M., 2000, "Alleviation of the Pressure Surge Observed in an Elbow Draft Tube by Installation of Fin," *Proceedings of 20th IAHR Symposium on Hydraulic Machinery and Systems*, Charlotte, NC.
[10] Nishi, M., Yoshida, K., Ma, Z., Fujii, M., and Miyamoto, K., 2002, "A Study on Hybrid Control of Draft Tube Surge," *Proceedings of 22nd IAHR Symposium on Hydraulic Machinery and Systems*, Lausanne, Switzerland.
[11] Ruprecht, A., Helmrich, T., Aschenbrenner, T., and Scherer, T., 2002, "Simulation of Vortex Rope in a Turbine Draft Tube," *Proceedings of 22nd IAHR Symposium on Hydraulic Machinery and Systems*, Lausanne, Switzerland.
[12] Buntic, O. I., Dietze, S., and Ruprecht, A., 2005, "Numerical Simulation of the Flow in Turbine-99 Draft Tube," Proceedings of Third IAHR/ERCOFTAC Workshop on Draft Tube Flow, Sweden.
[13] Fluent, I., 2006, *FLUENT User's Guide*, Fluent Inc.
[14] Delbende, I., Chomaz, J. M., and Huerre, P., 1998, "Absolute/Convective Instability in the Batchelor Vortex: A Numerical Study of the Linear Impulse Response," J. Fluid Mech., **355**, pp. 229–254.
[15] Wu, J. Z., Xiong, A. K., and Yang, Y. T., 2005, "Axial Stretching and Vortex Definition," Phys. Fluids, **17**, p. 038108.
[16] Zhu, Y., 2006, "Stability Study of Giant Francis Turbines," M.S. thesis, Tsinghua University, China (in Chinese).
[17] Huerre, P., and Monkewitz, P., 1990, "Local and Global Instabilities in Spatially Developing Flows," Annu. Rev. Fluid Mech., **22**, pp. 473–537.
[18] Yin, X., and Sun, D., 2003, *Vortex Stability*, National Defense Industry, Beijing (in Chinese).
[19] Ruith, M. R., Chen, P., Meiburg, E., and Maxworth, T., 2003, "Three-Dimensional Vortex Breakdown in Swirling Jets and Wakes," J. Fluid Mech., **486**, pp. 331–378.
[20] Olendradu, C., and Sellier, A., 2002, "Viscous Effects in the Absolute-Convective Instability of the Batchelor Vortex," J. Fluid Mech., **459**, pp. 371–396.
[21] Sabourin, M., 2002, "Numerical Simulation and Flow Analysis of an Elbow Diffuser," Ph.D. thesis, École Polytechnique Fédérale de Lausanne, Lausanne, Switzerland.
[22] Liu, S. H., Wu, X. J., and Wu, Y. L., 2006, "Analysis of the Influence of Runner-Hub Shape on the Internal Flow in Francis Turbine," J. Hydraul. Eng., **25**(1), pp. 67–71 (in Chinese).
[23] Blommaert, G., 2000, "E´tude du Comportement Dynamique des Turbines Francis: Contro^le Actif de Leur Stabilite de Fonctionnement," Ph.D. thesis, École Polytechnique Fédérale de Lausanne, Lausanne, Switzerland.
[24] Susan-Resiga, R., and Vu, C. T., Muntean, S., Ciocan, G. D., and Nennemann, B., 2006, "Jet Control of the Draft Tube Vortex Rope in Francis Turbines at Partial Discharge," *Proceedings of the 23rd IAHR Symposium on Hydraulic Machinery and Systems*, Yokohama, Japan, Oct. 17–21, Paper No. 192.

Simulation of Turbine Blade Trailing Edge Cooling

Jongwook Joo

Paul Durbin

Aerospace Engineering,
Howe Hall,
Iowa State University,
Ames, IA 50011

The cause of overprediction of cooling efficiency by unsteady Reynolds averaged simulations of turbine blade trailing edge cooling flow is investigated. This is due to the deficiency in the level of unsteady coherent energy very near to the wall. Farther from the wall, the Reynolds averaged simulation produces the correct level of mixing. Eddy simulations of the instantaneous turbulent eddying produce a close agreement to data on film effectiveness. In particular, they reproduce the reduction in cooling effectiveness toward the trailing edge that has been seen in experiments. The scale adaptive simulation model of Menter and Egorov (2005, "A Scale-Adaptive Simulation Modeling Using Two-Equation Models," AIAA Paper No. 2005-1095) is invoked for the eddy simulations.
[DOI: 10.1115/1.3054287]

1 Motivation

Trailing edges of turbine blades are thin, difficult to cool, and susceptible to excessive heating by hot ambient gases. In the standard cooling strategy, the rear portion of the blade has an opening on the pressure side through which gas that has transited internal passages exits. After exiting it creates a jet tangential to the surface.

The terminology used herein is as follows (see Fig. 1). The opening is referred to as a *breakout* and the flow from the opening is called *pressure side bleed*. Cooling air exits from a rectangular *nozzle* in the breakout and is expected to form a cooling shield over the surface. The exposed portion of the wall jet is bounded by raised portions of the blade called *lands*. The upper edge of the nozzle is called the *nozzle lip*. It turns out to be important that the thickness of the nozzle lip is comparable to the nozzle opening below it. This is because vortices shed from the lip are able to reach the wall and affect surface transport. Our results suggest that the significant elements are that the nozzle lip geometry produces shedding and that it is near the heat transfer surface; any role of the precise geometry is assumed to be subsidiary, unless it is such as to alter shedding.

The adiabatic *cooling effectiveness* is the ratio of hot gas temperature minus surface temperature to hot gas minus coolant temperature

$$\eta_{\text{ad}} = (T_g - T_s)/(T_g - T_c)$$

If the surface is maintained at the coolant temperature, this is unity; as the surface heats up toward T_g, it decreases. The aim of film cooling is to keep η_{ad} near unity. Unfortunately, laboratory tests show that the film cooling effectiveness decreases to about 0.5 near the trailing edge at typical blowing ratios (blowing ratio is the ratio of the bulk mass flow from the slot to that in the freestream). This low performance of film cooling implies that some kind of mixing phenomenon between the coflowing hot gas and the cooling air streams occurs. Since its source is not well understood, it will be called *anomalous mixing*; the motive for the present work is to understand its origin. As will be seen, the phenomenon that we are labeling "anomalous" can be simulated.

Most numerical studies of the trailing edge configuration have employed Reynolds averaged Navier–Stokes (RANS) models [1–4]. Unsteady RANS shows that coherent vortex shedding from the nozzle lip plays a critical role in the flow around the breakout. Figure 2 is an illustration that shows shedding from the upper nozzle lip. Unfortunately, in all of these studies the natural unsteadiness was unable to reproduce the drop in effectiveness seen in laboratory experiments; in the case computed by Medic and Durbin [4] and Holloway et al. [3], the observed effectiveness was 0.5, while the computed effectiveness was 0.9. An unknown process seemed to enhance mixing beyond what could be explained by vortex shedding alone.

One should not be misled by Fig. 2: the geometry is three-dimensional and so are the vortices. They have an intricate form, shown at the left side of Fig. 3. Nevertheless, being a property of the averaged flow field, these vortices are periodic in time.

The air flow is supplied from a plenum. Further RANS simulations [4], in which the plenum flow was pulsed periodically, were able to reproduce the observed drop in effectiveness. The pulsation was a computational artifice that produced a relatively good agreement with the laboratory measurements of effectiveness. The forcing caused the shed vortices to develop into vortex loops (right image in Fig. 3), which enhanced mixing and decreased η_{ad} to the levels seen in the experiment. These simulations suggest a possible cause of the strong mixing present in real trailing edge breakouts. Shed vortices may have a more looped shape than predicted. However, the vortex loops seen by Medic and Durbin [4] were produced by an artifice. Is there any reason for the coherent vortex loops to form more naturally?

This and other questions can be answered by simulating the turbulent eddying flow downstream of the breakout. Trailing edge film cooling flow is challenging to compute, but, fluid dynamically, quite interesting and of some practical importance. Eddy simulation promises detailed information that can reveal the complex, and poorly understood, mixing mechanisms that occur in this flow.

Menter and Egorov [1] presented a form of eddy simulation, which they called scale adaptive simulation (SAS). Functionally, it involves adding a term that constrains the level of eddy viscosity provided by the RANS model, thereby permitting chaotic eddying to occur. The natural instability of separated shear layers is exploited to permit eddies to develop.

One of the illustrations in Ref. [1] is a trailing edge cooling geometry. This simulation was described only briefly, but it was noted that SAS produced a significantly better agreement to experimental data than unsteady RANS. The particular geometry was a breakout without lands. The coherent unsteadiness seen in the present simulations was not present. Experiments without lands show that the tangential jets are highly unsteady, with no clear coherence [5,6]. In another context, Viswanathan et al. [7] invoked implicit large eddy simulation (LES) in the trailing edge region at the origin of a jet; their interest was rather different from the present.

Contributed by the Fluids Engineering Division of ASME for publication in the JOURNAL OF FLUIDS ENGINEERING. Manuscript received May 7, 2008; final manuscript received October 23, 2008; published online January 9, 2009. Assoc. Editor: Ugo Piomelli.

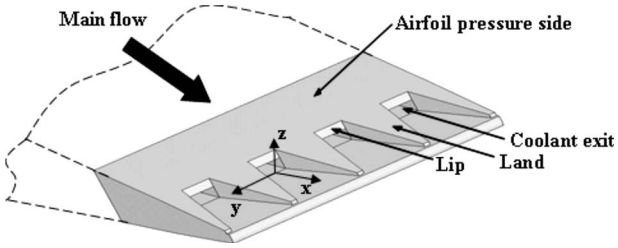

Fig. 1 Trailing edge cooling slots at pressure side breakout

At this point our terminology should be explained. We use "eddy simulation" as a general term to refer to computations in which the chaotic state of turbulence is resolved. The primary distinction is between statistical approaches based on Reynolds averaged equations [8] and turbulence-resolving approaches. The words eddy simulation are the common component, and the essential element, of a variety of Navier–Stokes computations of turbulent flow. SAS grew out of detached *eddy simulation*. It is formulated as a hybrid RANS/LES approach. The eddying region is regarded as a large *eddy simulation* region. As will be seen, the Reynolds number is fairly low in the present simulation, the fully RANS region permitted by SAS is absent, and our simulation turns out to be similar to LES. Rather than describe this as a qualified version of either detached or large eddy simulation, it is preferable to adopt the generic term eddy simulation.

2 Numerical Methods and Models

The simulations made use of the SUMB computational fluid dynamics code, as described in Ref. [9]. This is a multiblock structured grid code. It solves the compressible Reynolds averaged Navier–Stokes equations, which are discretized into finite volumes. Solution variables are collocated at cell centers, and time accuracy is achieved by dual time stepping. The true time step is discretized by second order backward Euler differencing, and each true time step is subintegrated into pseudotime by the five stage Runge–Kutta scheme of Jameson [10]. Convergence is accelerated by multigrid iterations, and the Runge–Kutta integrations function as a smoother on the successively coarser grids.

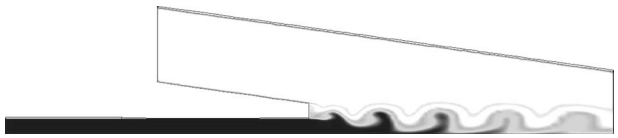

Fig. 2 Vortex shedding from upper nozzle lip: temperature contours from Ref. [4]

SUMB is a fully compressible Navier–Stokes code. The present simulations were nearly incompressible; the reference Mach number was 0.2. The basic equations that SUMB solves are the unsteady, compressible momentum, continuity, and energy equations

$$\frac{\partial \rho \boldsymbol{U}}{\partial t} + \nabla \cdot \rho \boldsymbol{U}\boldsymbol{U} = \nabla \cdot \boldsymbol{\Sigma}$$

$$\frac{\partial \rho}{\partial t} + \nabla \cdot \rho \boldsymbol{U} = 0 \tag{1}$$

$$\frac{\partial \rho e_t}{\partial t} + \nabla \cdot (\rho e_t + P)\boldsymbol{U} = \boldsymbol{\nabla} \cdot (\kappa + \kappa_T)\, \boldsymbol{\nabla} T$$

where the stress tensor is

$$\Sigma_{ij} = -P\delta_{ij} + (\mu + \mu_T)\left(\frac{\partial U_i}{\partial x_j} + \frac{\partial U_j}{\partial x_i}\right) - \frac{2}{3}(\mu + \mu_T)\frac{\partial U_k}{\partial x_k}\delta_{ij} \tag{2}$$

and the total energy is

$$e_t = C_v T + \tfrac{1}{2}|\boldsymbol{U}|^2$$

C_v is the specific heat capacity. The equation of state $P = \rho RT$ completes the system. The equation for a diffusive, passive scalar is

$$\frac{\partial C}{\partial t} + \nabla \cdot \rho \boldsymbol{C} = \boldsymbol{\nabla} \cdot (\alpha + \alpha_T)\, \boldsymbol{\nabla} C \tag{3}$$

Equations (2) and (3) contain eddy transport coefficients, μ_T and α_T. The eddy diffusivity is given by $\alpha_T = \nu_T / \mathrm{Pr}_T$ with $\mathrm{Pr}_T = 0.9$ and $\nu = \mu/\rho$. A turbulence model—in the present case, SST (Shear Stress Transport [11]) for RANS and SST-SAS for eddy

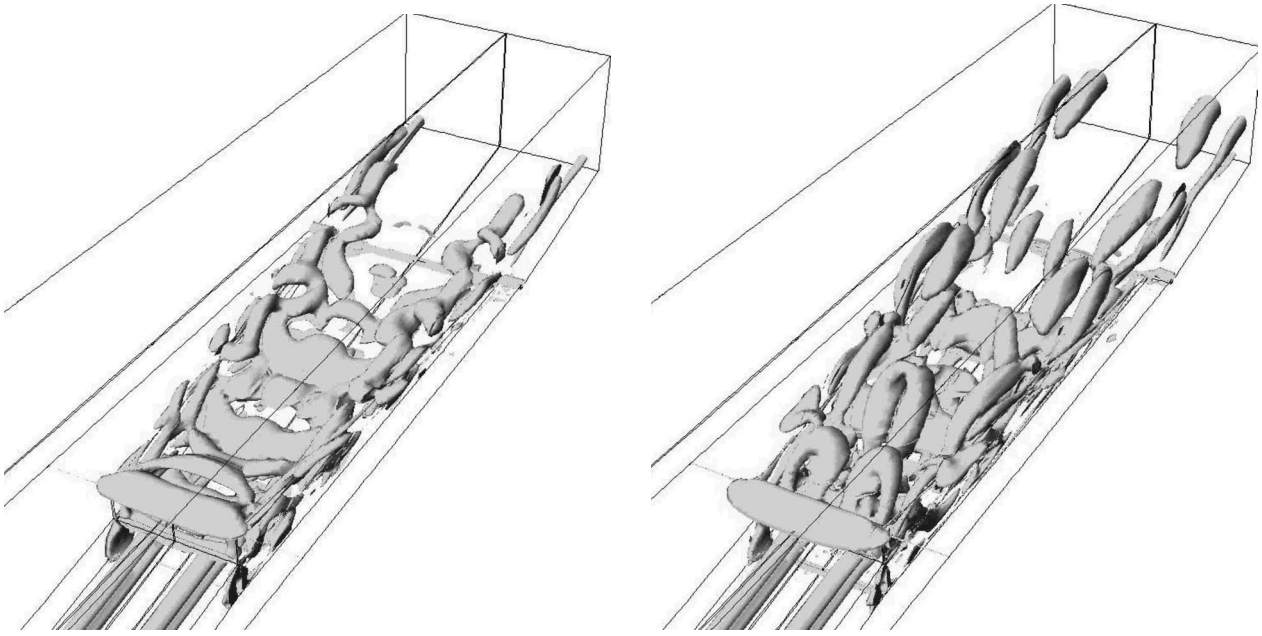

(*a*) (*b*)

Fig. 3 Natural (left) and forced (right) unsteadiness in RANS simulations [4]

simulation—determines the eddy viscosity throughout the flow field: that is, $\mu_T(\boldsymbol{x})=[\rho k\omega](\boldsymbol{x})$.

A number of modifications to the numerical discretization and time advancement methods were effected for the present application. These were required in order to obtain the accuracy and stability needed for eddy simulation.

2.1 Scale Adaptive Simulation. The SST RANS model [11] is a variant of the k-ω model. The scale adaptive SST model is the RANS model with an extra term in the ω equation. In SAS, the adaptive scale is provided by the von Karman length [12]

$$L_{\mathrm{vK}}^2=\frac{|\kappa \boldsymbol{S}|^2}{|\nabla^2 \boldsymbol{U}|^2} \tag{4}$$

where $\kappa=0.41$. The denominator denotes $\nabla^2 U_i \nabla^2 U_i$ and

$$|\boldsymbol{S}|^2=2S_{ij}S_{ji} \quad \text{with} \quad 2S_{ij}=\partial_i U_j+\partial_j U_i \tag{5}$$

In parallel shear flow, this scale becomes $L_{\mathrm{vK}}=|d_y U/d_y^2 U|$. If L_{vK} was used in an eddy viscosity transport model, assuming that destruction and production were in balance, would give

$$\nu_T \sim L_{\mathrm{vK}}^2|\boldsymbol{S}| \tag{6}$$

Thus L_{vK} can be understood to be a bit like a mixing length.

The use of a flow dependent length scale is the scale adaptive aspect of the SAS formulation. Although Menter and Egorov [12] argued that L_{vK} was a natural flow scale, as opposed to the grid scale Δ, when it is evaluated by finite differences on a typical SAS grid, L_{vK} varies in approximate proportion to Δ; indeed, it draws a connection to LES subgrid models.

In order to ensure that the model dissipates small scales, the eddy viscosity is prevented from dropping below the level of the Smagorinsky subgrid model. A limiter is applied to redefine the von Karman length as

$$L_{\mathrm{vK}}=\max\left[\frac{\kappa|\boldsymbol{S}|}{|\nabla^2 \boldsymbol{U}|},\frac{0.358C_\mu\Delta}{\beta-C_\mu\alpha}\right] \tag{7}$$

where $C_\mu=0.09$ and $\beta=3/40$ in the k-ω model (it is interpolated between this and 0.0828 in the SST model).

The SST-SAS model was originally derived from an eddy viscosity transport equation by adjoining the k-equation to it. Then it was converted into a pair of equations for k and ω. The outcome is just to add the term

$$Q_{\mathrm{SAS}}=\rho\ \max\left\{2.65\frac{L}{L_{\mathrm{vK}}}|\boldsymbol{S}|^2-6k\ \max\left[\frac{|\nabla\omega|^2}{\omega^2},\frac{|\nabla k|^2}{k^2}\right],0\right\} \tag{8}$$

to the ω equation, where

$$L=\frac{\sqrt{k}}{C_\mu^{1/4}\omega}$$

Constants given in Ref. [13] have been substituted to obtain a numerical value 2.65 in Eq. (8). The max functions in Eq. (8) help preserve the RANS behavior near walls.

2.2 Treatment of Convection. Eddy simulation requires convection schemes with low dissipation. The native discretizations in SUMB are unsatisfactory for present purposes. Alterations were made to their treatment of convection. Initially a centered discretization was tried for convective flux interpolation, which proved to be unstable. A skew symmetric convective form was found to be stable and accurate. The compressible skew form for the flux derivative is

$$\frac{\partial \rho u_i u_j}{\partial x_j}=\frac{1}{2}\left[\frac{\partial \rho u_i u_j}{\partial x_j}+\rho u_j\frac{\partial u_i}{\partial x_j}+u_i\frac{\partial \rho u_j}{\partial x_j}\right] \tag{9}$$

The rationales given in the literature for this form are consistent with kinetic energy conservation, via the discrete product rule, and reduction in aliasing error [14].

A finite volume discretization of Eq. (9) was implemented into the simulation code. Fluxes on the centers of cell faces are approximated by the average of neighboring cell center values. The terms that are not in conservation form are obtained from cell center values time derivatives obtained by the Gauss' theorem. In short, standard second order centered formulas are used.

The skew form (9) was adopted for both the momentum and the energy equations. Transported scalars are especially prone to numerical oscillations. It has become common practice in eddy simulation to invoke some degree of upwinding to obtain smooth scalar fields. The second order upwind method of Barth and Jespersen [15] was selected. It invokes a limiter to minimize numerical diffusion; thus, on a smooth field it relaxes to second order central differencing.

The scalar flux $C\equiv\int\nabla\cdot(\rho\phi\boldsymbol{u})dV$ is expressed as a difference between face centered values. For instance, in the x_i direction

$$C=(\rho\phi\boldsymbol{u}\cdot\boldsymbol{A})_{i+1/2,j}-(\rho\phi\boldsymbol{u}\cdot\boldsymbol{A})_{i-1/2,j} \tag{10}$$

The velocity is interpolated to the cell face. The face-center scalar is evaluated by a limited linear interpolation

$$\phi_{i+1/2}=\begin{cases}\phi_i+\Phi\ \nabla\ \phi_i\cdot\boldsymbol{\Delta S} & \text{if } u>0\\ \phi_{i+1}+\Phi\ \nabla\ \phi_{i+1}\cdot\boldsymbol{\Delta S} & \text{if } u<0\end{cases} \tag{11}$$

where $\boldsymbol{\Delta S}$ is a vector from the upstream cell center (i or $i+1$) to the center of the face ($i+1/2$). The gradients, $\nabla\phi_i$, are computed by Gauss' theorem. The coefficient Φ is a limiter that satisfies $0\le\Phi\le1$. It introduces upwind biasing. The limiting scheme is described in Ref. [15].

2.3 Implicit Compact Filtering. A very weak numerical instability was observed as simulations proceeded. As it was of high spatial frequency, a low pass filter was applied periodically to suppress it. A compact Padé type of formulation was used. Several families of filtering schemes were discussed in Ref. [16]. The present choice is

$$\alpha\hat{f}_{i+1}+\hat{f}_i+\alpha\hat{f}_{i-1}=af_i+\tfrac{1}{2}b(f_{i+1}+f_{i-1})+\tfrac{1}{2}c(f_{i+2}+f_{i-2}) \tag{12}$$

where

$$a=\tfrac{1}{8}(6\alpha+5),\quad b=\tfrac{1}{2}(2\alpha+1),\quad c=\tfrac{1}{8}(2\alpha-1)$$

$$\alpha=0.475$$

This is applied separately along each computational coordinate. $\hat{f}$ is the filtered value of a variable and f is the value before filtering. Near boundaries, the full stencil is not available. At such locations the explicit filter

$$\hat{f}_1=\frac{15f_1+4f_2-6f_3+4f_4-f_5}{16}$$

was applied. The filtering operation is to replace all field variables, f, by their filtered values, $\hat{f}$. The filter is designed to be flat at a low wavenumber and to cut off at a high wavenumber. It will be seen in Fig. 23 that the cutoff is well above frequencies of present concern. The compact filter (Sec. 2.3) was applied once every 47 time steps to remove gridwise oscillation.

2.4 Inflow Conditions. In order to inject a turbulent inflow, the entrance to the computational domain was treated as an interface between two flow fields, rather than an inlet, per se. In particular, the usual characteristic inflow conditions would permit four quantities to be given, and the fifth would be extrapolated from the interior. However, at an interface between computational blocks, all five variables are prescribed from an adjacent block. On the inlet plane, all three components of $\boldsymbol{u}$, the pressure, p, and density ρ are prescribed as a function of position at each time.

It proved necessary to include eddies at the inflow in order to stimulate turbulent motion in the separation region. To this end, inflow data were generated by a separate large eddy simulation of

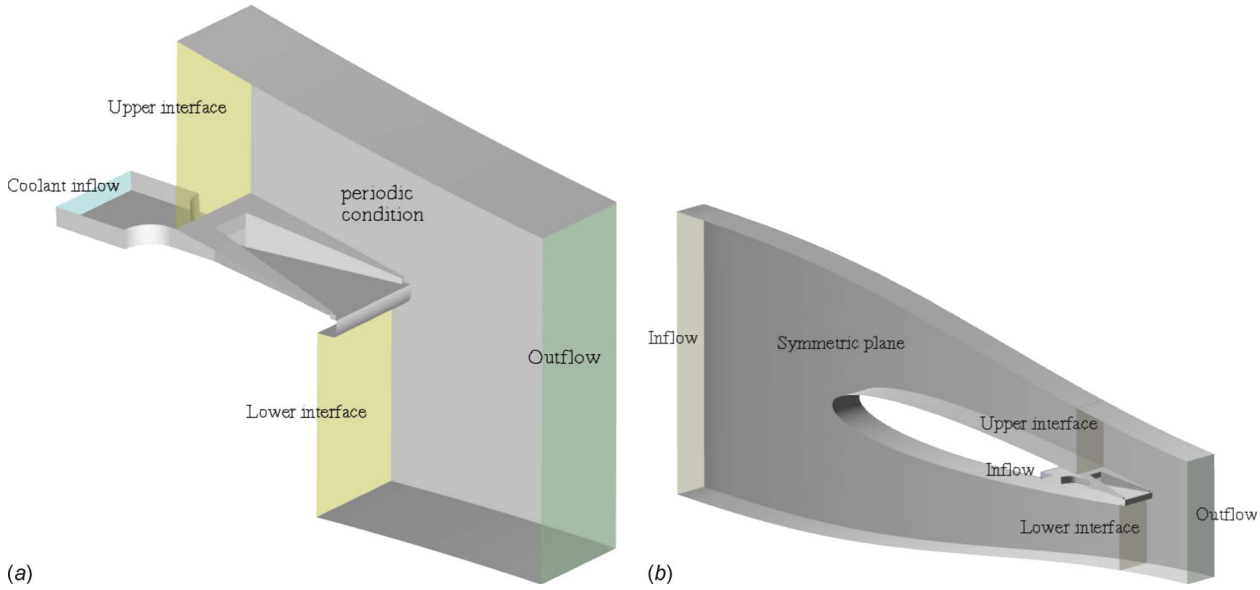

Fig. 4 Schematic of the eddy simulation setup and of the whole channel RANS simulation setup

a turbulent boundary; the LES code was provided by Kang and Choi [17]. The rescaling and recycling techniques of Lund et al. [18] were used to create a fully developed boundary layer.

While the LES simulation provides a full velocity field, quantities such as k and ω also are needed for the SST-SAS model. In the SAS mode, k and ϵ can be understood as subgrid scale residual kinetic energy and dissipation. Although more sophisticated methods could be investigated, currently a rather straightforward approach was used. Assuming that the LES field resolves almost all turbulent kinetic energy, a box filter was applied over the field. The filter width was small enough to preserve most of the energy. The residual kinetic energy was defined as

$$k = \tfrac{1}{2}U_iU_i - \tfrac{1}{2}\hat{U}_i\hat{U}_i$$

ϵ was estimated from subgrid scale dissipation as

$$\epsilon \approx 2\nu_{T,\mathrm{SGS}}S_{ij}S_{ij}$$

Finally ω was evaluated as $\omega = \epsilon/(0.09k)$.

3 Flow Configuration

The computational domain is portrayed at the left of Fig. 4. The inflows above and below the blade are labeled as "interfaces" because data from a large eddy simulation are provided there. The coolant inflow data are provided by a large eddy simulation of a fully developed channel flow. The bulk velocity is unity by the present nondimensionalization. The lateral boundary conditions are periodic, emulating a row of cooling slots along a trailing edge.

The eddy simulation was preceded by a RANS computation on the domain shown at the right of Fig. 4. This contains a whole blade in a domain that was designed to emulate the pressure field of a turbine stage (this particular configuration is being studied in experiments at Stanford University). SUMB was used for both RANS and eddy simulations. The RANS simulation provided a mean flow at the inlet to the eddy simulation. This procedure is illustrated in Fig. 5. Data are extracted from the RANS computation, then boundary layer turbulence is added (as described in Sec. 2.4) to generate an inflow for the eddy simulation.

The grid sections in Fig. 6 give an overview of how the full domain was meshed for the eddy simulation. The computational domain extends inside the blade, starting in a plenum. Above the blade the grid becomes coarse in the freestream. This is a structured multiblock grid; the total number of computational blocks is 54.

Lengths are nondimensionalized by the slot height, h, and velocities by the bulk velocity of the cooling jet, U_0. In these units, the nozzle lip thickness is 0.7. The surface between the lands slopes at about 3 deg from the horizontal, so the wall is at a distance $0.05x$ above the x axis. The origin is at the center of the breakout. The trailing edge is 8.3 slot heights from the breakout. The width of the breakout is 5. The overall domain width is 12: periodic boundary conditions make this the repeat unit of a periodic array of trailing edge cooling slots. The Reynolds number based on the height and the bulk velocity of the channel is 7385. This is representative of the Reynolds numbers of high pressure turbine blades.

A time step of 0.0257 was used for the blowing ratio 1 case. For the blowing ratio of 1.5 case, the time step was reduced to 0.0185 due to the increased jet Reynolds number.

To assess the temporal resolution, two different time steps, of 0.0514 (in units of h/U_0) and 0.0257, were tested. With the larger time step, turbulent fluctuations were somewhat damped. The well resolved energy spectra in Sec. 4.2 indicate that the current temporal resolution is sufficient.

Before collecting statistics, simulations were run for ten flow-through times. Then statistics were collected over 13.8 flow-through times.

Unsteady RANS simulations were also done in the trailing edge geometry. The time step size was 0.063, which resolves one shedding period into 66 time steps. Nine flow-through times were allowed for initial transients. After this, the periodic Reynolds averaged state was reached.

Extensive grid refinement and validation studies are presented in Ref. [19]. Under the scale adaptive modeling approach, the greatest concern is to resolve the separated region. In a preliminary study, very coarse grids with high stretching ratios were tested. Severe grid-to-grid point oscillations and spurious streamwise waves in the vorticity field were observed. As a result of this preliminary study, a base grid was created with 8×10^6 computational cells. The final grid was created by refining this in each of the x, y, and z directions. Overall comparisons between the 8×10^6 point grid and final grid resolutions are summarized in Tables 1 and 2. For the RANS simulations presented herein, a

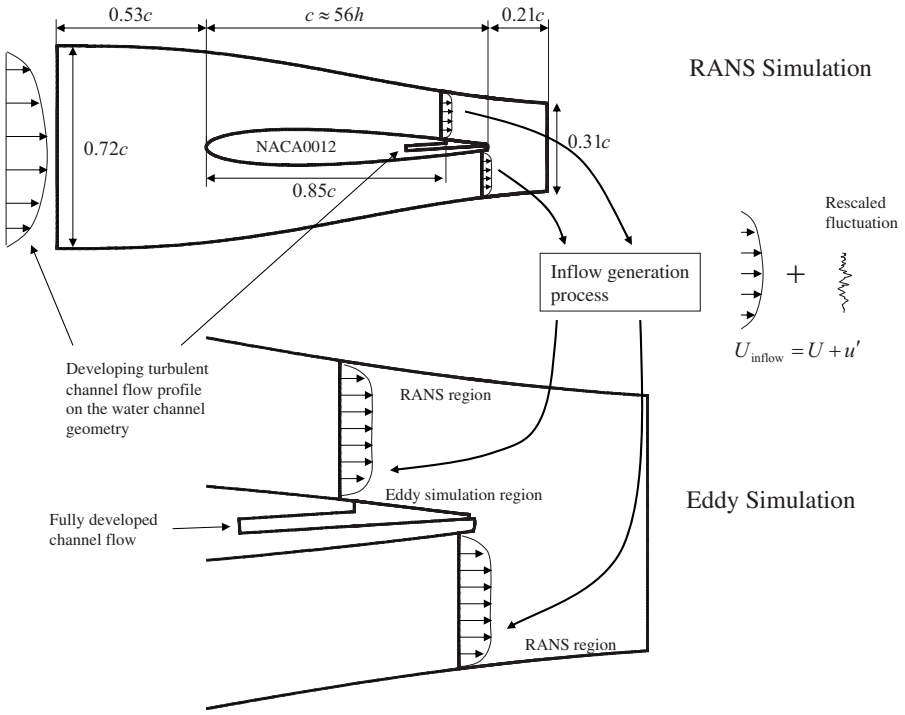

Fig. 5 Schematic of the procedure of the trailing edge simulation

base grid of 2.47×10^6 nodes was compared with a fine grid of 4.94×10^6 nodes to verify grid independence [19].

Comparisons are illustrated in Fig. 7: a good number of similar comparisons were made by Joo [19]. Overall, the base and final cases are in good agreement, indicating that the final grid provides sufficient resolution.

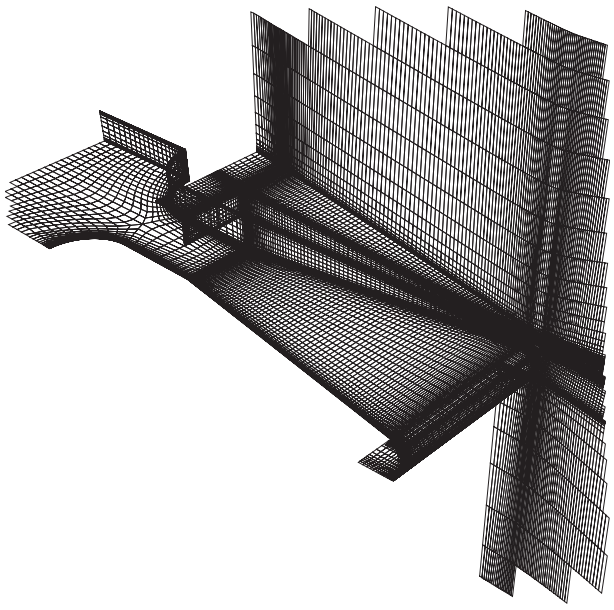

Fig. 6 Sections of the grid for the trailing edge and coolant passage

Table 1 Grid refinement for the eddy simulations

Case	Grid size near the slot region	Total no. of computational cells
Base	$200\times100\times80$	8.04×10^6
Final	$224\times152\times128$	20.0×10^6

4 Results

An overview of the simulation is provided in Fig. 8. This consists of three copies of the exterior flow domain to create an impression of the trailing edge geometry. The contours are surfaces of constant Q, where $Q\equiv|S|^2-|\Omega^2|$. The Q isosurfaces give an impression of vortices forming in the detached shear layers over the cooling slot.

Mean flow profiles at the two blowing ratios of BR=1 and BR=1.5 are provided in Fig. 9. These are shown at midspan ($z=0$). The wake of the upper nozzle lip is visible at $x=1$. By $x=3$ the profile has developed into a wall jet in a coflowing stream. For the case of BR=1, the bulk velocity of the jet matches that of the freestream and the profile develops the appearance of an accelerated boundary layer. For BR=1.5 the character of a wall jet in coflow is present in the trailing edge. A RANS computation with BR=1 is included in Fig. 9 for comparison. The eddy simulation and RANS profiles are quite similar.

At $x=1$, the profiles of resolved turbulent intensity in Fig. 10 show a local maximum in the wake of the upper nozzle lip. The maximum is most pronounced for the case with BR=1.5. The

Table 2 Maximum and mimimum grid sizes in the slot region of the eddy simulations

Case	Base	Final
$\Delta y^+_{\min}$ at $x=0$	0.8	0.8
$\Delta y^+_{\max}$	43.62	24.1
$\Delta x^+_{\min}$	7.2	7.2
$\Delta x^+_{\max}$	33.4	27.65
$\Delta z^+_{\min}$	1.6	1.6
$\Delta z^+_{\max}$	59.5	32.5

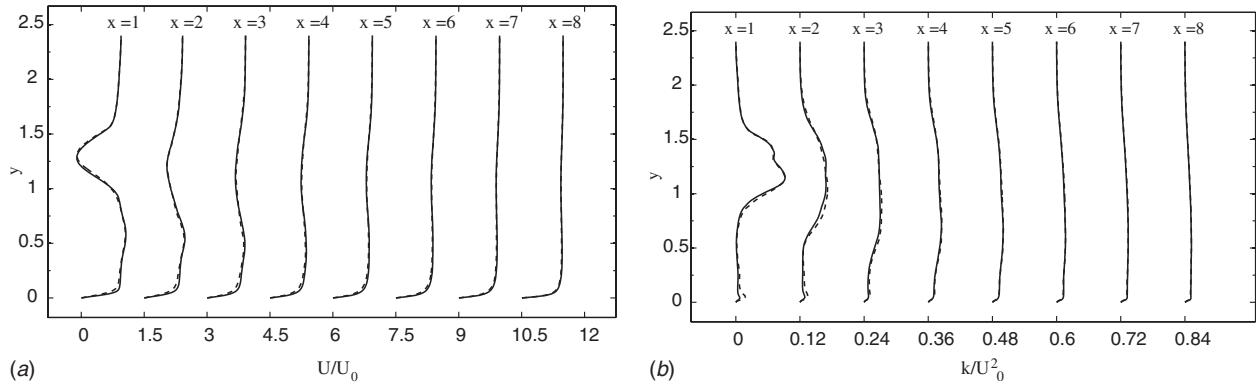

Fig. 7 Comparison of mean velocity and turbulent kinetic energy profiles between the base and final grids: (—) final grid; (- - -) base grid.

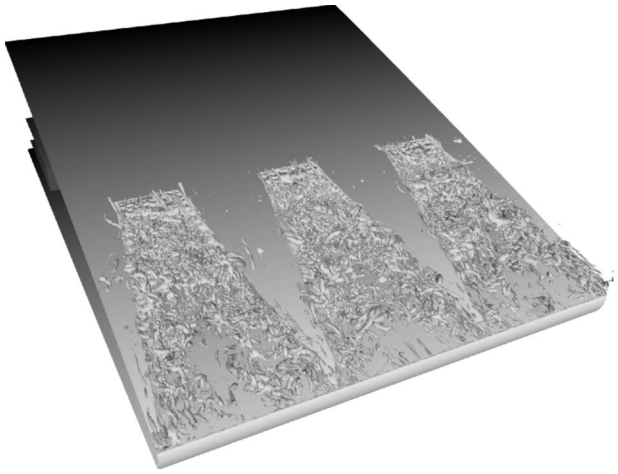

Fig. 8 *Q* isosurface of eddy simulation with BR=1

profiles spread into the slot with downstream distance. Turbulent intensity levels are similar to those seen in wall jets [20].

Because RANS simulations were done with the SST eddy viscosity model, only k and Reynolds shear stress are available for comparison. They are included in Figs. 11 and 10 for BR=1. Aside from the immediate vicinity of the breakout, the resolved kinetic energy in the eddy simulation is similar to the k profiles from the SST model.

In the eddy simulation, most of the fluctuating kinetic energy is resolved. A comparison between resolved kinetic energy and k from the SST-SAS model is presented in Fig. 12. At the present Reynolds number k is relatively small.

Correspondingly, the SAS viscosity is less than three times the molecular viscosity in the central region of the slot. Profiles of ν_T/ν are contained in Fig. 13. Final and base grid results are shown. As expected, the subgrid viscosity grows smaller as the grid is refined. The case with the higher blowing ratio has a higher ν_T but is still well below RANS levels. Clearly, at the current Reynolds number, the full force of the hybrid RANS/eddy simulation character of SST-SAS does not come into play. Rather the SAS model functions like a LES subgrid model. Indeed, with the present resolution the simulation is close to direct numerical simulation (DNS) in places.

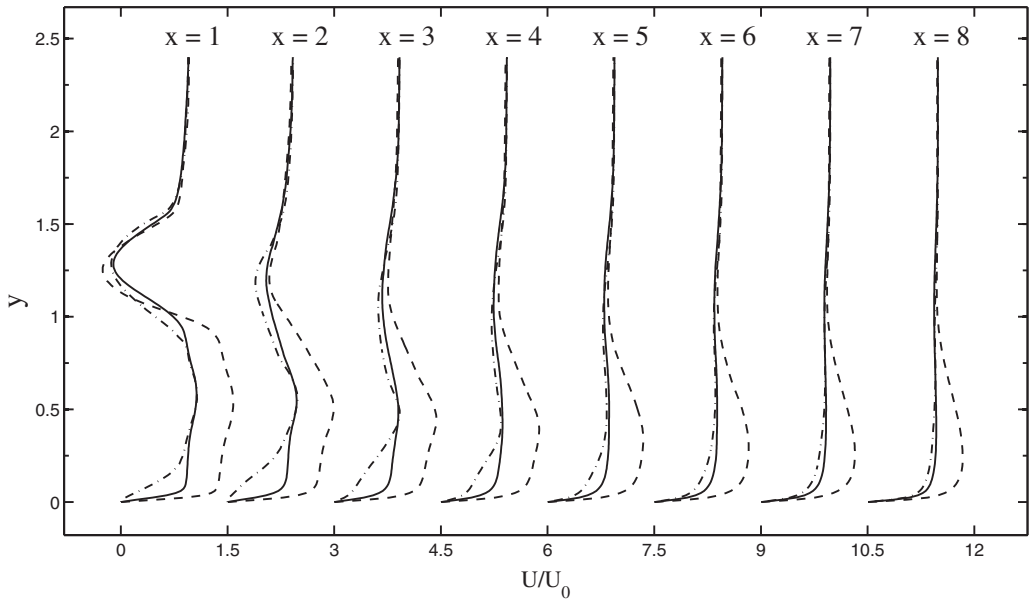

Fig. 9 Mean velocity profiles in planes of constant *z*. (—) Eddy simulation with BR=1, (- - -) eddy simulation with BR=1.5, and (–·–) RANS with BR=1.

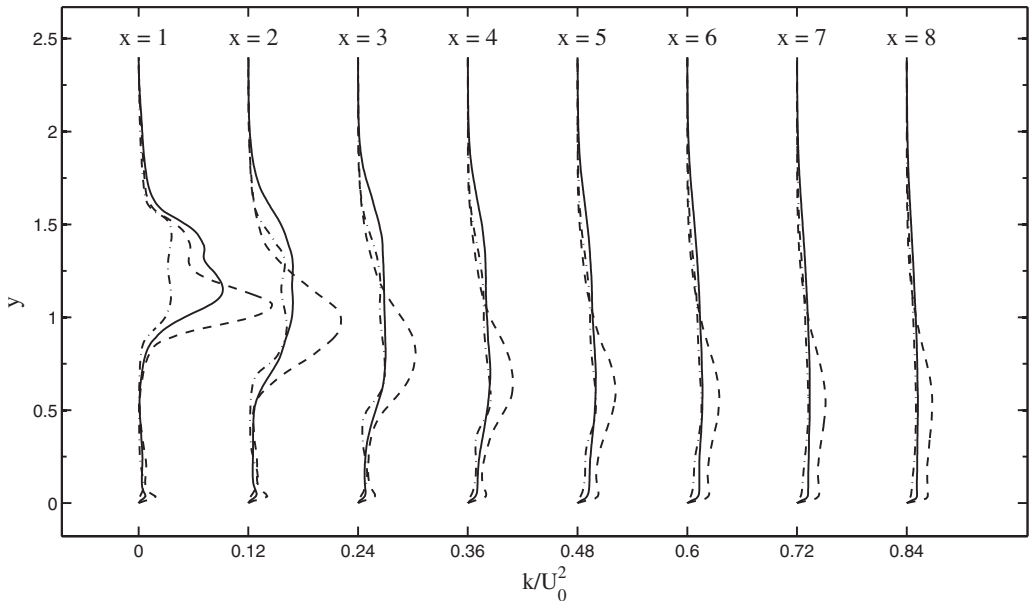

Fig. 10 Turbulent kinetic energy profiles at the center plane. (—) Eddy simulation with BR=1, (- - -) eddy simulation with BR=1.5, and (–·–) RANS with BR=1.

4.1 Scalar Mixing. Ultimately, we are concerned with turbulent mixing and heat transfer. Although we will refer to the "temperature" field, a passive scalar was traced rather than temperature, per se. This parallels the experimental practice of using CO_2 to study film effectiveness. Then the surface concentration is analogous to the adiabatic temperature. The analogy is exact if temperature can be treated as a passive scalar.

Mean temperature profiles in the middle of the slot are plotted in Fig. 14. These have the aspect of a spreading thermal mixing layer. At the inflow, the cooling stream temperature is defined as 0 and the freestream temperature is normalized to 1.

Improved predictions of film cooling effectivness are presented in Fig. 15. The experimental data in these figures are from the geometry of Holloway et al. [2], which is similar to the present. The unsteady RANS simulation overpredicts the adiabatic effectiveness. Effectiveness is defined as

$$\eta_{ad} = \frac{T_\infty - T_{wall}}{T_\infty - T_{jet}}$$

where T_{wall} is the adiabatic wall temperature. Hence the decrease in η_{ad} with x shows an increased wall temperature.

The case with higher blowing ratio provides better protection of the surface—that is, higher η_{ad}—but is far less than predicted (incorrectly) by unsteady RANS. The ability of the eddy simula-

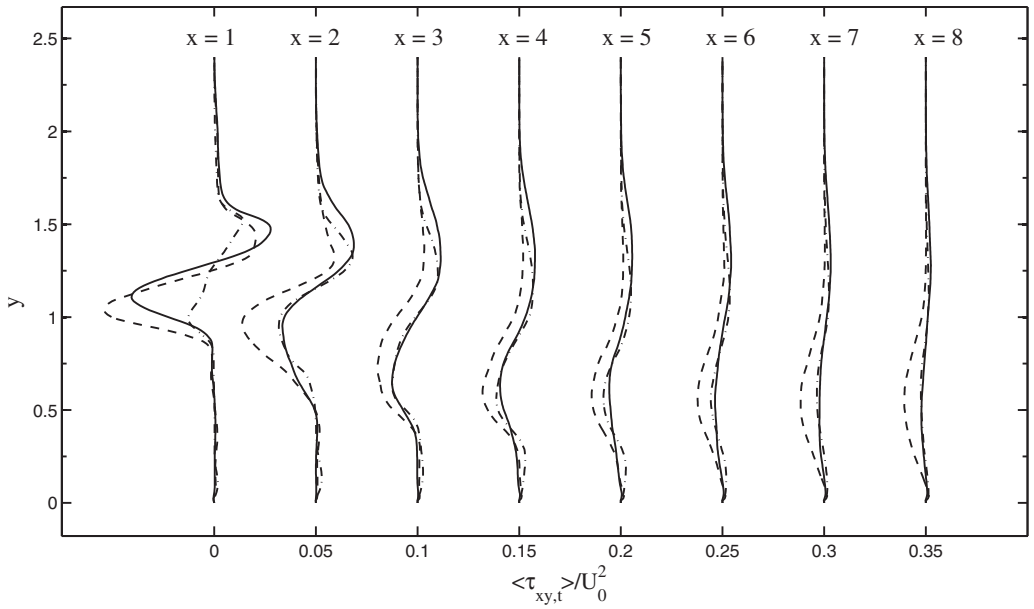

Fig. 11 Turbulent shear stress profiles at the center plane. (—) Eddy simulation with BR=1, (- - -) eddy simulation with BR=1.5, and (–·–) RANS with BR=1.

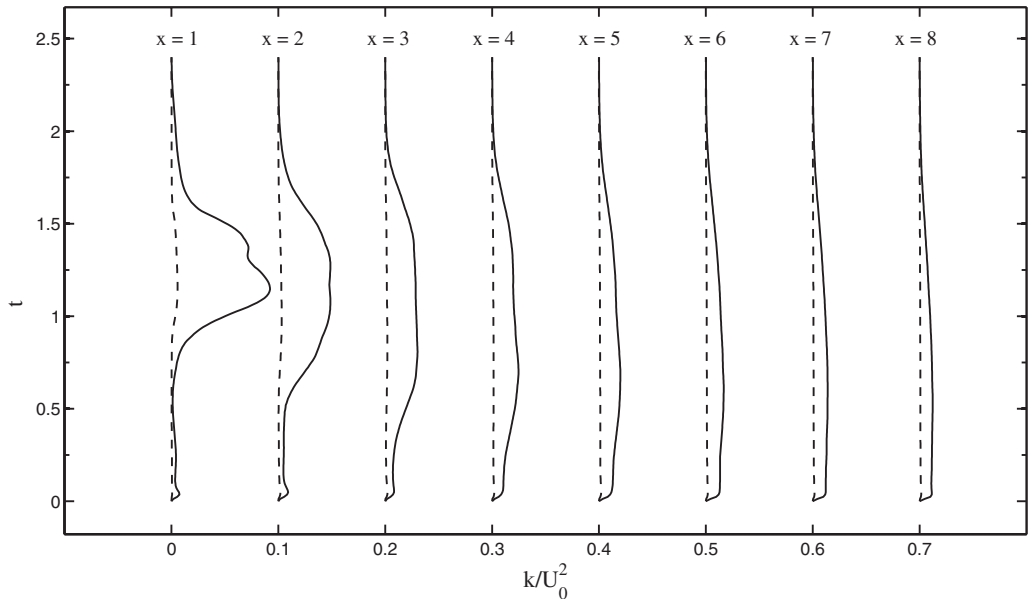

Fig. 12 Resolved and modeled turbulent kinetic energy profiles of eddy simulation (BR=1) at the center plane. (—) Resolved turbulent kinetic energy; (- - -) modeled turbulent kinetic energy.

tion to predict lower effectiveness indicates that the anomalous mixing is being captured. It will emerge that the cause is not the formation of the vortex loops seen in Fig. 3.

Time averaged effectiveness on the wall between the lands is contour plotted in Fig. 16. This shows the hot region near the trailing edge more clearly. It would be beneficial if the cooling jet did operate as in the right pane—the RANS results; unfortunately experiments are more similar to the left pane—the SST-SAS results.

Sectional views of the SAS and RANS simulations are provided in Fig. 17. The large scale undulations seen in the eddy simulation are suggestive of the ensemble average unsteadiness seen in the RANS result. The large scale coherent unsteadiness has the same qualitative appearance. Temperature is contoured in these plots, with dark areas being the cool fluid and white areas the hot. In Fig. 16 the dark areas are where the lower surface is hottest; in Fig. 17 this is the region toward the end of the blade surface where some white just reaches the surface in the upper pane of Fig. 17. It seems that the qualitative features of mixing within the slot are captured by the RANS simulation. But *a discrepancy to the eddy simulation appears in the mixing just next to the lower wall*; it is the origin of incorrect cooling effectiveness.

The cooler layer next to the wall is disrupted by the large eddies in the eddy simulations, while the coherent vortex shedding does not carry hot fluid to the wall in the RANS computation. This may stem, in part, from a transition in the initial separated shear layer.

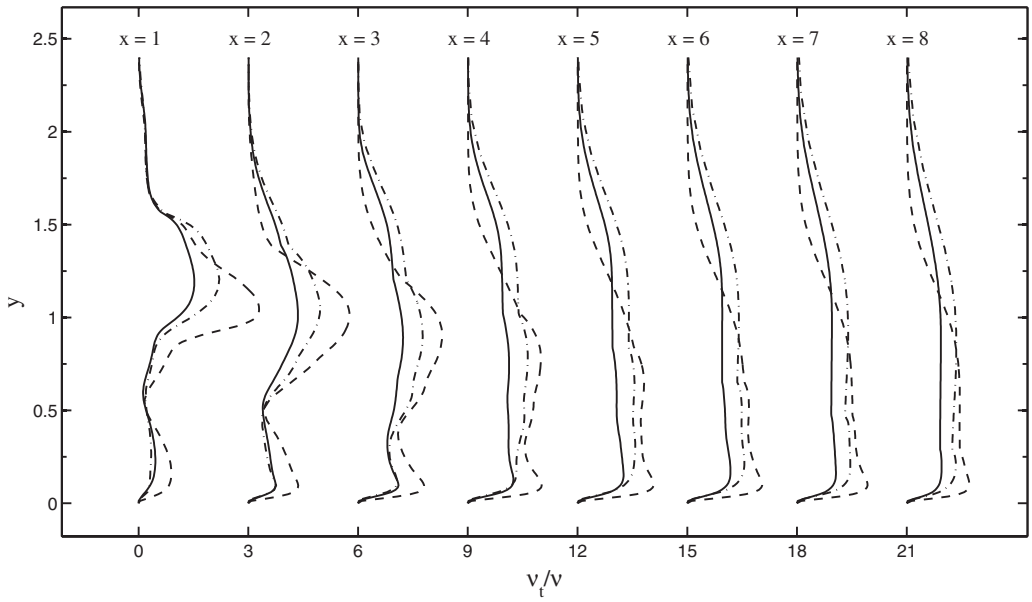

Fig. 13 Ratio of eddy viscosity to molecular viscosity profiles of eddy simulation at the center plane. (—) Final grid case with BR=1, (- - -) final grid case with BR=1.5, and (–·–) base grid case with BR=1.

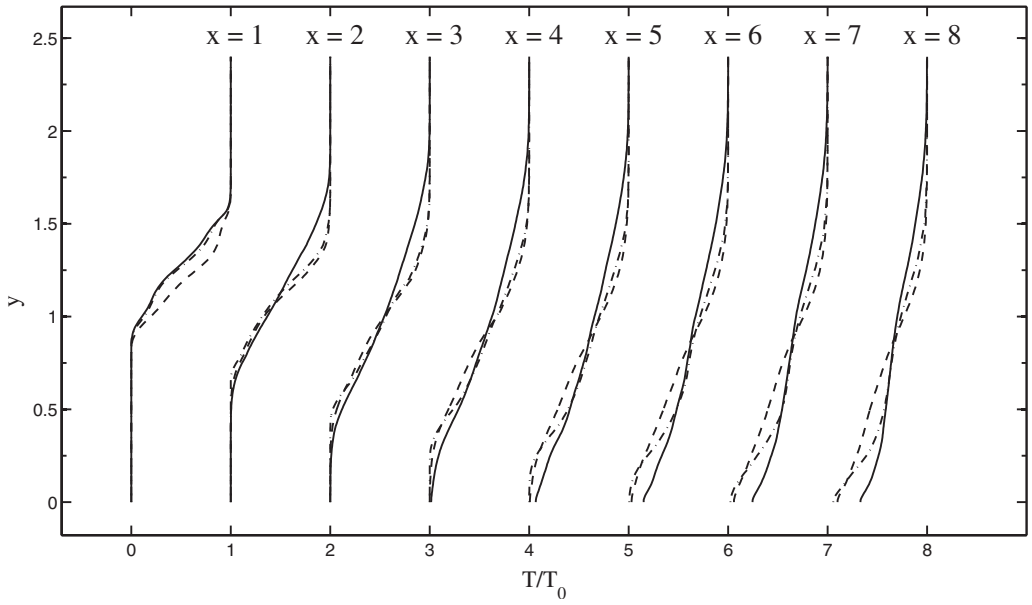

Fig. 14 Temperature profiles at the center plane. (—) Eddy simulation with BR=1, (- - -) eddy simulation with BR=1.5, and (–·–) RANS with BR=1.

The RANS model assumes that the layer is turbulent from the outset; in the eddy simulation the layer starts nearly laminar and becomes turbulent as three-dimensional instabilities grow.

The time-averaged temperatures in Fig. 18 show the diffusion of the high freestream temperature toward the wall. The averaged effect of the eddies is to enhance diffusion; the dark region next to the wall is penetrated by gray contours in the left pane. In the lower pane the averaged effect of diffusion by Reynolds averaged vortices is too weak to mix the hotter fluid with the wall. Thus, it might be supposed that the turbulence model dissipates the vortices too strongly. It is probably more correct to say that it does not allow sufficient three-dimensionality to occur.

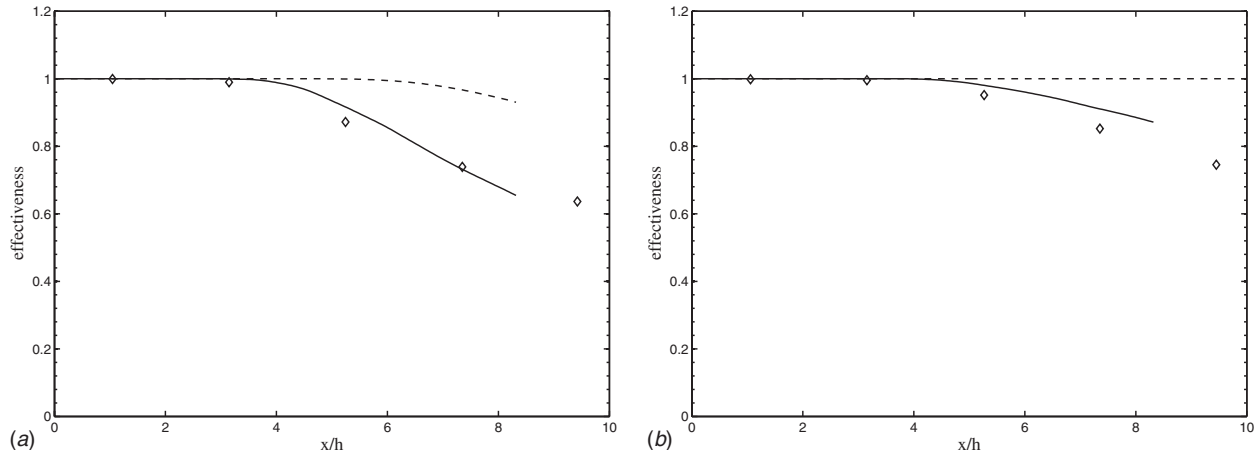

Fig. 15 Film cooling effectiveness on the center line for BR=1 and 1.5. (—) Eddy simulation, (- - -) RANS [4], and ◇ experiment [2].

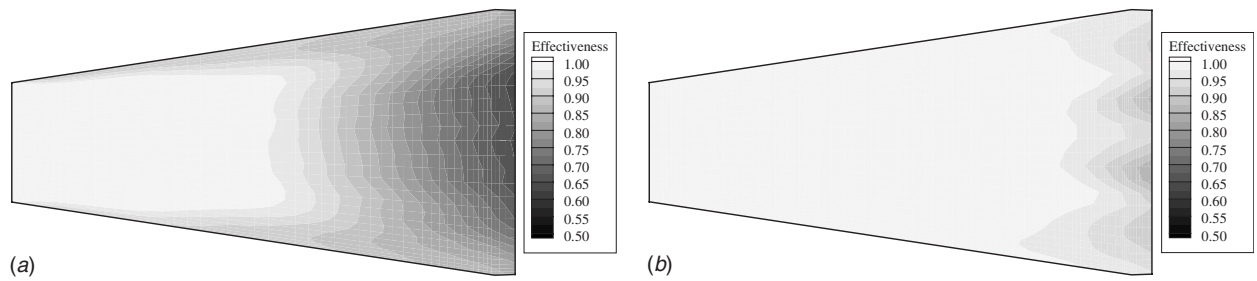

Fig. 16 Film cooling effectiveness contours at the bottom wall. Left: eddy simulation with BR=1; right: RANS with BR=1.

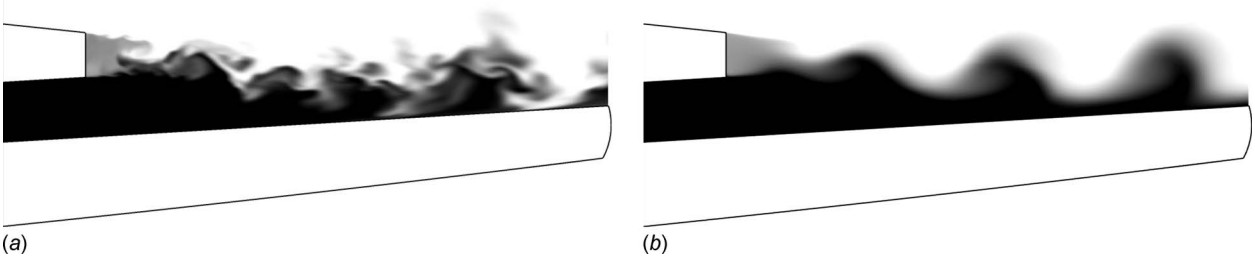

Fig. 17 Instantaneous temperature contours at the center plane. Top: eddy simulation with BR=1; bottom: RANS with BR=1.

Figure 19 contains end views of the temperature field in the slot at the downstream position, $x=2$. There is a somewhat higher mixing adjacent to the lands than in the center of the slot. In the uppermost case, the hotter fluid has penetrated almost to the wall on the sides of the slots.

Progressing down the slot, Figs. 20 and 21 show the development of the temperature contours. Undulations of the contours for the BR=1 cases are caused by the secondary flow. The RANS results show a significant penetration of the higher temperatures into the slot flow by $x=8$; they simply do not break through to the wall. Hence, the fact that η_{ad} remains near to unity is a bit misleading. The discrepancy between RANS and eddy simulation is not in the amount of mixing, but in its spatial character. It seems that the eddy viscosity model does not provide enough turbulent transport very near to the surface.

Views of the instantaneous temperature contours for BR=1, at various downstream locations, are contained in Fig. 22. Streamwise vortices appear to mix the fluid next to the two lands. Hot fluid penetrates into those areas, leaving a tongue of cooler fluid in the middle.

4.2 Spectra. Temporal energy spectra of velocity and temperature were calculated at selected locations within the slot. Representative spectra are presented in Fig. 23. These show a peak at the nondimensional shedding frequency of 0.37 based on the height and the bulk velocity of the slot jet: fh/U_0. Recalling that the lip thickness above the slot is 0.7 times the slot height, the shedding Strouhal number is 0.26 when based on this thickness. The RANS simulation produced a Strouhal number of 0.24.

Velocity spectra at other locations were similar to those in Fig. 23 [19]. Temperature spectra were more variable. Near the wall, the peak was very weak. The wall blocks eddy motions that would carry hot streaks to the wall.

A $-5/3$ line is included in Fig. 23, although the Reynolds number is too low for the energy cascade to create small scale universality. This line suggests that the numerical high frequency cutoff is above the energetic turbulent scales. The velocity spectra all contain an appreciable broadband component, even those close to the lower wall.

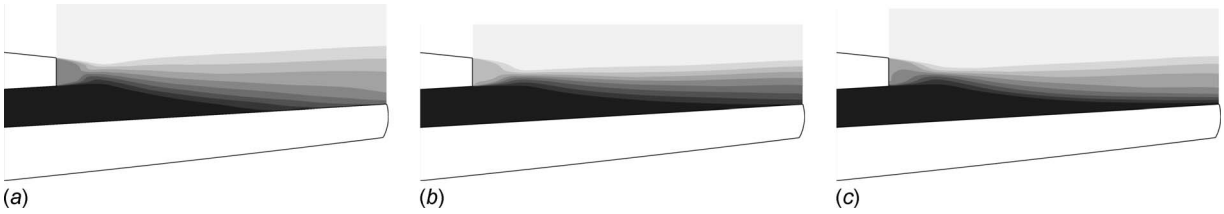

Fig. 18 Mean temperature contours at the center plane. Top left: eddy simulation with BR=1, top right: eddy simulation with BR=1.5, and bottom: RANS with BR=1.

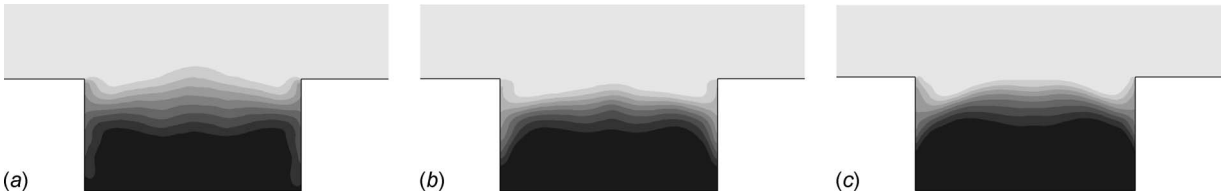

Fig. 19 Mean temperature contours at *x*=2 plane. Top left: eddy simulation with BR=1, top right: eddy simulation with BR=1.5, and bottom: RANS with BR=1.

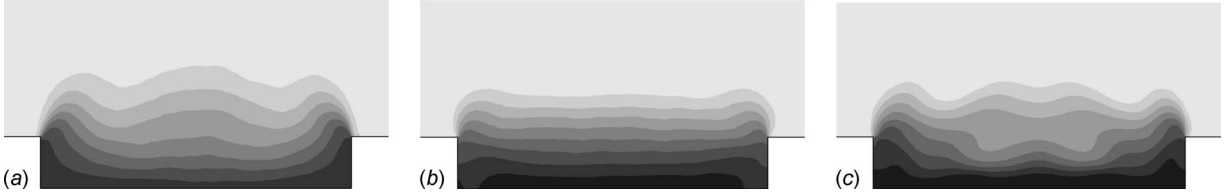

Fig. 20 Mean temperature contours at *x*=6 plane. Top left: eddy simulation with BR=1, top right: eddy simulation with BR=1.5, and bottom: RANS with BR=1.

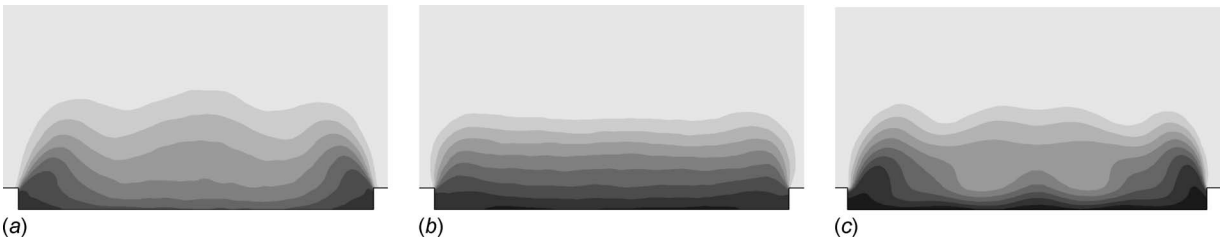

Fig. 21 Mean temperature contours at the $x=8$ plane. Top left: eddy simulation with BR=1, top right: eddy simulation with BR=1.5, and bottom: RANS with BR=1.

5 Eddy Versus Unsteady Reynolds Averaged Simulation

From a practical standpoint the question is whether anything can be concluded about why unsteady RANS does not predict the decline of film cooling effectiveness, η_{ad}, toward the trailing edge. What property of the SST-SAS simulation leads to a more correct behavior?

Although the unsteady RANS simulation overpredicted film cooling effectiveness, the mean temperature profile shows that some degree of mixing occurred down to some point around $y=0.5$. Figures 24 and 25 show turbulent kinetic energy and mean temperature profiles. One of these figures is in the central plane and the other is in a plane at $z=0.5$. These two sets of profiles differ due to the secondary flow next to the lands.

Around $y=0.6$ the total kinetic energy of the RANS simulation—that is k, which is called the modeled kinetic energy in the figures, plus the time average of the mean fluctuation $1/2\langle(U(t)-\langle U\rangle)^2\rangle$, which is called the resolved kinetic energy of RANS—is of a level similar to the eddy simulation. At that height, the mean temperature also is very comparable to eddy simulation. Moreover when the total kinetic energy of RANS is higher than eddy simulation in Fig. 25, the temperature is also higher for the RANS case. This shows that there is more mixing in the RANS simulation at those heights.

However, if we look closer to the lower wall, the total kinetic energy of the RANS simulation is significantly lower than that seen in the eddy simulation; and so is the mean temperature. This indicates a strong correlation between the level of turbulent kinetic energy and the degree of mixing. Because η_{ad} is a measure of the wall temperature, it is very directly related to mixing close to the surface. Below a y of around 0.3 at $x=4$, the resolved kinetic energy of RANS decreases sharply. This means that the resolved coherent motion does not penetrate below that height. *This would appear to be the primary factor in overpredicting cooling efficiency.*

The turbulent kinetic energy of the eddy simulation is composed of around 35% large scale components in the frequency band between zero and the shedding frequency (Fig. 23). The higher frequency components of turbulent kinetic energy in the eddy simulation correspond to the modeled turbulent kinetic energy, k, in the unsteady RANS simulation. Taken together, the set curves in Fig. 24 or in Fig. 25 imply that the deficiency of *resolved eddying motion* relatively near the wall is the biggest cause of deficient mixing in the RANS simulation.

Also we can now understand the role of vortex loops in Fig. 3—recall that these were created by the contrivance of pulsating the plenum flow. The subharmonic vortex loops create a type of three-dimensional coherent unsteadiness that can convect heat to the surface. Figure 17 shows that the coolant jet along the surface is shielded from the coherent vortex motion in the RANS case without forcing. The coherent vortex shedding does not penetrate the film right next to the wall. Three-dimensional disruptions of

Fig. 22 Instantaneous temperature contours of eddy simulation (BR=1) at x-normal planes. Top left: $x=4$, top right: $x=6$, and bottom: $x=8$.

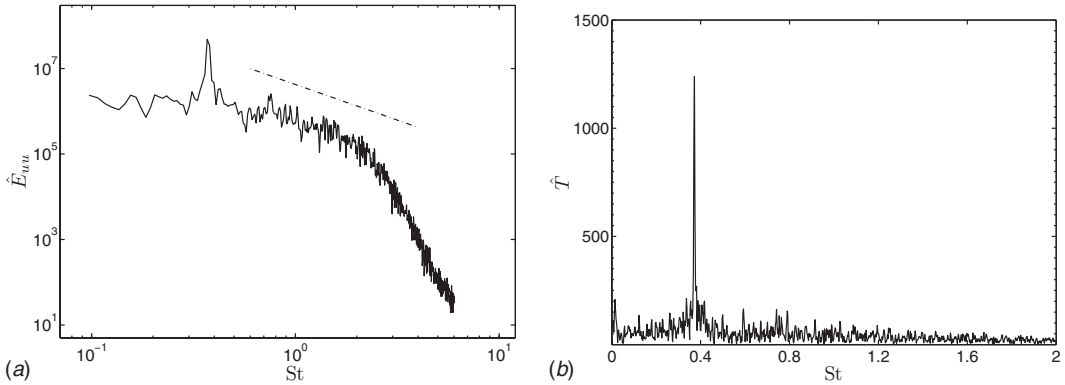

Fig. 23 One-dimensional streamwise energy and temperature spectra in the center plane at $x=4$, $y=0.571$ for the u spectrum, and $y=0.794$ for the temperature spectrum. (–·–) $k^{-5/3}$.

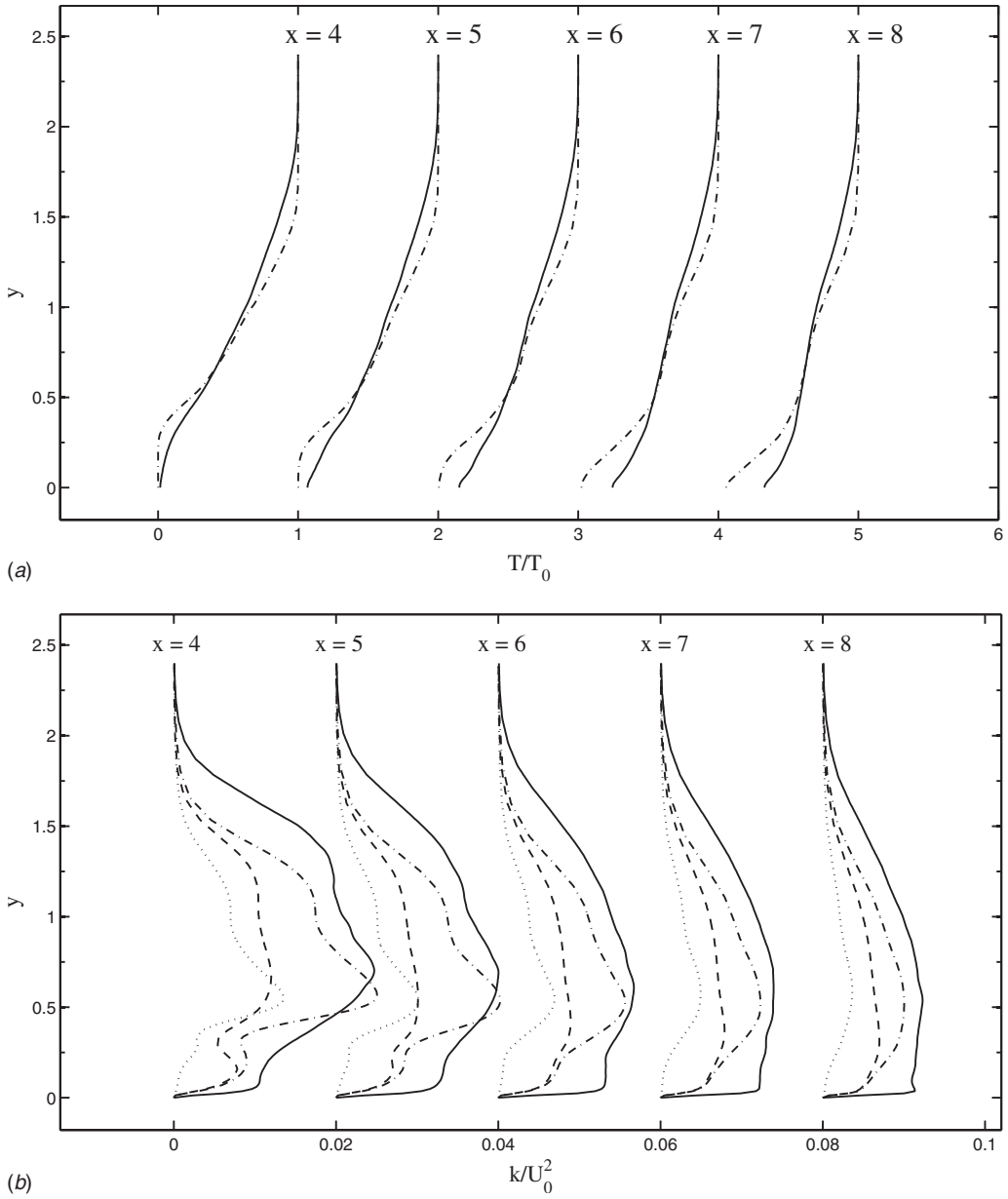

Fig. 24 Comparison between turbulent kinetic energy and temperature mean profiles at the center plane with BR=1. Top: turbulent kinetic energy, (—) eddy simulation, (- - -) modeled turbulent kinetic of RANS, (···) resolved turbulent kinetic energy of RANS, and (–·–) sum of the modeled and resolved turbulent kinetic energy of RANS. Bottom: mean temperature profiles, (—) eddy simulation, and (–·–) RANS.

those vortices are required in order for fluctuations to penetrate the wall. Thus one explanation of the anomalous mixing is that it arises from distortions of the coherent shed vortices. The relatively low Reynolds number ensures that coherent unsteadiness is as important as broadband turbulent in the trailing edge slots.

6 Conclusion

Unsteadiness in the trailing edge cooling slots consists of a coherent component and a broadband component. The coherent component is three-dimensional vortex shedding. The eddy simulations discussed herein need not distinguish the components. Indeed, they are not independent: vortex shedding influences incoherent turbulence; in fact, irregularity of the vortices is categorized as a contribution to the incoherent component.

Both components are explicitly distinguished in unsteady RANS simulation: the coherent component appears as mean unsteadiness and the broadband component is represented by a closure model. These are coupled through turbulent kinetic energy production. Our primary conclusion is that the RANS representation is satisfactory above a layer next to the surface. Within that layer, RANS shows a suppression of mixing that does not occur in the eddy simulation. Evidence that the coherent motion is able to penetrate closer to the wall than predicted has been provided by the eddy simulation. Transition from laminar to turbulent flow after the trailing edge caused some additional difference between RANS and eddy simulations.

The dominant effect in this flow is three-dimensional vortex shedding caused by the upper nozzle lip. It has a profound influence on surface heat transfer because the lip is in proximity to the wall. These aspects of the geometry are essential to the fluid mechanics. We speculate that the particular lip thickness is not critical. However, our simulations offer a suggestion that any alter-

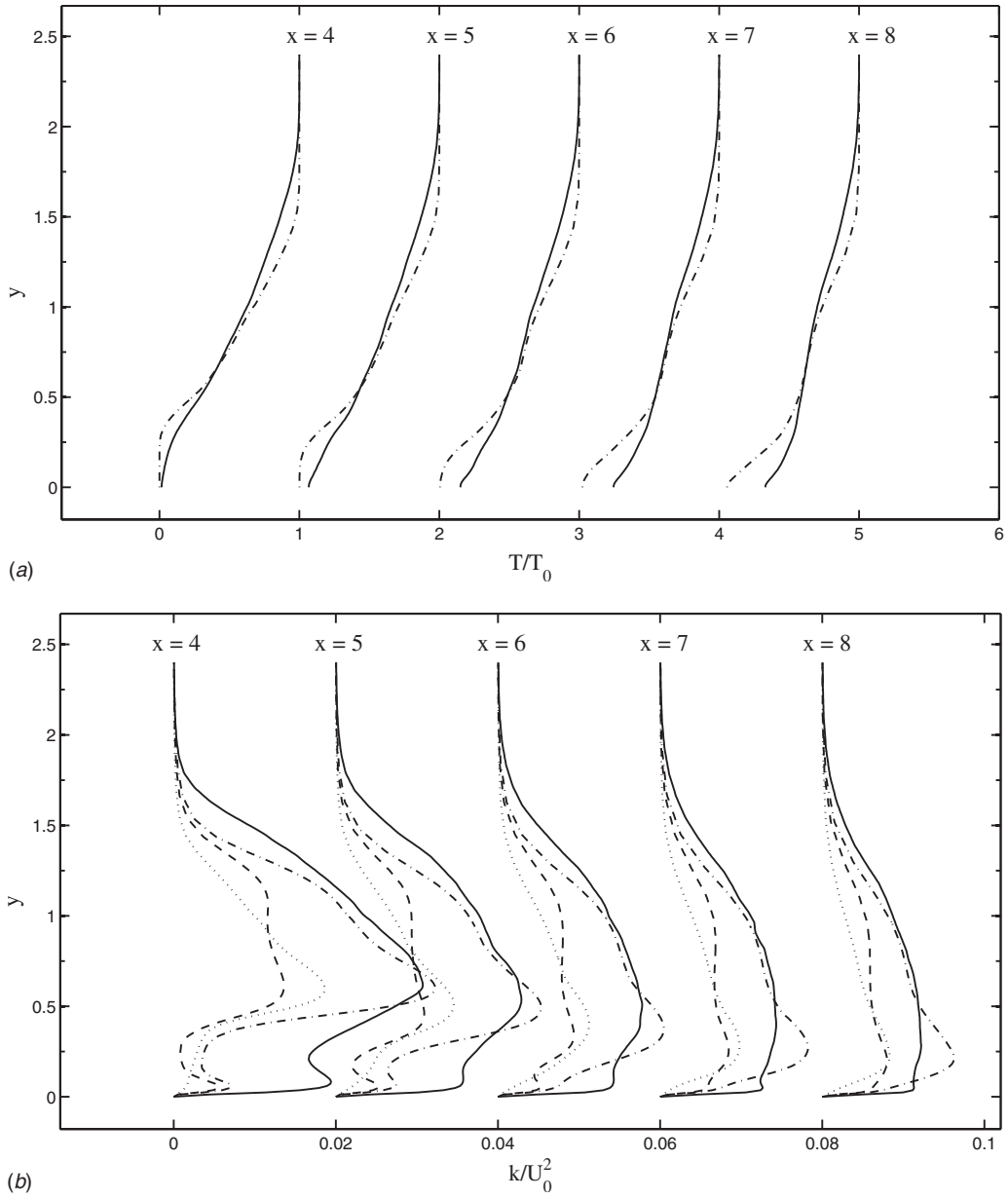

Fig. 25 Comparison between turbulent kinetic energy and temperature mean profiles at the $z = 0.5$ plane with BR=1. Top: turbulent kinetic energy, (—) eddy simulation, (- - -) modeled turbulent kinetic of RANS, (···) resolved turbulent kinetic energy of RANS, and (–·–) sum of the modeled and resolved turbulent kinetic energy of RANS. Bottom: mean temperature profiles, (—) eddy simulation, and (–·–) RANS.

ation to the nozzle lip that affects shedding might have a large effect on cooling. For instance distortion of the straight edge between the lands, or its junction with the lands, could influence adiabatic effectiveness.

Acknowledgment

This work was sponsored by the Airforce Office of Sponsored Research under Grant No. FA9550-05-1-0183 and by the Department of Energy Advanced Strategic Computing (ASC) program. We are grateful to Professor J.K. Eaton for discussing the work with us.

References

[1] Menter, F. R., and Egorov, Y., 2005, "A Scale-Adaptive Simulation Modeling Using Two-Equation Models," AIAA Paper No. 2005-1095.
[2] Holloway, S. D., Leylek, J. H., and Buck, F. A., 2002, "Pressure-Side Bleed Film Cooling: Part 1, Steady Framework for Experimental and Computational Results," ASME Turbo Expo 2002, Paper No. GT-2002-30471.
[3] Holloway, S. D., Leylek, J. H., and Buck, F. A., 2002, "Pressure-Side Bleed Film Cooling: Part 2, Unsteady Framework for Experimental and Computational Results," ASME Turbo Expo 2002, Paper No. GT-2002-30472.
[4] Medic, G., and Durbin, P. A., 2005, "Unsteady Effects on Trailing Edge Cooling," ASME J. Heat Transfer, **127**, pp. 388–392.
[5] Martini, P., Schultz, A., Whitney, C. F., and Lutum, E., 2004, "Experimental and Numerical Investigation of Trailing Edge Film Cooling Downstream of a Slot With Internal Rib Arrays," ASME J. Turbomach., **126**, pp. 229–236.
[6] Martini, P., Schultz, A., and Bauer, H. J., 2006, "Film Cooling Effectiveness and Heat Transfer on the Trailing Edge Cut-Back of Gas Turbine Airfoils With Various Internal Cooling Designs," ASME J. Turbomach., **128**, pp. 196–205.
[7] Viswanathan, K., Schur, M., Spalart, P. R., and Strelets, M., 2008, "Flow and Noise Predictions for Single and Dual Stream Beveled Nozzles," AIAA J., **46**, pp. 601–626.
[8] Iaccarino, G., Ooi, A., Durbin, P. A., and Behnia, M., 2003, "Reynolds Averaged Simulation of Unsteady Separated Flow," Int. J. Heat Fluid Flow, **24**, pp. 147–156.
[9] van der Weide, E., Kalitzin, G., Schlüter, J., and Alonso, J., 2006, "Unsteady

Turbomachinery Computations Using Massively Parallel Platforms," AIAA Paper No. 2006-421.
[10] Jameson, A., 1985, "Transonic Flow Calculations for Aircraft," *Numerical Methods in Fluid Dynamics* (Lecture Notes in Mathematics), Vol. 1127, pp. 156–242.
[11] Menter, F. R., 1994, "Two-Equation Eddy-Viscosity Turbulence Models for Engineering Applications," AIAA J., **32**, pp. 1598–1605.
[12] Menter, F. R., and Egorov, Y., 2005, *Scale-Adaptive Simulation of Aerodynamic Flows*, ANSYS Technical Report.
[13] Menter, F. R., Kuntz, M., and Bende, R., 2003, "A Scale-Adaptive Simulation Model for Turbulent Flow Predictions," AIAA Paper No. 2003-0767.
[14] Blaisdell, G., Spyropoulos, E., and Qin, J., 1996, "The Effect of the Formulation of Nonlinear Terms on Aliasing Errors in Spectral Methods," Appl. Numer. Math., **21**, pp. 207–219.
[15] Barth, T., and Jespersen, D., 1989, "The Design and Application of Upwind Schemes on Unstructured Meshes," AIAA Paper No. 89-0366.
[16] Lele, S. K., 1992, "Compact Finite Difference Schemes With Spectral-Like Resolution," J. Comput. Phys., **103**, pp. 16–42.
[17] Kang, S., and Choi, H., 2002, "Suboptimal Feedback Control of Turbulent Flow Over a Backward-Facing Step," J. Fluid Mech., **463**, pp. 201–227.
[18] Lund, T. S., Wu, X., and Squires, K. D., 1998, "Generation of Turbulent Inflow Data for Spatially-Developing Boundary Layer Simulation," J. Comput. Phys., **140**, pp. 233–258.
[19] Joo, J., 2008, "Eddy Simulation of Turbine Blade Trailing Edge Cooling," Ph.D. thesis, Stanford University.
[20] Craft, T. J., and Launder, B. E., 2001, "On the Spreading Mechanism of the Three-Dimensional Wall Jet," J. Fluid Mech., **435**, pp. 305–326.

Efficiency Improvement of Centrifugal Reverse Pumps

Shahram Derakhshan
Department of Mechanical Engineering,
University of Tehran,
P.O. Box 11365/4563,
Tehran 14147, Iran

Bijan Mohammadi
Mathematics and Modeling Institute,
University of Montpellier,
34095 Montpellier, France

Ahmad Nourbakhsh
Department of Mechanical Engineering,
University of Tehran,
P.O. Box 11365/4563,
Tehran 14147, Iran

Pumps as turbines have been successfully applied in a wide range of small hydrosites in the world. Since the overall efficiency of these machines is lower than the overall efficiency of conventional turbines, their application in larger hydrosites is not economical. Therefore, the efficiency improvement of reverse pumps is essential. In this study, by focusing on a pump impeller, the shape of blades was redesigned to reach a higher efficiency in turbine mode using a gradient based optimization algorithm coupled by a 3D Navier–Stokes flow solver. Also, another modification was done by rounding the blades' leading edges and hub/shroud interface in turbine mode. After each modification, a new impeller was manufactured and tested in the test rig. The efficiency was improved in all measured points by the optimal design of the blade and additional modification as the rounding of the blade's profile in the impeller inlet and hub/shroud inlet edges in turbine mode. Experimental results confirmed the numerical efficiency improvement in all measured points. This study illustrated that the efficiency of the pump in reverse operation can be improved just by impeller modification. [DOI: 10.1115/1.3059700]

Keywords: blade rounding, blade shape optimization, efficiency improvement, reverse pump, small hydrosite

1 Introduction

Small hydropowers are important especially in remote areas. However, the cost per kilowatt of the energy produced by these plants is higher than large hydropower plants. Using reverse pumps is an alternative to overcome this problem. Reverse pumps have been successfully applied in a wide range of small hydrosites in the world. A turbine will normally show a higher efficiency than a pump that is designed for the same operating conditions. On the other hand, the best efficiency of a reverse pump is almost the same as that of the pump mode [1–3]. Therefore, the application of reverse pumps in larger capacities is not economical. By increasing the overall efficiency of reverse pumps, they can be economically applied in the higher power capacities.

Lueneburg and Nelson [4], Williams [5], Cohrs [6], Hirschberger and Kuhlmann [7], and Singh [8] reported efficiency improvement by some modifications on pump components.

The aim of this study was the optimization of the impeller geometry of a pump to improve its turbine mode maximum efficiency. An old impeller can be replaced by a new one to reach higher efficiency in turbine mode. A pump manufacturer will produce two impellers for its centrifugal pumps: one for pump running and another for turbine running. The additional modification proposed by Singh [8] can be done on the other component of the pump (i.e., volute and impeller clearance).

In this paper, shapes of the blades were redesigned using a gradient based optimization method involving incomplete sensitivities for radial turbomachinery developed by Derakhshan et al. [9] to obtain higher efficiency. Optimization program was coupled to FINETURBO V.7, to solve 3D incompressible Navier–Stokes equations, and AUTOGRID5 mesh generator developed by Numeca. In the next step, the optimized impeller was modified by rounding of leading edges and hub/shroud inlet edges in turbine mode. After each modification, a new impeller was manufactured and tested in the test rig. Finally, results were presented and discussed.

Contributed by the Fluids Engineering Division of ASME for publication in the JOURNAL OF FLUIDS ENGINEERING. Manuscript received April 16, 2008; final manuscript received November 15, 2008; published online January 15, 2009. Assoc. Editor: James A. Liburdy.

2 Efficiency Improvement of Centrifugal Reverse Pump

The main objective was to reach higher efficiency by redesigning the blades. Using the gradient based optimization algorithm and incomplete sensitivities method developed by Derakhshan et al. [9], the shape of the blades was redesigned. In the next step, the optimized impeller was modified by rounding of leading edges and hub/shroud inlet edges in turbine mode.

The following steps were done to modify the pump impeller to reach higher efficiency in turbine mode.

2.1 3D Shape Optimization of the Blade. The general form of a shape optimization problem can be written as [10]

$$\min_{x_c} J(x_c, W(x_c), \nabla_{x_c} W(x_c))$$

$$S(x_c, W(x_c), \nabla_{x_c} W(x_c)) = 0 \tag{1}$$

$$g_1(x_c) \le 0, \quad g_2(W(x_c)) \le 0$$

where x_c is the control variable for the shape, W is the flow variable, S is the state equation, g_1 is the geometrical constraints, g_2 is the state constraints, and J is the cost function that should be minimized.

The local optimization algorithm can be summarized as follows.

For the optimization loop,

1. Provide initial shape parametrization, x_c^1.
2. For $k=2,3,\ldots,k_{\max}$: Do.
3. Compute the flow state: $W(x_c^k)$.
4. Compute the cost function: $J(x_c^k, W(x_c^k))$.
5. Compute the incomplete sensitivity of the cost function: $dJ(x_c^k, W(x_c^k))/dx_c$.
6. If $(|(dJ(x_c^k, W(x_c^k)))/dx_c| < \varepsilon$ or $J(x_c^k, W(x_c^k)) < \varepsilon)$: STOP.
7. Compute x_c^{k+1} minimizing J using incomplete gradient and the approximate inverse of Hessian by BFGS (Broyden, Fletcher, Goldfarb, and Shanno) and evaluating when it is necessary $W(x_c^{k+1})$ and $J(x_c^k, W(x_c^k))$.

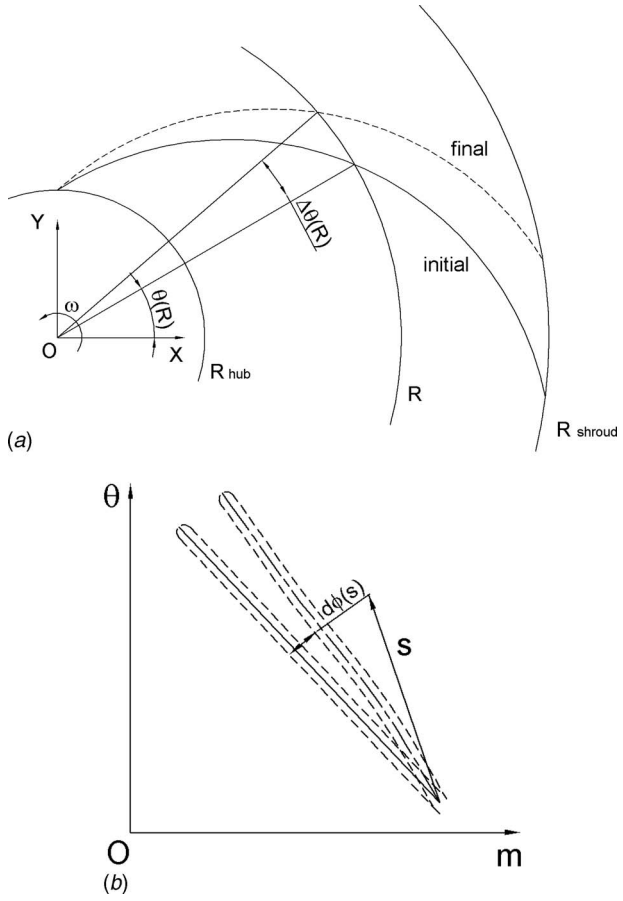

Fig. 1 Radial blade parametrization. (*a*) First parametrization, blade angle distribution from leading to trailing edges. (*b*) Second parametrization, rotation midspan and shroud-span around leading edge with respect to hub-span.

2.1.1 Shape Parametrization. Several parametrizations are possible to describe aerodynamic or hydrodynamic shapes. In radial turbomachinery, one can be to consider the spanwise blade angle distribution from leading to trailing edges. The performance of a radial turbomachine (i.e., centrifugal pump) is intensely influenced by these blade angles [11]. Previous results have shown that hydraulic efficiency is not sensitive to small perturbations in blade thicknesses [11]. On the other hand, thickness is one of the manufacturing constraints. Therefore the blade thicknesses were frozen in the optimization process. Also in this optimization, other manufacturing constraints were ignored. The meridian plan of the hub and shroud and the outlet diameter (in centrifugal pump) were fixed. The optimization was performed in two steps.

2.1.2 Primal Optimization. For a radial blade, the camber lines in hub-span, midspan, and shroud-span were linked through the following relation:

$$d\theta(R) = \theta(R) - \theta_{\text{initial}}(R) = \frac{c_1(R-R_1) + c_2(R-R_1)^2 + c_3(R-R_1)^3}{R} \tag{2}$$

where θ is the tangential angle, R is the blade radius, and R_1 is the radius of the blade leading edge in hub-span (in centrifugal pump). The profile is fixed in R_1. The coefficients c_1, c_2, and c_3 are control parameters (Fig. 1(*a*)).

2.1.3 Final Optimization. The optimal shape from primal parametrization was used as initial guess for the second level parametrization. The camber lines of midspan and shroud-span were linked to the blade camber line in hub-span through

$$d\varphi(i) = \frac{c_{3i-2}S + c_{3i-1}S^2 + c_{3i}S^3}{S} \tag{3}$$

where $i=2,3$, $m=\int\frac{dm}{R}$, and $dm=\sqrt{dR^2+dz^2}$, in m-θ conformal plan $s=\sqrt{m^2+\theta^2}$. Here the blade camber lines in midspan and shroud-span are rotated around trailing edge, which is fixed with respect to the hub-span camber line of the blade (Fig. 1(*b*)). The coefficients c_4, c_5 and c_6 are control parameters for midspan and c_7, c_8 and c_9 for shroud-span.

2.1.4 Sensitivity and Incomplete Sensitivity. The gradient of a cost function $J(x_c, q(x_c), W(q(x_c)))$, function of shape control parameters x_c, geometric entities $q(x_c)$ (normal, volume, surface, etc.), and state variables W can be derived using chain rule

$$\frac{dJ}{dx_c} = \frac{\partial J}{\partial x_c} + \frac{\partial J}{\partial q}\frac{\partial q}{\partial x_c} + \frac{\partial J}{\partial W}\frac{\partial W}{\partial q}\frac{\partial q}{\partial x_c} \tag{4}$$

where f and g are functions involving geometric quantities and state quantities, respectively. For incomplete sensitivity application, the cost function should be expressed as a function of the aerodynamic coefficients or more generally [12]

$$J = \int_\Gamma f(x,q(x))g(W(q(x)))d\gamma \tag{5}$$

The dominant part in the gradient comes from geometrical quantities sensitivities and not from state linearization [12]. More precisely, the last term in gradient expression can be neglected:

$$\frac{dJ}{dx_c} \approx \frac{\partial J(W)}{\partial x_c} + \frac{\partial J(W)}{\partial x_q}\frac{\partial x_q}{\partial x_c} \tag{6}$$

This gradient approximation avoids the evaluation of an adjoint state and decreases the computational cost. Typical functionals in this class are aerodynamic or hydrodynamic forces on a shape along an arbitrary direction as

$$T_r = \left(\int_\Gamma [T\cdot n]d\Gamma\right)\cdot\sigma \tag{7}$$

where $T=-pI+(\nu+\nu_t)(\nabla u_t+\nabla u^T)$. Here, n is the normal to the shape, σ is an arbitrary direction, and T is the Newtonian stress tensor.

In this optimization, incomplete sensitivities were improved by adding supplementary terms to add physical sense to the approximate gradient. In other words, reduced order models (i.e., wall functions) can improve incomplete sensitivity in an inexpensive way. The method and its formulation can be found in the Appendix and in our previous work [9].

2.1.5 Cost Function and Its Reformulation. The aim of this study was blade shape optimization of pump impeller in reverse operation to reach higher efficiency in its rated point defined as

$$\eta_h = \frac{T_r\omega}{\gamma q h} \tag{8}$$

where h is head (m), q is flow rate (m^3/s), T_r (N m) is the axial torque from the fluid to the impeller, $\omega=(2\pi N)/60$, and γ is specific gravity ($kg/m^2\,s^2$).

To use incomplete sensitivities, the cost function must be based on information of the shape (or part of it). In Eq. (8) increasing the torque improves the efficiency $J=-T_r/T_{r0}$, where

$$T_r = \int_{\Gamma_w}[T\cdot n]Rd\Gamma, \quad T=-pI+(\nu+\nu_t)(\nabla u_t+\nabla u^T)$$

However one may need to improve the hydraulic efficiency of the pump at constant design point (constant specific speed). So

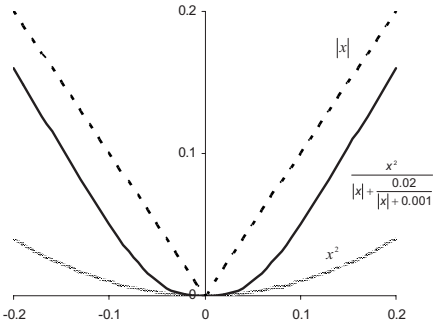

Fig. 2 Comparison of $|x|$, absr(x), and x^2

looking for higher hydraulic efficiency should be done at the given head (total pressure difference between outlet and inlet) and flow rate. The flow is constant in the optimization process and can be imposed through boundary conditions. Head (or pressure difference) can be added as a penalty in the cost function

$$J = -\frac{T_r}{T_{r0}} + \alpha\frac{|h-h_0|}{h_0} \tag{9}$$

Unfortunately, this new term does not enter into the incomplete sensitivity validity domain as it is defined away from the shape and also does not include any geometric quantity. Eventually, the cost function accounting for constant head can be reformulated to adapt the incomplete sensitivity method using reformulated pressure difference (or head) based on axial and radial forces and blade volume in radial turbomachinery

$$J = -\frac{T_r}{T_{r0}} + \alpha\frac{|F_a-F_{a0}|}{F_{a0}} + \beta\frac{|F_R-F_{R0}|}{F_{R0}} + \gamma\frac{|V_b-V_{b0}|}{V_{b0}} \tag{10}$$

which enters the incomplete sensitivity validity domain. Indeed, the cost function is the rotor axial torque with state constraints on hydrodynamic axial (F_a), radial forces (F_r), and geometrical constraint on the blade volume (V_b). The details of this reformulation can be found in the authors' previous work [9].

Hydraulic efficiency will be improved by increasing torque and at the same time keeping F_a, F_R, and V_b, and therefore the head unchanged.

Indeed, one could have used x^2 for penalty, but in this case the conditioning of the problem degrades. To illustrate this point, consider that $|x|$ and $x^2\cdot|x|$ do not change the condition number, but is not differentiable. Therefore, it would be best to use a regularized $|x|$, which is x away from 0 and x^2 close to 0. We used the following regularized form:

$$\text{absr}(x) = \frac{x^2}{|x| + \dfrac{\varepsilon_1}{|x|+\varepsilon_2}}$$

Figure 2 shows the behavior of the different functions near 0. The absr(x) remains differentiable near 0 and has the same behavior with x^2 away from the origin. In the sequel, we used regularized $|x|$ in the functional.

2.1.6 Black-Box Sensitivity Evaluation. Obviously, incomplete sensitivities can be obtained by linearizing the functional and keeping all state based quantities unchanged. However, it might be interesting to avoid any extra programming effort for the user. This is a demand from industry where people are often not professional enough or are black-box solver users. This is one of the main interests of gradient free approaches such as genetic algorithms. We describe a possible implementation of incomplete sensitivities where a change in the functional does not imply any new coding for the calculation of the gradient other than coding the functional itself. We also take this opportunity to show how to adapt an existing optimization platform to incomplete sensitivities.

2.1.7 Finite Difference Method. The easiest and most used approach to compute sensitivities is to apply Taylor expansion and to find each component of the gradient individually (e^j denotes variation along jth component)

$$\frac{dJ}{dx_c}e^j = \frac{1}{\varepsilon}(J(x_c+\varepsilon e^j, q(x_c+\varepsilon e^j),\ W(x_c+\varepsilon e^j)) - J(x_c, q(x_c), W(x_c))) \tag{11}$$

Incomplete sensitivities approach suggests freezing the state variable in the previous formula

$$\frac{dJ}{dx_c}e^j \sim \frac{1}{\varepsilon}(J(x_c+\varepsilon e^j, q(x_c+\varepsilon e^j),\ W(x_c)) - J(x_c, q(x_c), W(x_c))) \tag{12}$$

This is easy to do using finite differences in an existing optimization procedure.

2.1.8 Complex Variable Method. The drawbacks of difference formula are well known (choice of the increment and difference between two close quantities). These can be avoided when working with complex values [13,14] where

$$\frac{dJ}{dx_c} = \frac{\text{Im}[J(x_c+i\varepsilon, q(x_c+i\varepsilon e^j), W(x_c+i\varepsilon))]}{\varepsilon} \tag{13}$$

Here again the incomplete sensitivity method suggests the following approximation:

$$\frac{dJ}{dx_c} \sim \frac{\text{Im}[J(x_c+i\varepsilon, q(x_c+i\varepsilon e^j), W(x_c))]}{\varepsilon} \tag{14}$$

where $i=\sqrt{-1}$. In practice, this method only requires a redefinition of all real variables of a computer program as complex. This is not convenient if a black-box solver is used. But with incomplete sensitivities, only the boundary integral calculations are involved.

2.1.9 Minimization Method. We briefly recall the minimization method to show where incomplete sensitivities appear in descent iterations. Our main interest goes to quasi-Newtonian methods such as BFGS coupled with a line search method [15]. The approximate inverse of the Hessian of the functional is built using successive gradient evaluations. Therefore, with incomplete sensitivities one might expect not only a deviation in the gradient but also in eigenvalues of the Hessian.

Consider the following general minimization problem [15] with box constraints:

$$\min f(x), \quad l \le x \le u \qquad x \in R^n \tag{15}$$

A quasi-Newton method searches for the minimum of the following function in each iteration:

$$\min|_x\left[\frac{1}{2}d^TBd + g_c^T + f(x)\right] \tag{16}$$

The minimum occurs if $Bd+g_c=0$. Therefore at point x_c, the search direction is defined by $d=-B^{-1}g_c$, where B is a positive definite approximation of the Hessian and g_c is the gradient (incomplete) at x_c.

A line search is then used to find a new point x_n

$$x_n = x_c + \lambda d \qquad \lambda \in (0,1] \tag{17}$$

such that

$$f(x_n) = f(x_c) + \alpha g_c^T d$$
$$\alpha \in (0,0.5) \tag{18}$$

Finally, the optimal conditions

$$|g_n(x_i)| \le \varepsilon, \quad l_i < x_i < u_i$$
$$g_n(x_i) < 0, \quad x_i = u_i \tag{19}$$
$$g_n(x_i) > 0, \quad x_i = l_i$$

are checked, where ε is a gradient tolerance. When optimality is not achieved, B is updated according to the BFGS [15] formula (starting from identity matrix)

$$B \leftarrow B - \frac{B\delta\delta^T B}{\delta^T B s} + \frac{yy^T}{y^T\delta}, \quad \begin{cases} \delta = x_n - x_c \\ y = g_n - g_c \end{cases} \tag{20}$$

Another search direction is then computed to begin the next iteration.

If one denotes $g_c = I_c + E_c$ and $g_n = I_n + E_n$, where I is the incomplete sensitivity and E is the remaining part, Eq. (20) suggests that for functionals in the validity domain of incomplete sensitivities, one has equidistribution of the error $E_c \cdot E_n = O(1)$ and $|E_c| \sim |E_n|$.

2.1.10 3D Flow Simulation. To have an efficient shape optimization for fluids, the optimization platform should be able to interact with various computational fluid dynamics (CFD) solvers. To achieve such adaptability, it is important to keep the interface free of constraints for a particular software. This is also one of the advantages of the incomplete sensitivity concept, as it lets the interface to be only surface based. FINE/TURBO, developed by Numeca, is an integrated software based on finite volume discretization for multiblock structured grids. The multiblock structured grids on the blades were prepared by AUTOGRID5 developed by Numeca [16]. The physical model used in the solver was the Reynolds-averaged Navier–Stokes equations in rotating frames of reference coupled with various turbulence models and near-wall treatment for low-Reynolds modeling. The standard high Reynolds k-ε turbulence model with extended wall functions could be chosen without any limitation [17–19].

The discrete schemes were second order in space [17] and first order in time with time marching to steady solutions. Mass flow rate, velocity direction, turbulence kinetic energy k, and turbulent dissipation ε were imposed at the inlet boundary, while at outlet boundary condition static pressure was prescribed. Finally, a periodic boundary condition was applied between two blades.

2.2 Rounding of Blade's Leading Edge and Hub/Shroud Inlet Edges of Reverse Pump. Figure 3 illustrates modifications of the edges, which involves rounding of the shape blade and the sharp edges of the hub/shroud in the inlet of the reverse pump's impeller. On the blade edge profile, the rounding r is taken to be equal to half of the blade thickness, and care is taken to ensure that the overall diameter is not altered. Therefore, there is a certain trade-off in selecting the rounding radius r. The hub and shroud are subjected to rounding both at the outer and at the inner edges of the hub and shroud.

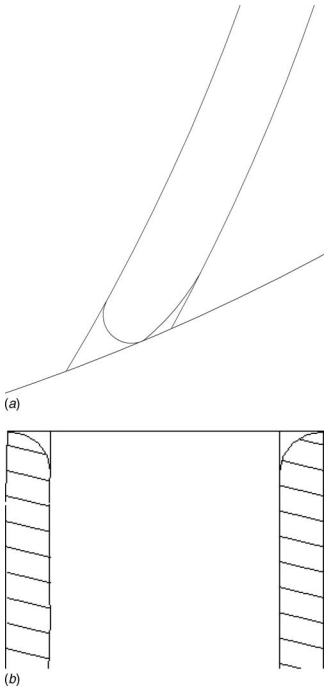

Fig. 3 (*a*) Rounding of blades profile at impeller inlet in turbine mode. (*b*) Rounding of hub/shroud inlet edges.

This modification could reduce the net flow separation loss component at the blades and impeller. However, this modification can also cause a rearrangement of inlet velocity triangle that can change the shock loss component. Loss reduction associated with the shock wave coming in contact with smoother geometric profiles and complex interaction in the clearance between volute and impeller (with rounded hub/shroud) can be expected.

3 Experimental Setup

A complete laboratory model of minihydropower plant was installed in University of Tehran [1], as shown in Fig. 4. The flow rate and head for the pump working as a turbine were generated in the experimental setup by several pumps.

When a pump works as a turbine, a control system is needed to automatically regulate the frequency. The classical governor used for standard turbines are expensive and not always recommended for small hydropower plants. Since these types of plants are being used more in isolated areas, an electronic load controller with ballast loads was built and used for keeping the frequency of the generator in these tests. A conventional synchronous generator

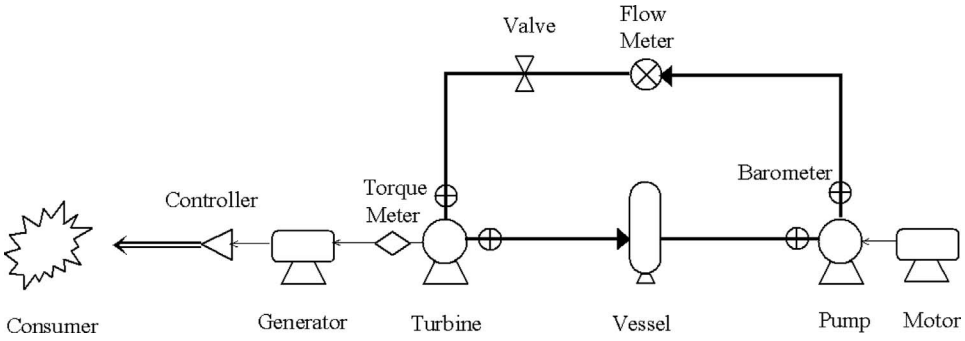

Fig. 4 The minihydropower established in University of Tehran

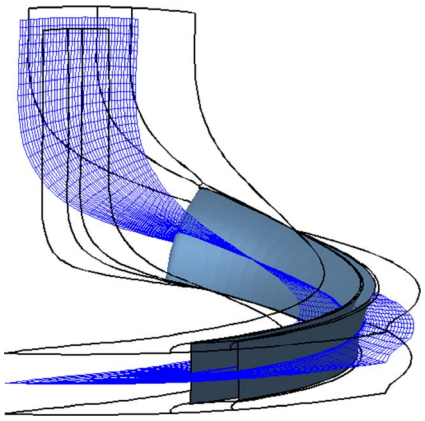

Fig. 5 Computational domain and the grid on midspan

was installed for producing electricity. For turbine shaft torque measuring, generator was changed to suspense state mode and using a scaled arm and several weights; the turbine shaft torque was measured. The flow rate was measured by the discharge law using various orifice plates for each test. Pressures were measured by some barometers. An industrial low specific speed centrifugal pump with a specific speed of 23.5 (m, m^3/s) was selected for testing as a turbine with one original impeller and three modified impellers. This pump had maximum input turbine shaft power, maximum head, and maximum flow rate of 20 kW, 25 m, and 120 l/s, respectively. For the reverse pump testing, a feed pump, several pipes, an orifice, a generator, and ballast loads were selected and installed in the test rig. In the application of the reverse pump, it should be considered that if a generator is to be coupled directly, a nominal speed corresponding to one of the synchronous speeds (e.g., 750 rpm, 1000 rpm, 1500 rpm, or 3000 rpm) should be chosen. For induction generators, and also induction motors, the slip factor must be taken into account (the tested pump rotates at 1450 rpm in pump mode). In practice, synchronous generators are usually used. The reverse pump was tested in $N_t=1500$ rpm.

After measuring all parameters, the reverse pump head, flow rate, output power, and efficiency were obtained. A first-order uncertainty analysis is performed using the constant odds combination method based on a 95% confidence level, as described by

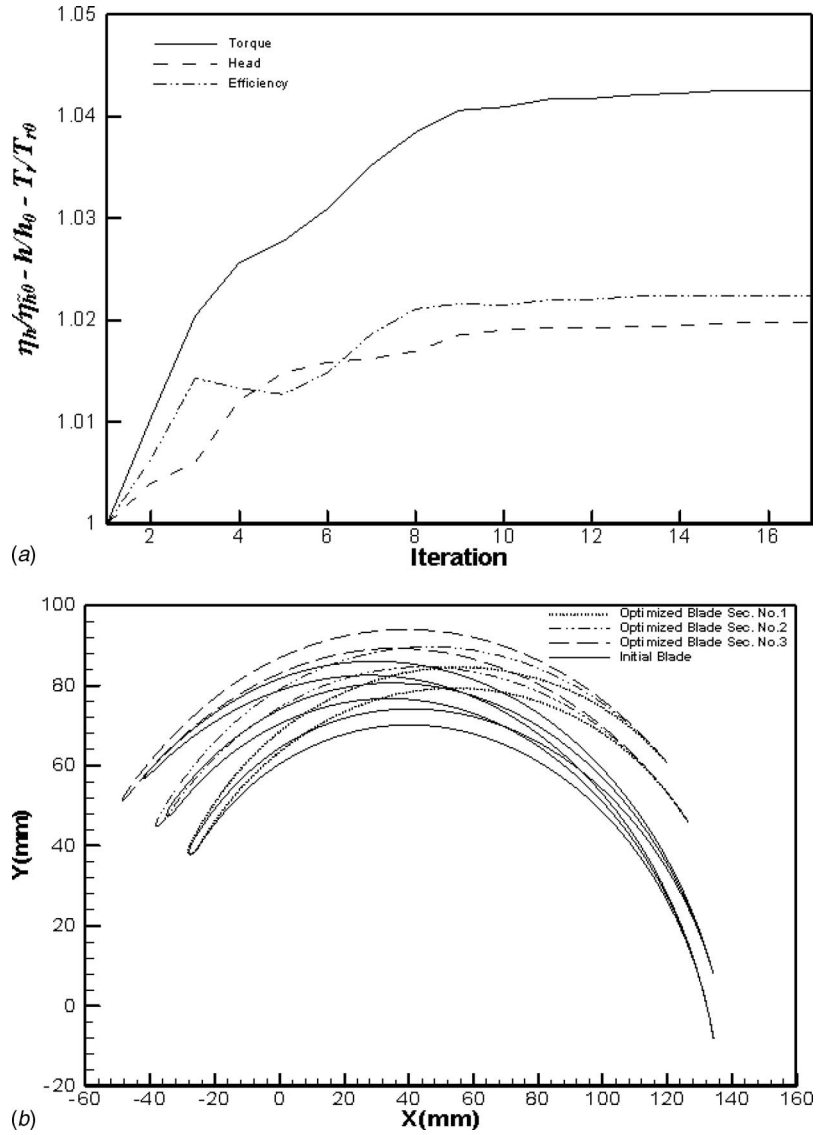

Fig. 6 Optimization for the first parametrization of a centrifugal pump blade. (*a*) Blade performance versus optimization iterations (η_h/η_{h0}, h/h_0, T_r/T_{r0}). (*b*) Initial and final blades, hub-span, midspan, and shroud-span.

Table 1 Optimization results

	Initial	Primal optimization	Final optimization
T_r/T_{r0}	1.0	1.0425(+4.25%)	1.0227(+2.27%)
h/h_0	1.0	1.0197(+1.97%)	1.0108(+1.08%)
η/η_0	1.0	1.0223(+2.23%)	1.0117(+1.17%)
Cost function gradient	0.045	0.006	0.004

Moffat [20]. The uncertainty of the head, flow rate, power, and efficiency are, respectively, ±5.5%, ±3.4%, ±5.1%, and ±5.5%.

4 Results

We considered a centrifugal pump in reverse rotation with a rotational speed of 1500 rpm, a flow rate of 126 m^3/h, and a total head rise of 38 m. The pump had seven blades with an inlet radius in the hub of 0.25 m. This pump was tested as a turbine in the test rig. The shape of impeller blades were optimized by the described optimization algorithm to reach higher efficiency in the rated point region. The cost function for optimization was

$$J = -\frac{T_r}{T_{r0}} + 0.05\frac{|F_a - F_{a0}|}{F_{a0}} + 0.1\frac{|F_R - F_{R0}|}{F_{R0}} + 0.001\frac{|V_b - V_{b0}|}{V_{b0}}$$

The initial geometry was available at hub-span, midspan, and shroud-span. The mesh used for FINE/TURBO was structured, multi-block, and of the HHOHH(O5H)-type. This was an elliptic mesh with about 400,000 nodes. The computational domain and grid view in midspan are shown in Fig. 5. To check if the grid was too coarse, simulations were made with one impeller channel and two different grids. The first grid had about 150,000 cells for one impeller channel and the second one consisted of about 400,000 cells. The simulation results showed differences of less than 1% for efficiency and head. The cost function included not only the

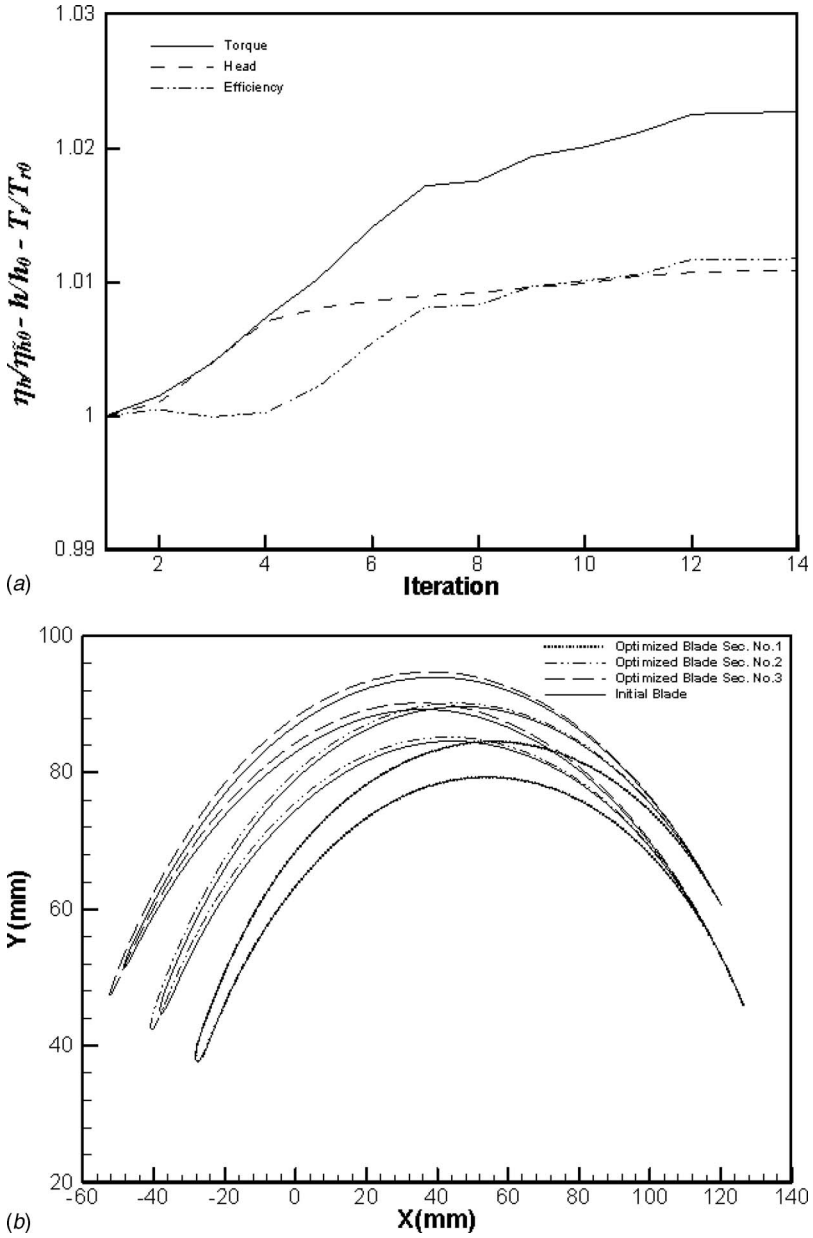

Fig. 7 Optimization for the second parametrization of a centrifugal pump blade. (*a*) Blade performance versus optimization iterations (η_h/η_{h0}, h/h_0, T_r/T_{r0}). (*b*) Initial and final blades, hub-span, midspan, and shroud-span.

torque to maximize, but also a state constraint on hydrodynamic forces as well as a geometrical constraint on the blade volume.

Results showed that the torque was increased by 4.25% and the head by 1.97% for a hydraulic efficiency improvement of 2.2% (see Fig. 6 and Table 1).

For the second optimization with the same cost function, the torque was increased by 2.27% and the head by 1.08% for a hydraulic efficiency improvement of 1.17% (see Fig. 7 and Table 1).

The initial and final optimization results are shown in Table 1. The final designs were more robust than the original shape as the gradients of all constraints were reduced. The optimization process was reasonably fast and required about 17 iterations of the optimization algorithm and 26 functional evolutions. On a 3 GHz computer with a 4 Gbyte RAM, the flow analysis and the complete optimization took almost 23 h and 2 h, respectively.

In the next modification, the leading edges of blades and the inlet edges of the hub and shroud were rounding according to Fig. 3. Finally, all impellers were manufactured and tested in the test rig.

Figures 8 and 9 show the results of the experiments. In these figures, ψ, ϕ, and π are defined as

$$\psi = \frac{gH}{n^2D^2}, \quad \phi = \frac{Q}{nD^3}, \quad \pi = \frac{P}{\rho n^3 D^5} \tag{21}$$

Table 2 shows the changes in hydraulic parameters in flow rate of best efficiency point (BEP). Efficiency improvement occurs in all flow rates of part load and overload zones. The optimized impeller gives an increase of −2.2%, +9.4%, +14.8%, and +2.9% for head, power, and efficiency, respectively. Table 3 shows the comparison between experimental and numerical optimization results. The experiment shows higher values for power, head, and efficiency. This confirms the numerical results and shows that the blade behavior was improved for a wider operating range. But the head is increased slightly more than numerical optimization data. In the optimized geometry, the inlet blade angle is bigger than that of the initial one.

Rounding of optimized impeller improved these values to +5.5%, 11.5%, 36.1%, and 5.5% for flow rate, head, power, and efficiency respectively. This modification could reduce net flow separation loss component at blades and impeller and also cause a rearrangement in the inlet velocity triangle and a change in the shock loss component.

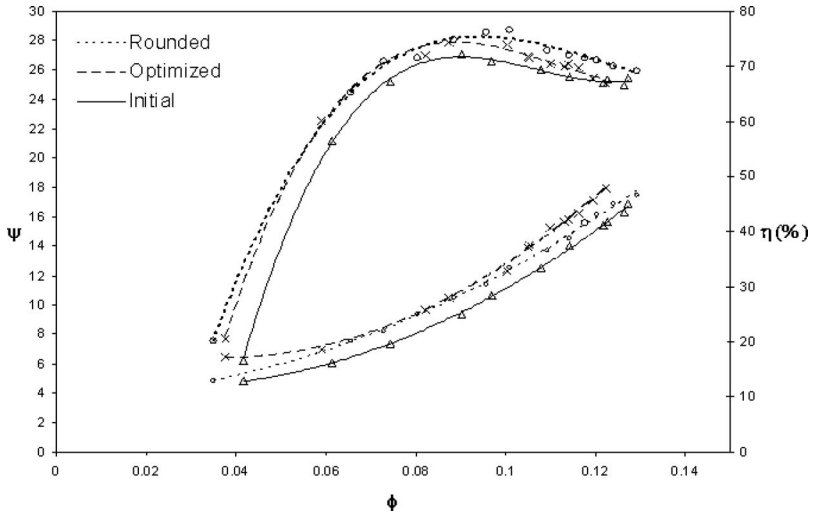

Fig. 8 Experimental results for head number and efficiency

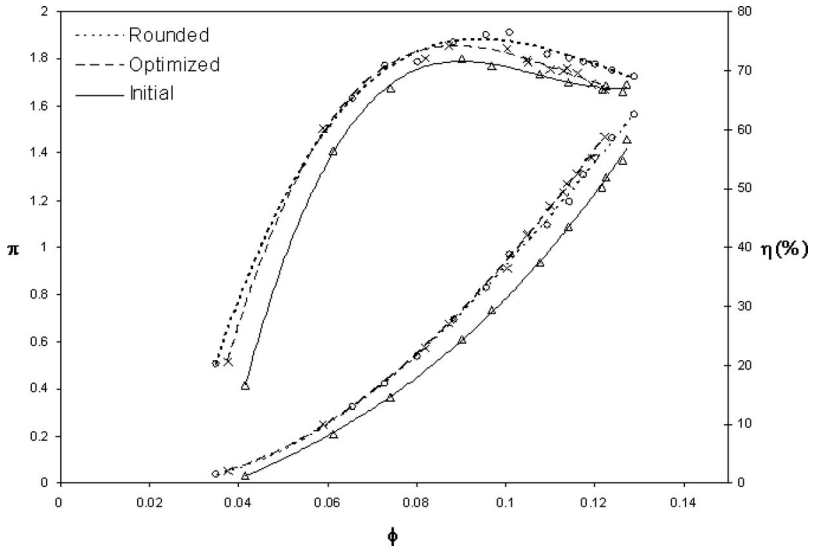

Fig. 9 Experimental results for power number and efficiency

Table 2 Experimental results

	Initial	Optimized	Inlet-rounded
ϕ	0.090	0.088(−2.2%)	0.095 (+5.5%)
ψ	9.6	10.5 (9.4%)	11.5 (19.8%)
p	0.61	0.70 (14.8%)	0.83 (36.1%)
η	0.725	0.746 (2.9%)	0.765 (5.5%)

Table 3 Comparison of numerical optimization and experimental results

	Initial	Numerical optimization	Experimental
T_r/T_{r0}	1.0	+9.65	+14.8
h/h_0	1.0	+1.82	+9.4
η/η_0	1.0	+2.61	+2.9

As we saw, by doing easy modifications on the impeller of the reverse pump, its maximum efficiency was increased.

5 Conclusions

Using the gradient based optimization process on the radial turbomachinery blade design developed in the authors' previous work [9], the blade shape of the impeller of a reverse pump was optimized to improve its maximum efficiency in rated point. The new design was experimentally tested for several operating points. The efficiency was improved in all measured points. Additional modification was the rounding of the blades profile in impeller inlet and hub/shroud inlet edges in turbine mode. Experimental results confirmed that the efficiency is improved in all measured points for this modification.

This study illustrated that just by impeller modification the efficiency of the pump in reverse operation can be improved.

Appendix: Sensitivities Improvement by Reduced Order Models

A middle path between full state equation linearization and incomplete sensitivities is the linearization low-order models to recover the neglected part in the gradient [9]. In other words, one would like to linearize the original state equation

$$x_c \to q(x) \to W(q) \tag{A1}$$

But the following form where the last normalization term is frozen. It must be easier to evaluate and linearize the low-complexity model $\tilde{W}(q) \sim W(q)$:

$$x_c \to q \to \tilde{W}(q)\left(\frac{W(q)}{\tilde{W}(q)}\right) \tag{A2}$$

where $\tilde{W}$ is the solution of a reduced order model. The last term is for the reduced order model to produce the same results. The incomplete gradient of J with respect to x_c can be improved by approximating the neglected part of the exact gradient by the linearized reduced order model:

$$\frac{dJ}{dx_c} \approx \frac{\partial J}{\partial x_c} + \frac{\partial J}{\partial q}\frac{\partial q}{\partial x_c} + \frac{\partial J}{\partial W}\frac{\partial \tilde{W}}{\partial q}(W)\frac{\partial q}{\partial x_c}\left(\frac{W}{\tilde{W}}\right) \tag{A3}$$

One notices that $\tilde{W}$ is never used in state evaluation, but only $\partial\tilde{W}/\partial q$ in the sensitivity evaluation. Also, the reduced order model needs only to be locally valid and is linearized around the solution of the full model. The scaling term in Eq. (22) also helps in recovering the right level for the gradient [2].

The expression of the discrete gradient calculated with respect to an arbitrary normal to the shape n_j is

$$\begin{aligned}\frac{dJ_h}{dn_j} &= \left(\sum_i^{N_h} \frac{d}{dn_j}[T_i \cdot n_i]\text{area}(e_i)\right)\cdot\sigma \\ &= \left(\sum_i^{N_h}\left\{\left[\frac{\partial T_i}{\partial n_j}\cdot n_i\right]\text{area}(e_i) + \left[T_i\cdot\frac{\partial n_i}{\partial n_j}\right]\text{area}(e_i)\right.\right. \\ &\quad \left.\left. + [T_i\cdot n_i]\frac{\partial \text{area}(e_i)}{\partial n_j}\right\}\right)\cdot\sigma\end{aligned} \tag{A4}$$

where n denotes the normal to the shape, σ is an arbitrary direction, $d\Gamma_h$ is the surface increment, e_i is a discrete surface element, and J_h is the discrete cost function.

Following the idea of gradient approximation by neglecting the state contributions, it is assumed that the state in a given point does not depend on its value at the other points ($\partial T_i/\partial n_j = 0$ for $i \neq j$). Therefore the state term in the sensitivities can be evaluated in an arbitrary point on the shape using reduced order models. State linearization is given by

$$\begin{aligned}\frac{\partial T}{\partial n}\cdot n &= \frac{\partial}{\partial n}[pI - (\nu+\nu_t)(\nabla u_t + \nabla u^T)]\cdot n \\ &= \frac{\partial p}{\partial n}\cdot n - \frac{\partial}{\partial n}[(\nu+\nu_t)(\nabla u_t + \nabla u^T)]\cdot n\end{aligned} \tag{A5}$$

The selection of reduced order models depends on the application of interest. In this work, boundary layer theory can be used by considering a local reference frame in a point of the shape with y indicating the direction normal to the wall and y_w denoting the wall location.

For sensitivity of the pressure and viscous shear with respect to variations in the shape in the normal direction, the terms to be evaluated in Eq. (24) are equivalent to the following in the local referential:

$$\frac{\partial p}{\partial y_w}, \quad \frac{\partial}{\partial y_w}\left((\nu+\nu_t)\frac{\partial u}{\partial y}\right) \tag{A6}$$

where u denotes the tangential velocity. In boundary layer theory, the pressure gradient normal to the wall is zero. So in this case if the shape variations are normal to the wall, pressure variation vanishes with respect to the small variation in y_w

$$\frac{\partial p}{\partial y_w} = -\frac{\partial p}{\partial y} = 0 \tag{A7}$$

For viscous effects, wall laws can be used as reduced order models. These models replace the no-slip boundary conditions by a relation between the variables and their derivatives for the tangential component of the velocity together with a nonpenetration condition

$$\frac{\tilde{u}}{u_\tau} = f(y^+(u_\tau)) \tag{A8}$$

where $u_\tau = \sqrt{\tau_w/\rho}$, the local friction velocity, is computed using the flow state provided by the Navier–Stokes solver, and the local Reynolds number is defined as $y^+ = (y - y_w)u_\tau/\nu$.

Using boundary layer assumption and shear conservation along the normal direction, the sensitivity term to be evaluated is

$$\frac{\partial}{\partial y_w}\left((\nu+\nu_t)\frac{\partial u}{\partial y}\right) = \frac{\partial \tau_w}{\partial y_w} = 2u_\tau\frac{\partial u_\tau}{\partial y_w} \tag{A9}$$

Now one can use the velocity gradient from the flow solver

$$\frac{\partial \tilde{u}}{\partial y_w} = \nabla u \cdot n(y_w) = \frac{\partial u_\tau}{\partial y_w} f(u_\tau) + u_\tau \frac{\partial f(u_\tau)}{\partial y_w} \tag{A10}$$

This eventually gives the expression for shear sensitivity with respect to the normal deformation to the wall

$$2u_\tau \frac{\partial u_\tau}{\partial y_w} = 2u_\tau^2 \left(\nabla u \cdot n(y_w) - u_\tau \frac{\partial f}{\partial y_w} \right) / u \tag{A11}$$

As mentioned, this is calculated around the "Navier–Stokes" solution (i.e., u_τ, ∇u, and u come from the flow solver).

Using, for instance, the universal log-low $f(u_\tau) = \ln(y^+)/\kappa + B$ with $\kappa = 0.41$ and $B = 5.36$:

$$\frac{\partial f}{\partial y_w} = \frac{-1}{\kappa(y - y_w)} \tag{A12}$$

This approach provides information on the state sensitivity with respect to the shape variations along the normal direction to the wall. In cases where incomplete sensitivities have both tangential and normal components to the shape, this contribution shall be added only to the normal component. If one would like to be efficient with incomplete sensitivities, it is wise to choose a shape variation parametrization normal to the shape.

References

[1] Derakhshan, S., and Nourbakhsh, A., 2008, "Experimental Study of Characteristic Curves of Centrifugal Pumps Working as Turbines in Different Specific Speeds," Exp. Therm. Fluid Sci., **32**, pp. 800–807.

[2] Williams, A., 1995, *Pumps as Turbines Users Guide*, International Technology, London.

[3] Chapallaz, J. M., Eichenberger, P., and Fischer, G., 1992, *Manual on Pumps Used as Turbines*, Vieweg, Braunschweig, Germany.

[4] Lueneburg, R., and Nelson, R. M., 1992, *Hydraulic Power Recovery Turbines*, Gulf Publishing Company, Houston, TX.

[5] Williams, A., 1992, "Pumps as Turbines Used With Induction Generations of Stand-Alone Micro-Hydroelectric Power Plants," Ph.D. M.E. thesis, Nottingham Polytechnic, Nottingham.

[6] Cohrs, D., 1997, *Untersuchungen an Einer Mehrstufigen Rückwärtslaufenden Kreiselpumpe im Turbinenbetrieb*, W. H. Faragallah, ed., Verlag und Bildarchiv, Sulzbach, Germany.

[7] Hirschberger, M., and Kuhlmann, J., 1993, "Entwicklung und Einsatz Doppelströmiger Kreiselpumpen als Entspannungsturbinen," *Pumpen als Turbinen*, W. H. Faragallah, ed., Verlag und Bildarchiv, Sulzbach, Germany.

[8] Singh, P., 2005, "Optimization of Internal Hydraulics and of System Design for Pumps as Turbines With Field Implementation and Evaluation," Ph.D. M.E. thesis, University of Karlsruhe, Karlsruhe.

[9] Derakhshan, S., Mohammadi, B., and Nourbakhsh, A., 2008, "Incomplete Sensitivities for 3D Radial Turbomachinery Blade Optimization," Comput. Fluids, **37**, pp. 1354–1363.

[10] Pironneau, O., 2008, *Optimal Shape Design for Elliptic Systems*, Springer, New York.

[11] Nourbakhsh, A., Jaumotte, A., Hirsch, C., and Parizi, H., 2008, *Turbopumps and Pumping Systems*, Springer-Verlag, Berlin.

[12] Mohammadi, B., and Pironneau, O., 2001, *Applied Shape Optimization for Fluids*, Oxford University Press, New York.

[13] Squire, W., and Trapp, G., 1997, "Using Complex Variables to Estimate Derivatives of Real Functions," SIAM Rev., **10**(1), pp. 110–112.

[14] Anderson, K., Newman, J., Whitfield, D., and Nielsen, E., 1999, "Sensitivity Analysis for the Navier–Stokes Equations on Unstructured Grids Using Complex Variables," AIAA J., **99**(329), pp. 1–8.

[15] Nocedal, J., and Stephen, J. W., 1999, *Numerical Optimization*, Springer, New York.

[16] Numeca, 2007, AUTOGRID V.5 User Guide.

[17] Numeca, 2007, FINETURBO V.8 User Guide.

[18] Hakimi, N., 1997, "Preconditioning Methods for Time Dependent Navier–Stokes Equations," Ph.D. thesis, Vrije Universiteit Brussel, Elsene.

[19] Launder, B. E., and Spalding, D. B., 1974, "The Numerical Computation of Turbulent Flow," Comput. Methods Appl. Mech. Eng., **3**, pp. 269–289.

[20] Moffat, R. J., 1982, "Contributions to the Theory of Single-Sample Uncertainty Analysis," ASME J. Fluids Eng., **104**, pp. 250–260.

Effect of Side Wind on a Simplified Car Model: Experimental and Numerical Analysis

Emmanuel Guilmineau
Laboratoire de Mécanique des Fluides,
CNRS UMR 6598,
Equipe Modélisation Numérique,
Ecole Centrale de Nantes,
1 Rue de la Noë,
BP 921001,
44321 Nantes Cedex 3, France
e-mail: emmanuel.guilmineau@ec-nantes.fr

Francis Chometon
Laboratoire d'Aérodynamique,
Conservatoire National des Arts et Métiers,
15 Rue Marat,
78210 Saint Cyr l'Ecole, France

A prior analysis of the effect of steady cross wind on full size cars or models must be conducted when dealing with transient cross wind gust effects on automobiles. The experimental and numerical tests presented in this paper are performed on the Willy square-back test model. This model is realistic compared with a van-type vehicle; its plane underbody surface is parallel to the ground, and separations are limited to the base for moderated yaw angles. Experiments were carried out in the semi-open test section at the Conservatoire National des Arts et Métiers, and computations were performed at the Ecole Centrale de Nantes (ECN). The ISIS-CFD flow solver, developed by the CFD Department of the Fluid Mechanics Laboratory of ECN, used the incompressible unsteady Reynolds-averaged Navier–Stokes equations. In this paper, the results of experiments obtained at a Reynolds number of 0.9×10^6 are compared with numerical data at the same Reynolds number for steady flows. In both the experiments and numerical results, the yaw angle varies from 0 deg to 30 deg. The comparison between experimental and numerical results obtained for aerodynamic forces, wall pressures, and total pressure maps shows that the unsteady ISIS-CFD solver correctly reflects the physics of steady three-dimensional separated flows around bluff bodies. This encouraging result allows us to move to a second step dealing with the analysis of unsteady separated flows around the Willy model. [DOI: 10.1115/1.3063648]

Keywords: generic car body, numerical simulation, experimental data, cross wind effect, vehicle aerodynamics

1 Introduction

As passenger vehicles become lighter to reduce fuel consumption, the stability and handling characteristics become more sensitive to aerodynamic forces. Moreover, a vehicle on the road is submitted to a nonuniform turbulent atmospheric flow and transient cross winds. These phenomena, such as passing or crossing maneuvers, are factors in the vehicle's dynamic stability [1].

From an experimental point of view, the cross wind effect has already been studied, and several techniques allow the reproduction of a side gust of wind in a wind tunnel. For Baker and Humphreys [2] and Macklin et al. [3], this reproduction was obtained by propelling the model on a rail crossing the test section of the wind tunnel. Ryan and Dominy [4] experimented on a generic hatchback model and used a technique where the side wind was produced by a cross jet. Another technique consists of using oscillating airfoil sections positioned upstream of a stationary model [5]. Many experimental studies of cross wind were carried out on car models [4–7] and lorry models [6,8], and real cars were also used in several studies [9,10]. The approach retained here consists in submitting the model to a periodic movement in a steady wind [11]. This approach does not directly simulate the side gust of wind, but it permits the analysis of the phenomena of phase shifting and hysteresis associated with an unsteady wind [12].

Numerical simulation is well integrated in the automotive industry and is now an engineering tool used in parallel with experiments performed during the design process of road vehicles. Much fundamental research is performed on the Ahmed body, which includes most of the aerodynamic features found on a real car. This simplified vehicle geometry has been widely used in a large number of experiments [13,14], and many numerical simulations have been performed at zero yaw angle to evaluate computational fluid dynamics (CFD) tools and their ability to predict drag and lift for several rear slant angles [15–20]. To date, most of the numerical simulations of the side wind effects on road vehicles are performed on trucks [21,22] and on trains [23,24]. In all these numerical studies, several methods were used to model turbulence: classic turbulence models such as k-ε, the detached eddy simulation (DES) or large eddy simulation (LES), and even the lattice Boltzmann approach. In this study, we will attempt to show that CFD can be used for industrial applications, such as complex geometries, while not being too high in terms of CPU time. We use Reynolds-averaged Navier–Stokes (RANS) simulations instead of LES since the CPU time is between four and five times higher for LES than for RANS. Another factor in our decision is the fact that LES is not yet sufficiently mature to be used to obtain design quantities, such as drag, in the external aerodynamics of ground vehicles [19] since such techniques require a fine resolution in the near-wall regions that leads to grids with a large number of points. Several approaches that reduce resolution requirements by modeling the near-wall region, such as the hybrid methods, so-called hybrid LES-RANS or DES, are still not fully developed, and several problems remain to be solved, such as the choice of a turbulence model and the question of where to put the matching line between the RANS and LES regions. Once these problems have been solved, these techniques will be available for use in vehicle aerodynamics.

The research presented in this paper is the first step toward a more general goal, which is the analysis of numerical simulations based on RANS equations approaches to calculate the evolution

Contributed by the Fluids Engineering Division of ASME for publication in the JOURNAL OF FLUIDS ENGINEERING. Manuscript received May 11, 2007; final manuscript received October 14, 2008; published online January 15, 2009. Assoc. Editor: Rajat Mittal.

of aerodynamic characteristics of passenger vehicles as a function of unsteady situations such as passing and crossing or the presence of an unsteady gust of wind. The approach is based on the comparison of experimental data with numerical data obtained on a new car model (Willy car model), which was tested for unsteady conditions [12].

The goal of the current project is to understand the physics of separated flow around bluff bodies with application to side gust wind effects on automobiles. We found that a generic model with no sharp corners on the fore body and a square base was more convenient for analyzing unsteady separations limited to its leeward side and base. An alternative would be to use the generic Ahmed body, which is built around a rectangular box with a vertical front end, parallel sides, roof and underbody, and a rear slant. This model is very useful for analyzing the total drag by its segmentation into the contribution of each part of the body [1] and is commonly used as a basic body for the comparison of CFD approaches. Many results show that there are large separations at the level of the parallel sides and roof [13]. These separations interact with the base flow and make the analysis of effects of the base slant angle variations more difficult. For these reasons, we did not choose the Ahmed body, preferring a model with no sharp corners.

In this paper, we study the aerodynamic characteristics of the Willy model in a steady cross wind. The technique used to simulate this condition is to yaw the model relative to the freestream flow above a fixed ground plane. The results presented here deal with the analysis of steady flows for various yaw angles β from $\beta=0$ deg to $\beta=30$ deg. The value $\beta=30$ deg corresponds to a side wind equal to half the value of the vehicle velocity.

2 Test Model

Experimental and numerical tests are performed on the square-back Willy test model,[1] which was designed to satisfy the following criteria:

- The geometry is realistic, compared with a real vehicle.
- The model's plane underbody surface is parallel to the ground.
- The separations are limited to the region of the base for a moderated yaw angle, i.e., $\beta=10$ deg.

The digital definition of the model for the axes (X,Y,Z) is analytical and obtained by combining the following elements (see Fig. 1):

1. A NACA mean line (A) of chord Ch and geometric factor $a=1$. The maximum camber of this mean line is located at midchord, $X/\mathrm{Ch}=0.5$. Its generic equation is (see Abbott and Von Doenhoff [25])

$$Y=0$$

$$Z=-\frac{1}{4\pi}\left[\left(1-\frac{X}{\mathrm{Ch}}\right)\ln\left(1-\frac{X}{\mathrm{Ch}}\right)+\frac{X}{\mathrm{Ch}}\ln\frac{X}{\mathrm{Ch}}\right] \quad (1)$$

   In Fig. 1(a), which describes the side view of the model, the origin of mean line (A) is Om, and point M is the location of its maximum camber at a distance of $Lm=\mathrm{Ch}/2$ from Om. The value of the camber is Ca.
2. A Rankine half-body with a downstream diameter ϕ. Curve (B), which is in the symmetry plane of the body, is obtained by distributing the thickness of the Rankine body on mean line (A) in direction Z. A cross section of the body, obtained at point M, is given in Fig. 1(c). Point b is the intersection of curve (B) with the cross section. Curve (abc) is an ellipse, and the sides (ga) and (cd) are vertical and are connected to the horizontal underbody (ef) by quarter circles of radius R. The points a, M, and c are on the same horizontal line.

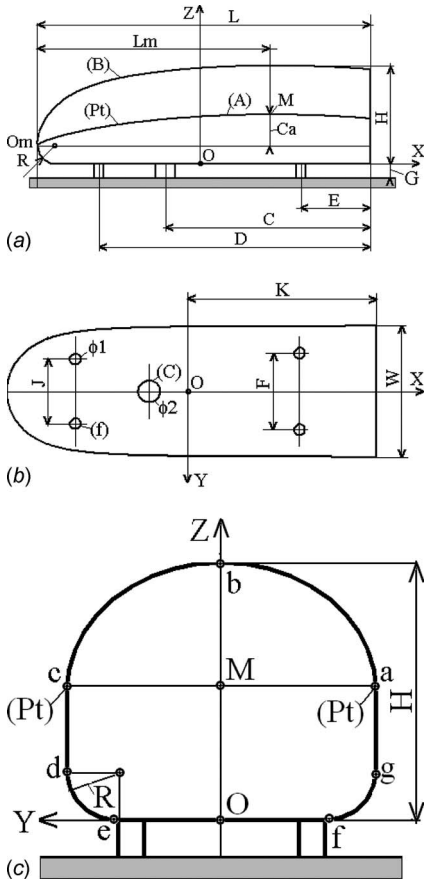

Fig. 1 Model definition

The digital definition of the model allowed the modification of the shape through four parameters. These parameters are $p_1=L/\phi$, where L is the length of the model, $p_2=Lm/L$ with the condition $0.5<p_2<1$, $p_3=Ca/\phi$ with the condition $0<p_3<0.5$, and p_4, which is the ratio between the axes of the ellipses of the upper surface. The value of the radius R is defined by

$$\frac{R}{L}=\frac{1-2p_3}{2p_1} \quad (2)$$

For the model analyzed in this work, $p_1=3.3750$, $p_2=0.7037$, $p_3=0.3050$, and $p_4=1.2$.

The overall length of the model is $L=675$ mm, the width is $W=240$ mm, the maximum height is $H=192$ mm, and its surface reference is the maximum cross section $S_{\mathrm{ref}}=41{,}791$ mm^2. The ground clearance is $G=29$ mm, and the diameter of the four feet (f), which are used to secure the model to the floor of the wind tunnel is $\phi1=20$ mm. A cylinder (c) with a diameter $\phi2=40$ mm is used to protect the pressure tubes passing from the pressure taps to the multimanometer. Other dimensions are defined in Table 1.

Table 1 Dimensions of the test model (data in mm)

L	W	H	C	D	E	F	G	J	K	$\phi1$	$\phi2$
675	240	192	415	550	140	140	29	118	345	20	40

[1]The geometry of the Willy square-back model is available. Please contact the corresponding author.

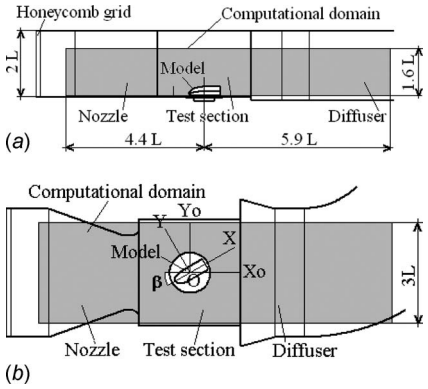

Fig. 2 Wind tunnel and model

3 Experimental Setup

The description of the model mounted in the Prandtl-type wind tunnel of the CNAM is given in Fig. 2. The semi-open test section of the wind tunnel has a cross section of 1.45×1.45 m^2, and the ground is fixed. Forces and moments are measured with a six-component balance. The reference axes (Xo,Yo,Zo) are the Eiffel axes, where Xo is parallel to the upstream velocity V_0. The Lilienthal axes (X,Y,Z) are linked to the model. The origin of the axes lies at point O located on the floor of the model. This point O is the center of rotation of the model (see Fig. 1).

The value of the yaw angle β is positive when the right side of the car model is windward. The turbulence level at the center of the test section is 2%. The results of the experiments given in this paper are obtained at a Reynolds number of 0.9×10^6 based on the velocity V_0 and the length L of the model. Force and moment coefficients are nondimensionalized by the maximum cross section S_{ref} of the model, its length L, and the freestream dynamic pressure $q_0 = \frac{1}{2}\rho V_0^2$. The drag coefficient Cx is given by

$$Cx = \frac{Fx}{q_0 S_{\text{ref}}} \tag{3}$$

where Fx is the drag force. The side force coefficient is given by

$$Cy = \frac{Fy}{q_0 S_{\text{ref}}} \tag{4}$$

where Fy is the side force. The moment coefficient is defined by

$$CN = \frac{N}{q_0 S_{\text{ref}} L} \tag{5}$$

where N is the moment along the Z axis. Uncertainty in the drag Cx is $\pm 1.7\%$, and uncertainty in the side force Cy and in the yawing moment CN is $\pm 1.9\%$. Tomographies of total pressure are measured using a Kiel probe with an external diameter of 6 mm and yaw and pitch ranges of about 40 deg. The nondimensional total pressure coefficient, Cp_i, is given by

$$Cp_i = \frac{p_{i0} - p_i}{q_0} \tag{6}$$

where p_{i0} and p_i are, respectively, the upstream and the local total pressure. For technical reasons, experimental total pressure tomographies are measured in (Yo,Zo) Eiffel planes. Nondimensional locations of the tomographies are given in the reference axis Xo, and the reference length is the length L of the model. Wall pressures are measured along the curve (Pt) of the model (see Figs. 1(*a*) and 1(*c*)). The internal diameter of the pressure taps is 1.5 mm. Pressure coefficients Cp are defined by

$$Cp = \frac{p - p_0}{q_0} \tag{7}$$

where p_0 and p are, respectively, the upstream static pressure and the local pressure. The uncertainty in the pressure coefficients is estimated to be $\pm 2.2\%$.

4 Numerics

4.1 Flow Solver. The ISIS-CFD flow solver, developed by the Equipe Modélisation Numérique (EMN) of the Fluid Mechanics Laboratory of the Ecole Centrale de Nantes, uses the incompressible unsteady Reynolds-averaged Navier–Stokes equations. This solver is based on the finite volume method to build a spatial discretization of the transport equations.

The incompressible unsteady Reynolds-averaged Navier–Stokes equations can be written (using the generalized form of Gauss' theorem) as

$$\frac{\partial}{\partial t}\int_V \rho dV + \int_S \rho(\boldsymbol{U} - \boldsymbol{U}_d)\cdot \boldsymbol{n} dS = 0 \tag{8a}$$

$$\frac{\partial}{\partial t}\int_V \rho U_i dV + \int_S \rho U_i(\boldsymbol{U} - \boldsymbol{U}_d)\cdot \boldsymbol{n} dS = \int_S (\tau_{ij} I_j - p I_i)\cdot \boldsymbol{n} dS \tag{8b}$$

where V is the domain of interest, or control volume, bounded by a closed surface S moving at a velocity $\boldsymbol{U}_d$ with a unit outward normal vector $\boldsymbol{n}$. $\boldsymbol{U}$ and p are, respectively, the velocity and pressure fields. τ_{ij} are the components of the viscous stress tensor, whereas I_j is the identity vector whose components are null, except for the component j, which is equal to unity.

All flow variables are stored at the geometric center of arbitrary shaped cells. Volume and surface integrals are evaluated with second-order accurate approximations. The face-based method is generalized to two-dimensional or three-dimensional unstructured meshes for which nonoverlapping control volumes are bounded by an arbitrary number of constitutive faces. Numerical fluxes are reconstructed on mesh faces by linear extrapolation of integrand from the neighboring cell centers. A centered scheme is used for the diffusion terms, whereas for the convective fluxes, the scheme implemented in the ISIS-CFD code is the gamma differencing scheme (GDS) [26]. Through a normalized variable diagram (NVD) analysis, this scheme enforces local monotonicity and convection boundedness criteria.

The velocity field is obtained from the momentum conservation equations, and the pressure field is extracted from the mass conservation constraint, or continuity equation, transformed into a pressure equation. The pressure equation is obtained in the spirit of Rhie and Chow [27]. Momentum and pressure equations are solved in a segregated manner as in the SIMPLE coupling procedure [28].

A second-order backward difference scheme is used to discretize time. All spatial terms appearing in Eqs. (8*a*) and (8*b*) are treated in a fully implicit manner. In this paper, we only use the steady equations. Therefore, the velocity $\boldsymbol{U}_d$ and the first term in Eqs. (8*a*) and (8*b*) are null. The numerical implementation is detailed by Queutey and Visonneau [29], other researchers of the EMN group of the laboratory.

4.2 Turbulence Modeling. Several turbulence closures are included in the flow solver, ranging from linear eddy-viscosity-based models to full second-order closures [30]. For these studies, the explicit algebraic stress model (EASM) has been chosen. Previous studies of the EMN group [31,32] have shown that anisotropic turbulence closures (such as Reynolds stress transport models (RSTM) or EASM) are the most reliable statistical turbulence modeling for predicting three-dimensional flows such as ship flows when intense longitudinal vortices spread out in the aft part

of the ship.

In the EASM approach, the Reynolds stress tensor is given by

$$\tau_{ij} = \tfrac{2}{3}k\delta_{ij} - 2\nu_t\Big[S_{ij} + a_2a_4(S_{ik}W_{kj} - W_{ik}S_{kj}) - 2a_3a_4\Big(S_{ik}S_{kj} - \tfrac{1}{3}S_{mn}S_{mn}\delta_{ij}\Big)\Big] \tag{9}$$

S_{ij} and W_{ij} are the strain rate and rotation rate tensors defined, respectively, as

$$S_{ij} = \frac{1}{2}\left(\frac{\partial u_i}{\partial x_j} + \frac{\partial u_j}{\partial x_i}\right), \quad W_{ij} = \frac{1}{2}\left(\frac{\partial u_i}{\partial x_j} - \frac{\partial u_j}{\partial x_i}\right) \tag{10}$$

The turbulent eddy viscosity is determined from

$$\nu_t = \max\left(-k\alpha_1, 0.0005\frac{k^2}{\varepsilon}\right) \tag{11}$$

where α_1 is obtained from the solution to the following cubic equation:

$$\left(\frac{\alpha_1}{\tau}\right)^3 + t\left(\frac{\alpha_1}{\tau}\right)^2 + s\left(\frac{\alpha_1}{\tau}\right) + r = 0 \tag{12}$$

where $\tau = k/\varepsilon$ is the turbulence time scale and

$$t = -\frac{\gamma_1}{\eta^2\tau^2\gamma_0}$$

$$s = \frac{1}{(2\eta^2\tau^2\gamma_0)^2}\left(\gamma_1^2 - 2\eta^2\tau^2\gamma_0 a_1 - \frac{2}{3}\eta^2\tau^2 a_3^2 + 2R^2\eta^2\tau^2 a_2^2\right) \tag{13}$$

$$r = \frac{\gamma_1 a_1}{(2\eta^2\tau^2\gamma_0)^2}$$

The root of Eq. (12) may be real or complex. The correct root is the root with the lowest real part [33]. The parameters are given by

$$\eta^2 = S_{ij}S_{ij}, \quad \{\mathbf{W}^2\} = -W_{ij}W_{ij}, \quad R^2 = -\{\mathbf{W}^2\}/\eta^2$$

$$a_1 = \tfrac{1}{2}\left(\tfrac{4}{3} - C_2\right), \quad a_2 = \tfrac{1}{2}(2 - C_4)$$

$$a_3 = \tfrac{1}{2}(2 - C_3), \quad a_4 = [\gamma_1 - 2\gamma_0(\alpha_1/\tau)\eta^2\tau^2]^{-1}\tau$$

$$\gamma_0 = C_1^1/2, \quad \gamma_1 = C_1^0/2 + (C_{\varepsilon 2} - C_{\varepsilon 1})/(C_{\varepsilon 2} - 1) \tag{14}$$

$$C_{\varepsilon 1} = 1.44, \quad C_{\varepsilon 2} = 1.83, \quad C_1^0 = 3.4$$

$$C_1^1 = 1.8, \quad C_2 = 0.36, \quad C_3 = 1.25, \quad C_4 = 0.4$$

To implement the EASM model, the turbulent velocity and length scales are determined by using two transport equations, the k-ω BSL model proposed by Menter [34]. Compared with the original model, only two natural modifications are introduced. First, the turbulent eddy viscosity ν_t is replaced by the value given by Eq. (11). Second, the contribution of the nonlinear part of the Reynolds stress used to turbulence production is taken into account in three-dimensional flow computation. The EASM model implemented can be integrated down to the wall and gives correct log law behaviors without any recalibration. Details of this model can be found in Ref. [32]. The CPU cost of the EASM model is 30% higher than the k-ω of Menter [34].

5 Computational Details

The computational domain starts at $4.4 \times L$ from the origin 0 in front of the model and extends to $5.9 \times L$ behind the model. The width of the domain is $3 \times L$, and its height is $1.6 \times L$ (see Fig. 2). The mesh is generated using HEXPRESS™, an automatic unstructured mesh generator. This software generates meshes containing only hexahedrals. For the surface of the model, we use a no-slip boundary condition, and the wall normal resolution is set to 0.006 mm, i.e., $y+=0.5$. For the wind tunnel floor, we use a wall function, and the distance between the floor and the first fluid points is set to 0.6 mm. This approach, used to take the walls into account, is the same as the approach proposed by Krajnović and Davidson [19], who used the LES approach around a generic ground model. At the outlet of the computational domain, the pressure is prescribed, while for the other boundaries we use a Dirichlet condition for velocity and turbulence.

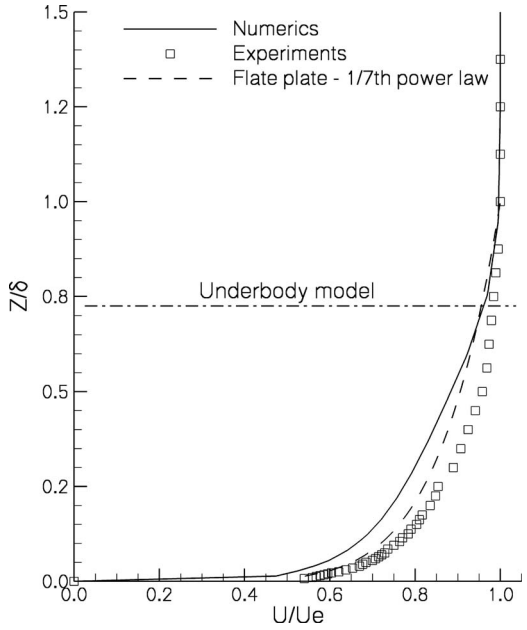

Fig. 3 Boundary layer profile at Xo=−670 mm at the yaw angle β=30 deg

The normalized experimental and numerical velocity profiles of the boundary layer on the floor of the wind tunnel, at Xo=−670 mm and Yo=10 mm, are given in Fig. 3. The results are obtained for an upstream velocity V_0=20 m/s and the model at the yaw angle β=30 deg. The flat plate 1/7th power law boundary layer profile is also given. The numerical result is typical of a turbulent boundary layer submitted to a weak positive pressure gradient, with a modification of the velocity gradient and an increase in the shape factor (see Cousteix [35]). The position of the underbody of the model given in Fig. 3 shows that the consequences of the discrepancies between the experiments and the present simulation should be limited to the underbody flow and should have only a weak influence on the rest of the model.

In order to establish a grid-independent solution, computations have been performed at the yaw angle β=10 deg for four meshes with approximately 1.6×10^6 points, 6.6×10^6 points, 10.8×10^6 points, and 19.3×10^6 points, which are named G0, G1, G2, and G3, respectively. Close to the wall of the model, the fine computational grid has Δx=1.6 mm in the streamwise direction and 0.7 mm$\leq \Delta y \leq$1.7 mm in the direction parallel to the surface and normal to the streamwise direction. The maximum size, $\Delta x = \Delta y = \Delta z$=0.1 m, are located at the top of the computational domain. The number of points of the mesh in the boundary layer is approximately 25 for the fine computational grid. Grid G3 is distributed on 60 blocks, grid G2 on 34 blocks, grid G1 on 20 blocks, and grid G0 on 8 blocks. The characteristics of these meshes are detailed in Table 2.

In this study, the computations are steady simulations. Consequently, any time step is used. To obtain converged results, 7000 nonlinear iterations are necessary. For the fine mesh, the CPU time is 70 h on an IBM Power 4.

Figure 4 presents the pressure coefficient along curve (Pt) of the

Table 2 Characteristics of the four meshes

	G0	G1	G2	G3
Number of points	1,609,155	6,651,159	10,808,408	19,273,500
Number of points on the model	30,905	102,522	205,366	342,432
Number of points on the plate	20,848	49,857	61,313	98,664
Number of cells	1,549,482	6,478,457	10,503,589	19,240,045

model (see Fig. 1) versus the mesh for $\beta=10$ deg. We note that the prediction of the pressure along curve (Pt) is independent of the mesh used. We only have a small difference near the base of the model with the coarse mesh.

Table 3 presents the drag coefficient versus the mesh. We note that the solution converges when the grid is increasingly fine. According to these results, all the numerical results presented thereafter were obtained on grids similar to grid G3, i.e., with approximately 20×10^6 points.

6 Results

6.1 Flow Structure. An experimental and a numerical reconstruction of the separated flow and of the wake obtained at $\beta=30$ deg are performed from tomographies of total pressure coefficients Cp_i drawn in Eiffel planes (Yo,Zo) (see Fig. 5). The experimental tomographies are postprocessed in order to suppress the noise measured outside the body, and experimental values are set to zero when the total pressure coefficients are in the range of $\Delta Cp_i=\pm0.04$. This general view shows that the numerical model reproduces the physics of the experimental three-dimensional turbulent wake. We note that the direction of the wake is strongly deviated by the upstream velocity. The diffusion of the numerical model is lower than the diffusion observed experimentally. This result must be considered as a quality of the solver even if the turbulence level of the wind tunnel produces more mixing of turbulence scales.

The details of the formation of the leeward side wake and of the vortices shedding are described in Fig. 6, where pseudostreamlines are drawn in Lilienthal (Y,Z) planes at $X/L=0$, which is at midlength of the body, at $X/L=0.30$, and at $X/L=0.45$, which is close to the base of the model. The yaw angle evolves from $\beta=10$ deg to $\beta=30$ deg. The rotation of the vortices is defined for an observer looking at the model backward.

The figures corresponding to the yaw angle $\beta=10$ deg show that the boundary layer does not separate on the leeward side of the body, except at the level of the base where vortex (V3) is shed at the confluence of the underbody and the leeward side of the body. The tomographies of total pressure drawn in Fig. 7 at $Xo/L=0.60$, just downstream the base of the model, confirm the thickening of the boundary layer on the leeward side. The flow separates at the level of the base, and a weak vortex (V2) is shed. Vortex (V3) is visible both in numerical results and experiments even if the diffusion is larger in experiments. The small loss of

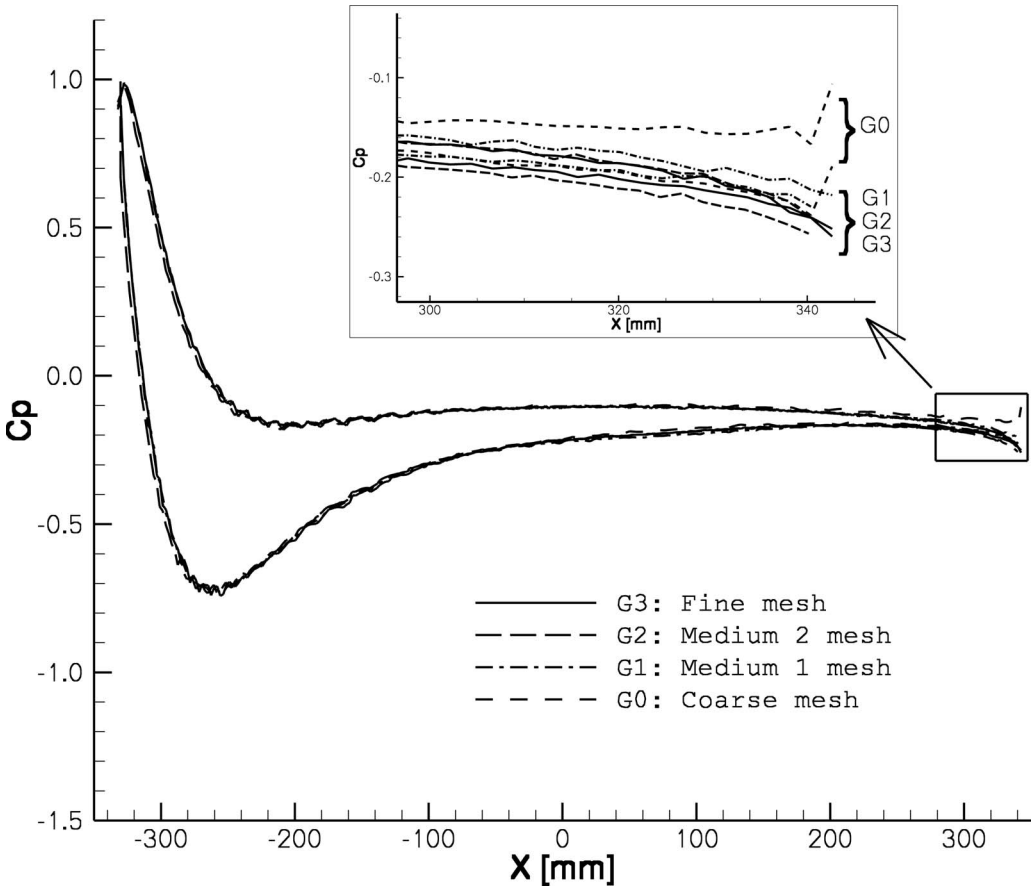

Fig. 4 $\beta=10$ deg: pressure coefficient along curve (Pt) versus the mesh

Table 3 $\beta=10$ deg: drag coefficient versus the mesh

	G0	G1	G2	G3
Cx	0.434	0.397	0.384	0.378

total pressure noted (V) in Fig. 7(*b*) obtained at $\beta=10$ deg is due to an interaction of an upstream obstacle with the boundary layer of the wind tunnel.

At $\beta=15$ deg, vortex (V3), which is visible at $X/L=0$, shows that the separation observed for $\beta=10$ deg moves upstream. As seen at $X/L=0.30$ and $X/L=0.45$, this vortex (V3) separated from the body and is transported in the direction of the freestream. Vortex (V2), fed in vorticity by the boundary layer, remains attached to the wall of the model, as shown in the cross flows obtained at $X/L=0.30$ and $X/L=0.45$.

At $\beta=20$ deg, the intensity of vortex (V2) increases. It remains attached to the wall, and consequently its loss of total pressure increases from $X/L=0.30$ to the abscissa $X/L=0.45$. Vortex (V3), which is attached at the level of the abscissa $X/L=0.00$, separates from the body and is convected in the direction of the freestream. Its loss of total pressure decreases from $X/L=0.30$ to $X/L=0.45$.

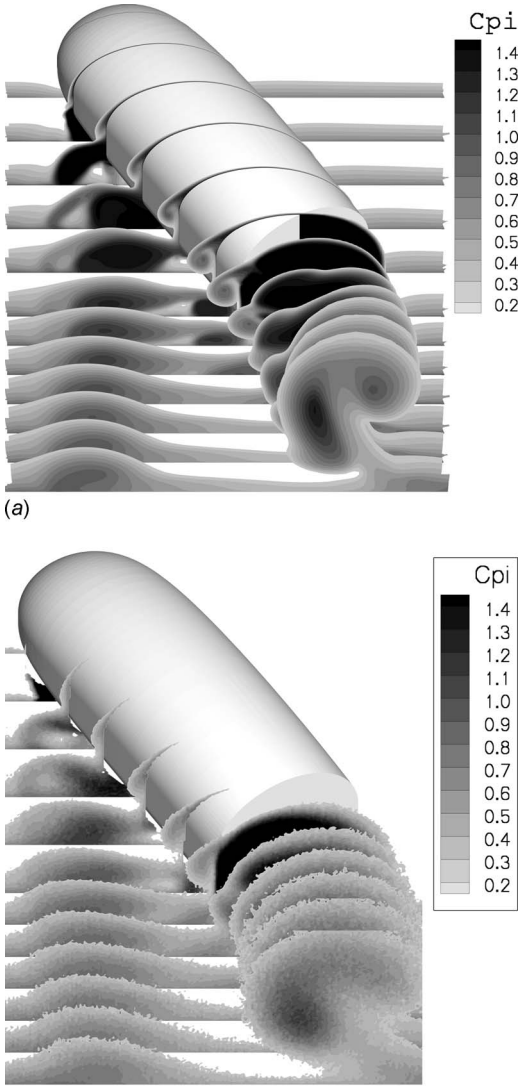

Fig. 5 $\beta=30$ deg: 3D view of the wake

Vortex (V1) is also visible in the cross flow drawn at $X/L=0.45$. The total pressure tomographies obtained at $Xo/L=0.60$ and drawn in Fig. 8 confirm this analysis. A stronger vortex (V2) is shed, while the free vortices (V1) and (V3) are diffused.

The cross flows obtained at a yaw angle $\beta=25$ deg are close to those obtained at $\beta=20$ deg. The cross flow drawn at $X/L=0.00$ shows that vortex (V2) moves upstream. Its intensity increases, and it remains attached to the body. Vortex (V3) becomes stronger and is almost diffused at $X/L=0.45$.

The results obtained at the yaw angle $\beta=30$ deg are described through cross flows in Fig. 6, tomographies drawn in Figs. 9, 11, and 12, and wall friction lines in Fig. 10. The cross flows drawn in Fig. 6 show that the intensities of the vortices continue to increase and that the main vortex (V2) remains attached to the wall. The vortex (V3), which appears at $X/L=0.30$ in Fig. 6 is diffused at $X/L=0.45$ and is visible in the numerical and experimental tomographies of total pressure drawn in Fig. 9. Vortex (V1), which is visible in Fig. 9(*a*) is diffused in the experimental results (see Fig. 9(*b*)).

Secondary vortices (V4) and (V5), which are linked to vortex (V2), are visible at $X/L=0.30$ and at $X/L=0.45$ (see Fig. 6). These cross flows are linked to the wall friction lines drawn in Fig. 10, where (S1) and (S2) are separation lines and (A1) and (A2) are attachment lines. The main counterclockwise vortex (V2), the secondary vortices (V4), which is counterclockwise, and (V5), which is clockwise, are shed from the separation lines (S1) and (S2). The saddle point denoted as (Sa) in Fig. 6 at $X/L=0.45$ guarantees the topology of the cross flow.

The results obtained at $\beta=30$ deg are completed by the tomographies drawn in Fig. 11, obtained in the wake at $X/L=0.65$. During its transport, the numerical vortex (V2) keeps its own individuality and is not mixed with the two counter-rotating vortices emitted from the base (see Fig. 11(*a*)). In a similar manner, these two counter-rotating vortices also remain separated, as confirmed by the attachment line (A3) shown in Fig. 10. In our experiments, the vortex system emitted from the base and vortex (V2) approach an isotropic state more rapidly [36]. Finally, all the vortices emitted in the wake gather in a unique structure linked to the floor boundary layer, as shown in the three-dimensional views in Fig. 5.

The numerical and experimental tomographies obtained in a horizontal plane at $Zo=-14.5$ mm, at midpoint of the ground clearance, are drawn in Fig. 12. The position of the cross section $Xo/L=0.55$ is given in order to locate vortices (V1), (V3), and (V6) (see Fig. 9). Again, if the directions of the wakes of the feet (f) and of the cylinder (c) are correct, the numerical diffusion is lower than the diffusion revealed in the experiments. This fact, which is common to the entire computation domain, is overstated here by the loss of velocity and, in turn, by the decrease in the local Reynolds number in the boundary layer developed at the level of the floor (see Fig. 3).

6.2 Wall Pressure and Forces. The evolution of the pressure coefficient *Cp* along curve (Pt), which is the projection of curve (A) on the side of the model, is drawn in Fig. 13 for different yaw angles β. Error bars are added on measured values. The results show that the pressure at the stagnation point is correctly predicted for all the angles and that wall pressure is correctly simulated on windward and leeward sides up to $\beta=15$ deg. As the yaw angle increases, the stagnation point moves windward. The negative pressure gradient on the windward side decreases along the body. Up to $\beta=15$ deg, the pressure becomes relatively constant and tends toward the upstream static pressure p_0. The flow is attached on the windward side, and the prediction aligns with the results of the experiments up to $\beta=30$ deg.

On the leeward side, the flow separates when the yaw angle is greater than 10 deg, as shown by the cross flow obtained at $X/L=0.30$ (see Fig. 6). The negative pressure gradient increases, and simulations and experiments align until the change in the sign of

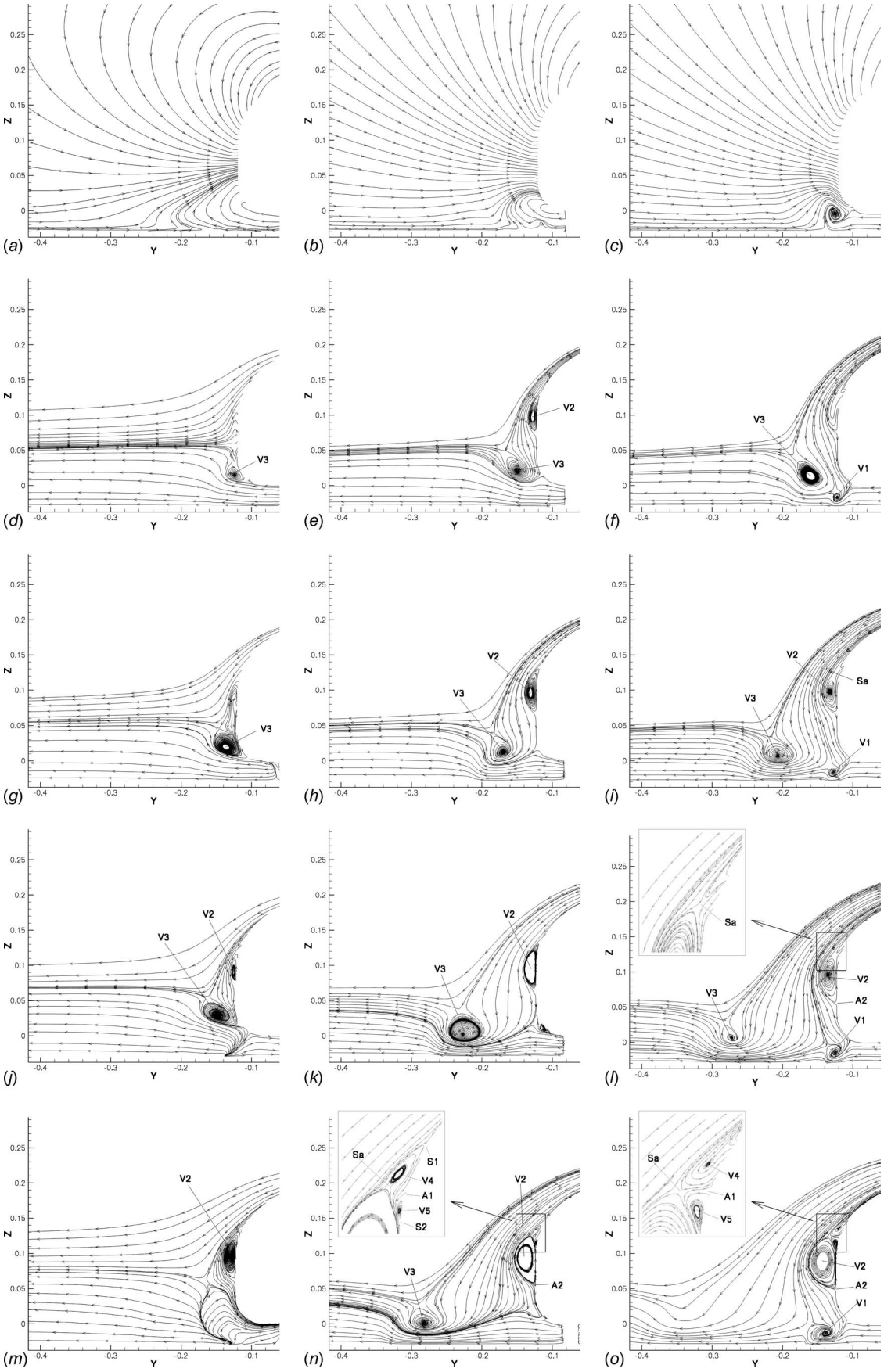

Fig. 6 Cross flows for several yaw angles

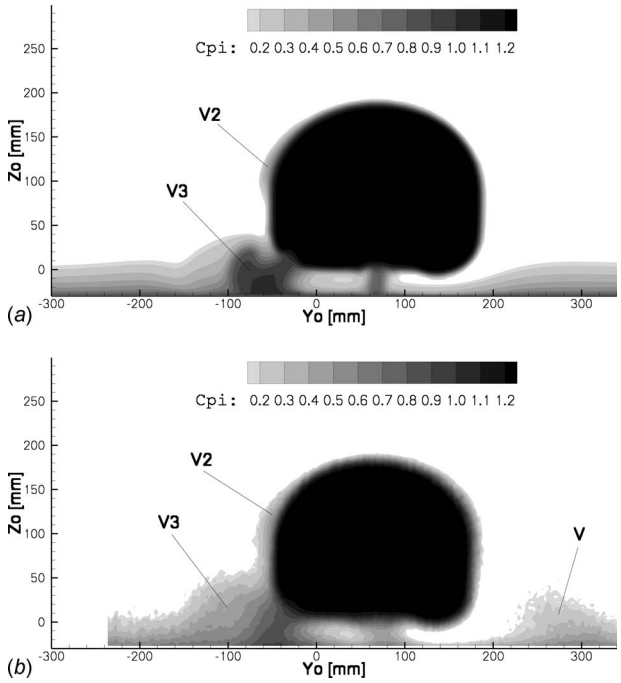

Fig. 7 $\beta=10$ deg: tomography at Xo/$L=0.60$

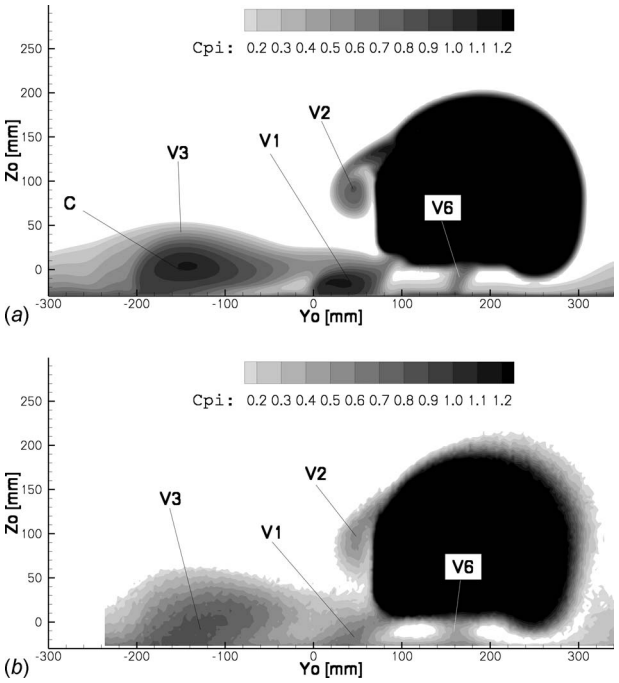

Fig. 9 $\beta=30$ deg: tomography at Xo/$L=0.55$

the pressure gradient. At approximately $X=-200$ mm, the rise of adverse pressure is the indication of a flow separation. The difference between experiments and simulations, which is particularly visible at $\beta=30$ deg, shows the tendency of the ISIS-CFD flow solver to overpredict vortex intensity (see Fig. 9). This behavior is also observed by Maddox et al. [21]. These authors simulate the flow around a simplified geometry of a ground transport system (GTS) at $\beta=0$ deg and $\beta=10$ deg. Calculations were conducted at a Reynolds number of 2×10^6 based on upstream velocity and model width. The grid used was made up of 6×10^6 cells. Pressure coefficients are well predicted at $\beta=0$ deg, but at $\beta=10$ deg the DES and RANS simulation techniques calculate an overly large separated region near the front corner of the model and, consequently, negative values of the pressure coefficients greater than those shown in the experiments. It must be noted that these discrepancies on the leeward side of the GTS are increased by the fact that the front of the model used by Maddox et al. [21] is not streamlined compared with the Willy model.

The drag coefficient and the side force coefficient, in the Lilienthal axis, are given in Fig. 14, where error bars are included. The drag, see Fig. 14(*a*), increases up to the yaw angle $\beta=20$ deg. After this angle, the drag decreases. This behavior is typical of a square-back model [1]. For the small yaw angles and up to $\beta=20$ deg, the numerical prediction underpredicts the drag and overpredicts this force for a larger yaw angle. We can connect this behavior with the prediction of production and transport of vorticity when the yaw angle increases (see Fig. 6). In fact, for a yaw angle less than $\beta=10$ deg, only vortex (V3) appears on the leeward side of the model, and separations are limited to the base. For $\beta=15$ deg, vortex (V2) remains weak at $X/L=0.30$ and $X/L=0.45$. The drag is then underestimated compared with the experimental data. When the yaw angle is greater than β

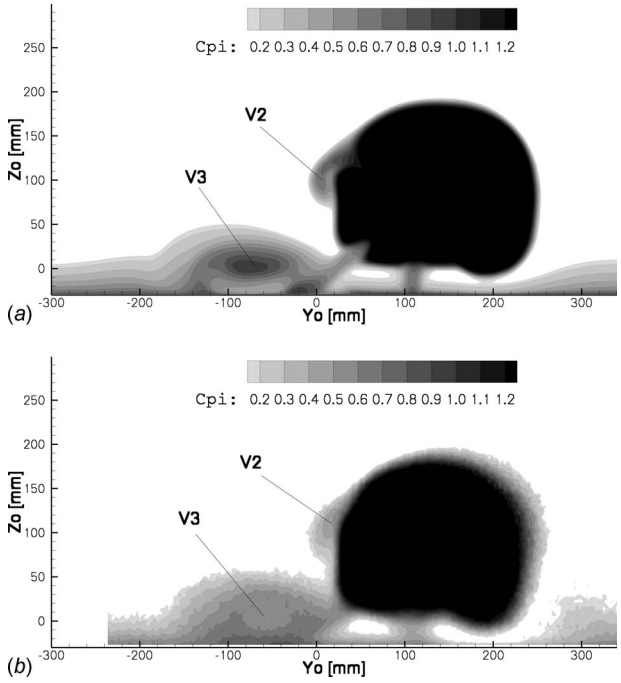

Fig. 8 $\beta=20$ deg: tomography at Xo/$L=0.60$

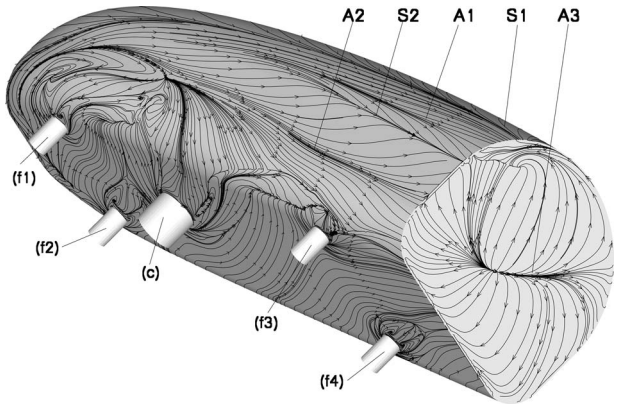

Fig. 10 $\beta=30$ deg: friction lines

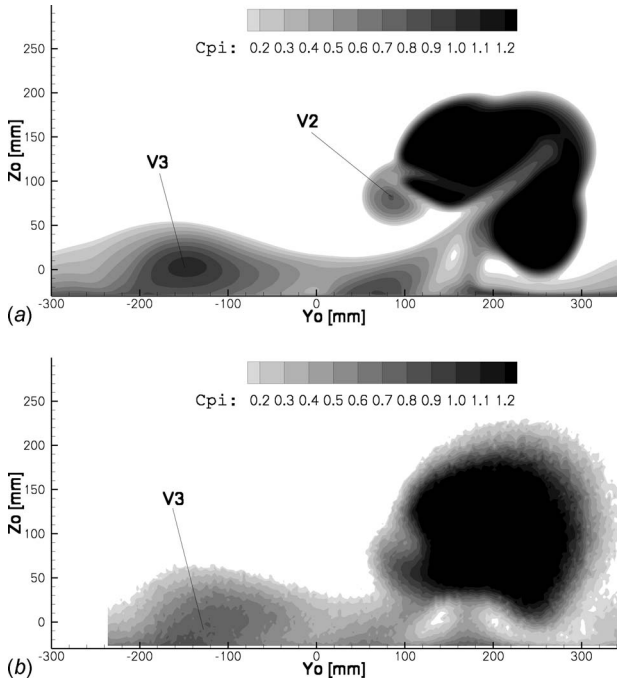

Fig. 11 $\beta=30$ **deg: tomography at** $Xo/L=0.65$

$=20$ deg, the intensity of vortex (V2) increases, and a larger amount of vorticity is shed and transported in the wake. This fact leads to an overestimation of the drag. This result is a classic defect of RANS simulations (see Maddox et al. [21]). The side force (see Fig. 14(*b*)) shows a linear evolution. We note that the experimental value of the slope is $(dCy/d\beta)_{\text{exp}} \sim -2.36$ rad^{-1}, and the numerical value of the slope is $(dCy/d\beta)_{\text{num}} \sim -2.94$ rad^{-1}. The yawing moment versus the yaw angle is presented in Fig. 15. This coefficient rises linearly with β up to $\beta=25$ deg. The linearity of the side force and the yawing moment are typical characteristics of real vehicles [1]. The slope of the

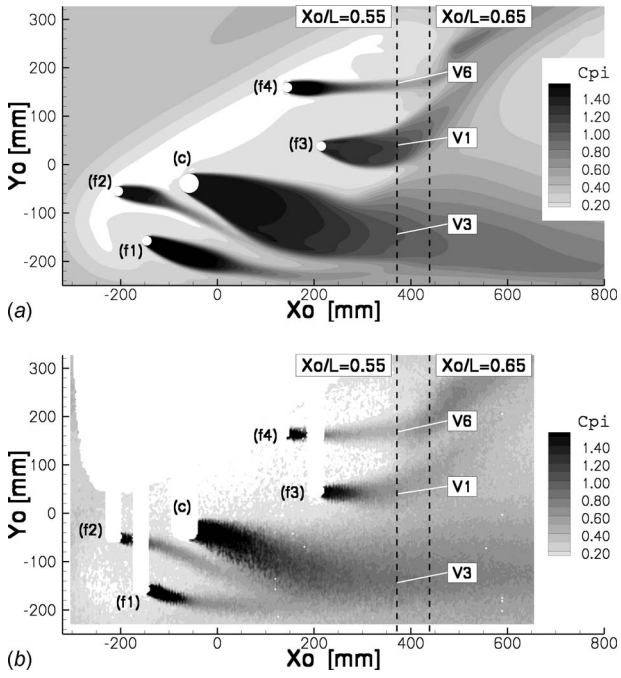

Fig. 12 $\beta=30$ **deg: tomography at** $Zo=-14.5$ **mm**

experimental curve is $(dCN/d\beta)_{\text{exp}} \sim 0.40$ rad^{-1} and $(dCN/d\beta)_{\text{num}} \sim 0.43$ rad^{-1} for the numerical curve. The values of the slopes measured for the Willy model align with the values commonly obtained on real vehicles. For the yaw angle $\beta=30$ deg, the flow solver tends to underpredict the value of the yawing moment. One hypothesis, in accordance with Fig. 13(*f*), is that the intensity of the computed vortex (V2) (see Fig. 10) on the leeward side of the model is too large compared with the experimental vortex. On real cars, this loss of *CN* is also observed when additional vortices are shed from separations on sharp edges at the back of a fastback vehicle.

6.3 Influence of the Cylinder (c) for $\beta=30$ **deg.** The friction lines obtained at $\beta=30$ deg on the underbody of the model, see Fig. 10, show that the wake of the cylinder (c) used to protect the pressure tubes interacts strongly with the wakes of feet (f1) and (f2), which are upstream the cylinder, and that the cylinder itself interacts with foot (f3), which is downstream. In future experiments dealing with the analysis of unsteady side gusts of wind, these interactions could deform conclusions concerning the unsteadiness of the wake. This fact is confirmed by the reading of the numerical friction lines obtained without the cylinder (c) at $\beta=30$ deg (see Fig. 16). Comparing of this result with Fig. 10 shows that the friction lines on the underbody are changed, the consequences being the formation of separation line (S3) starting at foot (f1) and finishing at foot (f3). Moreover, the change in the relative positions of the singular friction lines (A2), (S2), (A1), and (S1) indicates a modification of the structure of the vortex system composed of the main vortex (V2) and of the secondary vortices (V5) and (V6) (see Fig. 6 and the frames obtained at $\beta=30$ deg).

Comparing Figs. 9 and 17, where the numerical tomographies obtained at $Xo/L=0.55$ are drawn just downstream the base, shows the changes in the wake when cylinder (c) is removed. When the cylinder is present, vortex (V3), which amalgamates the wakes of the cylinder and of feet (f1) and (f2), is intense, and the loss of total pressure is $Cp_i=1.2$ at the level of its center C (see Figs. 9(*a*) and 12). Without the cylinder, this vortex, named (V3) in Fig. 17, is weak and amalgamates the wakes of feet (f1) and (f2) only. The pressure coefficient in its center is close to $Cp_i=0$. Finally, the trajectory of vortex (V1) is not deviated by the wake of the cylinder and moves from about $Y=+15$ mm (see Fig. 9(*a*)) to $Y=-10$ mm (see Fig. 17). The trajectory of the wake (V6) of foot (f4) is not changed. Future experiments analyzing the physics of unsteady side gusts will be performed on the Willy model, and it appears that the presence of the cylinder will deform the analysis concerning the effects of phase shift or hysteresis linked to the unsteadiness of the wake. To conclude this point, the cylinder will be removed, the wall pressure measurements will be performed by dynamic pressure transducers placed inside the model, and electric wires will pass through the feet of the model.

7 Conclusion

This paper presents numerical simulations and experiments on a square-back model, which has been designed for the analysis of side wind effects on automobiles. Simulations are performed using Reynolds-averaged Navier–Stokes equations, and the steady flow on the model is investigated at several yaw angles from 0 deg to 30 deg. The ECN ISIS-CFD flow solver, used to perform calculations, is based on the finite volume method to build the spatial discretization of the transfer equations. A particularity of this solver is to permit the use of hybrid conditions for wall boundaries. Experiments, used as reference, were carried out at the CNAM. The numerical simulations are reproduced under the same conditions as the experiments. The numerical forces and moment coefficients, the wall pressure, and the total pressure in the wake are compared with experimental data. The results confirm the ability of the ISIS-CFD code to capture the physics of three-dimensional separated flows around a square-back body for which the leeward

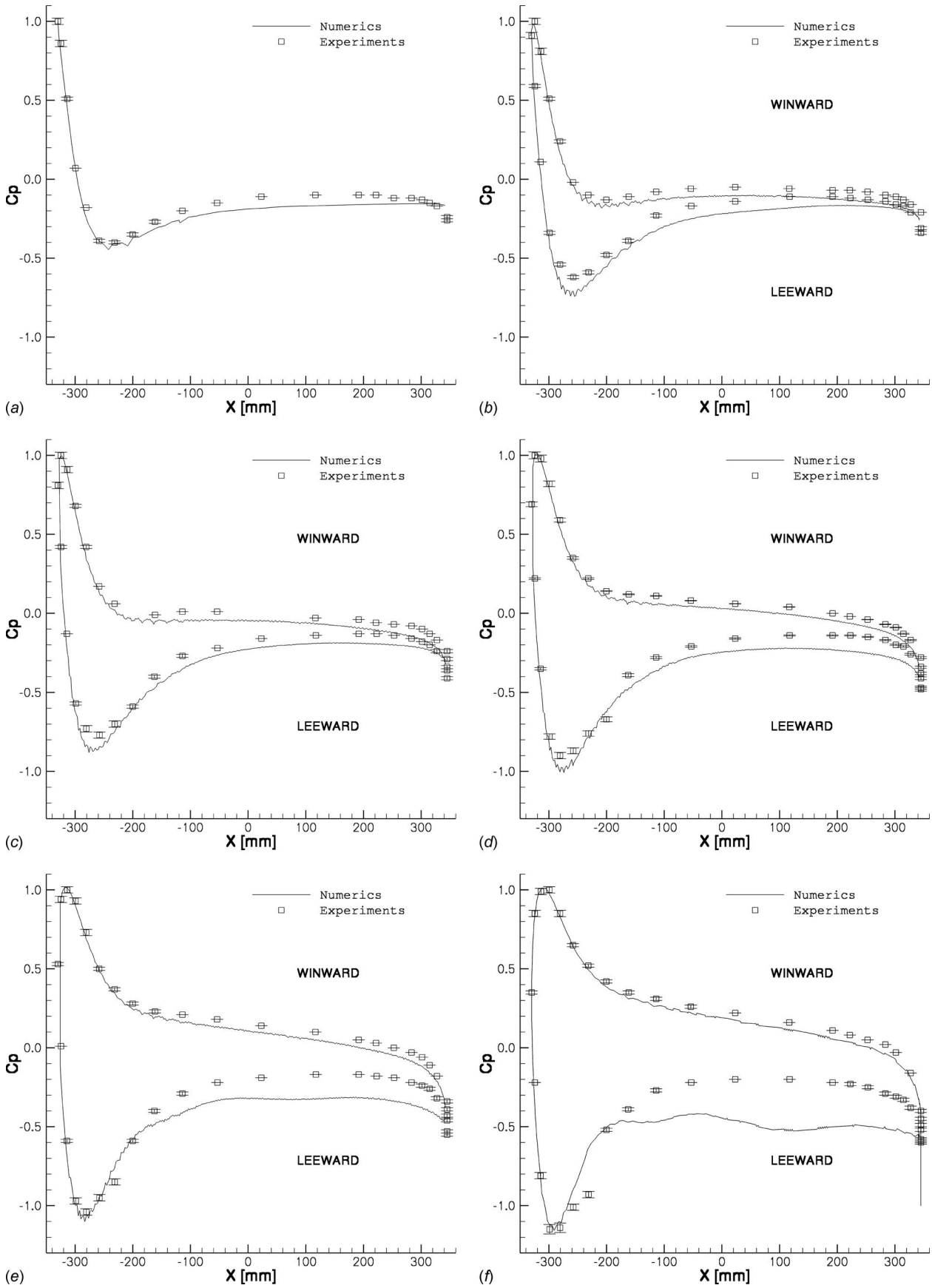

Fig. 13 Pressure coefficient along curve (Pt)

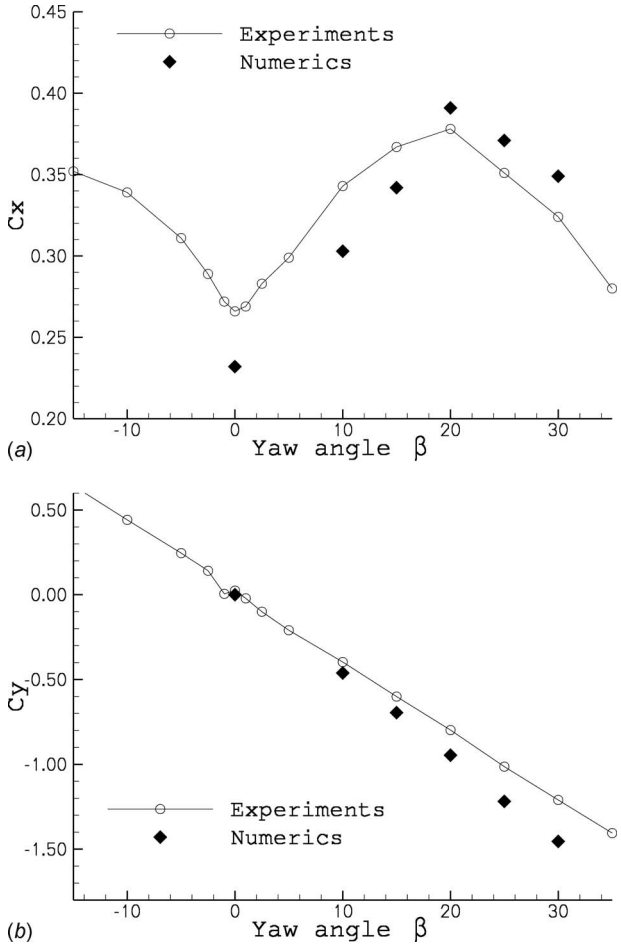

Fig. 14 Force coefficient versus the yaw angle

separations take place on smooth surfaces and are not induced by sharp corners except at the base. The typical characteristics of the model, such as drag, side force, and yaw moment coefficients, are correctly reproduced. Nevertheless, the code is less diffusive than experiments and for large yaw angles overpredicts the vorticity shed leeward. A direct consequence is the overproduction of side force. These results also show that the feet, which are necessary to secure the model in the wind tunnel, modify the flow around the body at large yaw angles and must be taken into account in numerical simulations. However, the cylinder (c), which is used to protect the pressure tubes passing from the pressure taps to the multimanometer, strongly perturbs the flow and must be removed in the future. All these results show the great interest of conducting experiments and computations in parallel.

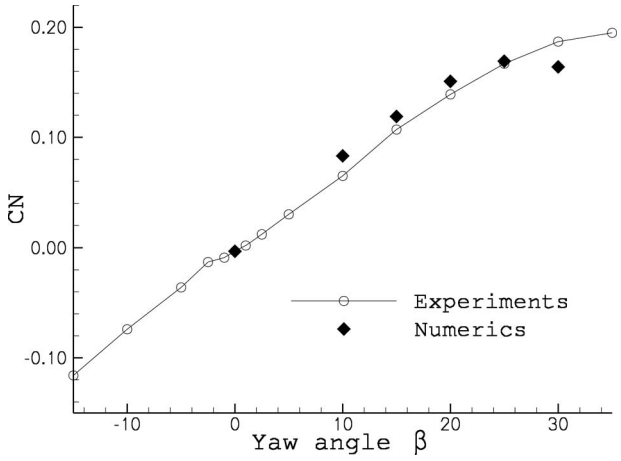

Fig. 15 Yawing moment versus the yaw angle

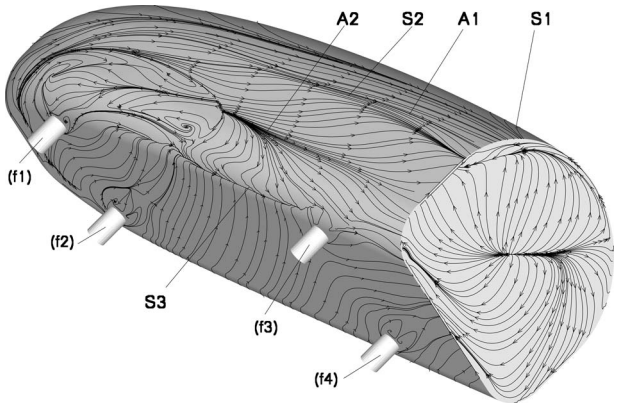

Fig. 16 β=30 deg: friction lines (without the cylinder (c))

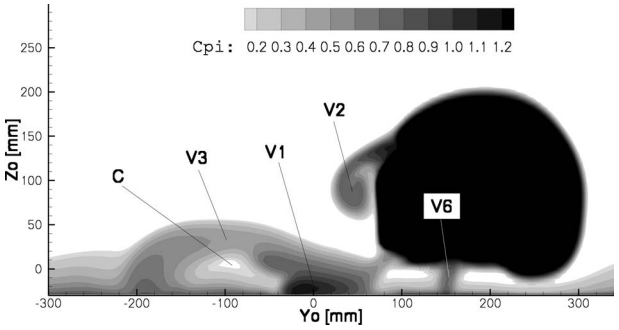

Fig. 17 β=30 deg: tomography at Xo/L=0.55 (without the cylinder (c))

The work presented in this paper is a first step for which the final objective is the numerical simulation of unsteady flow around a model submitted to side wind and the clear ability of numerics to capture hysteresis or phase phenomena for 3D flows.

Acknowledgment

Experiments were performed by Didier Legrand and E. Aïssaoui in the framework of preparation for an engineering degree from the CNAM. We would like to thank them for their help and cooperation. The authors gratefully acknowledge the Scientific Committee of IDRIS (Project No. 0129) and of CINES (Project No. dmn2049) for the CPU time.

References

[1] Hucho, W. H., 1998, *Aerodynamics of Road Vehicles*, SAE International, Warrendale, PA.
[2] Baker, C. J., and Humphreys, N. D., 1996, "Assement of the Adequacy of Various Wind Tunnel Techniques to Obtain Aerodynamic Data for Ground Vehicles in Cross Winds," J. Wind. Eng. Ind. Aerodyn., **60**, pp. 49–68.
[3] Macklin, A. R., Garry, K. P., and Howell, J. P., 1996, "Comparing Static and Dynamic Testing Techniques for the Crosswind Sensitivity of Road Vehicles," SAE Technical Paper No. 960674.
[4] Ryan, A., and Dominy, R. G., 1998, "The Aerodynamic Forces Induced on a Passenger Vehicle in Response to a Transient Cross-Wind Gust at a Relative Incidence of 30°," SAE Technical Paper No. 980392.
[5] Passmore, M. A., Richardson, S., and Iman, A., 2001, "An Experimental Study of Unsteady Vehicle Aerodynamics," Proc. Inst. Mech. Eng., Part D (J. Automob. Eng.), **215**, pp. 779–788.
[6] Baker, C. J., 1991, "Ground Vehicles in High Cross Winds, Part 1: Steady Aerodynamic Forces," J. Fluids Struct., **5**, pp. 69–90.
[7] Ryan, A., and Dominy, R. G., 2001, "Wake Surveys Behind a Passenger Car

Subjected to a Transient Cross-Wind Gust," SAE Technical Paper No. 2000-01-0874.
[8] Garry, K. P., 1996, "Some Effects of Ground Clearance and Ground Plane Boundary Layer Thickness on the Mean Base Pressure of a Bluff Vehicle Type Body," J. Wind. Eng. Ind. Aerodyn., **62**, pp. 1–10.
[9] Howell, J. P., 1996, "The Side Load Distribution on a Rover 800 Saloon Car Under Crosswind Conditions," J. Wind. Eng. Ind. Aerodyn., **60**, pp. 139–153.
[10] Özdemir, E., and Özdemir, I. B., 2004, "Turbulent Structure of Three-Dimensional Flow Behind a Model Car: 2. Exposed to Crosswind," J. Turbul., **5**, N3.
[11] Garry, K. P., and Cooper, K. R., 1986, "Comparison of Quasi-Static and Dynamic Wind Tunnel Measurements on Simplified Tractor-Trailer Models," J. Wind. Eng. Ind. Aerodyn., **22**, pp. 185–194.
[12] Chometon, F., Strzelecki, A., Ferrand, V., Dechipre, H., Dufour, P., Gohlke, M., and Herbert, V., 2005, "Experimental Study of Unsteady Wakes Behind an Oscillating Car Model," SAE Technical Paper No. 2005-01-0604.
[13] Ahmed, S. R., Ramm, G., and Faltin, G., 1984, "Some Salient Features of the Time-Averaged Ground Vehicle Wake," SAE Technical Paper No. 840300.
[14] Lienhart, H., and Becker, S., 2003, "Flow and Turbulence in the Wake of a Simplified Car Model," SAE Technical Paper No. 2003-01-0656.
[15] Han, T., 1989, "Computational Analysis of Three-Dimensional Turbulent Flow Around a Bluff Body in Ground Proximity," AIAA J., **27**, pp. 1213–1219.
[16] Bayraktar, I., Landman, D., and Baysal, O., 2001, "Experimental and Computation Investigation of Ahmed Body for Ground Vehicle Aerodynamics," SAE Technical Paper No. 2001-01-2742.
[17] Sims-Williams, D. B., and Duncan, B. D., 2003, "The Ahmed Model Unsteady Wake: Experimental and Computational Analyses," SAE Technical Paper No. 2003-01-1315.
[18] Kapadia, S., Roy, S., and Wurtzler, K., 2003, "Detached Eddy Simulation Over a Reference Ahmed Car Model," 41st Aerospace Sciences Meeting and Exhibit, AIAA Paper No. 2003-0857.
[19] Krajnović, S., and Davidson, L., 2005, "Flow Around a Simplified Car—Part 1: Large Eddy Simulation," ASME J. Fluids Eng., **127**, pp. 907–918.
[20] Fares, E., 2006, "Unsteady Flow Simulation of the Ahmed Reference Body Using a Lattice Boltzmann Approach," Comput. Fluids, **35**, pp. 940–950.
[21] Maddox, S. M., Squires, K. D., and Forsythe, J. R., 2004, "Detached-Eddy Simulation of the Flow Around the Ground Transportation System," *The Aerodynamics of Heavy Vehicles: Trucks, Buses, and Trains*, R. McCallen, F. Browand, and J. Ross, eds., Springer, New York, pp. 89–104.
[22] MacCallen, R., Flowers, D., Dunn, T., Owen, J., Browand, F., Hammache, H., Leonard, A., Brady, M., Salari, K., Rutledge, W., Ross, J., Storms, B., Heineck, J. T., Driver, D., Bell, J., Walker, S., and Zilliac, G., 2000, "Aerodynamic Drag of Heavy Vehicles (Calls 7-8): Simulation and Benchmarking," SAE Technical Paper No. 2000-01-2209.
[23] Khier, W., Breuer, M., and Durst, F., 2000, "Flow Structure Around Trains Under Side Wind Conditions: A Numerical Study," Comput. Fluids, **29**, pp. 179–195.
[24] Hemida, H., 2006, "Large-Eddy Simulation of the Flow Around Simplified High-Speed Trains Under Side Wind Conditions," Ph.D. thesis, Chalmers University of Technology, Göteborg, Sweden.
[25] Abbott, I. H., and Von Doenhoff, A. E., 1959, *Theory of Wing Sections*, Dover, New York.
[26] Jasak, H., Weller, H. G., and Gosman, A. D., 1999, "Resolution NVD Differencing Scheme for Arbitrarily Unstructured Meshes," Int. J. Numer. Methods Fluids, **31**, pp. 431–449.
[27] Rhie, C. M., and Chow, W. L., 1983, "A Numerical Study of the Turbulent Flow Past an Isolated Aerofoil With Trailing Edge Separation," AIAA J., **21**, pp. 1525–1532.
[28] Issa, R. I., 1986, "Solution of the Implicitly Discretized Fluid Flow Equations by Operator-Splitting," J. Comput. Phys., **62**, pp. 40–65.
[29] Queutey, P., and Visonneau, M., 2007, "An Interface Capturing Method for Free-Surface Hydrodynamic Flows," Comput. Fluids, **36**, pp. 1481–1510.
[30] Duvigneau, R., Visonneau, M., and Deng, G. B., 2003, "On the Role Played by Turbulence Closures in Hull Ship Optimization at Model and Full Scale," J. Mar. Sci. Technol., **8**, pp. 11–25.
[31] Deng, G. B., and Visonneau, M., 1999, "Comparison of Explicit Algebraic Stress Models and Second-Order Turbulence Closures for Steady Flow Around Ships," Seventh Symposium on Numerical Ship Hydrodynamics, Nantes, France, pp. 4.4-1–4.4-15.
[32] Deng, G. B., Queutey, P., and Visonneau, M., 2005, "Three-Dimensional Flow Computation With Reynolds Stress and Algebraic Stress Models," *Engineering Turbulence Modelling and Experiments 6,Proceedings of the ERCOFTAC International Symposium on Engineering Turbulence Modelling and Measurements—ETMM6*, W. Rodi and M. Mulas, eds., Elsevier, New York, pp. 389–398.
[33] Jongen, T., and Gatski, T. B., 1999, "A Unified Analysis of Planar Homogeneous Turbulence Using Single-Point Closure Equations," J. Fluid Mech., **399**, pp. 117–150.
[34] Menter, F. R., 1993, "Zonal Two-Equation k-ω Turbulence Models for Aerodynamic Flows," AIAA 24th Fluid Dynamics Conference, AIAA Paper No. 93-2906.
[35] Cousteix, J., 1989, *Turbulence et Couche Limite*, Cepadues-Editions, Toulouse, France.
[36] Bernard, P. S., 2006, "Turbulent Flow Properties of Large-Scale Vortex Systems," Proc. Natl. Acad. Sci. U.S.A., **103**, pp. 10174–10179.

Passive Manipulation of Separation-Bubble Transition Using Surface Modifications

Brian R. McAuliffe[1]
e-mail: brian.mcauliffe@nrc-cnrc.gc.ca

Metin I. Yaras
e-mail: metin_yaras@carleton.ca

Department of Mechanical and Aerospace Engineering,
Carleton University,
1125 Colonel By Drive,
Ottawa, ON, K1S 5B6, Canada

Through experiments using two-dimensional particle-image velocimetry (PIV), this paper examines the nature of transition in a separation bubble and manipulations of the resultant breakdown to turbulence through passive means of control. An airfoil was used that provides minimal variation in the separation location over a wide operating range, with various two-dimensional modifications made to the surface for the purpose of manipulating the transition process. The study was conducted under low-freestream-turbulence conditions over a flow Reynolds number range of 28,000–101,000 based on airfoil chord. The spatial nature of the measurements has allowed identification of the dominant flow structures associated with transition in the separated shear layer and the manipulations introduced by the surface modifications. The Kelvin–Helmholtz (K-H) instability is identified as the dominant transition mechanism in the separated shear layer, leading to the roll-up of spanwise vorticity and subsequent breakdown into small-scale turbulence. Similarities with planar free-shear layers are noted, including the frequency of maximum amplification rate for the K-H instability and the vortex-pairing phenomenon initiated by a subharmonic instability. In some cases, secondary pairing events are observed and result in a laminar intervortex region consisting of freestream fluid entrained toward the surface due to the strong circulation of the large-scale vortices. Results of the surface-modification study show that different physical mechanisms can be manipulated to affect the separation, transition, and reattachment processes over the airfoil. These manipulations are also shown to affect the boundary-layer losses observed downstream of reattachment, with all surface-indentation configurations providing decreased losses at the three lowest Reynolds numbers and three of the five configurations providing decreased losses at the highest Reynolds number. The primary mechanisms that provide these manipulations include: suppression of the vortex-pairing phenomenon, which reduces both the shear-layer thickness and the levels of small-scale turbulence; the promotion of smaller-scale turbulence, resulting from the disturbances generated upstream of separation, which provides quicker transition and shorter separation bubbles; the elimination of the separation bubble with transition occurring in an attached boundary layer; and physical disturbance, downstream of separation, of the growing instability waves to manipulate the vortical structures and cause quicker reattachment.
[DOI: 10.1115/1.2978997]

1 Introduction

Separation bubbles are a common occurrence over airfoils at low Reynolds numbers. Under these conditions, the detrimental effects of laminar-flow separation on airfoil performance, through decreased lift and increased form drag, are a major concern for the design of low-Reynolds-number airfoils, such as those being developed for microair vehicles and for axial turbomachinery blade rows. The characteristics of separation bubbles are strongly dependent on the transition process occurring in the separated shear layer.

The process of laminar-to-turbulent transition in a separation bubble under low-freestream-turbulence conditions shares characteristics with the transition process observed in planar free-shear layers. In such flows, transition is initiated through receptivity of the inflectional velocity profile to small disturbances, which promotes the growth of two-dimensional instability waves [1,2]. This instability process is often referred to as the Kelvin–Helmholtz (K-H) instability mechanism [2,3] and has also been associated with transition in separation bubbles [4–9]. The K-H instability results in roll-up of the vorticity contained in the shear layer and leads to the growth of large-scale spanwise-oriented vortical structures, which interact with each other and provide the conditions under which breakdown to small-scale turbulence occurs. Ho and Huerre [3] provide a thorough review of the dominant instabilities and flow structures that arise during transition of planar free-shear layers. A similar roll-up of vorticity has been observed in separation bubbles under low-freestream-turbulence conditions [5–9], which subsequently break down into small-scale turbulence. The substantial cross-stream mixing associated with small-scale breakdown to turbulence in a separation bubble assists in reattachment of the shear layer to the surface, downstream of which a turbulent boundary layer prevails [8,10,11]. The reattachment length and the losses arising in the separated shear layer are strongly dependent on the nature of the dominant flow structures that develop in this layer.

Various techniques have been developed to control the separation and transition processes occurring over low-Reynolds-number airfoils. Gad-el-Hak [12] discusses many of these techniques, including both passive methods, such as shaping, roughness, and turbulators, as well as some active methods that include surface heating/cooling, suction, and acoustic excitation. In gas-turbine engines, the disturbance environment resulting

[1]Present address: Aerodynamics Laboratory, Institute for Aerospace Research, National Research Council of Canada, Building M-2, 1200 Montreal Road, Ottawa, ON, K1A 0R6, Canada.

Contributed by the Fluids Engineering Division of ASME for publication in the JOURNAL OF FLUIDS ENGINEERING. Manuscript received March 15, 2007; final manuscript received July 18, 2008; published online January 8, 2009. Assoc. Editor Juergen Kompenhans.

from elevated levels of freestream turbulence and the presence of turbulent wakes convecting from upstream blade rows has been used to design high-lift airfoils that are less prone to separation and stall at low Reynolds numbers [13]. These airfoils require these high-disturbance environments in order to perform reliably. Many additional techniques have been observed to affect transition over low-Reynolds-number airfoils. Passive methods include the use of circular and rectangular trip wires [14,15], low-profile vortex-generators submerged in the boundary layer [16], and three-dimensional surface protrusions or indentations [17–21]. Active methods of separation and transition control include aspiration techniques through either suction [22] or blowing [23–26].

In general, active methods are more effective at manipulating the transition process, but the energy expenditure required by these devices could potentially result in a decrease in the overall system performance. Conversely, passive methods, which require no energy expenditure, can work very well for a specific operating condition, but generally result in performance degradation under flow conditions where control of the transition process is not needed. Of the passive techniques that have been employed for control of separation bubbles, surface indentation methods appear to provide the best compromise between improved low-Reynolds-number performance and minimal penalties at higher Reynolds numbers.

In this first part of the paper, the nature of separation bubbles under low-Reynolds-number and low-freestream-turbulence conditions is examined. Through use of spatially-resolved particle image volcimetry (PIV) measurements, the dominant flow structures involved in the transition and reattachment processes are identified. The feasibility of manipulating the transition process in a separated shear layer through passive forcing is evaluated in the second part of the paper. A series of surface disturbances in the form of two-dimensional surface modifications located upstream of the point of separation are experimentally evaluated with regard to their ability for promoting or delaying transition and reattachment of the separated shear layer. The tested surface perturbations cover a broad range, including a constant-height step, constant-depth grooves, a backward-facing step followed by a ramp, and a sinusoidal groove, with the goal of identifying the configuration that provides the best trade-off between improved aerodynamic performance at low Reynolds numbers and minimal aerodynamic penalties at higher Reynolds numbers.

2 Experimental Setup and Procedures

Tow-Tank Facility. Measurements were performed in the low-Reynolds-number pilot tow-tank facility of the National Research Council of Canada (NRC). This facility consists of an enclosed tank of a 3-m working length and 1 m $\times$ 1 m cross section in which an airfoil model can be towed through water or glycerin. Water has been used as the working fluid for the present investigation. Details of the facility are documented by Hanff [27], and a schematic of the facility is shown in Fig. 1.

One major advantage of the NRC facility over conventional wind or water tunnels is the excellent "inflow quality" due to the stagnant freestream conditions, namely, 0% freestream-turbulence intensity and zero end-wall boundary-layer blockage. An advantage of using water over air is the lower freestream velocity required to achieve a given Reynolds number. This lowers the frequency range of turbulence and allows examination of flow-structure evolution from the PIV measurements, which in the present experiments, have a relatively low sampling rate (14.8 Hz). The presence of a roof also prevents the effects associated with a free surface.

Airfoil Model. The main disadvantage of using conventional airfoils for a parametric study of separation-bubble transition is the streamwise movement of the separation location with variations in operating conditions. This has been observed in an earlier study performed in the present facility, which documented the transition process occurring in separation bubbles over a low-Reynolds-number airfoil [8]. A new airfoil has been designed to alleviate this problem while providing a pressure distribution consistent with those observed over airfoils in which laminar separation bubbles are common.

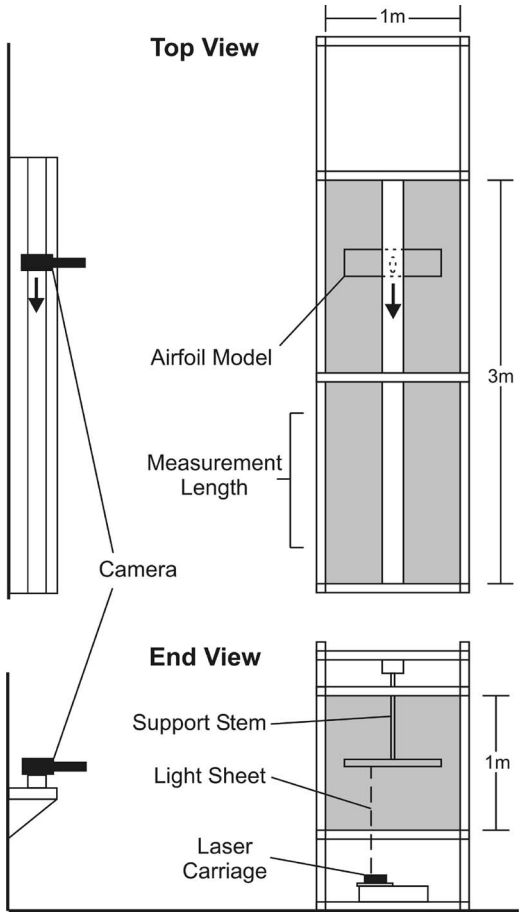

Fig. 1 Schematic of low-Reynolds-number tow-tank facility

The airfoil design is a variation of that used by Bao and Dallmann [28] in their study of separation bubbles and is shown in Fig. 2. Separation is induced by means of a curved backward-facing ramp over the upper surface of the airfoil. To ensure that separation occurs as a result of the induced pressure field and not due to a discontinuous change in surface curvature, the ramp consists of a seventh-order polynomial fitted between two flat sections. The seventh-order polynomial provides a smooth change in slope and surface curvature over the length of the airfoil surface. In the study of Bao and Dallmann [28], a long flat section preceded the step, providing a Blasius boundary-layer profile upstream of the ramp. In the present study, this flat section has been shortened to provide an inflectional decelerating boundary-layer profile over a sufficient distance upstream of separation. This better represents the boundary-layer conditions encountered upstream of typical separation bubbles occurring over conventional airfoils. Ellipses were used for the leading and trailing edges of the airfoil, with major-to-minor axis ratios of 3:1 for the leading edge

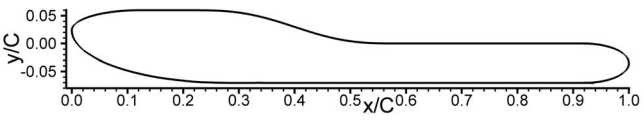

Fig. 2 Airfoil geometry

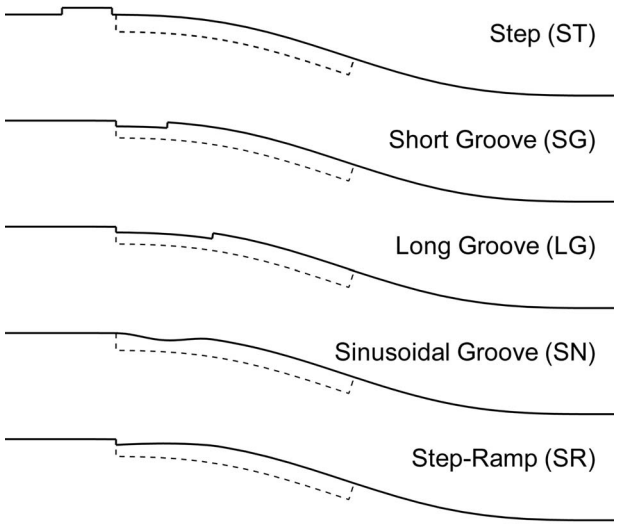

Fig. 3 Geometry of surface modifications (dashed line indicates extent of flexible vinyl strip)

quarter-ellipses and 2:1 for the trailing edge half-ellipse.

The test model is two dimensional, with a chord length of 25 cm and an aspect ratio of 3.0, spanning the middle 76% portion of the tank. Despite the relatively low aspect ratio, the low level of lift produced by the airfoil at the tested angle-of-attack of −0.4 deg provides a large spanwise extent (greater than 50%) over which the flow is two dimensional. This was confirmed through preliminary measurements at a selection of spanwise locations. These measurements indicated negligible change in the separation and mean reattachment locations within this spanwise extent at all flow Reynolds numbers tested.

Surface Modifications. Several two-dimensional surface modifications have been examined for the airfoil and are shown in Fig. 3 with their identifying acronyms. The recessed surface modifications were machined into thin flexible vinyl strips 47 mm wide and 3.2 mm thick, which were then mounted in a matching groove machined into the airfoil surface, shown with dashed lines in Fig. 3. The protrusion (step (ST) configuration) consisted of mounting a thin strip of the same vinyl material on the airfoil surface.

The surface modifications have been designed to provide a perturbation to the separating shear layer at a frequency matching that of the dominant instability frequency of the layer at one of the test conditions. To this effect, the streamwise lengths of the surface modifications have been selected to provide passive forcing at intervals of the instability wavelength, which was observed to be $\Lambda_x = 18$ mm, or 7.2% of chord, for the clean airfoil configuration at a Reynolds number of 39,000.

The protrusion/indentation height of the surface modifications were set to 70% of the displacement thickness at separation, which was based on the results of the passive control studies of Volino [15], Zhang and Hodson [19], and Zhang et al. [20] performed on low-pressure-turbine airfoils. This corresponds to 1 mm based on the clean-airfoil configuration at a Reynolds number of 39,000. These studies, in which similar constant-height protrusion/indentation modifications were examined at higher Reynolds numbers, also suggest that instabilities are promoted by the edge of a sharp backward-facing step as this would provide a receptivity site for infinitesimal disturbances [29]. Accordingly, some of the configurations include such a backward-facing step (ST, short groove (SG), long groove (LG), and step-ramp (SR)) to promote disturbance-initiation in the inflectional boundary layer prior to separation. The steps coincide with the leading edge of the machined groove ($x/C = 0.232$), which is slightly upstream of the separation location for the clean-airfoil cases ($x_s/C \approx 0.3$).

Operating Conditions. The shear layer over the upper surface of the airfoil has been examined at various Reynolds numbers, all at an angle-of-attack of −0.4 deg. ± 0.1 deg. Four Reynolds numbers of 28,000, 39,000, 51,000, and 101,000, based on airfoil chord and towing speed, were examined for all airfoil surface configurations. The freestream-turbulence intensity is zero by virtue of the stagnant tow-tank conditions, and the Reynolds number was kept constant to within ±1000 during each measurement case. Due to slowly-changing temperature variations during the course of the experimental study, the uncertainty in the stated Reynolds numbers is ±2000. Measurements were made at a spanwise location approximately 8 cm from midspan (≈10% of airfoil span).

Instrumentation and Data Acquisition. PIV was used to measure the shear layer over the upper surface of the airfoil. The *La Vision Flowmaster* PIV system used for this study consists of a data acquisition computer with a programmable timing unit, a set of two *Big Sky* Nd:YAG lasers, and a *La Vision ImagerProPlus2M* digital change coupled device (CCD) camera with 1600 pixel × 1200 pixel resolution. A 300-mm-focal-length *Nikon* lens was used, which as a result of its distance from the model, provided a streamwise field of view of 44% of airfoil chord. The upper surface of the airfoil was therefore examined over two regions. Twenty micrometer polyamide particles were used as the seeding material, which provided a particle image diameter of approximately 2–4 pixels. These seeding particles have a specific gravity of 1.03, which ensures that they closely follow the motion of the working fluid. In the two-image cross-correlation mode, the PIV system has a maximum frame-pair acquisition rate of 14.8 Hz, which is limited by the repetition rate of the Nd:YAG lasers.

Camera-Model Tracking-Error Correction. As a result of small vibrations of the camera-lens assembly combined with the notable distance between the camera traverse system and the tow-tank (see Fig. 1), image-to-image variations in the location of the airfoil could not be neglected. The error introduced by this jitter is on the order of the freestream particle displacements between two sequential images in any image pair. If not corrected for, this level of error would prevent a quantitative analysis of the PIV results. To correct for this error, a fixture containing eight light-emitting diodes (LEDs) was placed in a cavity inside the model. The cavity is open at the side of the model allowing the camera to capture the image of the LEDs, whose spanwise location is coincident with the focus plane of the lens. A mask with an orifice of approximately 10 μm in diameter is placed over each LED, which provides a marker of approximately 10 pixels in diameter in the PIV images. For each measurement region examined, two markers are selected as reference, and a marker identification algorithm is used to locate the centroids of these markers within each image. From these marker-centroid locations, displacement and rotation corrections are performed to align the markers with a reference image. As a result of nonuniformity in the marker intensity distributions, uncertainty in the location of the airfoil in the corrected images is approximately 0.5 pixels. Details of an earlier four-LED version of the marker fixture are described by Hanff [27].

Measurement and Data Processing Details. Approximately 300 PIV image pairs were collected for the highest Reynolds number, and approximately 500 image pairs were collected for the remaining three Reynolds numbers. The LA VISION DAVIS (Version 7) software was used to evaluate the recorded image data, which makes use of a double-frame fast Fourier transform (FFT)-based cross-correlation technique. The time between laser pulses was selected such that the freestream particle displacements for each image pair were approximately 20 pixels. To ensure adequate spatial resolution while maintaining minimal cross-correlation errors, an iterative multigrid processing technique was used, similar to that described by Scarano and Riethmuller [30]. Prior to detailed processing, approximately 50 image pairs were evaluated, and the

average of the resulting vector fields was then used as an initial condition for the detailed processing. Using the initial averaged vector field as a start, four cross-correlation passes were performed using 32×32 pixel^2 interrogation windows with 75% overlap. An image reconstruction technique was used to reduce errors associated with shear across the interrogation windows. This reconstruction technique uses the pixel displacement field evaluated from the previous evaluation pass to deform the second image of an image pair such that its new particle-image field closely matches that of the first image. This process reduces correlation-peak identification errors associated with large particle displacements and strong shear, and allows for quicker convergence of the correlation algorithm. The image reconstruction technique also improves the accuracy of oversampled data. This has been verified for the current results, which are oversampled by means of the 75% window overlap, by comparing the two frames of an image pair for which one frame has been deformed using the converged vector field. Very little difference is observed in regions with negligible out-of-plane particle motion, and a maximum uncertainty due to oversampling in highly-sheared regions is on the order of 0.5 pixels. The final vector spacing is 8 pixels (0.22% of chord length), which results in at least six velocity vectors across the shear layer at the location of transition onset for the highest Reynolds number tested, and at least 15 velocity vectors for the remaining three Reynolds numbers.

For a given particle-displacement vector field, errors in the freestream-flow regions due to uncertainty in the cross-correlation algorithm are estimated to be approximately 0.1 pixels or lower, which is consistent with current state-of-the-art FFT-based PIV algorithms [31–33]. In regions of high shear with negligible out-of-plane particle loss, the uncertainty is estimated to be below 0.5 pixels, as noted in the previous paragraph. The number of outlier vectors in a given vector field is below 2%, with the majority of those occurring in the reattachment region of the separation bubble, where the highest three-dimensional fluctuation levels are observed and out-of-plane particle motion is inevitable. The iterative multipass intermediate filtering, and intermediate smoothing techniques used for image analysis [30,34,35] have provided reduced uncertainty in regions of poorly correlated displacements due to this out-of-plane particle motion. The interpolated particle-displacement vectors in these regions have magnitudes and directions similar to the surrounding well-correlated displacements. Smoothing of the converged vector field, which is often used to reduce errors in the vorticity field, has not been applied to the current data to prevent any degradation of the shear-layer resolution near transition onset. Probability density functions examined for several vector fields confirmed that negligible peak-locking effects are present in the data.

The total uncertainty in the mean ensemble-averaged particle-displacement vectors due to camera-model-tracking error, uncertainty in the cross-correlation evaluation, and the presence of unfiltered outlier vectors is estimated to be below 5% of the model velocity for the highest Reynolds number tested, and below 3% for the remaining three Reynolds numbers. The majority of this uncertainty results from errors in the camera-model-tracking correction, described in the previous section, that creates a bias error for all vectors in a given particle-displacement field. Due to the biased nature of this error over a vector field, any parameters that depend on velocity gradients, such as vorticity or strain rate, are unaffected by this error. This bias error error is, however, different for each vector field and thus accounts for the majority of the uncertainty associated with the ensemble-averaged parameters. Table 1 provides estimates for the uncertainty bounds for various parameters reduced from the PIV data. The uncertainties at the highest Reynolds number examined are greater than those at the lower Reynolds numbers as a result of the thinner shear layers and the smaller number of vector fields used for averaging, and are therefore given as a separate set.

Table 1 Maximum estimated uncertainties for reduced PIV data

Parameter	Reynolds number range	
	28,000–51,000	101,000
$u,v/U_\infty$	±0.03	±0.05
$U_{\text{freestream}}/U_\infty$	±0.03	±0.03
U_{rms}/U_∞	±0.05	±0.10
$\langle u'u'\rangle,\langle v'v'\rangle/U_\infty^2$	±0.005	±0.010
$\langle u'v'\rangle/U_\infty^2$	±0.005	±0.005
δ^*, θ	$\pm10\%$	$\pm15\%$
H	±0.3	±0.5
$\text{Sr}_{\theta s}$	±0.003	±0.005
Ω_z^*	±0.7	±1.0

3 Results and Discussion

Assessment of the effects of the examined surface modifications requires a thorough understanding of the transition and reattachment processes for the clean airfoil. The first part of this section discusses the physics of the transition process in the separation bubbles over the clean airfoil, which is followed by results and discussion of the flow-manipulation study.

Separation-Bubble Transition for the Clean-Airfoil Cases. At all Reynolds numbers examined, a separation bubble develops over the airfoil surface in the region of the backward-facing ramp. Figure 4 shows streamlines associated with the ensemble-averaged flow-fields over the airfoil for all Reynolds numbers examined, and provides an indication of the range of separation-bubble shapes and sizes observed in the present study. Separation occurs around $x/C=0.3$, and the reattachment length decreases with the increasing Reynolds number, as expected. Large clockwise recirculation regions are observed in the downstream region of the bubbles. As will be shown, this large-scale reattachment vortex evident in the averaged flow field is not readily identifiable in the instantaneous flow field where many smaller-scale vortical structures that originate from instability of the separated shear layer prevail. At the three lower Reynolds numbers, a small ensemble-averaged forward-flow region is observed near the surface at the upstream end of the strong recirculation region and is indicated by streamlines emanating from the surface with a component in the downstream direction. This occurs in the region of

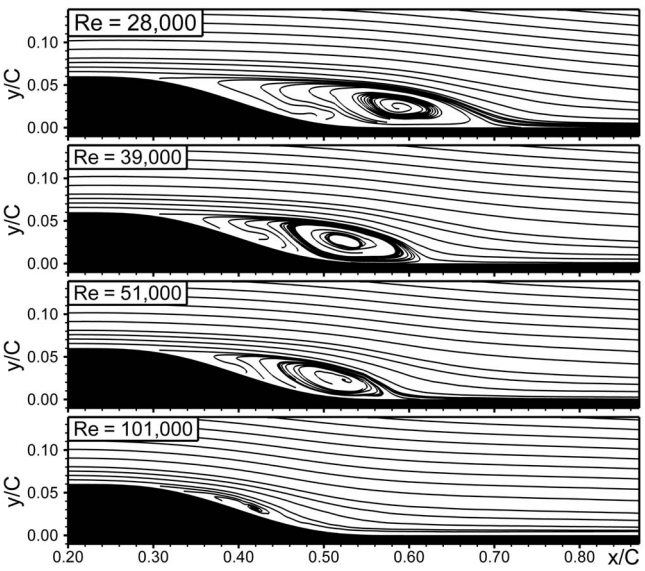

Fig. 4 Ensemble-averaged streamlines over airfoil

the separation bubble that is often called the "dead-air" or "dead-water" region, where the velocity is much lower than that of the freestream flow, and is not a phenomenon associated with typical separation bubbles that occur over conventional airfoils. This forward flow is associated with a secondary vortex that has been observed in the lower corner behind sharp backward-facing steps [36]. As with the large-scale reattachment vortex of the separation bubble, this secondary vortex is not distinguishable in the instantaneous velocity field, which is dominated by smaller-scale transient flow structures. The secondary vortex is driven by the aforementioned reattachment vortex through shear, and accordingly has a sense of rotation that is opposite that of the reattachment vortex. Along its upper portion, the secondary vortex is parted from the freestream flow by the separated shear layer, and the direction of the shear force in this region is such to retard the motion of this vortex. As a result, the strength of the secondary vortex is dictated by the relative magnitudes of the shear forces developing between the secondary and reattachment vortices and between the secondary vortex and the separated shear layer. A more shallow orientation of the separated shear layer relative to the wall, as in separation bubbles over conventional airfoils, would tend to increase the length of the region where the secondary vortex is in contact with the separated shear layer, in relation to the extent of the interaction zone between the secondary and reattachment vortices. This explains why the secondary vortex, which is observed behind the backward-facing ramp of the present cases and behind vertical backward-facing steps in published literature, is typically not noticeable in separation bubbles over conventional airfoils. Based on comparison of the present results to those published by the present authors for a conventional airfoil [8], the presence of an ensemble-averaged secondary vortex in the separation bubble does not appear to alter the time-averaged location and rate of transition in the separated shear layer.

For all four Reynolds numbers, the freestream velocity distributions measured at the edge of the shear layer are presented in Fig. 5(*a*). This edge is easily identified in the laminar part of the shear layer, as the streamline-curvature induced by the airfoil geometry provides a maximum in the wall-normal velocity profiles at the edge of the shear layer. Over the turbulent part of the shear layer, this edge has been identified as the dividing line outside of which the $\langle u'v' \rangle$ velocity correlation values are negligible. Upstream of separation ($x_s/C \approx 0.3$), the freestream velocity and acceleration magnitudes change over the Reynolds number range examined. As the Reynolds number is reduced, the thicker boundary layer developing over the elliptic leading edge provides reduced streamline curvature and hence a reduced suction-peak velocity magnitude. The change in lift distribution as a result of the Reynolds-number-dependent separation-bubble size also contributes to this effect. It is also noted that, for all cases, acceleration of the freestream flow is observed over the aft region of the airfoil.

The shear-layer integral parameters are presented in Figs. 5(*b*) and 5(*c*), and have been calculated from wall-normal (*y*-direction) velocity profiles accounting for the negative mass and momentum deficit in the reverse-flow region near the surface. In a previous study of separation-bubble transition over a low-Reynolds-number airfoil [8], the authors observed that neglecting these negative deficits, or using positive deficits associated with the velocity magnitude, can cause significant differences in the calculated integral parameters through the transition region. However, due to the low velocity magnitude of the reverse flow in the present cases, this difference is small. Downstream of separation, the displacement thickness increases at a high rate due to the thick dead-water region resulting from the the shear layer moving away from the surface. The momentum thickness, however, remains low until the effects of transition in the separated shear layer become pronounced. The high values of displacement thickness prior to transition result in high values of the shape factor, as observed in Fig. 5(*c*). The peak shape factors for the three lower Reynolds numbers

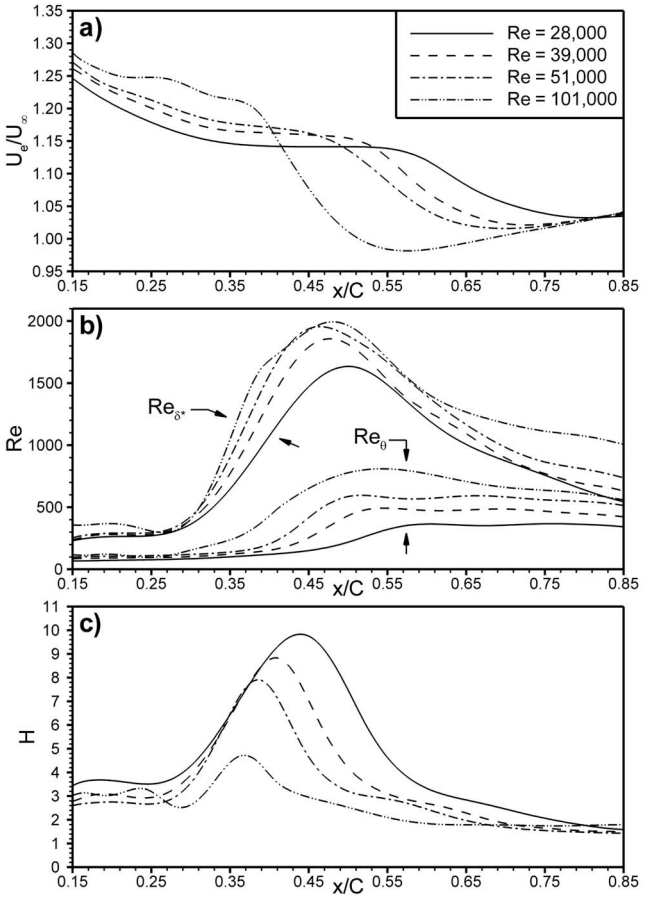

Fig. 5 Shear layer property distributions over airfoil; (*a*) shear-layer edge velocity, (*b*) displacement and momentum thicknesses, and (*c*) shape factor

($H \approx 8-10$) are indicative of the separated shear layers being located far from the surface, and are consistent with values observed in a previous study by the authors over a conventional airfoil [8].

Transition of shear layers in low-disturbance environments occurs through receptivity of the shear layer to infinitesimal disturbances. According to the classification by Saric et al. [29], two distinct receptivity sites are encountered prior to separation over the present airfoil. The first receptivity site is the leading-edge region where the boundary layer is thin and grows rapidly, and where streamwise pressure gradients are strong relative to the boundary-layer scales. The second receptivity site is localized at $x/C=0.12$, where a discontinuity in surface curvature occurs as the leading-edge ellipse joins the flat surface segment upstream of the curved ramp. Upon penetrating the boundary layer, the disturbances grow in the boundary layer and are promoted by the inflectional cross-stream velocity distribution owing to the adverse streamwise pressure gradient [37].

In the present experiments, transition of the separated shear layer occurs in a manner similar to that which occurs in planar free-shear layers and in separation bubbles over conventional airfoils under low levels of freestream disturbances. Under these conditions, the small disturbances that penetrate the boundary layer at the upstream receptivity sites grow to the point of separation at the beginning of the backward-facing ramp, and amplify further in the separated shear layer, which is inviscidly unstable due to the inflectional velocity profile. Amplification of the most unstable frequency associated with this Kelvin–Helmholtz instability mechanism leads to roll-up of the vorticity contained in the shear layer to produce a train of discrete vortices, which grow as they convect downstream. Figure 6 presents a series of *x*-*y* plots

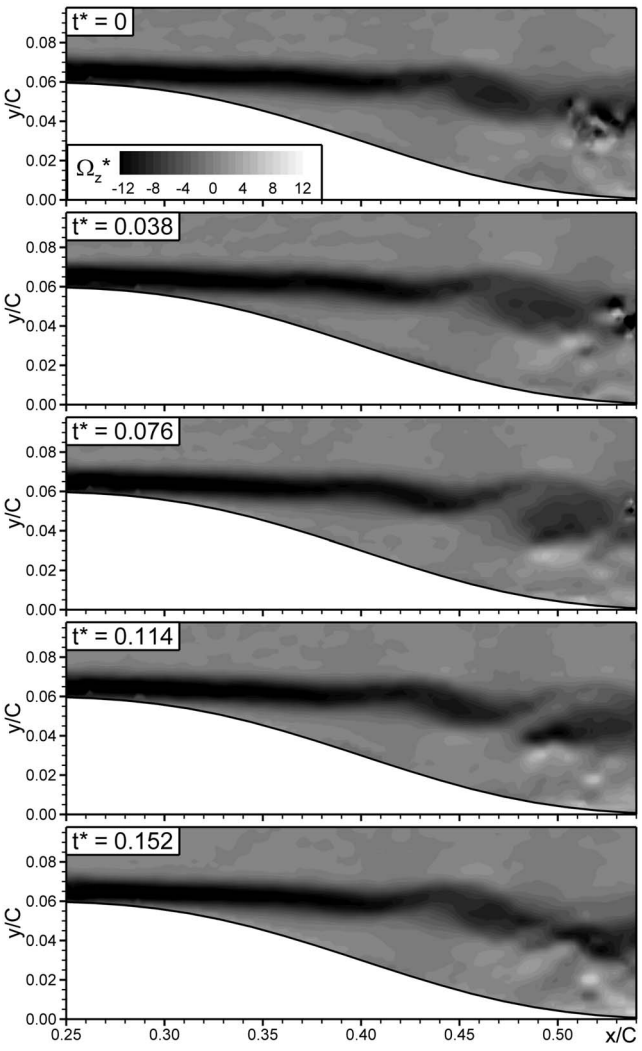

Fig. 6 Instability growth in the separated shear layer for Re =39,000

of normalized spanwise vorticity ($\Omega_z^* = \Omega_z C / U_\infty$), which show the formation and growth of these spanwise-oriented vortices over one period of the dominant instability frequency, at a Reynolds number of 39,000. The plots correspond to a series of instances in time, with time stated in a normalized form ($t^* = t \cdot U_\infty / C$).

Estimates of the dominant streamwise wavelengths (Λ_x) and the corresponding convection speeds (U_c) have been used to calculate the frequencies associated with the instability waves and roll-up vortices ($f = U_c / \Lambda_x$). The wavelengths are estimated based on a spatial correlation of the velocity field data, the method for which is described in detail later in the paper. The convection speed is estimated as the flow speed along the line of maximum vorticity in the laminar separated shear layer [6]. This estimation for the convection speed has been verified by examining the propagation rate of vortex centers in the present data, which agrees well with the maximum-vorticity line estimates.

The Strouhal number associated with the formation frequency of the instability waves and spanwise vortices, based on conditions at separation ($\mathrm{Sr}_{\theta s} = f\theta_s / U_{es}$), is in the range 0.015–0.016 for the three lowest Reynolds numbers examined. This is consistent with the momentum-thickness-based Strouhal number for planar free-shear layers ($\mathrm{Sr}_\theta = f\theta / \Delta U$) of 0.016 identified by Ho and Huerre [3]. The characteristic velocity of ΔU used for Sr_θ represents the velocity difference across the layer, which is equivalent to the freestream velocity over a separation bubble due to negligible velocity inside the bubble. In previous studies [8,9], the authors have identified and discussed the similarity of $\mathrm{Sr}_{\theta s}$ in separation bubbles with that of planar free-shear layers based on numerous experimental and computational results found in open literature. In general, $\mathrm{Sr}_{\theta s}$ for a separation bubble is at or below the value for planar free-shear layers. This is consistent with linear stability theory (LST) results presented by Rist and Maucher [38], which show that the most unstable frequency increases with increasing distance of the shear layer from the surface. In the limit as surface-distance approaches infinity, corresponding to a planar free-shear layer, the frequency would approach that given by Ho and Huerre [3]. In the present cases, the large distance of the separated shear layer from the surface, as a result of the airfoil surface curving away from the layer, would account for the similarity of $\mathrm{Sr}_{\theta s}$ of the separation bubbles and Sr_θ of planar free-shear layers. A slightly higher value for $\mathrm{Sr}_{\theta s}$ of 0.020 is observed for the highest Reynolds number. However, the uncertainty in this value is approximately 0.005, and is much higher than that for the lower Reynolds numbers due to the relatively thin boundary layer at separation. For this case, a resolution of only six vectors across the boundary layer at separation yields larger uncertainties in the momentum thickness at separation and the inferred frequency of vorticity roll-up.

Once the roll-up of vorticity is initiated in the separated shear layer as a result of the Kelvin–Helmholtz instability, the rate of amplification is very high in the streamwise direction. As seen in Fig. 6, over a distance of approximately two wavelengths, the spanwise-oriented vortices grow to a level where the wall-normal extent is approximately equal to that of the streamwise wavelength, and small-scale fluctuations in the vorticity contours near $x/C = 0.5$ indicate that breakdown to small-scale turbulence has been initiated. In the region $0.45 < x/C < 0.50$ the vortices grow to a sufficient strength that they provide a significant level of cross-stream momentum exchange and initiate the process of reattachment of the shear layer to the surface.

The location of transition onset in a shear layer can be defined as the streamwise location where small-scale fluctuations, smaller than those associated with the dominant instability waves, are initiated and provide a mechanism for dissipation of energy at the Kolmogorov scale. In a direct numerical simulation (DNS) of transition in a separation bubble under low-freestream-turbulence conditions [11], the present authors observed that this small-scale breakdown to turbulence is initiated in the high-shear braid region between sequential large-scale spanwise vortices. Due to convection of the vortices through the shear layer, the small-scale breakdown occurs in a time-periodic manner. Through these DNS results, it was also observed that the most upstream location where small-scale breakdown occurs corresponds with deviation of the fluctuation growth rates from the exponential growth associated with amplification of the dominant instability. This has therefore been used as a means for identifying the transition onset location in the present study. Figure 7 shows the growth of $\langle v'v' \rangle$ and $\langle u'v' \rangle$ fluctuation correlations in the shear layer for the case presented in Fig. 6 (Re=39,000). Deviation from exponential growth occurs at about $x/C = 0.44$, and is identified as the location of transition onset. Although both the $\langle v'v' \rangle$ and $\langle u'v' \rangle$ distributions deviate from exponential growth at the same streamwise location, the $\langle v'v' \rangle$ curve exhibits exponential growth further upstream than the $\langle u'v' \rangle$ curve, thus providing a greater streamwise extent of exponential growth. This is observed at all Reynolds numbers, and therefore the $\langle v'v' \rangle$ distributions have been used in identifying transition onset. The uncertainty in identifying transition onset for the present measurements, and those of the flow-manipulation study, is $\pm 0.01C$.

In planar free-shear layers, the spanwise vortices produced by the Kelvin–Helmholtz instability are unstable to subharmonic disturbances [39], which results in a vortex-pairing phenomenon.

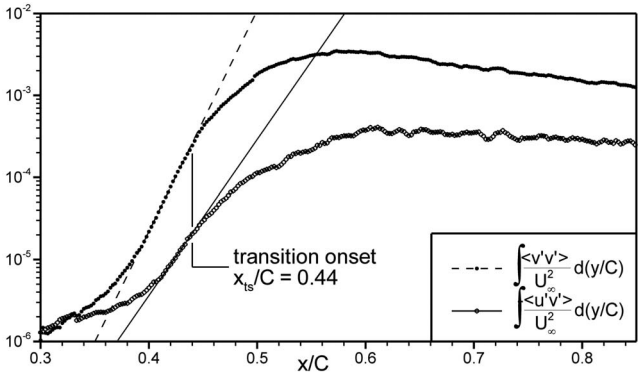

Fig. 7 Fluctuation growth rates and transition onset location for Re=39,000

This pairing phenomenon is observed in the present experiments at all Reynolds numbers, and is shown for Re=28,000 in Fig. 8 through a series of x-y plots of normalized spanwise vorticity. At $t^*=0$, a large vortex resulting from roll-up of the separated shear layer is observed at approximately $x/C=0.55$. In the next frame ($t^*=0.0544$) an upstream vortex, identified by a region of concentrated negative vorticity, enters the field of view, and the subharmonic instability causes it to shift toward the higher-velocity side of the shear layer. As this upstream vortex convects at a higher rate and catches up to the downstream vortex, the two become stretched and elongated as they rotate about each other due to mutual induction of their vorticity fields. The stretched vortices subsequently merge into a single vortex structure. The trajectories of the two vortex cores are traced out in Fig. 8 and show the difference in convection rates of the two vortices due to the subharmonic instability. As the vortices merge, the production of smaller-scale turbulence is observed near the core of the new vortex, indicated by the stronger vorticity fluctuations, and at $t^*=0.2722$ the new vortex is dominated by small-scale fluctuations. During this vortex-pairing process, the resultant stronger new vorticies have approximately double the spacing of the primary vortices, hence the identification of this process as a subharmonic of the primary instability. The same phenomenon has been observed in other studies of separation bubbles [4,7,8,40]. However, the presence of pairing has only been observed at lower Reynolds numbers ($\mathrm{Re}_\theta O(100)$), similar to those of the present study.

In some instances, a secondary pairing process is observed in and downstream of the reattachment region. This secondary pairing process does not occur in as coherent a manner as the primary pairing process associated with the subharmonic instability of the separated shear layer. Some indications of this secondary pairing are seen in the downstream regions of Fig. 8, but the process is more distinct at a Reynolds number of 39,000, as shown in Fig. 9. In this figure, two occurrences of the secondary pairing phenomenon are identified, and the trajectories of the pairing vortices are shown. The vortices do not have a distinctive structure but are identified by clusters of strong vorticity fluctuations. The most interesting observation associated with this secondary pairing event is the presence of intervortex regions with a negligible velocity and vorticity fluctuations (apparent for $0.3432 \leqslant t^* \leqslant 0.6864$ in Fig. 9). These regions are comprised of freestream fluid entrained toward the surface by the large-scale vortices generated in the transition region. The boundary layers in the intervortex regions have velocity profiles similar to time-averaged turbulent profiles, despite the low fluctuation levels, with vorticity concentrated at a thin region near the surface. The occurrence and streamwise extent of this laminarlike intervortex region decrease with an increasing Reynolds number, and is scarcely observed at a Reynolds number of 101,000 where $\mathrm{Re}_{\theta s}=185$. At even higher

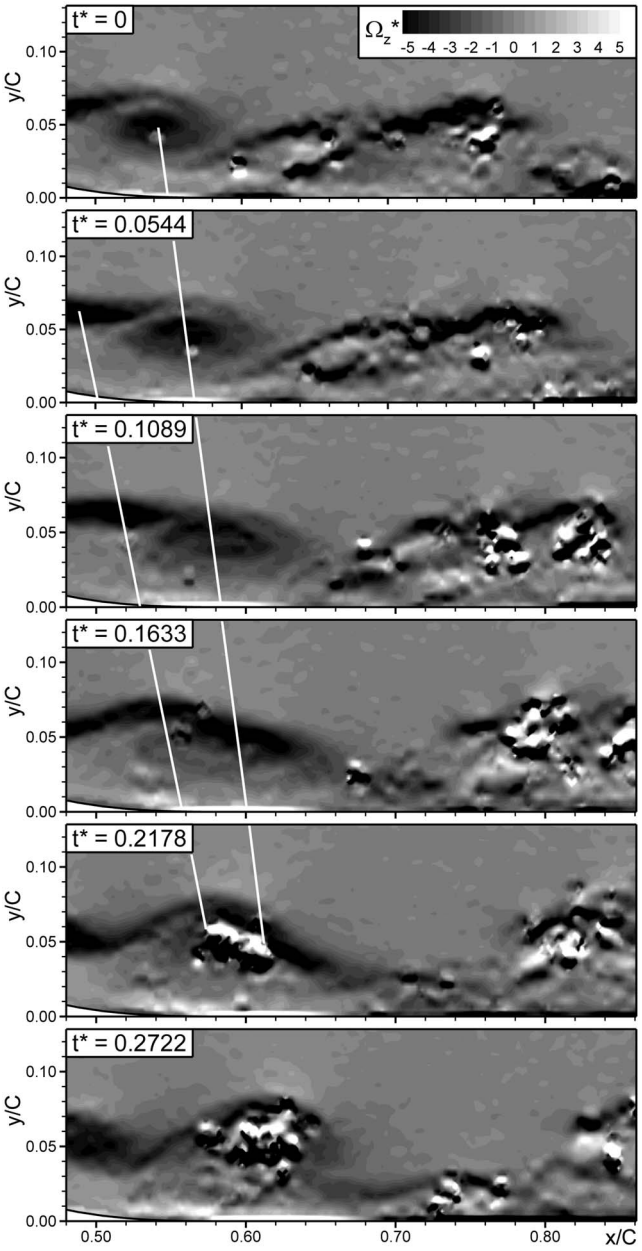

Fig. 8 Vortex-pairing phenomenon observed at Re=28,000

Reynolds numbers, for example, in a direct numerical simulation performed by the authors where $\mathrm{Re}_{\theta s}=267$, there is no evidence of such laminar flow regions downstream of a Kelvin–Helmholtz-type transition/reattachment process. The persistence of the laminar intervortex regions at the lowest Reynolds numbers may be a result of the local boundary-layer Reynolds number being below the critical Reynolds number for flow instability. At Re=28,000, the momentum thickness Reynolds number downstream of reattachment is on the order of 350, which, for the accelerating freestream flow observed downstream of reattachment (see Fig. 5), is likely to be stable to disturbances [41].

As observed in some large-eddy and direct-numerical simulations of transition in separation bubbles [6,7,9,40] the large-scale spanwise vortices generated in the transition region become stretched and reoriented as they convect downstream, resulting in hairpin-shaped structures similar to the dominant structures observed in turbulent boundary layers [42]. The secondary pairing events noted above may be the result of these hairpinlike structures being stretched in the streamwise direction and locally merg-

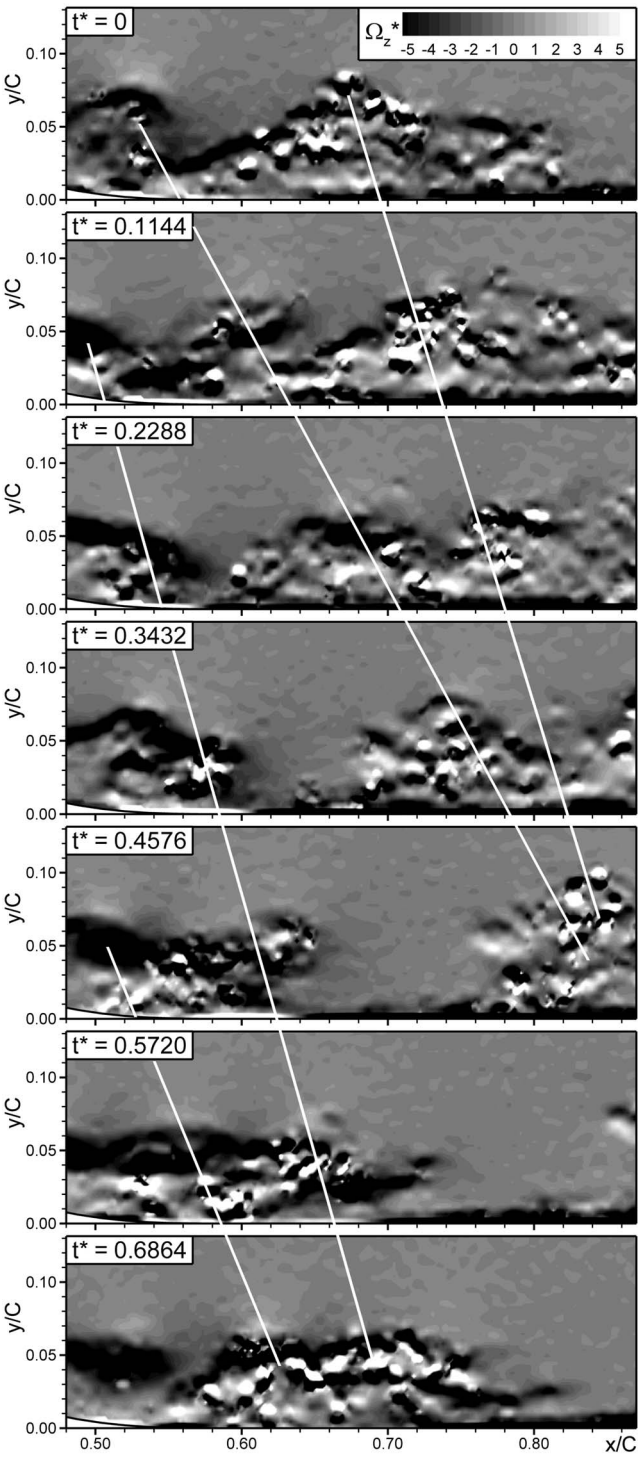

Fig. 9 Secondary pairing phenomenon observed at Re =39,000

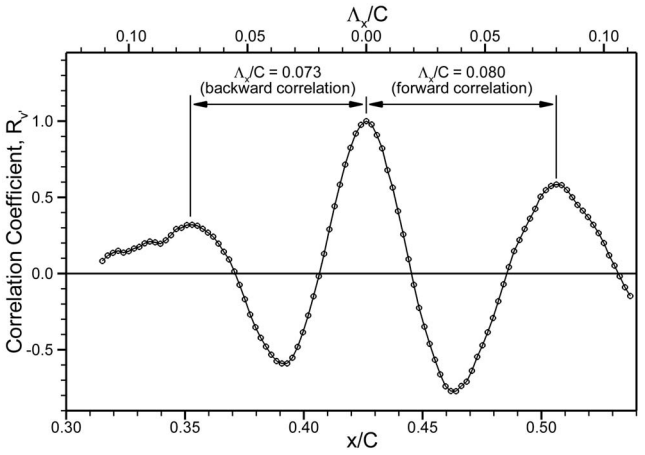

Fig. 10 Streamwise correlation function of wall-normal velocity fluctuations at $x/C=0.426$ and $y/C=0.061$ for Re=39,000

ing with similar upstream or downstream vortex structures. It is conceivable, however, that a secondary subharmonic vortex-pairing process is active, given that it is a common feature of planar free-shear layers [2,3,43] with which the separation bubbles examined herein share many commonalities. As described by Ho and Huang [43], the change of the local length scale of a planar free-shear layer as a result of the vortex merging makes the original subharmonic instability become neutrally stable, and the new subharmonic becomes the wave of most rapid amplification. This process leads to a secondary pairing phenomenon, and is suggested as the dominant mechanism associated with growth of planar free-shear layers [3]. Either scenario described above could provide the conditions under which laminar intervortex regions would be observed in a two-dimensional x-y measurement plane. In any case, recovery to an equilibrium turbulent boundary layer generally takes many bubble lengths downstream of reattachment, indicated by the presence of laminar intervortex regions observed near the airfoil trailing edge. Long recovery lengths downstream of a separation bubble are generally associated with a slow breakdown of the large-scale vortex structures, as discussed by Alam and Sandham [44] and McAuliffe and Yaras [9] through results of direct numerical simulations.

As mentioned above, the secondary pairing process is not a consistent phenomenon, and most often the vortices generated from the primary pairing event remain relatively coherent as they convect downstream of the separation bubble. The dominant streamwise wavelengths associated with the large-scale vortices have been identified by means of a spatial correlation of the wall-normal velocity fluctuation. The correlation coefficient $R_{v'}$ is defined as

$$R_{v'}(x,x+\Delta x)=\frac{1}{N}\sum_{i=1}^{N}\frac{v_i'(x)}{\sqrt{\langle v'v'(x)\rangle}}\frac{v_i'(x+\Delta x)}{\sqrt{\langle v'v'(x+\Delta x)\rangle}} \tag{1}$$

where N is the number of vector fields used in the ensemble average and i is an index identifying the instantaneous vector fields. Normalization of the instantaneous fluctuation values by the local ensemble-averaged rms values, $\sqrt{\langle v'v'\rangle}$, is required since the fluctuation levels change with streamwise distance, and this ensures that the correlation value will be bounded in the range $-1 \leqslant R_{v'} \leqslant 1$. Figure 10 provides an example of the correlation function at a location of $x/C=0.426$ and $y/C=0.061$ for Re=39,000. Apart from the autocorrelation peak centered at the location about which the correlation is being performed ($x/C=0.426$), two distinct correlation peaks are observed in Fig. 10 and provide estimates for the dominant wavelength prevailing in the separated shear layer. Since the dominant length scale changes with streamwise distance due to changes in the vortex convection rates and the vortex-pairing phenomenon, the length scales identified by the correlation function are not necessarily indicative of the dominant wavelength at the location about which the correlation is being performed. Differences in the forward and backward correlated wavelengths in Fig. 10 provide evidence of this discrepancy. It can be assumed that the observed dominant length scale is more representative of those that occur at a distance halfway between the correlation location and the location of the respective correlation peak. Wavelengths extracted in this manner provide a clear

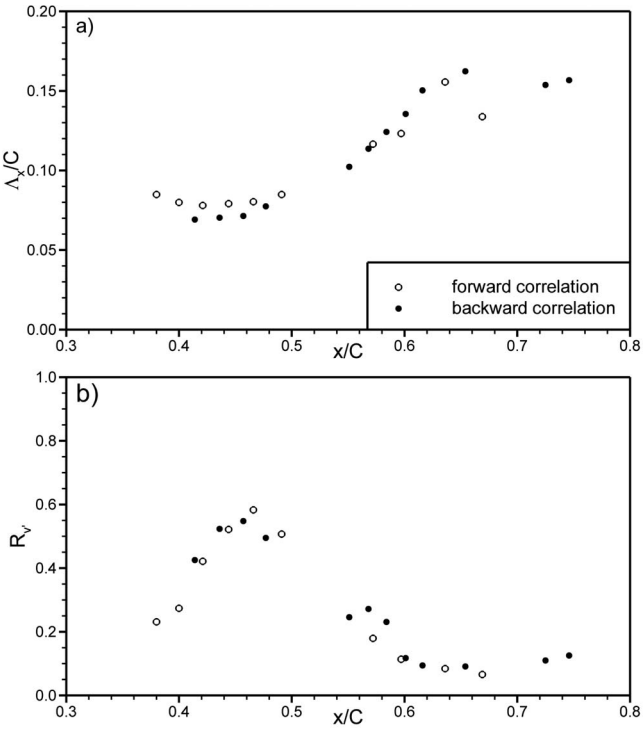

Fig. 11 Streamwise correlation of dominant wavelengths for Re=39,000; (*a*) wavelength distribution and (*b*) correlation peak distribution

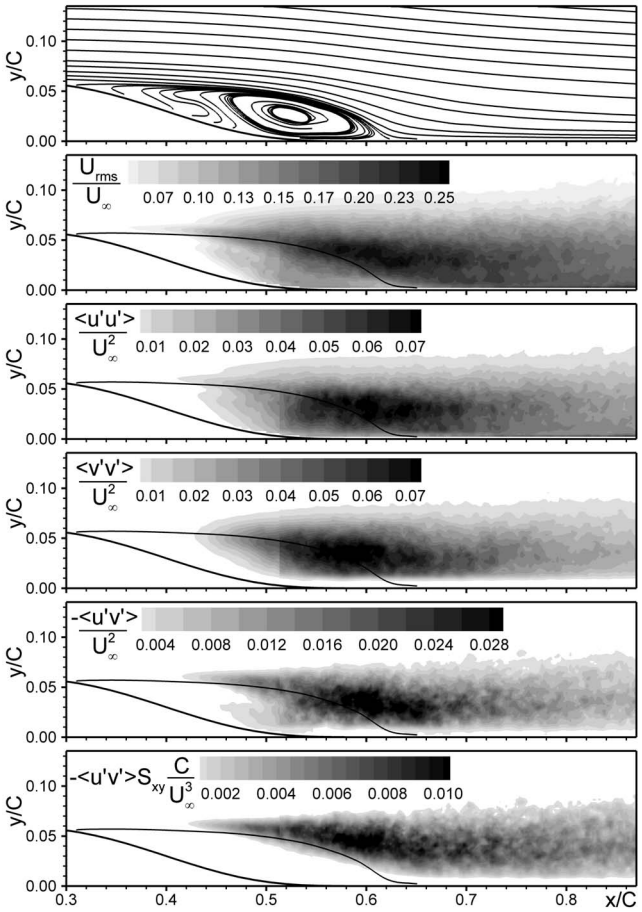

Fig. 12 Mean streamlines and contour plots of velocity correlations at Re=39,000 (dividing streamline overlaid on contour plots)

picture of the change in length scale with streamwise distance due to the vortex-pairing phenomenon, as shown in Fig. 11(*a*). For a given streamwise location, there is a slight discrepancy in the length scale extracted using the forward and backward correlation peaks, but the general trend of increasing length scale is captured well. Over the aft region of the airfoil, the dominant length scale is approximately double that of the primary instability wavelength that develops in the separated shear layer, providing evidence that the primary pairing event is dominant and secondary pairing is not a consistent phenomenon. The correlation peak values associated with the dominant wavelengths are shown in Fig. 11(*b*), and illustrate the growth and decay in coherence of these dominant length scales with downstream distance. The highest level of coherence is observed near transition onset ($x_{ts}/c=0.44$), downstream of which the combined effect of small-scale breakdown to turbulence and distortion of the large-scale vortices results in lower correlation values.

For practical purposes, the ensemble-averaged statistics associated with the velocity fluctuations in separation bubbles are important, particularly for validation and development of transition models and turbulence-closure models for use in computational fluid dynamics (CFD) software [45,46]. In Fig. 12, contour plots of velocity correlations are shown for Re=39,000 with the averaged streamline patterns provided in the upper plot of the figure, and with the dividing streamline that bounds the averaged reverse-flow region overlaid on the subsequent contour plots. On the contour plots in Fig. 12, a slight discontinuity in the fluctuation fields is observed at $x/C \approx 0.51$, which is the interface of the two measurement regions from which the data have been processed. Velocity fluctuations are first observed to grow along the line of maximum vorticity in the separated shear layer, which is consistent with growth of vorticity fluctuations by means of the inviscid Kelvin–Helmholtz instability, as observed in Fig. 6. The highest fluctuation levels are observed near the ensemble-averaged reattachment location and decay with downstream distance as a result of damping due to the presence of the wall. In the plots of U_{rms} and $\langle u'u' \rangle$, a secondary fluctuation peak is observed inside the bubble along the line of maximum reverse-flow velocity. This is consistent with other measurement and simulation results of separation bubbles [5,8,10,11,47] and is predicted by LST. As discussed by the authors in a previous study [9], with the use of LST results presented by Rist and Maucher [38], this inner peak is a result of a viscous instability associated with the reverse-flow below the separated shear layer.

Of the statistical parameters presented in Fig. 12, the Reynolds shear-stress component $\langle u'v' \rangle$ provides a measure of the wall-normal momentum exchange occurring as a result of the transition process, and also has peak levels near the ensemble-averaged reattachment location. The energy transfer facilitated by the $\langle u'v' \rangle$ Reynolds shear-stress component is quantified by $-\langle u'v' \rangle S_{xy}$, which is the work done by this shear stress on the time-mean flow field through the strain rate S_{xy}. This energy transfer is noted to occur predominantly in the outer part of the separated shear layer as a result of the high rates of strain occurring in that region. Downstream of the bubble, significant levels of $-\langle u'v' \rangle S_{xy}$ are observed across the reattached shear layer.

Passive Manipulation of Separation-Bubble Transition. Several two-dimensional surface modifications have been examined, and include both surface protrusions (ST configuration) and surface indentations (SG, LG, SN, SR configurations). The geometry of these configurations was provided in Fig. 3. In the following discussion on the effects of the surface modifications with regard to the separation-bubble characteristics and boundary-layer losses downstream of reattachment, the acronym CL refers to the clean-

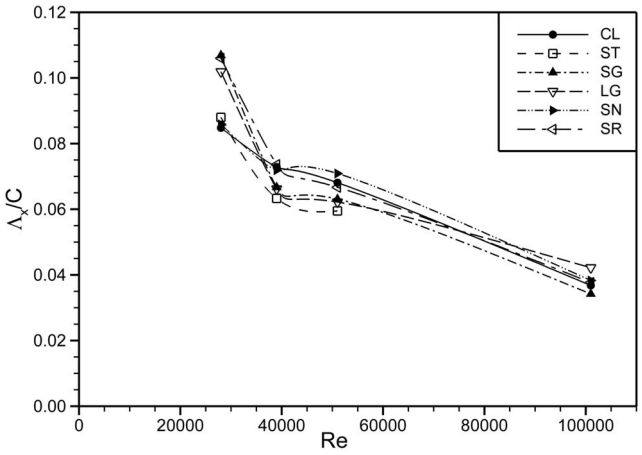

Fig. 13 Dominant wavelengths observed in the separated shear layer for all configurations

airfoil configuration that was discussed in the preceding section. In this section, a comparison of the general performance of the airfoil with the surface modifications is given first, followed by individual discussions of the flow physics for each modification.

The surface modifications examined have been designed to provide passive forcing of the shear layer at a frequency similar to that of the dominant instability observed in the separated shear layer. The passive forcing was achieved by selecting a streamwise disturbance length of comparable magnitude to the wavelength of the separated-shear-layer instability of the clean airfoil. The 39,000 Reynolds-number case was selected as the baseline condition, for which the dominant wavelength is 7.2% of chord length, and therefore the other Reynolds numbers examined represent off-design conditions. The device length for the ST and SG configurations are half of this dominant wavelength. For some of the configurations, local steps and curvature discontinuities in the surface shape provide sources of disturbances with a broad band of frequencies.

Figure 13 shows the dominant streamwise wavelengths of the observed instabilities for all configurations examined. These wavelengths have been identified using the spatial correlation technique described earlier in the paper, which makes use of Eq. (1). A distinct change in the dominant instability wavelength is observed in Fig. 13 for many of the configurations. At a Reynolds number of 28,000, all flow control configurations show similar or increased wavelengths compared to the clean-airfoil case, whereas at Reynolds numbers of 39,000 and 51,000 the dominant wavelengths are similar or lower. This trend is contrary to what was expected, in that for a particular configuration the dominant wavelength was expected to be similar at all Reynolds numbers due to the spatial nature of the forcing device. Despite this, there is a distinct effect of spatial forcing on the instability wavelengths compared to the clean-airfoil case.

Important parameters that define the characteristics of the separation bubbles, as well as the reattached turbulent boundary layer, are given in Table 2. The maximum expected uncertainties in these parameters were provided in Table 1. The ensemble-averaged locations of separation, transition onset, and reattachment for all cases are shown in Fig. 14 with a schematic of the airfoil for reference. The SG and SR configurations show similar separation locations compared to the clean-airfoil case, with a greater downstream shift for the SR configuration. For the ST and LG configurations, separation occurs well upstream of the clean-airfoil separation point, at the location where a sharp backward-facing step associated with these surface-modification configurations is present. The SN case also shows an upstream movement of the separation location, except at a Reynolds number of 101,000 where separation occurs at the most downstream location of any of the separation-bubble cases examined.

In the present study, transition onset is defined as the location where small-scale fluctuations, smaller than those associated with

Table 2 Characteristics of separation bubbles and reattached boundary layer for all configurations

		Separation			Transition			Reattachment		$x/C=0.85$	
Conf.	Re $\times 10^{-3}$	$\frac{x_s}{C}$	$\frac{U_{es}}{U_\infty}$	$\mathrm{Re}_{\theta s}$	$\frac{x_{ts}}{C}$	$\frac{x_{ts}-x_s}{C}$	$\mathrm{Sr}_{\theta s}$	$\frac{x_r}{C}$	$\frac{x_r-x_s}{C}$	Re_θ	H
CL	28	0.292	1.160	83	0.488	0.196	0.0159	0.684	0.392	342	1.60
	39	0.293	1.180	100	0.438	0.145	0.0159	0.618	0.325	422	1.49
	51	0.297	1.192	120	0.411	0.114	0.0150	0.581	0.284	516	1.43
	101	0.323	1.221	185	0.381	0.058	0.0197	0.456	0.133	562	1.79
ST	28	0.229	1.210	79	0.444	0.215	0.0138	0.673	0.444	364	1.65
	39	0.229	1.221	100	0.403	0.174	0.0172	0.621	0.392	497	1.51
	51	0.229	1.242	118	0.383	0.154	0.0168	0.582	0.353	596	1.43
	101	0.229	1.346	215	0.229	0.000	—	0.240	0.011	457	1.46
SG	28	0.295	1.171	85	0.492	0.197	0.0128	0.689	0.394	301	1.67
	39	0.294	1.181	103	0.439	0.145	0.0176	0.630	0.336	400	1.45
	51	0.304	1.183	125	0.410	0.106	0.0171	0.585	0.281	505	1.43
	101	0.323	1.252	231	0.385	0.062	0.0256	0.418	0.095	636	1.40
LG	28	0.232	1.201	75	0.479	0.247	0.0120	0.664	0.432	336	1.51
	39	0.232	1.218	95	0.418	0.186	0.0143	0.596	0.364	407	1.42
	51	0.232	1.232	108	0.402	0.170	0.0136	0.557	0.325	461	1.40
	101	0.232	1.289	162	0.410	0.178	0.0160	—	—	494	1.45
SN	28	0.247	1.198	83	0.497	0.250	0.0157	0.681	0.434	327	1.54
	39	0.247	1.209	106	0.435	0.188	0.0163	0.619	0.372	396	1.43
	51	0.247	1.221	129	0.413	0.166	0.0146	0.570	0.323	477	1.41
	101	0.350	1.210	225	0.390	0.040	0.0247	0.443	0.093	534	1.39
SR	28	0.300	1.172	86	0.509	0.209	0.0129	0.687	0.387	306	1.68
	39	0.304	1.176	104	0.452	0.148	0.0177	0.635	0.331	368	1.47
	51	0.308	1.186	123	0.418	0.110	0.0159	0.588	0.280	478	1.44
	101	0.330	1.218	201	0.403	0.073	0.0196	0.457	0.127	577	1.74

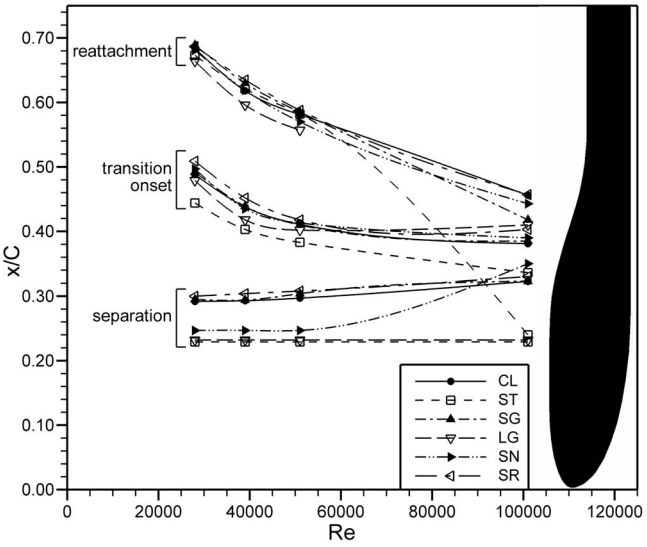

Fig. 14 Separation, transition onset, and reattachment locations for all configurations

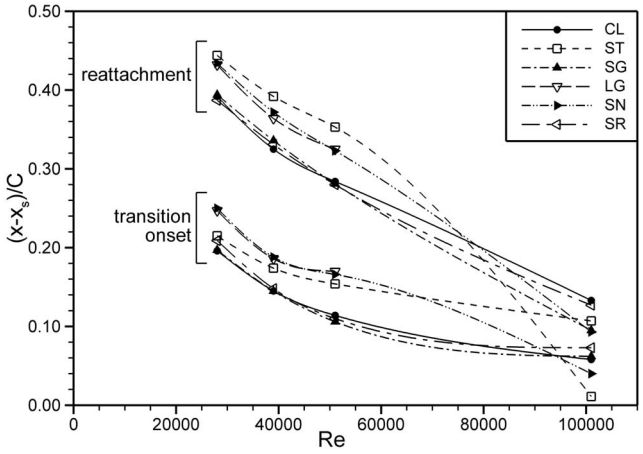

Fig. 15 Transition onset and reattachment lengths, relative to separation, for all configurations

the dominant instability waves, are initiated and provide a mechanism for dissipation of energy at the Kolmogorov scale. As discussed earlier in the paper with regard to the clean-airfoil configuration, this is identified by the streamwise location at which the growth of fluctuation levels in the shear layer begins to deviate from the exponential growth associated with amplification of the Kelvin–Helmholtz instability. The location of transition onset for the SG and SN cases is almost coincident with that for the clean airfoil at the three lower Reynolds numbers examined, with a slight deviation seen at the highest Reynolds number (see Fig. 14). The ST configuration at the three lower Reynolds numbers and the LG configuration over the full Reynolds-number range, show upstream movement of the transition onset location, resulting primarily from the upstream movement of the separation point. Similarly, for the highest Reynolds number, the SR case shows downstream movement of transition onset by a distance equivalent to the downstream movement of separation. For the ST configuration at the highest Reynolds number, the protrusion initiates transition near the trailing edge of the step, which then occurs in an attached boundary layer over the backward-facing ramp.

Reattachment locations show similar movement, relative to the clean airfoil, to that of the transition onset location, except for the ST configuration. The ST configuration shows similar reattachment locations to the clean airfoil (Fig. 14), except at a Reynolds number of 101,000 where reattachment occurs shortly downstream of the step as noted above. A time-averaged reattachment point is not provided in Table 2 and Fig. 14 for the LG configuration at a Reynolds number of 101,000, reasons for which will be discussed later.

The transition onset and reattachment locations, measured relative to the separation location, provide a better measure of the manipulation by the surface modifications on the transition process within the separation bubble. Figure 15 shows these relative locations for all configurations, for which three distinct trends are observed. At the three lower Reynolds numbers, the SG and SR configurations show similar relative locations of transition onset and reattachment as those for the clean airfoil. For the LG and SN configurations, the relative transition onset and reattachment locations are further downstream, except at the highest Reynolds number. At the three lower Reynolds numbers, the ST configuration shows a delayed transition onset compared to the clean airfoil, but not to the same extent as the LG and SN configurations. However, the reattachment length for the ST configuration is the longest of all the configurations examined at the three lower Reynolds numbers and is shortest at the highest Reynolds number. It is again noted that reattachment occurs shortly downstream of the step for the ST configuration at the highest Reynolds number, and transition occurs in an attached boundary layer over the backward-facing ramp.

The losses associated with manipulation of the separation bubble through surface modifications can be evaluated by examining the momentum thickness of the boundary downstream of reattachment. Figure 16 shows momentum-thickness Reynolds numbers for all cases at a location of $x/C=0.85$, which is downstream of the reattachment location for all conditions. The curve-fits in Fig. 16 are provided only as a guide for the eye and do not indicate the trends expected at intermediate Reynolds numbers. As would be expected with an increasing flow Reynolds number, the momentum-thickness Reynolds number increases for almost all configurations. The ST configuration, however, shows lower losses at Re=101,000 than at 39,000 and 51,000. At the three lower Reynolds numbers examined, all configurations except ST provide a decrease in losses over those of the clean airfoil. At the highest Reynolds number, the SG and SR configurations show increased losses compared to the clean airfoil, with a decrease observed for all other configurations. The configuration that shows the most consistent improvement in losses at the three lower Reynolds numbers is the SR configuration; however, it provides a slight increase in losses at the highest Reynolds number.

In the following, details regarding the ways in which each sur-

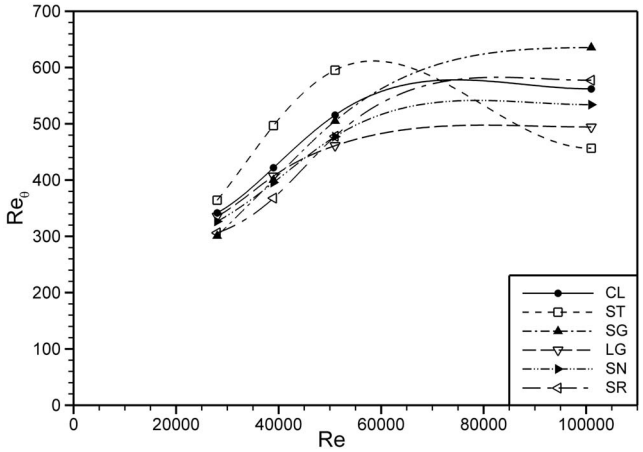

Fig. 16 Momentum-thickness Reynolds numbers for all configurations at $x/C=0.85$

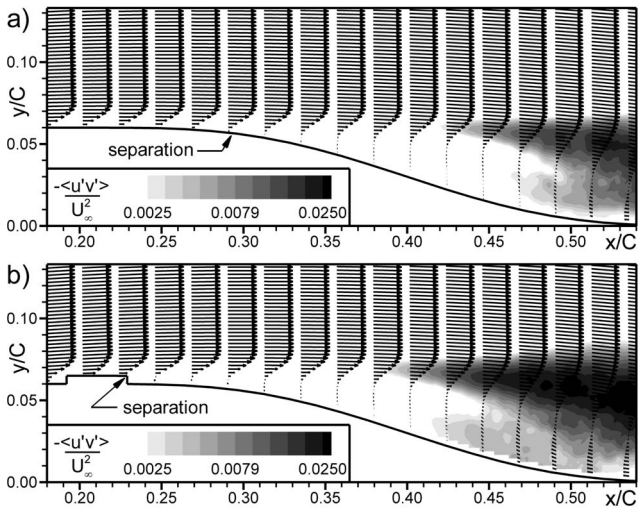

Fig. 17 Velocity-vector profiles and $\langle u'v' \rangle$ distributions at a Reynolds number of 39,000 for (*a*) the clean airfoil and (*b*) the ST configuration

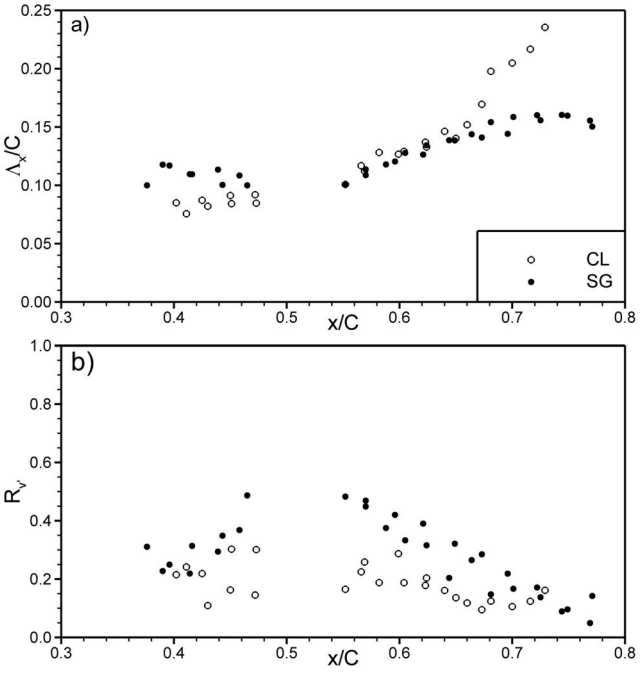

Fig. 18 Streamwise correlation of dominant wavelengths for SG and CL configurations for Re=28,000; (*a*) wavelength distributions and (*b*) correlation peak distributions

face modification affects the separation bubble are discussed to provide a physical explanation of the performance trends observed. The discussions revolve around the performance trends presented in Figs. 13–16, without explicit reference to these figures.

ST Configuration. The step associated with the ST configuration provides a disturbance comparable to a trip wire placed upstream of separation. Trip wires generally promote transition in the separated shear layer, resulting in decreased separation-bubble lengths, but often have increased losses for conditions where a separation bubble would not develop in the absence of the tripping device. For the present configuration, this trend is reversed and losses are higher than those for the clean airfoil at the three lower Reynolds numbers, with a decrease in losses observed only at the highest Reynolds number.

At the three lower Reynolds numbers, separation occurs at the trailing edge of the surface protrusion providing a separated shear layer at a greater distance from the airfoil surface than all other configurations examined. This is observed in Fig. 17 through a comparison of the velocity-vector profiles over the backward-facing ramp for the clean-airfoil and ST configurations at a Reynolds number of 39,000. Despite the higher losses associated with the ST configuration at these Reynolds numbers, transition onset relative to the separation point is delayed. Of all the configurations examined, this configuration is observed to have the highest levels of velocity fluctuations in the transition and reattachment regions. By examining the instantaneous velocity and vorticity fields (not shown here), it was observed that the greater distance of the shear layer from the surface reduces the damping effect of the wall. As a result, the large-scale vortical structures, as well as the smaller-scale turbulence, can spread over a greater transverse, or wall-normal, distance. This greater displacement of the separated shear layer from the surface also provides the conditions, which result in longer reattachment lengths, relative to the location of separation.

The ST configuration provides the greatest loss reduction at a Reynolds number of 101,000. For this case, a small recirculation zone is observed right behind the step, but is not well defined due to the spatial resolution of the PIV measurements. The separated shear layer over this recirculation zone reattaches over a short streamwise distance, yielding a transitional boundary layer downstream of the step, which does not separate, over the backward-facing ramp of the airfoil. The absence of a separated shear layer over the backward-facing ramp prevents the growth and shedding of large-scale vortical structures, thereby reducing the thickness of the shear layer, as well as the fluctuation levels present therein. In a study of a range of disturbance strips over a low-pressure turbine airfoil in the presence of periodically passing turbulent wakes, Zhang et al. [20] provide similar conclusions regarding the use of a rectangular step upstream of separation. In their case however, separation was still present downstream of the step, but the disturbances promoted by the step hastened the transition process within the separation bubble providing lower losses at the trailing edge of the airfoil. Volino [15] observed similar effects induced by a rectangular protrusion located upstream of separation.

SG Configuration. The SG configuration provides the greatest reduction in loss at a Reynolds number of 28,000. However, the loss reduction diminishes with an increasing Reynolds number and a significant increase in loss is observed at the highest Reynolds number of 101,000.

At a Reynolds number of 28,000 the primary pairing process is suppressed. Figure 18 shows the wavelength and associated correlation coefficient distributions for this case compared with those for the clean airfoil at the same Reynolds number. As a result of the higher mean velocities in the outer part of the reattached turbulent boundary layer, the convection rate of the shed vortices is increased over that observed in the separated laminar shear layer, which is what causes the observed increase in dominant length scale for the SG configuration. Conversely, a continual increase in wavelength is observed for the clean-airfoil case. The higher correlation levels for the SG configuration also indicate greater coherence of the shed vortices. The passive forcing appears to promote a frequency lower than that of the natural frequency of the shear layer, indicated by the increased instability wavelength, which according to Ho and Huerre [3] should result in suppression of the subharmonic that initiates the pairing process. In examining instantaneous velocity and vorticity plots, the primary pairing process is rarely observed and the occurrence of laminarlike intervortex regions is significantly reduced from what was observed for the clean-airfoil at this Reynolds number.

At Reynolds numbers of 39,000 and 51,000 the transition pro-

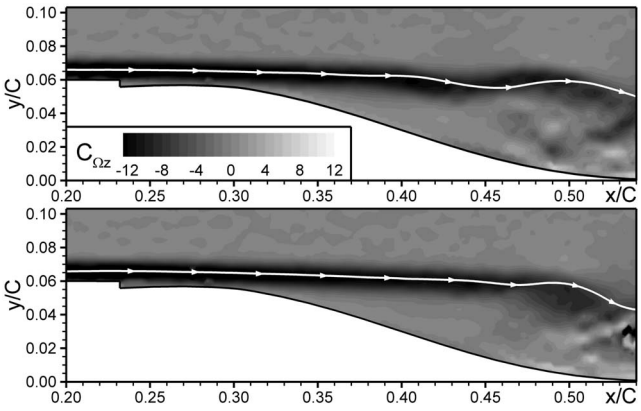

Fig. 19 Variation in instability growth and wavelength for the SR configuration at Re=39,000 for uncorrelated instants in time

cess and associated flow structures are very similar to those of the clean airfoil, which includes the presence of the primary and secondary pairing events. There are however slight increases in the length-scale correlations observed in the reattached boundary layer, which indicates that the shed vortices remain coherent for a longer streamwise distance. This may provide the mechanism for the slight decrease in losses observed for these two Reynolds numbers, over the respective clean-airfoil cases.

At the highest Reynolds number examined, the separation and transition onset locations are very similar to the clean-airfoil case. However, the groove seems to provide a disturbance source that modifies the vortical structures originating from the periodic roll-up of the separated shear layer in a manner that yields earlier reattachment. This modification to the structure of turbulence developing in the separated shear layer also yields a thicker reattached boundary layer, hence higher losses than the clean-airfoil case.

SR Configuration. The SR configuration provides the greatest delay in separation of all configurations examined, except at a Reynolds number of 101,000 where the SN configuration provides a greater delay. For all conditions, a small separated-flow region occurs in the leading-edge region of the surface modification, as would be expected in the lower corner behind a backward-facing step. Laminar reattachment of this shear layer shortly downstream of the step, and prior to the larger-scale separation bubble, provides a highly inflectional laminar boundary layer, which separates further downstream than in the clean-airfoil cases. As previously noted, this configuration provides the most consistent reduction in losses at the three lower Reynolds numbers.

At a Reynolds number of 28,000, the SR configuration provides the same manipulation to the transition process, as does the SG configuration. The passive forcing promotes a lower instability frequency, which results in suppression of the subharmonic that initiates the pairing process, and the primary instability wavelength remains the dominant length scale present over the airfoil.

The dominant instability wavelengths at Reynolds numbers of 39,000 and 51,000 are almost identical to those for the clean airfoil, indicating negligible influence of the surface modification on the frequency of maximum amplification in the separated shear layer. Despite this, at a Reynolds number of 39,000 the disturbance appears to suppress the instability growth during some periods of the shear-layer development. Figure 19 shows two *x-y* plots of normalized spanwise vorticity for a Reynolds number of 39,000 at two uncorrelated moments in time. Visible growth of the instability wave is observed at a more upstream location in the upper plot than in the lower plot. The wavelength of the instability in the upper plot is also larger than that in the lower plot, indicating that a broad range of frequencies are present in the separated shear layer. These trends are also noted to occur for the clean airfoil but not to the same extent. At this Reynolds number, the maximum wavelength-correlation peak is much lower than that for the clean airfoil (0.35 for SR and 0.6 for CL), which is another indicator of this broader range of frequencies.

A different effect is observed at a Reynolds number of 51,000, where breakdown to small-scale turbulence is promoted by the surface modification, resulting in a shorter bubble length. The reattachment point is almost coincident with the clean-airfoil case despite the delayed separation. The shorter bubble length provides a lower momentum thickness downstream of the bubble, therefore lower losses.

At the highest Reynolds number of 101,000, the SR surface modification has no significant effect on the separation bubble. The velocity fluctuation levels observed in and downstream of the separation bubble are very similar to the clean-airfoil case. This results in similar loss levels for the two configurations.

LG Configuration. For the LG configuration, separation occurs off the sharp backward-facing step at the leading edge of the groove. At the three lower Reynolds numbers, transition onset occurs upstream of the corresponding clean-airfoil locations, but the separation-to-transition length is longer and is likely a result of the lower momentum-thickness Reynolds numbers at separation.

The dominant instability wavelengths are very similar to those for the SG configuration, however the trend in losses relative to the clean-airfoil is opposite to that of the SG case. At the lowest Reynolds number, the losses are equivalent to the clean-airfoil case, but a decrease in losses is observed with an increasing Reynolds number, and at a Reynolds number of 101,000 this configuration provides greatly reduced losses.

Despite the increased instability wavelength at a Reynolds number of 28,000, the pairing process is not suppressed as was seen for the SG and SR cases. At this Reynolds number, there are no distinct differences in the transition and reattachment processes from that which occurs over the clean airfoil.

The earlier transition onset (relative to the leading edge of the airfoil) that occurs for this configuration over the clean airfoil is the primary difference that leads to decreased losses at Reynolds numbers of 39,000 and 51,000. As the instability waves grow and develop into discrete large-scale vortices, the closer proximity of the shear layer to the surface due to earlier separation provides a greater level of damping to the growing vortices, which no longer grow to as great an extent in the transverse direction, before being influenced and distorted by the presence of the wall. The vortices shed from the bubble therefore have a lower wall-normal extent and result in a thinner boundary layer downstream of reattachment. At Re=51,000, the downstream edge of the groove provides a greater influence on the disturbance level in the separated shear layer. Disturbances with a smaller length-scale than that of the dominant instability wavelength are observed in the separated shear layer, which also results in lower correlation of the dominant wavelength prior to transition. At this Reynolds number, there is also a greater level of small-scale fluctuations present soon after transition onset, and in the near-wall region below the separated shear layer, which results in a shorter reattachment length relative to transition onset. This is observed in Fig. 20, which shows velocity-vector profiles and $\langle u'v' \rangle$ fluctuation levels for the LG configuration compared to the corresponding clean-airfoil case.

At a Reynolds number of 101,000, a very different process leads to the significant loss reduction observed. As with the lower Reynolds-number cases, separation occurs off the backward-facing step at the leading edge of the groove. However, instability waves are observed in the separated shear layer upstream of the groove trailing edge. These instability waves interact with the trailing edge step of the groove to provide an unsteady separated shear layer downstream of the groove. Figure 21 presents an example of an instantaneous velocity field in the region downstream of the groove. The instability waves introduce local regions of reverse flow near the surface as they grow and convect down-

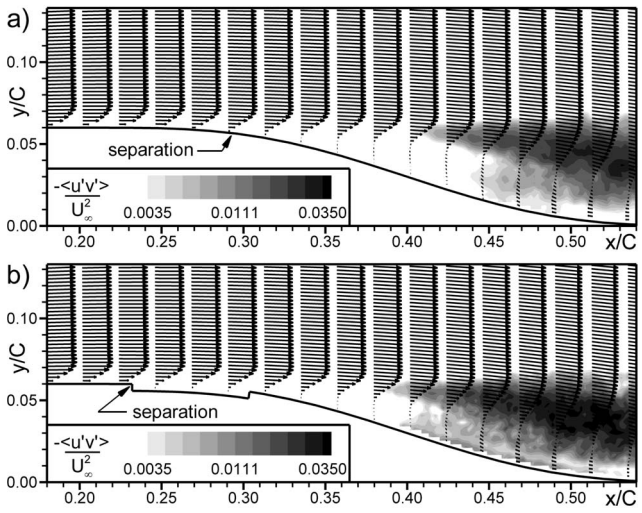

Fig. 20 Velocity-vector profiles and $\langle u'v' \rangle$ distributions at a Reynolds number of 51,000 for (*a*) the clean airfoil and (*b*) the LG configuration

stream. The ensemble-averaged velocity field shows a highly inflectional shear layer in this region with no reverse-flow present. However, the fluctuation growth levels show similar trends to the separation-bubble cases, and the instability Strouhal number based on conditions at the leading edge of the groove is 0.0160, which is in good agreement with values that have been observed in separated shear layers. This would indicate that, although no ensemble-averaged separation bubble is present, instability growth occurs in the same manner as in shear layers that are observed as separated when viewed through time-averaged data. The unsteady nature of the shear layer also reduced the occurrence and size of large-scale vortices shed downstream. This results in the loss reduction observed at this Reynolds number.

SN Configuration. The SN configuration provides transition and reattachment locations (relative to the airfoil leading edge) that closely match those of the clean airfoil, however separation occurs sooner for the three lower Reynolds numbers and losses are reduced over the full Reynolds-number range examined. Separation at the three lower Reynolds numbers occurs slightly downstream of the start of the sinusoidal groove, in the region where increase in surface curvature becomes pronounced. The dominant instability wavelengths for this configuration also most closely match those of the clean-airfoil cases.

At the three lower Reynolds numbers examined, there are no distinct differences in the development of the vortical structures observed in and downstream of the separation bubble as compared to the clean airfoil. The only difference is the earlier separation, which occurs near the groove leading edge. However, the shear layer remains marginally separated over the length of the groove, and as the surface curves back toward the clean-airfoil shape near

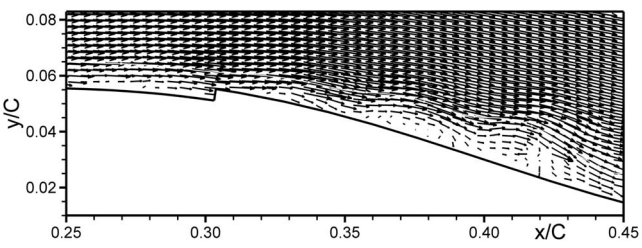

Fig. 21 Unsteady separation observed downstream of the groove of the LG configuration at Re=101,000

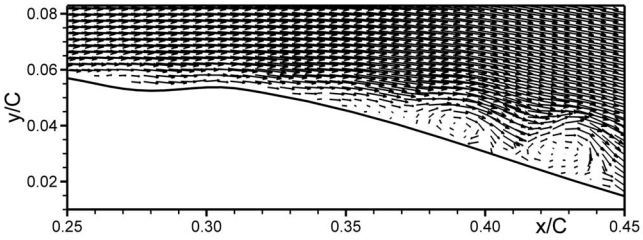

Fig. 22 Unsteady separation observed downstream of the surface modification for the SN configuration at Re=101,000

the trailing edge of the groove, the height of the reverse-flow region decreases. At the trailing edge of the groove, the reverse-flow near the surface is almost eliminated, downstream of which the separated shear layers develop in the same manner as that over the clean airfoil.

Despite the negligible manipulation of the shear layer at the lower Reynolds numbers, a significant difference in the separation-bubble characteristics is observed at Re=101,000. As with the LG configuration at this Reynolds number, instability waves begin to develop shortly downstream of the groove leading edge. These instabilities grow quickly and interact with the trailing edge region of the groove providing a highly unsteady separation process. However, unlike the LG configuration, ensemble-averaged reverse flow is present near the surface. Figure 22 provides an example of the instantaneous velocity field downstream of the groove. The instability waves initiate shedding of vortices downstream of the groove, which results in the highly unsteady separation, with a separation location that varies over the range of $0.33 < x/C < 0.38$. The transition length for this case is the shortest of any of the configurations for which an ensemble-averaged separation bubble is present over the backward-facing curved ramp, and the shorter separation bubble results in lower losses than the clean airfoil at this Reynolds number.

4 Conclusions

Transition in a separation bubble, and passive manipulation thereof, have been examined experimentally using PIV in a water tow-tank facility. An airfoil has been designed that provides a suction-side pressure distribution similar to that occurring over typical low-Reynolds-number airfoils while minimizing the streamwise movement of separation over a range of operating conditions. Measurements were performed at four Reynolds numbers, based on towing speed and chord length, in the range 28,000–101,000 and under negligible freestream-turbulence conditions.

In the first part of the paper, measurements for the clean-airfoil configuration are presented to study the physical mechanisms associated with transition in a separation bubble. The Kelvin–Helmholtz instability mechanism, generally associated with free-shear-layer transition, has been identified as the dominant transition mechanism. This instability leads to roll-up of the vorticity contained in the shear layer into discrete spanwise-oriented vortices that grow and shed from the shear layer, initiating small-scale breakdown to turbulence. The normalized frequency of maximum amplification for the instability is noted to be consistent with that observed in planar free-shear layers. A pairing process has been identified whereby a subharmonic instability causes two sequential vortices to rotate about each other and merge to form a train of larger vortices with double the spacing of the primary vortices. A secondary pairing of these larger vortices is sometimes observed. When this secondary pairing occurs, a region of laminar flow is observed between the large-scale vortices. This laminar intervortex region consists of freestream fluid entrained toward the surface as a result of strong circulation associated with the large-scale vortices. A data-processing method is provided for re-

liably extracting the wavelength of the vortical structures originating in the separated shear layer resulting from the primary and subharmonic instabilities.

Several two-dimensional surface modifications have been made to the airfoil surface to provide passive forcing of the separated shear layer in an effort to manipulate the transition process and mitigate the performance penalties typically associated with separation bubbles. The tested configurations consist of a constant-height step, constant-depth grooves, a backward-facing step followed by a ramp, and a sinusoidal groove. The various geometries provide variation in the separation, transition onset, and reattachment locations over the airfoil surface. For all but the constant-height step, the boundary-layer losses are reduced downstream of the separation bubble for the three lower Reynolds numbers examined. At the highest Reynolds number examined, only three of the five tested geometries result in decreased losses.

The spatial nature of the PIV measurements has allowed a detailed analysis of the manner in which the surface modifications affect the transition process occurring in the separated shear layer. The observed decrease in boundary-layer losses occurs through various manipulation mechanisms. At the lowest Reynolds number of 28,000, two of the configurations provide forcing at a frequency lower than the dominant Kelvin–Helmholtz frequency identified for the clean airfoil. This suppresses the subharmonic instability associated with vortex pairing and results in significantly reduced occurrence of the vortex-pairing phenomenon and a reduced level of small-scale breakdown to turbulence. At the intermediate Reynolds numbers of 39,000 and 51,000, the greatest levels of loss reduction result from a promotion of the small-scale breakdown providing reduced bubble lengths and thinner boundary layers downstream of reattachment. At the highest examined Reynolds number of 101,000, two different manipulations have been identified for reducing losses. The first, by use of a rectangular surface protrusion upstream of the clean-airfoil separation location, initiates transition earlier and eliminates the separation bubble in the region of the strong adverse pressure gradient. The second manipulation, induced by providing a physical disturbance to the instability waves developing in the separated shear layer, results in a highly unsteady separation process downstream of the disturbance. These two manipulations either eliminate or reduce the size of the large-scale vortical structures that are shed downstream of the bubble and provide a decrease in the boundary-layer thickness over the aft region of the airfoil.

The results of the flow-control study indicate that there is no optimal solution to passive transition control in a separation bubble. Depending on the flow Reynolds number and pressure distribution present over the airfoil, different physical mechanisms can be manipulated to affect the separation, transition, and reattachment processes. The results presented herein provide some guidelines for developing passive control techniques for use in practical applications for which separation bubbles generate an undesirable level of boundary-layer losses.

Acknowledgment

The authors gratefully acknowledge the financial support of Pratt and Whitney Canada in this project. The first author would like to thank the Natural Sciences and Engineering Research Council of Canada (NSERC) for financial support through a postgraduate scholarship. Dr. Ernest Hanff and Dr. Ian Campbell of the National Research Council of Canada (NRC) were generous in providing access to the experimental facility and the PIV system, respectively. Thanks also go to Mr. James Ross of the NRC and Mr. Alex Proctor of Carleton University for their help in the design and manufacture of the airfoil. Mr. Todd Brown and Mr. Brian Jahraus of the NRC are acknowledged for their technical assistance during the experimental portion of this work.

Nomenclature

C = airfoil chord length, 0.25 m
f = frequency
H = shear-layer shape factor, δ^*/θ
N = number of data points
Re = flow Reynolds number, $U_\infty C/\nu$
Re_{δ^*} = displacement-thickness Reynolds number, $U_e\delta^*/\nu$
Re_θ = momentum-thickness Reynolds number, $U_e\theta/\nu$
$R_{v'}$ = streamwise correlation of v' (Eq. (1))
S_{xy} = strain rate, $\frac{1}{2}(\partial u/\partial y)+(\partial v/\partial x)$
Sr_θ = instability Strouhal number of a planar free-shear layer, $f\theta/\Delta U$
$\mathrm{Sr}_{\theta s}$ = instability Strouhal number of a separation bubble, $f\theta_s/U_{es}$
t^* = normalized time, tU_∞/C
U = velocity magnitude
U_c = instability and spanwise-vortex convection speeds
ΔU = velocity difference across a planar free-shear layer
u = x-velocity component
v = y-velocity component
x = streamwise coordinate
y = wall-normal coordinate
δ = shear-layer thickness
δ^* = displacement thickness, $\int_0^\delta(1-(u/u_e))dy$
Λ_x = streamwise length scale
ν = kinematic viscosity
Ω_z = spanwise vorticity, $(\partial v/\partial x)-(\partial u/\partial y)$
Ω_z^* = nondimensional spanwise vorticity, $\Omega C/U_\infty$
θ = momentum thickness, $\int_0^\delta(u/u_e)(1-(u/u_e))dy$

Subscripts

e = boundary-layer edge
r = reattachment
s = separation
ts = transition onset
∞ = freestream condition

Superscripts

$'$ = fluctuation quantity

Mathematical Descriptions

$\langle a\rangle$ = ensemble average of variable $a=(1/N)\Sigma_i^N a_i$

References

[1] Dovgal, A. V., Kozlov, V. V., and Michalke, A., 1994, "Laminar Boundary Layer Separation: Instability and Associated Phenomena," Prog. Aerosp. Sci., **30**, pp. 61–94.
[2] Estevadeordal, J., and Kleis, S. J., 1999, "High-Resolution Measurements of Two-Dimensional Instabilities and Turbulence Transition in Plane Mixing Layers," Exp. Fluids, **27**, pp. 378–390.
[3] Ho, C., and Huerre, P., 1984, "Perturbed Free Shear Layers," Annu. Rev. Fluid Mech., **16**, pp. 365–424.
[4] Malkiel, E., and Mayle, R. E., 1996, "Transition in a Separation Bubble," ASME J. Turbomach., **118**, pp. 752–759.
[5] Spalart, P. R., and Strelets, M. K., 2000, "Mechanisms of Transition and Heat Transfer in a Separation Bubble," J. Fluid Mech., **403**, pp. 329–349.
[6] Yang, Z., and Voke, P. R., 2001, "Large-Eddy Simulation of Boundary-Layer Separation and Transition at a Change of Surface Curvature," J. Fluid Mech., **439**, pp. 305–333.
[7] Abdalla, I. E., and Yang, Z., 2004, "Numerical Study of the Instability Mechanism in Transitional Separating-Reattaching Flow," Int. J. Heat Fluid Flow, **25**, pp. 593–605.
[8] McAuliffe, B. R., and Yaras, M. I., 2005, "Separation-Bubble-Transition Measurements on a Low-Re Airfoil Using Particle Image Velocimetry," ASME Paper No. GT2005-68663.
[9] McAuliffe, B. R., and Yaras, M. I., 2008, "Transition Mechanisms in Separation Bubbles Under Low and Elevated Freestream Turbulence," ASME J. Turbomach., **130**, in press.
[10] Volino, R. J., 2002, "Separated Flow Transition Under Simulated Low-Pressure Turbine Airfoil Conditions: Part 1—Mean Flow and Turbulence Statistics," ASME J. Turbomach., **124**, pp. 645–655.
[11] McAuliffe, B. R., and Yaras, M. I., 2008, "Numerical Study of Instability

Mechanisms Leading to Transition in Separation Bubbles," ASME J. Turbomach., **130**, pp. 021006.
[12] Gad-el-Hak, M., 1990, "Control of Low-Speed Airfoil Aerodynamics," AIAA J., **28**, pp. 1537–1552.
[13] Howell, R. J., Ramesh, O. N., Hodson, H. P., Harvey, N. W., and Schulte, V., 2001, "High Lift and Aft-Loaded Profiles for Low-Pressure Turbines," ASME J. Turbomach., **123**, pp. 181–188.
[14] Lake, J. P., King, P. I., and Rivir, R. B., 2000, "Low Reynolds Number Loss Reduction on Turbine Blades With Dimples and V-Grooves," AIAA Paper No. 00-0738.
[15] Volino, R. J., 2003, "Passive Flow Control on Low-Pressure Turbine Airfoils," ASME J. Turbomach., **125**, pp. 754–764.
[16] Kerho, M., Hutcherson, S., Blackwelder, R. F., and Liebeck, R. H., 1993, "Vortex Generators Used to Control Laminar Separation Bubbles," J. Aircr., **30**, pp. 315–319.
[17] McAuliffe, B. R., 2003, "An Experimental Study of Flow Control Using Blowing for a Low-Pressure Turbine Airfoil," MS thesis, Carleton University, Ottawa, ON, Canada.
[18] Robarge, T. W., Stark, A. M., Min, S.-K., Khalatov, A. A., and Byerley, A. R., 2004, "Design Considerations for Using Indented Surface Treatments to Control Boundary Layer Separation," AIAA Paper No. 2004-425.
[19] Zhang, X.-F., and Hodson, H., 2005, "The Combined Effects of Surface Trips and Unsteady Wakes on the Boundary Layer Development of an Ultra-High-Lift LP Turbine Blade," ASME J. Turbomach., **127**, pp. 479–488.
[20] Zhang, X.-F., Vera, M., and Hodson, H., 2006, "Separation and Transition Control on an Aft-Loaded Ultra-High-Lift LP Turbine Blade at Low Reynolds Numbers: Low-Speed Investigation," ASME J. Turbomach., **128**, pp. 517–527.
[21] Bohl, D. G., and Volino, R. J., 2005, "Experiments With Three Dimensional Passive Flow Control Devices on Low-Pressure Turbine Airfoils," ASME Paper No. GT2005-68969.
[22] Merchant, A., 2003, "Aerodynamic Design and Performance of Aspirated Airfoils," ASME J. Turbomach., **125**, pp. 141–148.
[23] Bons, J. P., Sondergaard, R., and Rivir, R. B., 2001, "Turbine Separation Control Using Pulsed Vortex Generator Jets," ASME J. Turbomach., **123**, pp. 198–206.
[24] Bons, J. P., Sondergaard, R., and Rivir, R. B., 2002, "The Fluid Dynamics of LPT Blade Separation Control Using Pulsed Jets," ASME J. Turbomach., **124**, pp. 77–85.
[25] Culley, D. E., Bright, M. M., Prahst, P. S., and Strazisar, A. J., 2004, "Active Flow Separation Control of a Stator Vane Using Surface Injection in a Multistage Compressor Experiment," ASME J. Turbomach., **126**, pp. 24–34.
[26] McAuliffe, B. R., and Sjolander, S. A., 2004, "Active Flow Control Using Steady Blowing for a Low-Pressure Turbine Cascade," ASME J. Turbomach., **126**, pp. 560–569.
[27] Hanff, E. S., 2004, "PIV Application in Advanced Low Reynolds Number Facility," IEEE Aerosp. Electron. Syst. Mag., **40**, pp. 310–319.
[28] Bao, F., and Dallmann, U. C., 2004, "Some Physical Aspects of Separation Bubble on a Rounded Backward-Facing Step," Aerosp. Sci. Technol., **8**, pp. 83–91.
[29] Saric, W. S., Reed, H. L., and Kerschen, E. J., 2002, "Boundary-Layer Receptivity to Freestream Disturbances," Annu. Rev. Fluid Mech., **34**, pp. 291–319.
[30] Scarano, F., and Riethmuller, M. L., 2000, "Advances in Iterative Multigrid PIV Image Processing," Exp. Fluids, **29**, pp. S51–S60.
[31] Westerweel, J., 2000, "Theoretical Analysis of the Measurement Precision in Particle Image Velocimetry," Exp. Fluids, **29**, pp. S3–S12.
[32] Stanislas, M., Okamoto, K., and Kähler, C. J., 2003, "Main Results of the First International PIV Challenge," Meas. Sci. Technol., **14**, pp. R63–R89.
[33] Stanislas, M., Okamoto, K., and Kähler, C. J., 2005, "Main Results of the Second International PIV Challenge," Exp. Fluids, **39**, pp. 170–191.
[34] Raffel, M., Willert, C., and Kompenhans, J., 1998, "Particle Image Velocimetry: A Practical Guide," *Experimental Fluid Mechanics*, Springer-Verlag, Berlin.
[35] Meunier, P., and Leweke, T., 2003, "Analysis and Treatment of Errors Due to High Velocity Gradients in Particle Image Velocimetry," Exp. Fluids, **35**, pp. 408–421.
[36] Hall, S. D., Behnia, M., Fletcher, C. A. J., and Morrison, G., 2003, "Investigation of the Secondary Corner Vortex in a Benchmark Turbulent Backward-Facing Step Using Cross-Correlation Particle Imaging Velocimetry," Exp. Fluids, **35**, pp. 139–151.
[37] Schlichting, H., and Gersten, K., 2000, *Boundary Layer Theory*, 8th ed., Springer-Verlag, Berlin.
[38] Rist, U., and Maucher, U., 2002, "Investigations of Time-Growing Instabilities in Laminar Separation Bubbles," Eur. J. Mech. B/Fluids, **21**, pp. 495–509.
[39] Kelly, R. E., 1967, "On The Stability of an Inviscid Shear Layer Which is Periodic in Space and Time," J. Fluid Mech., **27**, pp. 657–689.
[40] Wissink, J. G., and Rodi, W., 2002, "DNS of Transition in a Laminar Separation Bubble," *Advances in Turbulence IX, Proceedings of the Ninth European Turbulence Conference*, Southampton, UK., I. P. Castro, and P. E. Hancock, eds.
[41] White, F. M., 1991, *Viscous Fluid Flow*, 2nd ed., McGraw-Hill, Boston.
[42] Panton, R. L., 2001, "Overview of the Self-Sustaining Mechanisms of Wall Turbulence," Prog. Aerosp. Sci., **37**, pp. 341–383.
[43] Ho, C., and Huang, L. S., 1982, "Subharmonics and Vortex Merging in Mixing Layers," J. Fluid Mech., **119**, pp. 443–473.
[44] Alam, M., and Sandham, N. D., 2000, "Direct Numerical Simulation of 'Short' Laminar Separation Bubbles With Turbulent Reattachment," J. Fluid Mech., **403**, pp. 223–250.
[45] Roberts, S. K., and Yaras, M. I., 2005, "Modeling Transition in Separated and Attached Boundary Layers," ASME J. Turbomach., **127**, pp. 402–411.
[46] Praisner, T. J., and Clark, J. P., 2007, "Predicting Transition in Turbomachinery, Part I—A Review and New Model Development," ASME J. Turbomach., **129**, pp. 1–13.
[47] Lang, M., Rist, U., and Wagner, S., 2004, "Investigations on Controlled Transition Development in a Laminar Separation Bubble by Means of LDA and PIV," Exp. Fluids, **36**, pp. 43–52.

PIV-POD Investigation of the Wake of a Sharp-Edged Flat Bluff Body Immersed in a Shallow Channel Flow

Arindam Singha
Department of Mechanical Engineering,
University of Windsor,
Windsor, N9B 3P4, Canada
e-mail: singha2@uwindsor.ca

A.-M. Shinneeb
e-mail: shinneeb@uwindsor.ca

Ram Balachandar
e-mail: rambala@uwindsor.ca

Department of Civil and Environmental Engineering,
University of Windsor,
Windsor, N9B 3P4, Canada

This paper reports particle-image velocimetry measurements of instantaneous velocity fields in the wake of a sharp-edged bluff body immersed vertically in a shallow smooth open channel flow. The maximum flow velocity was 0.19 m/s and the Reynolds number based on the water depth was 18,270. The purpose of the present study is to show the vertical variation of the velocity field in the near region of a shallow wake. Measurements of the flow field in the vertical central plane and in the horizontal near-bed, mid-depth, and near-surface planes were taken. Then, the mean flow quantities such as the mean velocity, turbulence intensity, and Reynolds stress fields were investigated. In addition, the proper orthogonal decomposition technique was used to reconstruct the velocity fields to investigate the energetic vortical structures. The results showed that the largest recirculation zone in the mean velocity fields occurred in the mid-depth velocity field, while the smallest one occurred near the bed. Also, the fluid was entrained from the sides toward the wake central plane in the three horizontal velocity fields but with different rates. This behavior was attributed to the existence of quasi-streamwise vortices near the boundaries. In addition, patterns of ejection and sweep events near the free surface similar to the features commonly observed near the wall-bounded flows were observed.
[DOI: 10.1115/1.3054283]

1 Introduction

Turbulent shallow flows such as jets, mixing layers, and wakes are commonly encountered in nature. Among them is the shallow wake flow, which has been studied less frequently than the unbounded (deep) wake. Shallow wakes are generated by flow past bluff objects placed in a body of fluid of finite depth. They are characterized by the proximity of a bottom solid wall and top free surface, while the horizontal extent can be considered infinite. Jirka and Uijttewaal [1] defined shallow flows as bounded flows in which the dimension in any two directions greatly exceeds the third dimension. Flow past bridge piers, mountains, and islands are some examples that are frequently observed in geophysical and atmospheric flows. Cooling flow over small heated electronic chips of a computer motherboard also generates shallow wakes [2]. In addition, density stratification in the vertical direction sometimes causes creation of shallow wakes [3]. The wide range of practical applications motivated a number of researchers to investigate shallow wakes (see Refs. [1,4]) because understanding the flow characteristics of shallow wakes would help predict the optimal positioning of pollutant discharge facilities to enable quick diffusion, control of sedimentation and biological activities, and design more effective heat transfer models.

A flow past unbounded bluff bodies is characterized by a periodic formation of the well-known von Karman vortex street, which sheds alternatively from the sides of the body into two staggered rows of vortices with opposite rotational sense. This type of wake flow was investigated extensively experimentally by Okajima [5], Roshko [6], Lyn et al. [7], and Chen and Liu [8], as well as numerically by Beaudan and Moin [9] and Dong et al. [10], in addition to others.

The physics of the wake flow of vertical bodies in a junction flow of a large depth is available in literature. Logory et al. [11] investigated the interaction of a bluff-body wake with the free surface and found that the wake width was nearly doubled close to the free surface. The presence of numerous surface-parallel and surface-normal vortices near the free surface, which enhanced mixing near the free surface, was also observed. Lawless et al. [12] studied the instantaneous patterns of flow structure past a surface-mounted cube and cylinder. It was observed that the junction region involves a highly dynamic vortex system and that the primary vortex exhibited a periodic orbital motion, in conjunction with patterns of unsteady flow down of the body. The turbulence characteristics and separation phenomena near a wing-plate junction were investigated experimentally by Devenport and Simpson [13]. A variety of ordered patterns of horseshoe vortices was calculated numerically at low Reynolds number by Visbal [14]. Seal et al. [15] found that the vortical flow pattern at the junction of a rectangular bluff body with a solid surface is characterized by unsteady formation and translation of vortices toward the body, which interacted with the existent corner vortex.

The extensive literature and review articles available about deep-flow wakes provide some measure of understanding of the characteristics of shallow wakes (see Refs. [16–18]). However, the simultaneous presence of the bounding surfaces (free surface and solid wall) makes this problem unique. For instance, the effect of the bounding surfaces imposes two different effects on the shallow wakes. First, the limited water depth causes the von Karman vortex shedding to be seen for a larger range of Reynolds number compared with the deep-flow wakes. Second, bottom friction acts as a mechanism for suppression of the vertical growth of the three-dimensional instabilities originating from the wake. Chen and Jirka [19] noted that the mechanism of vortex stretching does not affect eddies of sizes comparable to the depth of the flow. It was argued that the resulting wake will carry dual characteristics—the structures of scales greater than the water depth exhibit inverse cascade in the spectral analysis, which is an indication of the two-dimensional turbulence. On the other hand,

Contributed by the Fluids Engineering Division of ASME for publication in the JOURNAL OF FLUIDS ENGINEERING. Manuscript received November 1, 2007; final manuscript received June 22, 2008; published online January 9, 2009. Assoc. Editor: Juergen Kompenhans.

the structures of scale smaller than the flow depth demonstrate the behavior of three-dimensional turbulence. Ingram and Chu [20] investigated the spreading characteristics of shallow wakes around the islands in Rupert Bay, Canada. They proposed a stability parameter $S=C_fB/H$, where C_f is the friction coefficient, B is the characteristic length scale of the bluff body, and H is the depth of the shallow water layer. Physically, this parameter can be understood as the relative impact of two effects: the stabilizing effect of the bottom friction and the destabilizing effect of the lateral shear originating from the sides of the body. If the stability parameter is less than a critical value ($S_c \approx 0.48$ as reported in Ref. [20]), the von Karman type of wake with alternate vortex shedding from both sides of the body is expected. On the other hand, for high enough stability parameter, the shear layer generated at the sides of the bluff body gets stabilized by the effect of bottom friction. Chen and Jirka [19] experimentally investigated the characteristics of shallow wakes generated by bluff bodies of different shapes (e.g., cylinder, flat plate, and porous plate) in a large water flume. In all the cases, the body was inserted vertically inside the flow. Based on their visualization study, three different types of wake were distinguished based on the stability parameter: vortex-street-like wake for $S \leq 0.2$, unsteady-bubble wake for $0.2 \leq S \leq 0.5$, and steady-bubble wake for $S \geq 0.5$. The most unstable wake was the vortex-street-like wake, which is qualitatively similar to the von Karman wake.

Balachandar et al. [21] investigated the effect of flow depth and bluff-body width on the concentration and velocity distribution in a shallow wake. Based on the findings, the shallow wake was reclassified into two groups: deep-shallow wake and shallow-shallow wake, depending on the value of the wake stability parameter. In the deep-shallow wake, continuous Karman vortex street was observed, and the structure of the flow was qualitatively similar to conventional deep wake. But in the shallow-shallow wake, the vortex street was found to be either completely absent or intermittent. Akilli and Rockwell [22] investigated the near wake of a circular cylinder in a shallow flow by means of flow visualization and a particle-image velocimetry (PIV). They reported mean velocity, vorticity, Reynolds stress, and streamline topology results at three vertical locations—near-bed, mid-depth, and near-surface planes. It was concluded that the vortex formation in the near-wake region is a highly three-dimensional process. In the near-bed region, the streamline topology resembles a form known as owl face of the first kind [23]. Lin et al. [24] investigated the flow past a confined cylinder placed in a rectangular duct by flow visualization, laser-Doppler anemometry (LDA), and the PIV technique. The results indicated the existence of several concentrated vortices in the boundary layer region. Fu and Rockwell [25] experimentally investigated the development of the horseshoe vortex system and the interaction of these vortices with the generated vortices (from the body sides) close to the wall. Their findings indicate that the near-wake flow instability is triggered by the instability of the upstream horseshoe vortex.

An up-to-date literature survey suggests that the effects of the shallowness on the near-wake flow region of bluff bodies are incomplete at best, although this problem is encountered in many practical applications. This paper reports PIV measurements of a wake flow generated by a vertical sharp-edged flat plate in a shallow channel flow. The purpose of the present study is to highlight the vertical variations in the flow field throughout a shallow flow layer in the near-wake region by studying the behavior of mean flow quantities and large-vortical structures.

2 Apparatus

The present experiments were conducted in a recirculating open water channel of rectangular cross section. The dimensions of the channel are 9.50 m long, 1.20 m wide, and 0.58 m deep. The side walls and the bottom of the flume were made up of Plexiglas to allow measurements of the flow field using the PIV technique. The mean freestream velocity (U_∞) of the channel flow was 0.19 m/s. The depth of the water H in the channel was controlled using a tailgate and maintained constant at ~103 mm. The corresponding Reynolds number Re_H and Froude number Fr_H were 18,270 and 0.19, respectively. A flow conditioner consisting of flow straighteners and wire screens were placed at the entrance of the channel to reduce turbulence. The straighteners were made up of plastic straws with a length to diameter ratio of 40, while the wire screens, which have a mesh size of 6.25 mm, were placed immediately upstream and downstream of the straighteners. Measurements were performed at 4.9 m downstream of the flow conditioner. To ensure fully-developed turbulent flow in the measurement area, the near wall flow was tripped using a 25 mm wide sand strip spanning the entire channel width and was positioned at 3 m upstream of the measurement station.

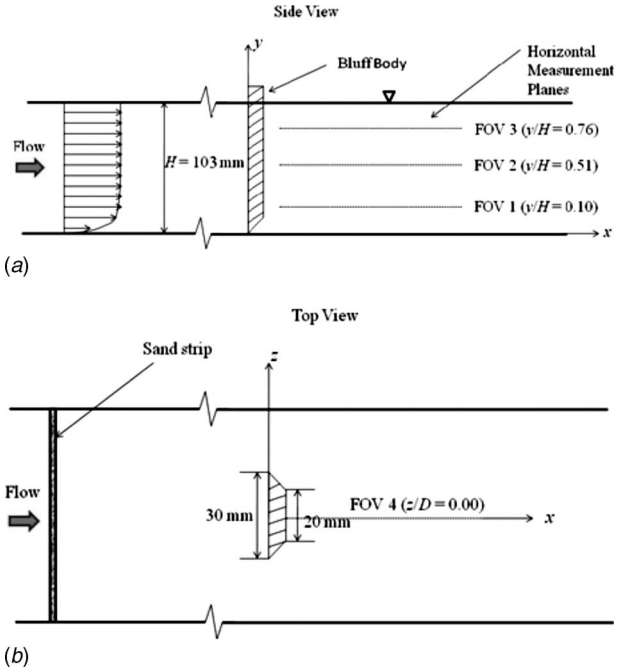

Fig. 1 Schematic showing (*a*) side view and (*b*) top view of the bluff body in the flume and the position of the four fields-of-view (not to scale)

The bluff body used in the present study was a sharp-edged flat plate 110 mm in height, 30 mm in width, and 6 mm in thickness, as shown in Figs. 1(*a*) and 1(*b*). The bluff body was designed to have a flat shape on the upstream side while it was chamfered at the edges in the downstream side. The body was inserted vertically in the channel flow, as shown in Fig. 1, and supported by a steel bar from the top of the flume (not shown). The bluff body was in physical contact with the solid bed and projects out of the free surface.

The coordinate system adopted in this study is also shown in Fig. 1. The origin of the coordinate system is located at the intersection of the vertical line-of-symmetry of the bluff body with the bed of the flume. The positive x-direction represents the distance measured along the channel flow starting from the origin at the upstream face of the bluff body and will be referred to as the streamwise direction. The positive y-direction, measured from the bed of the flume, represents the vertical direction. A right-hand rule was adopted for the coordinate system, and the z-direction was defined accordingly. The z-direction will be referred to as the transverse direction hereafter.

3 PIV System and Post-Processing Analysis

The PIV system incorporated 140 mJ/pulse dual Nd:YAG (yttrium aluminum garnet) lasers of 532 nm wavelength generated

Table 1 Summary of the characteristics of the velocity fields

FOV	Location along x-axis (mm)	Image size (mm^2)	Spatial resolution (mm)	Time separation (ms)
		Horizontal (x,z) fields-of-view		
1	49.8	91.0×91.0	0.716	1.4
2	36.4	97.8×97.8	0.770	1.3
3	54.4	103.6×103.6	0.815	1.6
		Vertical (x,y) fields-of-view		
4	48.7	98.9×98.9	0.778	1.8

from a New Wave Research Solo PIV. The laser sheet was formed through a 500 mm or 1000 mm spherical lens and a −15 mm or −25 mm cylindrical lens depending on the desired size of the field-of-view (FOV). The resulting light sheet was approximately 1 mm thick in the area of interest. The light sheet was oriented vertically or horizontally according to the desired measurement plane. The vertical orientation of the light sheet included the vertical central plane (FOV4) while the horizontal orientation included the horizontal mid-depth plane (FOV2), a plane near the bed (FOV1), and a plane near the free surface (FOV3) (see Fig. 1). The light sheet entered either from the side or underneath the flume while the optical axis of the camera was positioned perpendicular to it. The water in the flume was seeded with hollow-glass-bead seed particles after filtering the water through a 5 μm filter. These seed particles have a specific gravity of 1.1 and a mean diameter of 12 μm, and thus they have the ability to faithfully follow the water flow.

The velocity fields were measured using a 2048×2048 pixels TSI PowerView Plus 4 MP camera with a pixel size of 7.4×7.4 μm^2 and provides 12 bit output. Two thousand image pairs were acquired at each location at a framing rate of 1.04 Hz. A TSI PIV LaserPulse synchronizer was used to synchronize the operation of the camera with the laser. The camera was fitted with a 60 mm Micro-Nikkor or a 28–105 mm Zoom-Nikkor lens according to the object's distance, which was adjusted to give the required field-of-view. Image calibration was achieved by taking a picture of a steel ruler with 0.1 mm divisions. It was confirmed that there was negligible distortion over the field-of-view.

Image analysis was performed with correlation analysis INSIGHT 3G® software developed by TSI. The images were analyzed with 32×32 interrogation areas using a fast Fourier transform (FFT) correlator. The interrogation areas were overlapped by 50%. The correlation peak was located within subpixel accuracy using a Gaussian curve-fitting method. This analysis process yielded a final interrogation area size of 16×16 pixels. Table 1 summarizes the size and the resulting spatial resolution of the velocity fields reported in this paper. Note that the first column *Location along x-axis* represents the streamwise distance from the bluff body to the left edge of the field-of-view. Following the correlation analysis, outliers were rejected using the cellular neural network method with a variable threshold technique, as proposed by Shinneeb et al. [26]. The percentage of vectors rejected varied from 3% to 8% primarily at the edges of the velocity fields. Rejected vectors were replaced using a Gaussian-weighted mean of their neighbors.

The uncertainty of the current measurements was assessed by measuring the size of the particle images in the PIV images using MATROX INSPECTOR® software. The mean particle-image size was found to be approximately 3.8 pixels. Prasad et al. [27] showed that when the ratio of particle-image diameter to the pixel size is $d_{par}/d_{pix}>3-4$, the uncertainty of the measurements is roughly 0.05–0.10 of the particle-image diameter. Since the maximum pixel displacement in this study is 8 pixels, the relative uncertainty is assessed to be in the range 2.4–4.8%, which are equivalent to 0.19–0.38 pixels.

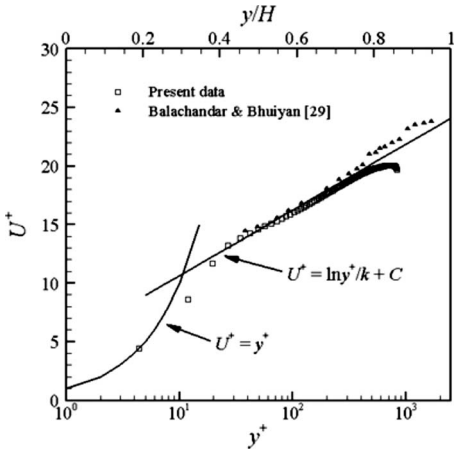

Fig. 2 Mean streamwise velocity distribution of the smooth channel flow using inner and outer coordinates

4 Results and Discussions

4.1 Mean Velocity Field of the Smooth Channel Flow. The purpose of this section is to provide a comparison of the present data with well-documented channel flow results in order to validate the quality of the PIV data. For this reason, the velocity field of the channel flow was measured along the vertical central plane of the flume before inserting the bluff body. The mean freestream velocity (U_∞) of the channel flow was 0.19 m/s. The boundary layer thickness δ was estimated (based on $0.995U_\infty$) to occupy ~80% of the shallow water layer H.

Although the resolution of the current PIV data is high, few data points in the thin viscous sublayer were missing. For this reason, a sixth order polynomial curve was used to fit the mean velocity profiles and generate the missing data points. The goodness-of-fit was assessed from the correlation coefficient of the least-square polynomial fit and was found to be 0.9982. The displacement thickness (δ^*) and momentum thickness (θ) were then estimated by integrating the velocity data using Simpson's one-third rule and found to be 8.7 mm and 5.4 mm, respectively. The resulting shape factor was 1.6 and the Reynolds number based on the momentum thickness (Re_θ) was 986.

Figure 2 shows the mean velocity distribution in the channel flow in terms of the wall velocity U^+ ($=U/u_\tau$) and both inner y^+ ($=yu_\tau/\nu$) and outer y/H vertical axes. The data were fitted with the well-recognized logarithmic velocity profile [28]

$$U^+ = \frac{1}{k}\ln y^+ + C \tag{1}$$

where k is the von Karman constant (=0.41) and C is a constant (≈5.2). The present channel flow data were also compared with the experimental data of Balachandar and Bhuiyan [29] for smooth channel flow at a Reynolds number, based on the depth of the flow, Re_H=51,000. Both theoretical and experimental data exhibit good agreement with the present channel flow data. The deviation of the present PIV data for $y/H>0.8$ may be attributed to the effect of the free surface on the velocity profile compared with the experimental unbounded case shown in the same figure. The friction velocity u_τ, defined as $\sqrt{\tau_w/\rho}$, was determined by the Clauser chart method [30], which is based on the assumption that the velocity profile follows a universal logarithmic form in the overlap region of the boundary layer. In this study, the friction velocity u_τ was estimated to be 9.5 mm/s. The corresponding skin friction coefficient C_f, defined by $2(u_\tau/U_\infty)^2$, was found to be

0.005. The viscous length scale l_v, defined by (ν/u_τ), (where ν is the kinematic viscosity of the fluid) was estimated to be 0.1 mm, which is approximately seven to eight times smaller than the spatial resolution of the present data (see Table 1).

4.2 Mean Velocity Field of the Wake Flow. This section describes the mean velocity field of the shallow wake behind the bluff body. The stability parameter S of the current wake flow was estimated to be 0.0015. This result indicates that the bottom friction is not dominated compared with the effect of the free-surface boundary, as in extreme shallow cases [31]. At this particular stability parameter, the shallow wake is expected to be a vortex-street type according to the classification of Chen and Jirka [19]. As illustrated by Balachandar et al. [21], this region of the wake corresponds to deep-shallow wake.

To have a clear perception of the differences of the wake flow in the three horizontal velocity fields, the streamline patterns of the mean velocity fields are shown in Fig. 3. The size and spatial resolution of these fields-of-view are given in Table 1 (see FOV1, 2, and 3). In these plots, the width of the body D (=30 mm) is used as a normalizing length scale. Figures 3(*a*)–3(*c*) show the existence of recirculation flow regions behind the bluff body, where the flow is positive at the outer edges of the fields-of-view and negative (reversed) near the vertical central plane $(z/D=0)$. In all cases, the wake appears almost symmetric about the x-axis. However, the size of the recirculation (wake) zones is different in the three fields. By comparing the three plots shown in Fig. 3, it is clear that the size of the recirculation zones in the mid-depth plane $(y/H=0.51)$ shown in Fig. 3(*b*) is larger compared with the zones in the near-bed $(y/H=0.10)$ and near-surface $(y/H=0.76)$ planes. The recirculation regions in the three cases appear to extend in the streamwise direction to $x/D\approx 2.5$, 4.0, and 3.3, corresponding to the horizontal velocity fields at $y/H=0.10$, 0.51, and 0.76, respectively. These differences are a clear indication of the three-dimensionality of the near-wake flow structure as a result of the distribution of the vortical structures throughout the water layer [32] (see Sec. 4.7).

The mode of instability of the current shallow wake can be assessed by defining the velocity deficit parameter R (see Refs. [31,33]): $R=(\langle u_r\rangle - U_\infty)/(\langle u_r\rangle + U_\infty)$, where $\langle u_r\rangle$ is the reverse velocity in the recirculation zone measured at the vertical central plane $(z/D=0)$, and U_∞ is the freestream velocity. Chen and Jirka [19] gave R values for a shallow wake (generated by a cylinder) based on the maximum reverse velocity measured at the mid-depth plane. To illustrate the vertical variation of the recirculation zones in the present data, the reverse velocity at the streamwise location $x/D=2$ is used as a basis for the comparison, which represents the location of the maximum value of $\langle u_r\rangle$ for the mid-depth plane. It is found that $\langle u_r\rangle=-0.014$, -0.060, and -0.041, corresponding to the vertical locations $y/H=0.10$, 0.51, and 0.76, respectively. According to the above relation, the corresponding values of velocity deficit parameter are $R=-1.16$, -1.92, and -1.55, respectively. Chen and Jirka [19] reported $R=-2.07$ for the case of unsteady-bubble and vortex-street modes of a shallow wake, and $R=-2.03$ for the case of an unbounded wake. By comparing the values of R with the present data, it can be observed that the recirculation zone in the mid-depth plane $(R=-1.92)$ seems to be more similar to the deep wake compared with the near-boundary planes.

4.3 Mean Velocity Profiles. More insight into the flow characteristics can be obtained by extracting the velocity profiles at specific downstream locations. Figure 4 shows the development of the mean streamwise velocity U profiles in the streamwise direction for the three horizontal planes $(y/H=0.10$, 0.51, and 0.76, respectively). The velocity profiles are normalized by the mean streamwise velocity U_s (U_s=0.147 m/s, 0.186 m/s, and 0.190 m/s, respectively) at the corresponding vertical location y/H of the channel flow without the body and plotted against the horizontal location z normalized by the width of the body D. In these figures, the velocity profiles are plotted at streamwise locations $x/D=2.5$, 3.5, and 4.5. Note that only every second point on the velocity data is shown to avoid cluttering.

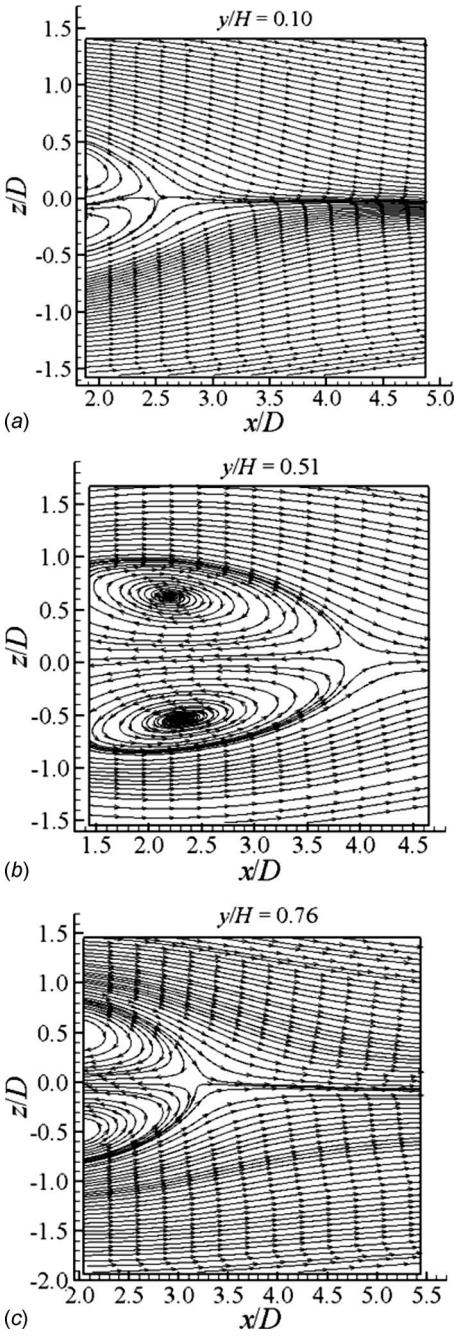

Fig. 3 Streamline patterns of the mean velocity fields in the wake of the bluff body for three horizontal planes: (*a*) *y*/*H* =0.10, (*b*) *y*/*H*=0.51, and (*c*) *y*/*H*=0.76

Figures 4(*a*)–4(*c*) show that all velocity profiles in the three planes are generally symmetrical about the vertical central plane $(z/D=0)$. These figures also show that the behavior of the velocity profiles may be divided into two regions: inner and outer. The points that demarcate the inner region from the outer region (labeled P and Q) are located at $|z/D|=0.74$, 0.99, and 0.97, which correspond to velocity fields shown in Fig. 4(*a*)–4(*c*), respectively. The location of these points also illustrates that the largest wake occurs in the mid-depth case $(y/H=0.51)$. The corresponding magnitude of the normalized streamwise velocities at these points

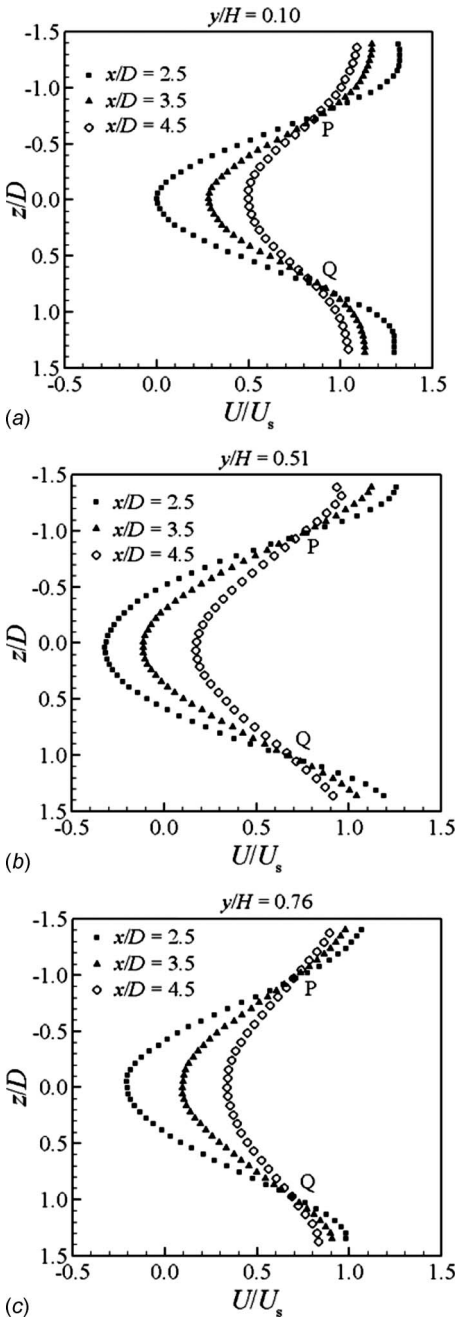

Fig. 4 Development of the mean streamwise velocity U/U_s in the streamwise direction x/D at different horizontal planes: (*a*) $y/H=0.10$, (*b*) $y/H=0.51$, and (*c*) $y/H=0.76$

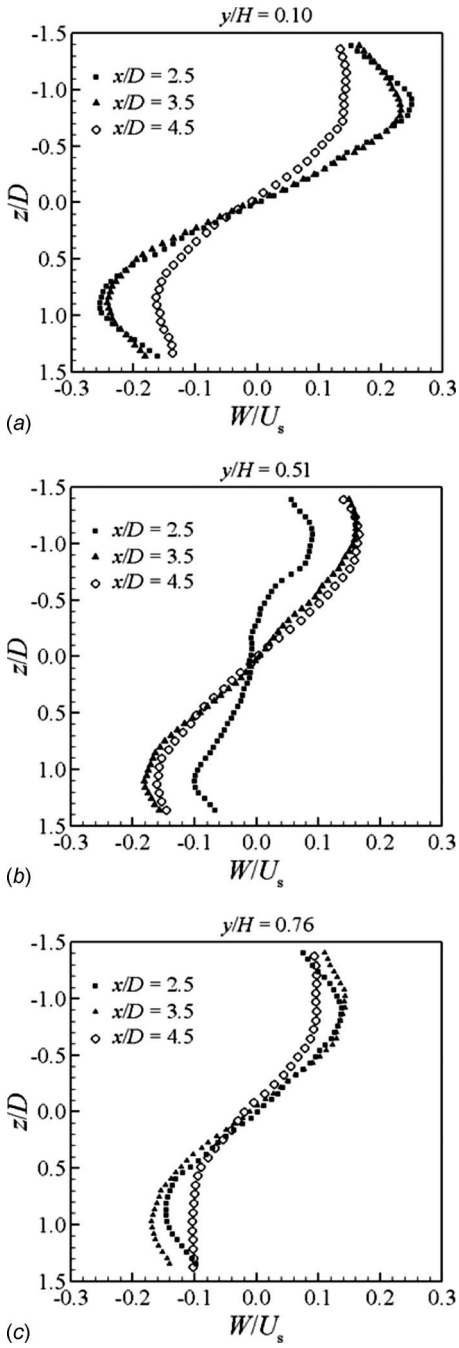

Fig. 5 Development of the mean transverse velocity W/U_s in the streamwise direction x/D at different horizontal planes: (*a*) $y/H=0.10$, (*b*) $y/H=0.51$, and (*c*) $y/H=0.76$

is $U/U_s=0.86$, 0.74, and 0.70, respectively. The mean streamwise velocity U profiles in the inner region ($|z/D| \leq 0.74$, 0.99, and 0.97) demonstrate an increasing trend of the velocity in the streamwise direction with a corresponding decrease in the outer region.

The mean transverse velocity W profiles for the three horizontal planes at $y/H=0.10$, 0.51, and 0.76 are shown in Figs. 5(*a*)–5(*c*), respectively. The velocity W and the horizontal locations z are also normalized by U_s and D, respectively. All figures show that the velocity is inward toward the vertical central plane at all streamwise locations ($x/D=2.5$, 3.5, and 4.5). The magnitude of the maximum velocity $|W/U_s|$ at $x/D=2.5$ is approximately 0.25, 0.10, and 0.14, which occurs at $|z/D| \approx 0.91$, 1.06, and 0.98, respectively. Figures 5(*a*) and 5(*c*) show that the velocity profiles of the near-bed and near-surface cases at $x/D=2.5$ and 3.5 are almost similar, but the velocity profiles seem to decrease at $x/D=4.5$. The maximum magnitude of the inward velocity toward the vertical central plane at $x/D=4.5$ in these cases are $|W/U_s|=0.16$ and 0.10 located at $|z/D|=0.82$ and 0.90, respectively. In contrast to the above behavior, Fig. 5(*b*) shows that the transverse inward flow in the mid-depth plane increased from $x/D=2.5$ to 3.5, then became constant from $x/D=3.5$ to 4.5.

To help the reader have a global view of the flow pattern under investigation, a vector plot of the mean velocity field in the three horizontal planes are shown in Fig. 6 superimposed by a gray contour of the mean transverse velocity W/U_s. In summary, the above results indicate that the transverse velocity W/U_s profiles in

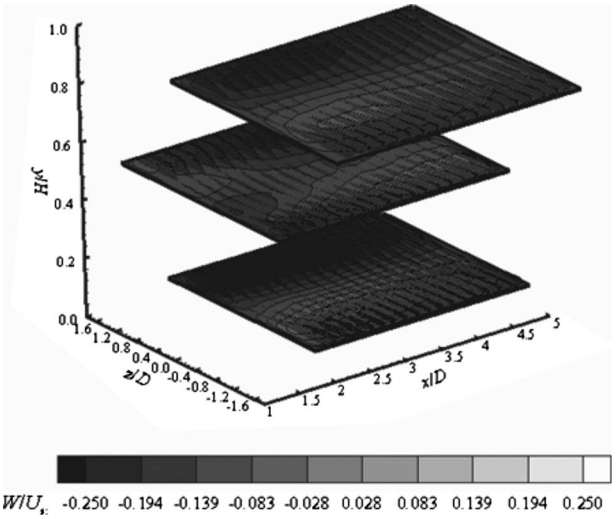

Fig. 6 A vector plot representing the mean flow field in the three horizontal planes (y/H=0.10, 0.51, and 0.76) superimposed by a gray contour of the normalized mean transverse velocity W/U_s

the near-bed and near-surface planes developed faster than the velocity profiles in the mid-depth plane. In addition, the profiles in the near-bed case indicate that the inward flow is enhanced compared with the near-surface case. The differences between the near-bed and near-surface profiles may be attributed to the formation/distribution of secondary vortices that may be developed near the boundaries. This issue will be discussed in Sec. 4.7.

4.4 Variation of the Streamwise Velocity in the Central-Plane of the Wake. The variation of the mean streamwise velocity in the central-plane (z/D=0) of the wake (U_c) with the streamwise distance x is shown in Fig. 7. This figure shows three curves extracted from the horizontal velocity fields at vertical locations y/H=0.10, 0.51, and 0.76, respectively. In this figure, the mean central velocity U_c (will be referred to as the central velocity hereafter) and the streamwise distance x are normalized by U_s and D, respectively. The central velocity U_c was obtained by fitting the horizontal profiles of the mean streamwise velocity U with a tenth order polynomial curve. Figure 7 illustrates that the streamwise location where the central velocity U_c becomes zero is at x/D =2.4, 3.9, and 3.1 corresponding to y/H=0.10, 0.51, and 0.76, respectively. U_c/U_s appears to vary linearly with x/D at a relatively high rate in the range $2.5 \le x/D \le 4.0$. However, U_c/U_s for the y/H=0.51 case appears to vary at a much slower rate in the

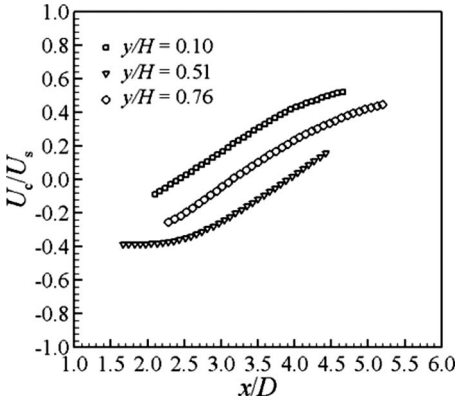

Fig. 7 Variation of the normalized mean central velocity U_c/U_s with downstream distance x/D

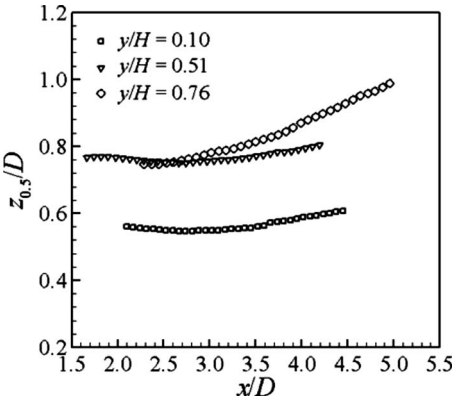

Fig. 8 Variation of the wake half-width $z_{0.5}/D$ with downstream distance x/D

range $x/D \le 2.5$ compared with the downstream rate. This is consistent with the relatively larger size of the recirculation zone at this vertical location compared with the other cases. Also, the rate of increase in U_c for the y/H=0.10 and 0.76 cases becomes slower and nonlinear for $x/D \ge 4.0$.

4.5 Half-Width of the Wake. The half-width of wake is defined as the transverse location z where the velocity defect Δu ($=U-U_s$) equals half of the maximum velocity defect $\Delta u_{\max}$. In this paper, $\Delta u_{\max}$ is defined as (U_c-U_s), where U_s represents the streamwise velocity at a corresponding vertical location without the body and U_c is the central velocity.

Figure 8 shows the variation of the wake half-width $z_{0.5}$ with the streamwise distance x at three vertical locations y/H=0.10, 0.51, and 0.76. Both half-width and the streamwise distance are normalized by the width of the bluff body D. The half-width $z_{0.5}$ appears to be constant in the beginning for y/H=0.10 and 0.51. Then they appear to spread nonlinearly in the streamwise direction. The growth rate of the near-surface (y/H=0.76) curve is also nonlinear, but appears higher compared with the other curves at these locations. This figure illustrates that the streamwise velocity U profiles is narrower in the near-bed plane compared with the other planes (see Fig. 4). Physically, the differences in the size of the recirculation zones may be explained by the differences in the entrainment rates (see Fig. 5) as a result of the distribution of the vortical structures throughout the water depth (see Sec. 4.7).

4.6 Turbulent Parameters. The development of the streamwise root-mean-square (rms) velocity $U_{\rm rms}$ in the streamwise direction x extracted from the horizontal velocity fields at y/H =0.10, 0.51, and 0.76 are shown in Figs. 9(*a*)–9(*c*), respectively. In this figure, $U_{\rm rms}$ is normalized by the upstream velocity U_s and x is normalized by the width of the bluff body D. Generally, the distribution of the $U_{\rm rms}$ velocity profiles in the three planes appear symmetrical about the vertical central plane (z/D=0) with two distinct peaks.

Figure 9(*a*) shows the streamwise root-mean-square velocity $U_{\rm rms}$ profiles extracted from the near-bed plane (y/H=0.10) at streamwise locations x/D=2.5, 3.5, and 4.5. The peaks of $U_{\rm rms}/U_s$ profiles at streamwise locations x/D=2.5 and 3.5 are approximately 0.39 and 0.35, respectively, which occurs at $|z/D| \approx 0.6$ and 0.5, while the minimum values are approximately 0.34 and 0.32. This figure shows that, as the flow proceeds downstream, the magnitude of $U_{\rm rms}$ in the core region ($|z/D|<1$) decreases with a relatively high rate until the profile becomes almost flat at x/D=4.5 ($U_{\rm rms}/U_s \approx 0.29$). For the region $|z/D|>1$, the change in $U_{\rm rms}/U_s$ is negligible. Generally, the streamwise turbulence intensity $U_{\rm rms}$ tends to approach zero in the outer region of the wake flow.

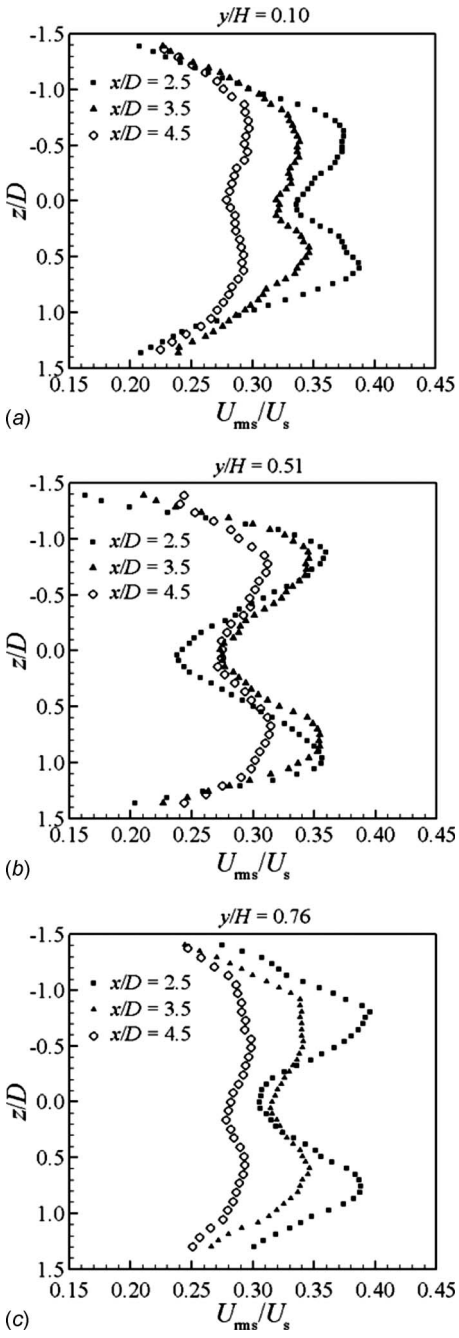

Fig. 9 Development of the relative streamwise root-mean-square velocity U_{rms}/U_s in the normalized streamwise direction x/D for horizontal planes at (*a*) $y/H=0.10$, (*b*) $y/H=0.51$, and (*c*) $y/H=0.76$

Figure 9(*b*) shows that the relative streamwise rms velocity U_{rms}/U_s profiles in the mid-depth plane ($y/H=0.51$) appear different compared with the profiles shown in Fig. 9(*a*). Although the shape of the profiles consists of two off-axis peaks and a valley, as in the previous case, the profile at $x/D=2.5$ has a much larger valley than the previous case where the minimum magnitude occurs at $z/D=0$. The peaks of this U_{rms}/U_s profile are 0.36, which occur at $|z/D|\approx 0.9$, while the magnitude of the minimum value is ~ 0.24. This distribution indicates that the recovery of the flow kinetic energy behind the bluff body is slower compared with the near-boundary planes. Further downstream, this figure shows that there is an increase in the streamwise rms velocity U_{rms} near the vertical central plane ($z/D=0$) with a corresponding decrease in the peak values.

The profiles shown in Fig. 9(*c*) illustrate the behavior of the streamwise rms velocity U_{rms} in the near-surface plane ($y/H=0.76$). Although the peaks of the U_{rms}/U_s profile at $x/D=2.5$ is comparable to the previous cases at the same location ($U_{rms}/U_s \approx 0.39$ at $|z/D|\approx 0.85$), the minimum value ($U_{rms}/U_s \approx 0.31$), which occurs at $z/D=0$, is smaller than the value shown in Fig. 9(*a*), but larger than the value shown in Fig. 9(*b*). This indicates that the recovery of U_{rms} in this plane is slower than the near-bed case, but faster than the mid-depth case. At locations farther downstream, the development of the U_{rms}/U_s profiles in the streamwise direction is similar to the near-bed case, where the off-axis peaks decrease while U_{rms} near $z/D=0$ increases then decreases. The relative streamwise rms velocity U_{rms}/U_s at $x/D=4.5$ appears to approach a flat shape in the core region ($|z/D|<0.95$) with a magnitude equal to ~ 0.29 and approaches zero in the outer region of the wake flow.

The relative transverse root-mean-square velocity W_{rms}/U_s profiles for the horizontal planes at $y/H=0.10$, 051, and 0.76 are shown in Figs. 10(*a*)–10(*c*). All profiles in these figures demonstrate a dome-type distribution. But the profiles extracted from the mid-depth ($y/H=0.51$) and near-surface ($y/H=0.76$) planes look broader than the near-bed profiles ($y/H=0.10$). The profiles extracted from the near-bed and near-surface planes show that the profiles at $x/D=2.5$ and 3.5 overlap in the core region ($|z/D|<0.6$ and 0.8 for the $y/H=0.10$ and 0.76 cases, respectively), while the profiles at $x/D=3.5$ and 4.5 overlap in the outer region ($|z/D|>0.6$ and 0.7, respectively). The peak values of the relative transverse turbulence intensity W_{rms}/U_s for the near-bed case are 0.58 at $x/D=2.5$ and 3.5, and 0.50 at $x/D=4.5$. while for the near-surface case are 0.47 at $x/D=2.5$ and 3.5 and 0.44 at $x/D=4.5$. This behavior indicates that there is an increase in W_{rms} in the streamwise direction from $x/D=2.5$ to 3.5 (in the outer region), then W_{rms} in the core region ($|z/D|<0.7$ and 0.9 for the $y/H=0.10$ and 0.76 cases, respectively) decreases in the streamwise direction from $x/D=3.5$ to 4.5.

The relative transverse turbulence intensity W_{rms}/U_s profiles shown in Fig. 10(*b*) shows that there is an increase in W_{rms} in the streamwise direction by comparing the profiles at $x/D=2.5$ and 3.5, then W_{rms} becomes constant as illustrated by the collapse of the profiles at $x/D=3.5$ and 4.5. The values of W_{rms}/U_s at $z/D=0$ are 0.31, 0.41, and 0.42 corresponding to streamwise locations $x/D=2.5$, 3.5 and 4.5, respectively.

To summarize the behavior of the streamwise and transverse rms velocities discussed above, the distribution of turbulent kinetic energy K in the streamwise direction obtained from these components $K=\frac{1}{2}(U_{rms}+W_{rms})$ are shown in Fig. 11. The turbulent kinetic energy K is normalized by the square of the upstream velocity U_s. Note that the relatively larger K/U_s^2 values shown in Fig. 11(*a*) compared with the other cases shown in Figs. 11(*b*) and 11(*c*), is because the upstream velocity U_s used to normalize the data was smaller (0.147). By comparing the three plots, it can be observed that there is an increase in K/U_s^2 in the mid-depth plane (in the region $|z/D|<1$) from $x/D=2.5$ to 3.5, while the other planes show negligible change. From $x/D=3.5$ to 4.5, the variation of K/U_s^2 is reversed, i.e., there is a decrease in the near-bed and near-surface planes (Figs. 11(*a*) and 11(*c*)) with a negligible change in the mid-depth plane (Fig. 11(*b*)). This behavior indicates that the turbulent energy is correlated in the three planes. In other words, there is transfer of energy throughout the water depth, which can be clarified by plotting the relationship between U_{rms} and W_{rms} along the central-plane ($z/D=0$). Figure 12 illustrates the variation of U_{rms}/W_{rms} in the streamwise direction x/D for the $y/H=0.10$, 0.51, and 0.76 planes. The negligible increase in K/U_s^2 from $x/D=2.5$ to 3.5 for the $y/H=0.10$ and 0.76 planes shown in Figs. 11(*a*) and 11(*c*) and the constant U_{rms}/W_{rms} ratio in

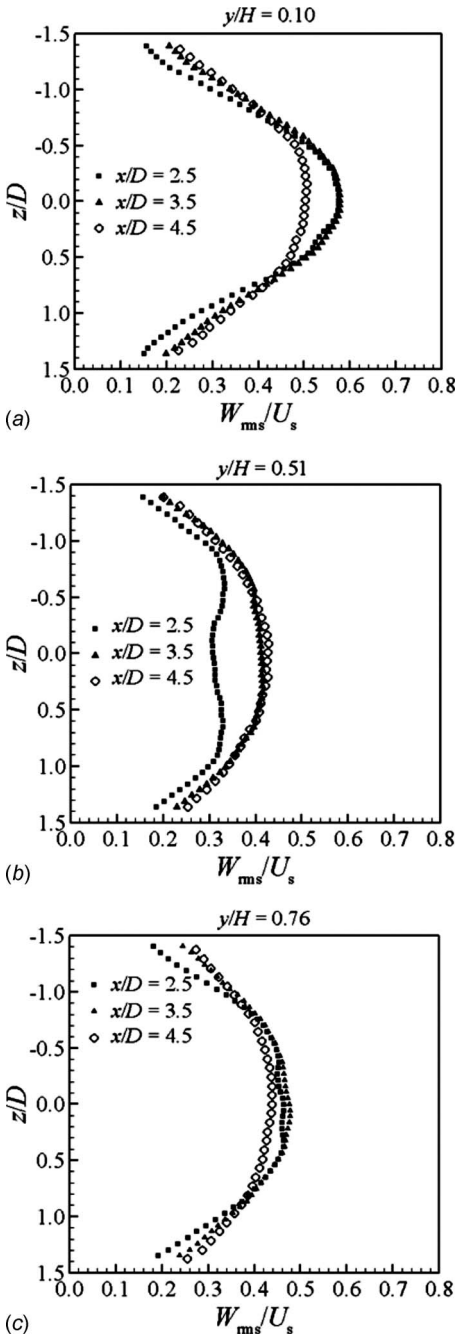

Fig. 10 Development of root-mean-square transverse velocity W_{rms}/U_s in the streamwise direction x/D for horizontal planes at (*a*) $y/H=0.10$, (*b*) $y/H=0.51$, and (*c*) $y/H=0.76$

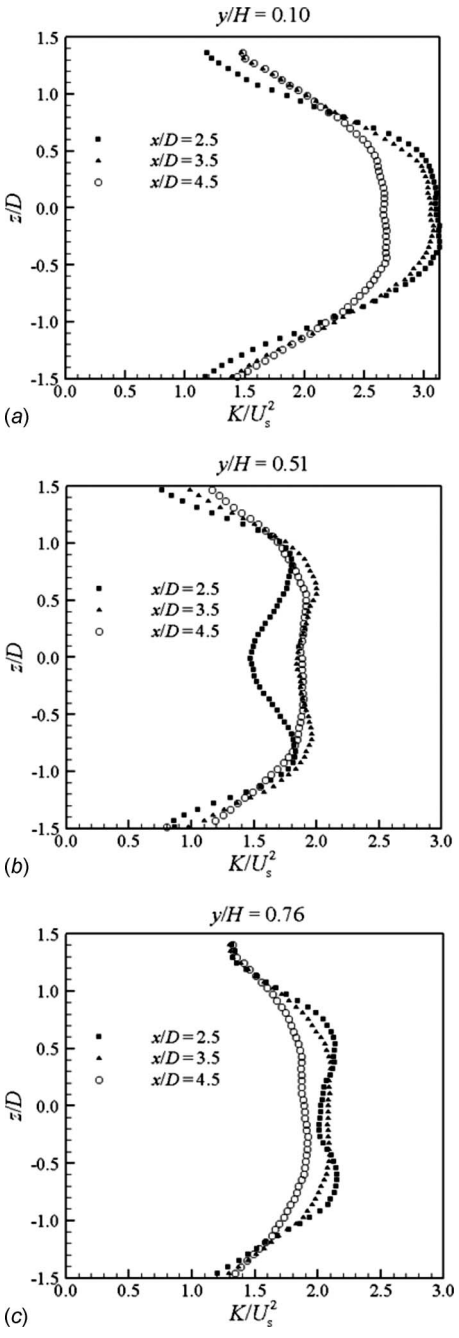

Fig. 11 Development of turbulent kinetic energy K/U_s^2 in the streamwise direction x/D for horizontal planes at (*a*) $y/H=0.10$, (*b*) $y/H=0.51$, and (*c*) $y/H=0.76$

Fig. 12 indicate that both U_{rms} and W_{rms} were constant in this region. On the other hand, the increase in K/U_s^2 for the $y/H=0.51$ plane shown in Fig. 11(*b*) and the decrease in U_{rms}/W_{rms} in Fig. 12 is a clear indication of the increase in U_{rms} with a higher rate compared with W_{rms} in this region (see also Figs. 9(*b*) and 10(*b*)). Further downstream ($x/D=3.5$ to 4.5), it can be concluded from Figs. 11 and 12 that both U_{rms} and W_{rms} decrease in the $y/H=0.10$ and 0.76 planes, while U_{rms} and W_{rms} for the $y/H=0.51$ plane seem to be constant. This behavior indicates that there is a transfer of energy from the streamwise and transverse components in the near-boundary planes to the vertical component V_{rms}, which maintained a constant U_{rms} and W_{rms} in the mid-depth plane. This observation is also supported by the behavior of the vortical structures that reside near the boundaries, which direct flow toward the mid-depth plane to be shown in Sec. 4.7.

The Reynolds shear stress $\langle uw\rangle/U_s^2$ profiles extracted from the horizontal planes at $y/H=0.10$, 0.51, and 0.76 are shown in Figs. 13(*a*)–13(*c*), respectively, at different streamwise locations. Figure 13(*a*) shows that the data extracted from the near-bed plane ($y/H=0.10$) are symmetric about the vertical central plane ($z/D=0$). It also shows that the Reynolds shear stress decreases in the streamwise direction. The maximum absolute values of $\langle uw\rangle/U_s^2$ at $x/D=2.5$, 3.5, and 4.5 are 0.089, 0.074, and 0.050, respectively, which are located at $z/D\approx\pm0.55$. These results indicate that the

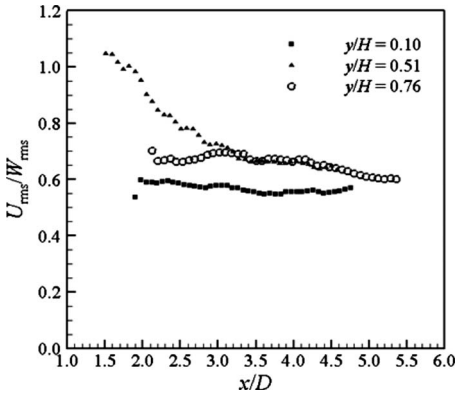

Fig. 12 Variation of U_{rms}/W_{rms} in the streamwise direction x/D. The three curves were extracted from the three horizontal planes along the vertical central-plane ($z/D=0$).

momentum exchange by the Reynolds stress is reduced in the streamwise direction because of the shallowness compared with the deep wakes [18].

Figure 13(*b*) shows the variation of the Reynolds shear stress $\langle uw\rangle/U_s^2$ profiles for the $y/H=0.51$ plane. Consistent with the behavior of the transverse rms velocity profiles shown in Fig. 10(*b*), Fig. 13(*b*) shows that $\langle uw\rangle/U_s^2$ increases then decreases in the streamwise direction, albeit the variation is small. The maximum absolute values of $\langle uw\rangle/U_s^2$ at $x/D=2.5$, 3.5, and 4.5 are 0.63, 0.72, and 0.61, respectively, which are located at $|z/D| \approx 0.94$, 0.80, and 0.74. This behavior indicates that the horizontal momentum exchange has been slightly enhanced at these streamwise locations.

The Reynolds shear stress $\langle uw\rangle/U_s^2$ profiles for the $y/H=0.76$ plane (Fig. 13(*c*)) show similar behavior as the profiles extracted from the near-bed plane ($y/H=0.10$). The maximum absolute values of $\langle uw\rangle/U_s^2$ are 0.089, 0.072, and 0.054, located at $|z/D| =0.82$, 0.84, and 0.86, respectively, corresponding to streamwise locations $x/D=2.5$, 3.5, and 4.5.

4.7 Coherent Structures. This section presents selected examples of large-vortical structures in the wake of the bluff body educed by the proper orthogonal decomposition (POD) technique. The procedures may be summarized as follows. The instantaneous velocity fields were processed using the POD via the method of snapshots [34]. Two thousand velocity fields were used in this process, which yielded a temporal correlation matrix of size 2000×2000. A complete description of the implementation of the POD using the method of snapshots may be found in Ref. [31]. The number of modes used for the POD reconstruction in this paper was six, which includes mode 0. Note that mode 0 represents a velocity field that resembles the mean velocity field. These POD-reconstructed velocity fields provide a unique set of flow visualization results obtained by a quantitative technique since they include mode 0. In other words, it is not common to include mode 0 in the POD reconstruction since the structures cannot be exposed in most cases. In addition, the current results highlight the dynamics of large (energetic) structures in this flow while the small (less energetic) structures were filtered out, which adds to the quality of the results compared with the conventional visualization. It should be pointed out that the time separation between two consecutive velocity fields was ~1 s. This time separation is too large to follow the same vortical structures in successive frames. However, some interesting features were captured. It should be pointed out that this work produced a large amount of data, which cannot be presented here owing to space limitations. Consequently, only some selected examples will be presented in this section.

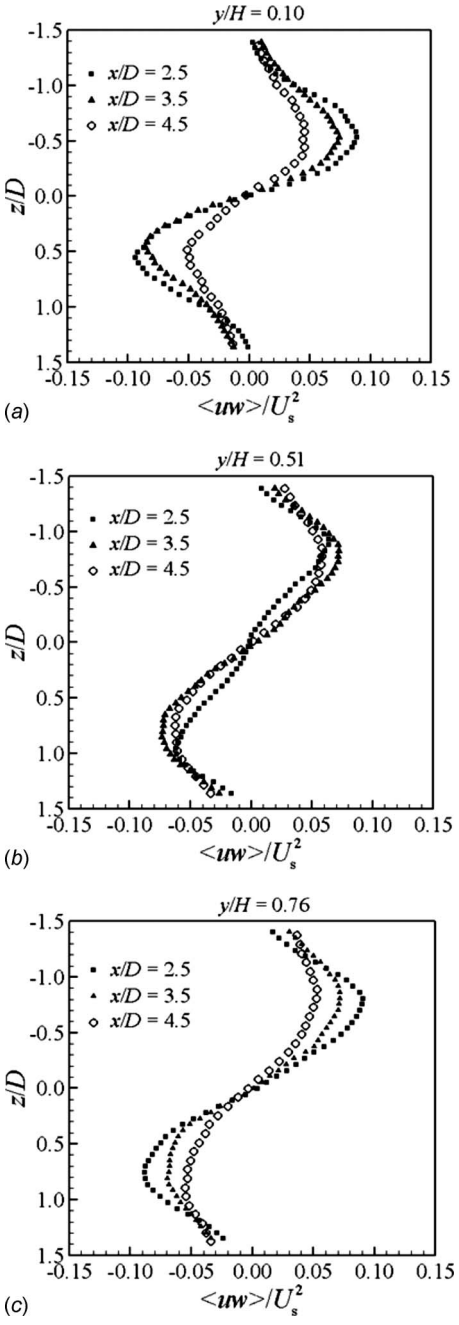

Fig. 13 Development of Reynolds stress ($\langle uw\rangle/U_s^2$) in the streamwise direction x/D for horizontal planes at (*a*) $y/H=0.10$, (*b*) $y/H=0.51$, and (*c*) $y/H=0.76$

Figure 14 shows some selected examples of the large-vortical structures extracted from the vertical central plane ($z=0$) of the shallow bluff-body flow. The streamwise x and vertical y axes are normalized by the water depth H. The total kinetic energy recovered in these fields was ~59.5%. This figure consists of three examples of streamline plots (a)–(c) representing POD-reconstructed velocity fields in order to highlight the features of the flow.

Figure 14(*a*) shows a vortical structure close to the free surface. This structure induces a strong backward flow being directed away from the free surface by a negative vertical velocity component (labeled E), and a forward flow being moved toward the free surface (labeled S). This behavior is very similar to the mechanism of the ejection and sweep events that occur near a solid wall.

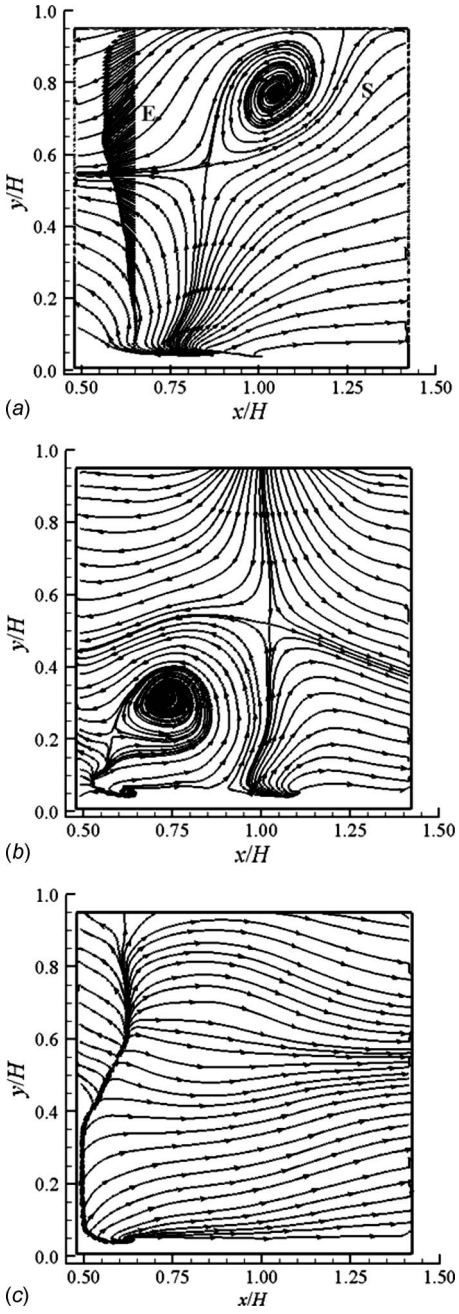

Fig. 14 Three examples (*a*), (*b*), and (*c*) show coherent structures identified on the vertical central plane by the POD technique. The total kinetic energy recovered in these fields is ~59.5% using the first six modes including mode 0.

The flow direction of the ejection-like event (labeled E) suggests that the identified structure is a cross section of a hairpin structure with two counter-rotating quasi-streamwise vortical elements. This observation is based on flow direction of the ejection-like event and the local maximum velocity (see Ref. [35]) as highlighted by the extracted velocity profile at $x/H=0.65$ shown in the same plot. The quasi-streamwise vortical elements are known to exist in junction flows since horseshoe vortices wrap around the obstacle [16]. The streamline patterns in Fig. 14(*a*) also shows an upward flow near the bed, which seems to be thrust by a quasi-streamwise vortical element that resides near the bed. This example illustrates the interaction between induced flows by the structures that reside near the bed and the free surface. Another example is shown in Fig. 14(*b*). This figure shows a cross section of a structure near the bed and a signature of a quasi-streamwise vortical element beside it (near the bed), which thrusts the flow upwards. In addition, there is a diverged downward flow that seems to be a result of a quasi-streamwise vortical element that resides near the free surface.

An interesting feature can also be seen in Fig. 14(*c*). It shows an element that appears as a thick vertical line. This element spans almost the entire water depth and extends close (and parallel) to the bed in the streamwise direction to $x/H \approx 0.75$. The direction of the flow at the sides of this element indicates that it is a side-section of a vortical element, which resembles a hairpin leg. However, the lower-lying portion of this element appears to reside ahead of the vertical portion of the element leg. Conversely, the hairpin vortex in a channel flow (without a bluff body) is supposed to be stretched in the streamwise direction according to velocity gradient in the boundary layer. This shape of the vortical element may be a result of the interaction of a hairpin vortex with quasi-streamwise elements that seem to be common in this kind of flow (see Ref. [16]).

It should be mentioned that similar structures (to those exposed along $z/D=0.0$) were also observed along the vertical plane at $z/D=0.5$. Accordingly, they are not presented in this paper because they would not add new information.

Figure 15 shows selected examples of the POD-reconstructed instantaneous velocity fields on the horizontal plane. The streamwise x and horizontal z locations are normalized by the width of the bluff body D. Each column in this figure shows three examples representing the velocity field in a horizontal plane at a specific vertical location. The total kinetic energy recovered (using the first six modes) was 90%, 86.7%, and 87.6% corresponding to horizontal velocity fields in planes at vertical locations $y/H=0.10$, 0.51, and 0.76, respectively. In these plots, the streamline patterns are presented because the most useful information regarding the dynamics of the structures is apparent in these plots.

At the first glance, all plots shown in Fig. 15 illustrate that the wake flow contains a large number of structures, which makes the flow meander about the vertical central plane. The meandering behavior was also predicted by the stability parameter S for this flow, which suggests a lesser effect of the bed friction on the flow compared with the shear stress generated in the shear layer of the wake flow.

Plots (i) in Figs. 15(*a*)–15(*c*) show that the vortical structures exist in pairs of opposite rotational sense. This suggests that the vortices are being shed from both sides of the bluff body. The vortical structures in these plots appear to undergo axial stretching generated by the surrounding flow with a corresponding horizontal compression as illustrated by the proximity of the streamlines at the edges of the vortices. In addition, the vortex pair shown in plot (i) of Fig. 15(*a*) appears to consist of a circular vortex and a spiral vortex where the flow is spiraling into its center (see Ref. [36]). Moreover, the vortex pairs shown in plots (i) of Figs. 15(*b*) and 15(*c*) show similar configuration, but the flow is spiraling out of the spiral vortices in these examples. This configuration seems to be a characteristic feature of vortex pairs in shallow wakes.

Plots (ii) in Fig. 15(*a*)–15(*c*) illustrate that the size of the vortices are relatively larger than the width of the bluff body. It appears that the vortices identified in the horizontal plane occupy more than 200% of the body width D. Furthermore, these plots show that the flow patterns are not symmetrical. They appear to meander like a sine wave about the vertical central plane. This behavior is due to the interaction of the vortices with the mean flow at either side of the vertical central plane.

Some interesting features about the interaction between the vortices are shown in plots (iii) of Figs. 15(*a*)–15(*c*). The plots in Figs. 15(*a*) and 15(*c*) show that the vortices are being compressed horizontally normal to the vertical central plane, which could lead to merging of the two structures. Furthermore, the plot shown in Fig. 15(*b*) illustrates the effect of stretching on the structures, which appear elongated in the streamwise direction. The presence

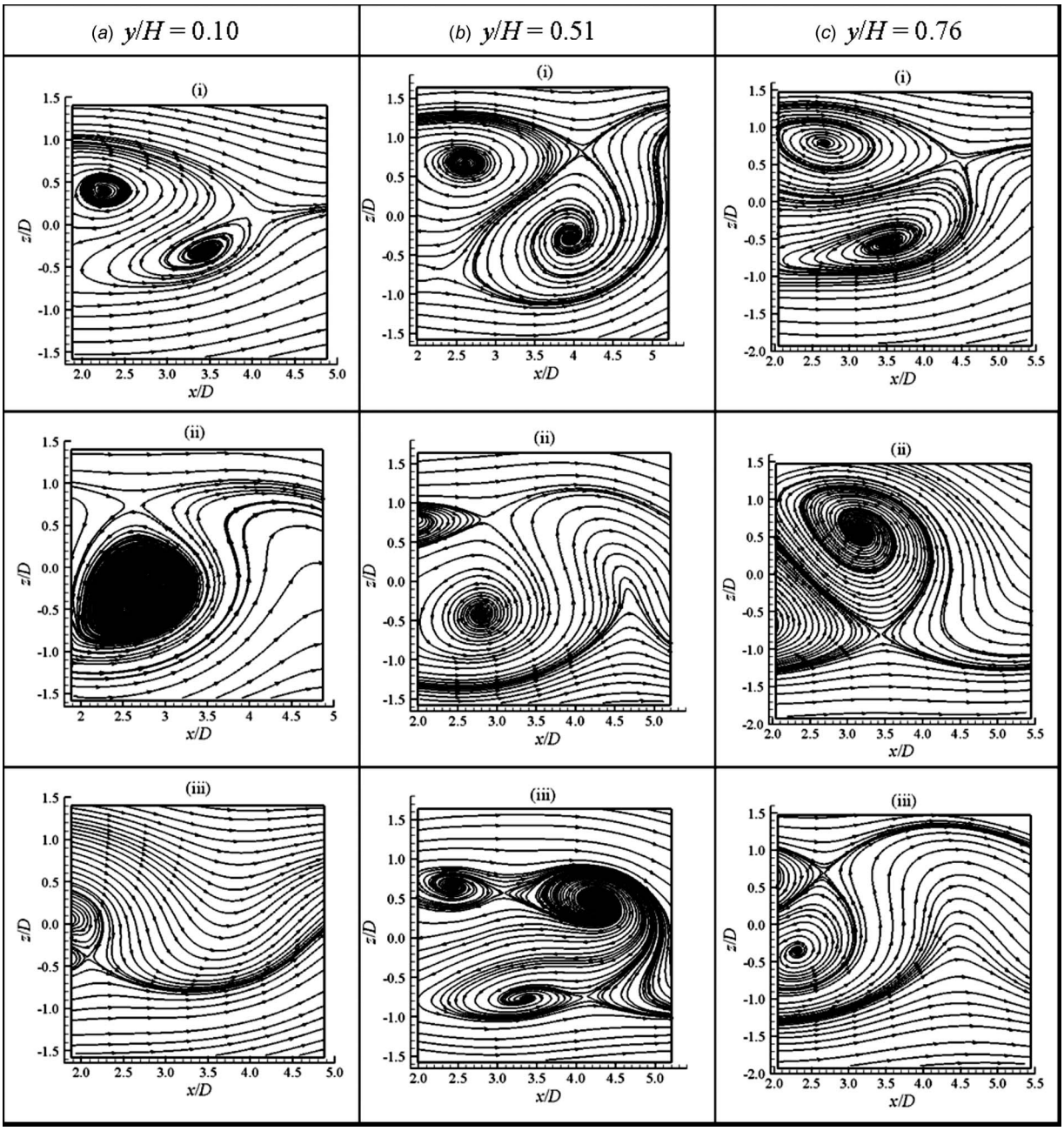

Fig. 15 Examples of POD-reconstructed instantaneous velocity fields on the horizontal plane at vertical locations (*a*) $y/H=0.10$, (*b*) $y/H=0.51$, and (*c*) $y/H=0.76$. Each column shows three examples representing the velocity field at a specific vertical location. The total kinetic energy recovered was 90%, 86.7%, and 87.6%, respectively, using the first six modes including mode 0.

of two connected structures for $z/D>0$ suggests the occurrence of the tearing process as a result of the vortex stretching by the instantaneous flow.

5 Conclusions

PIV measurements have been conducted to investigate the wake flow of a sharp-edged bluff body immersed in a shallow smooth open channel flow. The purpose of the present study is to highlight the vertical variation of the wake turbulent flow field throughout the shallow water layer. The conclusions may be summarized as follows.

- The size of the recirculation zones in the mean velocity fields appears to be different at different vertical locations. It was found that the largest recirculation zone occurs in the mid-depth velocity field, while the smallest one occurs near the bed. This is a clear indication of the three-dimensionality of the near-wake flow. The differences in the wake size are attributed to the formation and distribution of the vortices (particularly the quasi-streamwise vortices) near the bed and the free surface, which are responsible for enhancing the entrainment (as shown in the transverse velocity W profiles) and the consequent reduction in the size of the recirculation zones.
- The POD results showed that the wake flow is rich with quasi-streamwise vortical elements that reside near the boundaries (bed and free surface). These elements were observed to thrust flow upwards from the bed and downwards

from the free surface. This observation is consistent with the correlated distribution of energy throughout the water layer, which is attributed to the redistribution of the kinetic energy between the three velocity components (U_{rms}, V_{rms}, and W_{rms}).

- The Reynolds stress $\langle uw \rangle$ results indicated a reduction in the transverse momentum exchange near the boundaries as the flow moves in the streamwise direction, which is consistent with the reduction of the streamwise and transverse fluctuations reflected by U_{rms} and W_{rms} results. Furthermore, the transverse momentum exchange in the mid-depth plane has been enhanced in the streamwise direction.
- The POD results showed the existence of structures near the free surface, which induced flow similar to the ejection and sweep events that commonly occur near the solid walls. The direction of the ejection-like event suggested that the shape of these structures is similar to the hairpin vortices with two counter-rotating quasi-streamwise vortical elements that usually exist near solid walls although the boundary conditions are different.
- The size of the vortices exposed on the horizontal plane appears to exceed 200% of the bluff-body width (>50% of the water depth) at these locations ($x/D<5$). Similar observation was previously reported in the far-field region of a wake flow [19]. In addition, these vortical structures undergo streamwise stretching and/or horizontal compression generated by the surrounding flow, which seems to be responsible for the occurrence of pairing and tearing processes.

Acknowledgment

The support of the Natural Sciences and Engineering Research Council of Canada (NSERC) is gratefully acknowledged.

Nomenclature

B = characteristic length scale (m)
C = constant (=5.2)
H = water layer depth (m)
k = von Karman constant (=0.41)
Re_θ = Reynolds number based on momentum thickness
Re_H = Reynolds number based on water depth
S = stability number
S_c = critical stability number
$\langle u_r \rangle$ = reverse velocity (m/s)
u_τ = friction velocity (m/s)
U, V, W = mean velocity components in x-, y-, and z-direction (m/s)
U_{rms}, V_{rms}, W_{rms} = root-mean-square velocity components in x-, y-, and z-direction (m/s)
U_c = central velocity (m/s)
U_s = upstream mean streamwise velocity at specific vertical locations (m/s)
U_∞ = freestream velocity (m/s)
U^+ = normalized velocity
y^+ = normalized inner vertical axis
δ^* = displacement thickness (m)
θ = momentum thickness (m)
ν = kinematic viscosity (m^2/s^2)

References

[1] Jirka, G. H., and Uijttewaal, W. S. J., 2004, "Shallow Flows: A Definition," *Shallow Flows*, Taylor and Francis, London.
[2] Sedighi, K., and Farhadi, M., 2006, "Three Dimensional Study of Vortical Structures Around a Cubic Bluff Body in a Channel," Facta Universitatis, Series Mech. Engrg., **4**(1), pp. 1–16.
[3] Scorer, R. S., 1978, *Experimental Aerodynamics*, Ellis Horwood, Chichester.
[4] Nezu, I., and Nagawaka, H., 1993, *Turbulence in Open Channel Flow*, Balkema, Rotterdam.
[5] Okajima, A., 1982, "Strouhal Numbers of Rectangular Cylinders," J. Fluid Mech., **123**, pp. 379–398.
[6] Roshko, A. J., 1993, "Perspectives on Bluff-Body Aerodynamics," J. Wind. Eng. Industrial. Aerodyn., **49**, pp. 79–100.
[7] Lyn, D. A., Einav, S., Rodi, W., and Park, J. H., 1995, "A Laser-Doppler Velocimetry Study of Ensemble-Averaged Characteristics of Turbulent Near-Wake of a Square Cylinder," J. Fluid Mech., **304**, pp. 285–319.
[8] Chen, J. M., and Liu, C. H., 1999, "Vortex Shedding and Surface Pressures on a Square Cylinder at Incidence to a Uniform Air Stream," Int. J. Heat Fluid Flow, **20**(6), pp. 592–597.
[9] Beaudan, P., and Moin, P., 1994, "Numerical Experiment of Fluid Flow Past a Cylinder at Subcritical Reynolds Number," Stanford University, Report No. TF-62.
[10] Dong, S., Karniadakis, G. E., Ekmerci, A., and Rockwell, D., 2007, "A Combined Direct Numerical Simulation-Particle Image Velocimetry Study of the Turbulent Near-Wake," J. Fluid Mech., **569**, pp. 185–207.
[11] Logory, L. M., Hirsa, A., and Anthony, D. G., 1996, "Interaction of Wake Turbulence With a Free Surface," Phys. Fluids, **8**(3), pp. 805–815.
[12] Lawless, M. R., Lane, S. N., and Best, J. L., 2003, "The Junction Vortex System: Time-Mean and Instantaneous Flow Fields," *Proceedings of the International Symposium on Shallow Flows*, Jun. 16–18, Technical University of Delft, Netherlands, Pt. 3, pp. 137–144.
[13] Devenport, W. J., and Simpson, R. L., 1990, "Time-Dependent and Time-Averaged Turbulence Structure Near the Nose of Awing-Body Junction," J. Fluid Mech., **210**, pp. 23–55.
[14] Visbal, M. R., 1991, "Structure of Laminar Juncture Flows," AIAA J., **29**, pp. 1273–1282.
[15] Seal, C., Smith, C. R., and Rockwell, D., 1997, "Dynamics of the Vorticity Distribution in End-Wall Junctions," AIAA J., **35**, pp. 1041–1047.
[16] Simpson, R. L., 2001, "Junction Flows," Annu. Rev. Fluid Mech., **33**, pp. 415–443.
[17] Bearman, P. W., 1984, "Vortex Shedding From Oscillating Bluff Bodies," Annu. Rev. Fluid Mech., **16**, pp. 195–222.
[18] Williamson, C. H. K., 1996, "Vortex Dynamics in the Cylinder Wake," Annu. Rev. Fluid Mech., **28**, pp. 477–539.
[19] Chen, D., and Jirka, G. H., 1995, "Experimental Study of Plane Turbulent Wakes in a Shallow Water Layer," Fluid Dyn. Res., **16**(1), pp. 11–41.
[20] Ingram, R. G., and Chu, V. H., 1987, "Flow Around Islands in Rupert Bay: An Investigation of the Bottom Friction Effect," J. Geophys. Res., **92**(C13), pp. 14521–14523.
[21] Balachandar, R., Tachie, M. F., and Chu, V. H., 1999, "Concentration Measurement in Intermediate Shallow Wakes," ASME J. Fluids Eng., **121**(1), pp. 34–43.
[22] Akilli, H., and Rockwell, D., 2002, "Vortex Formation From a Cylinder in Shallow Water: Flow Structure and Topology," Phys. Fluids, **14**(9), pp. 2957–2967.
[23] Perry, A. E., and Chong, M. S., 1994, "Topology of Flow Patterns in Vortex Motions and Turbulence," Appl. Sci. Res., **53**(3–4), pp. 357–374.
[24] Lin, C., Chiu, P. H., and Shieh, S. J., 2002, "Characteristics of Horseshoe Vortex System Near a Vertical Flat Plate Juncture," Exp. Therm. Fluid Sci., **27**, pp. 25–46.
[25] Fu, H., and Rockwell, D., 2005, "Shallow Flow Past a Cylinder: Transition Phenomenon at Low Reynolds Number," J. Fluid Mech., **540**, pp. 75–97.
[26] Shinneeb, A.-M., Bugg, J. D., and Balachandar, R., 2004, "Variable Threshold Outlier Detection in PIV Data," Meas. Sci. Technol., **15**, pp. 1722–1732.
[27] Prasad, A. K., Adrian, R. J., Landreth, C. C., and Offutt, P. W., 1992, "Effect of Resolution on the Speed and Accuracy of Particle Image Velocimetry Interrogation," Exp. Fluids, **13**, pp. 105–116.
[28] Pope, S. B., 2000, *Turbulent Flows*, Cambridge University Press, Cambridge.
[29] Balachandar, R., and Bhuiyan, F., 2007, "Higher-Order Moments of Velocity Fluctuations in an Open Channel Flow With Large Bottom Roughness," J. Hydraul. Eng., **133**, pp. 77–87.
[30] Clauser, F., 1954, "Turbulent Boundary Layers in Adverse Pressure Gradient," J. Aerosp. Sci., **21**, pp. 91–108.
[31] Shinneeb, A.-M., 2006, "Confinement Effects in Shallow Water Jets," Ph.D. thesis, University of Saskatchewan, Canada.
[32] Monkewitz, P. A., 1988, "The Absolute and Convective Nature of Instability in Two-Dimensional Wakes at Low Reynolds Numbers," Phys. Fluids, **31**(5), pp. 999–1006.
[33] Chen, D., and Jirka, G. H., 1997, "Absolute and Convective Instabilities of Plane Turbulent Wakes in Shallow Water Layers," J. Fluid Mech., **338**, pp. 157–172.
[34] Sirovich, L., 1987, "Turbulence and the Dynamics of Coherent Structures. Part I: Coherent Structures," Q. Appl. Math., **45**(3), pp. 561–571.
[35] Adrian, R. J., 2007, "Hairpin Vortex Organization in Wall Turbulence," Phys. Fluids, **19**, p. 041301.
[36] Perry, A. E., and Steiner, T. R., 1987, "Large-Scale Vortex Structures in Turbulent Wakes Behind Bluff Bodies. Part 1: Vortex Formation Processes," J. Fluid Mech., **174**, pp. 233–270.

Quasi-1D Unsteady Conjugate Module for Rocket Engine and Propulsion System Simulations

Bryan T. Campbell
Engineering Specialist
Systems Engineering,
Aerojet,
P.O. Box 13222,
Department 5271,
Sacramento, CA 95813-6000

Roger L. Davis
Professor
Department of Mechanical and Aeronautical Engineering,
University of California, Davis,
Davis, CA 95616

A new quasi-one-dimensional procedure (one-dimensional with area change) is presented for the transient solution of real-fluid flows in lines and volumes including heat transfer effects. The solver will be integrated into a larger suite of software modules developed for simulating rocket engines and propulsion systems. The solution procedure is coupled with a state-of-the-art real-fluid property database so that both compressible and incompressible fluids may be considered using the same procedure. The numerical techniques used in this procedure are described. Test cases modeling transient flow of nitrogen, water, and hydrogen are presented to demonstrate the capability of the current technique.
[DOI: 10.1115/1.3059704]

1 Introduction

This paper addresses development of a quasi-one-dimensional (one-dimensional with area change), unsteady conjugate flow/heat transfer solver with real-fluid properties suitable for use in system-level transient simulations of hydraulic and pneumatic systems and, in particular, rocket engine and propulsion systems. The solver module described here is an integral part of a rocket engine system modeling tool currently under development. The solver is geared toward modeling the dynamic behavior of fluid-filled lines and passages (i.e., the solution domain is much larger in one dimension than in the others) where heat transfer is important. Existing software models available for such simulations (e.g., GFSSP [1], ROCETS [2], and NPSS [3]) are typically based on lumped analysis approaches, which do not fully capture the flow dynamics, mainly due to the elimination of the unsteady momentum terms. Although so-called "continuity" waves can be captured using a lumped analysis, neglecting these terms leads to an inability to capture true "dynamic" waves required for simulating such phenomenon as water-hammer and pressure surge [4]. Since these phenomena play an important role in the operation and testing of liquid rocket engines and propulsion systems, a method that captures these effects is desired.

Several approaches for simulating the dynamic behavior of such "fluid-transmission" lines have been reported. The "lumped-analysis" approach treats a flow passage as a series of fluid control volumes that conserve mass and energy linked by flow resistance elements that compute the flow between the volumes [5]. While this approach does conserve momentum in a quasi-steady sense at the flow resistances, the unsteady momentum term in the governing equations is neglected. Another approach uses the method of characteristics [6], which is a general method for solving hyperbolic partial differential equations. The governing equations for fluid flow are compatible with this method, and it has been used for simulation of fluid transmission lines [7]. While the unsteady momentum terms are retained using this method, other problems, particularly at the boundaries of components, make it problematic to apply to a modular system-level simulation tool. Modal methods have also been used when solution in the frequency domain is possible [8]. This technique represents the pressure and flow distribution in the flow domain as a sum of an infinite series of mode shapes, similar to a Fourier series solution. While this method presents an elegant and efficient method for simulating simple flow situations (e.g., incompressible flow, inviscid flow, laminar flow, etc.), the addition of turbulent flow, real-fluid properties, and heat transfer complicates application of the method and reduces its attractiveness.

The current technique focuses on application of standard finite-volume methods to the development of an unsteady conjugate solver capable of capturing wave dynamics, real-fluid effects, and heat transfer. In addition, the solution method must be computationally efficient enough to operate as a module in a larger system-level simulation. Sections 2–5 describe the modeling approach, numerical methodologies, and test cases that have been used during development of this model.

2 Approach

The intention of the model developed here is to represent fluid lines and flow passages as a quasi-1D domain. The intended components to be modeled using this method are fluid lines and internal flow passages where the length of the domain is much larger than the hydraulic diameter of the domain. Flow separations and nonaxial velocities are minimal for these types of components; hence, the quasi-1D assumption incorporating 1D flow with area change is valid. The solver is targeted to the commercial SIMULINK® dynamic simulation software package from The MathWorks (Natick, MA) for integration into a larger suite of modules developed for simulating rocket engines and propulsion systems. A FORTRAN95 code is also being developed in parallel [9] to provide comparison test cases.

The solver is being developed to model the effects of friction, minor losses (e.g., bends), real-fluid properties, heat transfer, and the capability to produce unsteady and steady-state solutions. Fluid equation of state closure is provided by the REFPROP fluid property database [10] available from the National Institute for Standards and Testing (NIST). This database uses state-of-the-art equation of state models to fully describe "real-fluid" properties over a wide range of thermodynamic conditions, including liquid, vapor, mixed phase, and supercritical fluid regimes. Properties that completely define the fluid thermodynamic state, as well as transport properties, are available as a function of any two thermodynamic parameters. Validated fluid models for over 80 pure fluids and over 180 fluid mixtures are available in the database. The database is accessed through a suite of FORTRAN subroutines that were compiled into the codes and obtain fluid equation of state model parameters from external files.

Friction and heat transfer are modeled as source terms in the fluid governing equations. This approach allows the flow to be

Contributed by the Fluids Engineering Division of ASME for publication in the JOURNAL OF FLUIDS ENGINEERING. Manuscript received June 24, 2007; final manuscript received April 7, 2008; published online January 12, 2009. Assoc. Editor: Malcolm J. Andrews.

modeled as 1D and facilitates computational efficiency. Friction (i.e., viscous losses and minor losses due to bends and fittings) and heat transfer coefficients are obtained from suitable correlations between the flow variables and source terms.

3 Governing Equations

The modeling procedure solves differential equations representing the physics of the problem. Equations are presented below for modeling the fluid dynamics, wall temperature, and source terms coupling the two.

3.1 Fluid. The differential equations governing the dynamics of the fluid consist of the quasi-one-dimensional continuity, Navier–Stokes, and energy equations simplified to model viscous effects and general acceleration in a noninertial frame using source terms [11].

$$\frac{1}{V}\frac{\partial UV}{\partial t}+\frac{\partial F}{\partial x}=\frac{S}{V} \tag{1}$$

$$U=\begin{vmatrix}\rho\\ \rho u\\ E\end{vmatrix},\quad F=\begin{vmatrix}\rho u_r\\ (\rho u u_r+p)\\ \rho u_r H_{\text{total}}\end{vmatrix},$$

$$S=\begin{vmatrix}0\\ \dfrac{pV}{A}\dfrac{dA}{dx}-\rho V a_r-\tau_w dx A_p-K\dfrac{\rho u_r^2}{2}A\\ \dfrac{\dot{q}_w}{V}-\tau_w u_r dx A_p-K\dfrac{\rho u_r^3}{2}A\end{vmatrix} \tag{2}$$

The required fluid properties at the solution nodes are computed using the NIST REFPROP real-fluid property database [10]. The independent variables in Eq. (2) above are fluid density (ρ), momentum (ρu), and total energy (E), which are computed as a function of time by integration of Eq. (1). Each time the independent variable derivative ($\partial U/\partial t$) is computed, the desired fluid properties are computed at each solution node as a function of the fluid density (ρ) and internal energy (e). Density is an independent variable, but internal energy must be computed using the independent variables:

$$e=\frac{E}{\rho}-\frac{u^2}{2}=\frac{E}{\rho}-\frac{(\rho u)^2}{2\rho^2} \tag{3}$$

Once density and internal energy are known at each node, the appropriate REFPROP subroutines [10] are called to compute fluid static pressure (p), static temperature (T_B), static enthalpy (H), and entropy (s):

$$\begin{aligned}p&=f(\rho,e)\\ T_B&=f(\rho,e)\\ H&=f(\rho,e)\\ s&=f(\rho,e)\end{aligned} \tag{4}$$

Fluid total enthalpy is determined from static enthalpy and velocity, and fluid total pressure and total temperature are computed with calls to the REFPROP subroutines based on the thermodynamic definition of fluid total conditions:

$$\begin{aligned}H_{\text{total}}&=H+\frac{u^2}{2}\\ p_{\text{total}}&=f(H_{\text{total}},s)\\ T_{B,\text{total}}&=f(H_{\text{total}},s)\end{aligned} \tag{5}$$

The specific fluid models used by the NIST REFPROP database and the associated accuracies for the fluids included in the database are discussed elsewhere [10].

3.2 Wall. The wall bounding the fluid computational domain is modeled using standard control volume methods for heat transfer [12]. Forced convection heat transfer between the fluid and wall as well as heat conduction within the wall are included in the model. Heat conduction between the wall and fluid is neglected due to its small magnitude compared with forced convection heat transfer. In addition, conduction in the wall is modeled as 1D neglecting radial conduction. These effects can be added to the model as required.

Based on these assumptions, the governing equation for heat transfer within the wall is [12]

$$\frac{\partial T_w}{\partial t}=\frac{1}{\rho_w c_w}\frac{\partial}{\partial x}\left(k_w\frac{\partial T_w}{\partial x}\right) \tag{6}$$

Equation (6) does not include the contribution due to forced convection heat transfer between the fluid and the wall. It is more convenient to add this term below to the discretized equations.

3.3 Source Terms. Equations (1)–(6) above require several source terms that are a function of the wall and fluid conditions. The wall shear stress can be related to a suitable friction factor, f, which is a function of the local Reynolds number and wall surface roughness. For single-phase flow in pipes, the Churchill correlation [13] can be used to determine wall friction factors using the equation

$$f=\frac{\tau_w}{\rho u_r^2}=\left[\left(\frac{8}{\text{Re}_D}\right)^{12}+\frac{1}{(A+B)^{3/2}}\right]^{1/12},$$

$$A=\left[2.457\ln\left(\frac{1}{(7/\text{Re}_D)^{0.9}+0.27(\varepsilon/D)}\right)\right]^{16},\quad B=\left(\frac{37{,}530}{\text{Re}_D}\right)^{16} \tag{7}$$

Similarly, forced convection heat transfer between the wall and fluid can be obtained using a suitable correlation. For single-phase flow in pipes, the Colburn correlation [14] can be used to determine the forced convection heat transfer from the wall to the fluid:

$$\dot{q}_w=h\cdot A_p\cdot(T_w-T_B),\quad \text{Nu}_D=\frac{hD}{k}=0.023\ \text{Re}_f^{0.8}\ \text{Pr}_f^{1/3} \tag{8}$$

The source term models given by Eqs. (7) and (8) are suitable general-purpose correlations for single-phase flows; however, the accuracy of these correlations depends on the specific fluid and specific flow situation. To improve accuracy, other fluid-specific and/or flow-specific correlations can be substituted as available.

Minor loss terms, term K in Eq. (2), represent flow losses in bends, sudden expansions/contractions, and other types of losses. These effects are modeled as head loss using loss coefficients [15], where the location of the losses along the solution domain and the associated loss coefficients are input to the flow solver procedure. Since the locations typically do not correspond exactly to the location of a solution node, the minor losses are distributed to the two nearest computational cells:

$$\begin{aligned}\delta K_i&=K_{\text{loss}}\cdot\left(1-\frac{x_i-x_{\text{loss}}}{x_i-x_{i-1}}\right),\quad K_i=\sum\delta K_i\\ \delta K_{i-1}&=K_{\text{loss}}\cdot\left(1-\frac{x_{\text{loss}}-x_{i-1}}{x_i-x_{i-1}}\right),\quad K_{i-1}=\sum\delta K_{i-1}\end{aligned} \tag{9}$$

Note that K_{loss} is the loss coefficient for a minor loss located at location x_{loss}, and $x_{i-1}<x_{\text{loss}}<x_i$. Since a face-centered discretization scheme is used (see below), the average of the minor loss coefficients for the two neighboring cells is used in the computation of the source vector (S) in Eq. (2).

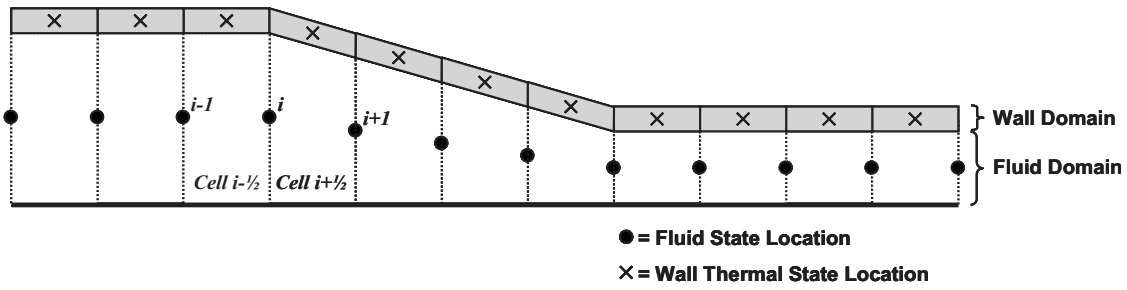

Fig. 1 Computational grid

4 Numerical Methods

Equations (1)–(6) may be solved with a variety of numerical schemes that are second order accurate in space and time for "steady" or transient flow. The flow solver is incorporated into SIMULINK® as an ANSI C executable S-function [16]. The model states are the flow and wall variables contained in the U vector and T_w at each computational node, and the main subroutine computes the time derivatives of the flow states (dU/dt and dT_w/dt). Once time derivatives of the system states are computed, standard SIMULINK® solvers are used to integrate the derivatives and to compute the time history of the model states. Multiple numerical schemes have been implemented in the FORTRAN95 code to provide flexibility and robustness when solving for different flow conditions. This version of the code uses solution methods similar to those discussed here and is described in detail elsewhere [9].

4.1 Computational Grid. The governing differential equations are solved on a 1D grid with varying areas, as shown in Fig. 1. In general, the computational domain has N computational cells. The fluid states (U) are located at the cell faces, as shown in the figure. The wall states (T_w) are located in the wall at the midpoint of the cells as shown. This staggered arrangement was selected to simplify application of boundary conditions for the fluid and wall. Thus, for N cells, there are $3(N+1)$ fluid states and N wall states.

4.2 Discretization. As discussed above, the main subroutine of the flow solver computes the model state derivatives (dU/dt and dT_w/dt) at each computational node. A finite-volume method is used to compute the fluid-state fluxes at the center of each fluid cell, so for cell $i+\frac{1}{2}$ in Fig. 1:

$$\left(\frac{\Delta U}{\Delta t}\right)_{i+1/2} = S_{i+1/2} - \left(\frac{F_{i+1}\cdot A_{i+1} - F_i \cdot A_i}{V_{i+1/2}}\right) \tag{10}$$

The fluid-state fluxes from each cell are distributed to the fluid-state derivatives computed at the neighboring faces:

$$\left(\frac{dU}{dt}\right)_i = 0.5 \cdot \left[\left(\frac{\Delta U}{\Delta t}\right)_{i-1/2} + \left(\frac{\Delta U}{\Delta t}\right)_{i+1/2}\right] \tag{11}$$

A similar method is used to compute wall-state fluxes at the center of each wall cell [12]; however, since the wall states are at the center of the wall cells, no distribution of fluxes is required:

$$\left(\frac{dT_w}{dt}\right)_i = \left(\frac{1}{\rho_w \cdot c_{w_i} \cdot \Delta x_i}\right)\left[\frac{k_+(T_{w_{i+1}} - T_{w_i})}{x_{i+1} - x_i} - \frac{k_-(T_{w_i} - T_{w_{i-1}})}{x_i - x_{i-1}} - \dot{q}_{w_i}\right] \tag{12}$$

where the wall material specific heat (c_w) is a function of local wall temperature and k_+ and k_- are weighted wall thermal conductivity values for neighboring cells computed using the harmonic mean discussed in Ref. [12]. Note that the forced convection heat transfer between the wall and fluid has been introduced.

4.3 Boundary Conditions. Fluid boundary conditions are applied each time step at the inlet and exit of each line in a network. These boundary conditions are specified depending on network connectivity and consist of a global inlet, global exit, or junction boundary condition. At the global inlet(s) to the network, the stagnation enthalpy and entropy are specified based on a given stagnation pressure and stagnation temperature and the predicted velocity. Resulting fluid density and internal energy are determined from REFPROP, thus allowing for determination of the fluid states at the inlet. At the global exit(s) to the network, the static pressure is specified. The internal energy and velocity states along with this specified pressure are used with REFPROP to determine density and total energy. The prescribed inlet and exit conditions may be specified as functions of time. At line junctions, the contributions of the time-rate changes in the primary variables contained in U of Eq. (1) and T_w of Eq. (6) are summed to give total time-rate change at the junction node. For each junction of a given line, the neighboring line numbers and boundaries (i.e., inlet or exit) are stored to make implementation of this boundary condition straightforward.

The main boundary conditions between the fluid and the wall are friction and heat transfer. Friction factors are computed for the flow at each cell face shown in Fig. 1 (denoted by "fluid-state location") using the correlation given in Eq. (7) and used directly in the computation of the source vector (S) in Eq. (1). Heat transfer is computed for each cell using the correlation given in Eq. (8). Since the wall temperature solution locations ("wall thermal state locations" in Fig. 1) correspond to the fluid domain computational cells, this heat flux is used directly in the computation of the wall temperature derivative given by Eq. (12). For the heat transfer term in the source vector (S), which is computed using a face-centered discretization (fluid-state locations in Fig. 1), the average heat transfer computed for the two neighboring cells is used.

4.4 Temporal Solution. Once the state derivatives are computed at each computational node, standard SIMULINK® solvers are used to solve the discretized equations as a function of time. Four variable-step solvers were investigated for solving Eqs. (1)–(6) on the computational domain, all of which are suited to stiff systems of differential equations like those considered here. The most rigorous of these is the implicit solver ode23s, which is a one-step solver based on a modified Rosenbrock formula of order 2 [17]. Ode15s is a multistep solver based on numerical differentiation formulas (NDFs) [17], which are related to the backward differentiation formulas (also known as Gear's method) but are more efficient [16]. Ode23t is an implementation of the trapezoidal rule using a "free" interpolant that is effective for moderately stiff problems [16]. Ode23tb uses the TR-BDF2 [18] two-stage procedure where the first stage is a trapezoidal rule step and the second stage is a backward differentiation formula of order 2 [16]. References [16,17] provide additional details on the solvers.

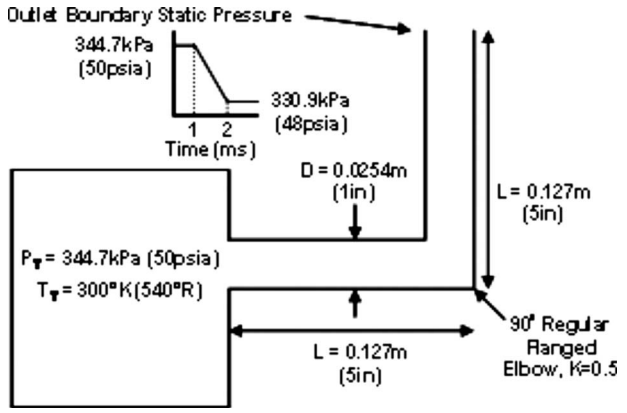

Fig. 2 Simple pipe geometry

5 Results

Several test cases have been generated to evaluate the merits of the procedure described here. Solutions were obtained with both versions of the solver for comparison. Results are presented below.

5.1 Gaseous Nitrogen Flow in a Pipe. A transient pipe flow simulation of gaseous nitrogen in a pipe has been performed to demonstrate the capability of the present procedure for gaseous flows. Although the current test case corresponds to low-speed flow, additional test cases have been executed with lower exit pressure and greater velocities such that greater compressibility effects were present. A 0.254 m (10 in.) pipe with a 0.0254 m (1 in.) diameter and 90 deg elbow at 0.127 m (5 in.) was used for these simulations, as shown in Fig. 2. The surface roughness of the pipe was 2.54×10^{-6} m (0.0001 in.), a typical value for commercially smooth pipe. The inlet total as well as initial exit static pressure were held at 345 kPa (50 psi (absolute)). The inlet total temperature was held at 300 K (540 R). Thus, the initial velocity of the flow in the pipe was zero. At 0.001 s, the exit static pressure was reduced to 331 kPa (48 psi (absolute)) over 0.001 s (linear ramp). This reduction in pressure simulates a fast-acting valve opening downstream of the line, which initiates a series of expansion and compression waves in the pipe and an increase in flow velocity. At steady-state, static pressure in the pipe settles to a nonuniform distribution along the length of the pipe with inlet pressure higher than exit due to friction losses. The flow velocity grows asymptotically until it reaches a steady-state distribution. The simulation was run to steady-state when both pressure and velocity distributions remain time independent. A grid-convergence study was performed in which 9, 17, 33, 65, and 129 uniformly spaced grid points were used along each pipe. The unsteady simulations with grid densities greater than or equal to 33 points per pipe predicted essentially the same waveforms, frequencies, and amplitudes indicating that grid-convergence occurred with 33 points over each 0.127 m (5 in.) pipe. The converged "steady-state" pressure losses and velocities were also predicted to be the same with grid densities greater than 33 points per pipe. The simulation results with 33 grid points (32 cells) are shown below.

Figure 3 shows the predicted pressure, velocity, and enthalpy as a function of time using the implicit SIMULINK® solver ode23s. Sinusoidal variation in pressure with time is evidence of the expansion and compression waves propagating through the pipe. Time-variation in the velocity corresponds to these waves. Velocity increases until it reaches an average value of 65.9 m/s (216.3 ft/s). Figure 4 shows the pressure, velocity, and enthalpy distributions at steady-state. Pressure and enthalpy decrease along the length of the pipe due to viscous effects, with a large jump at 0.127 m (5 in.) due to the minor loss in the elbow. Figure 5(*a*)

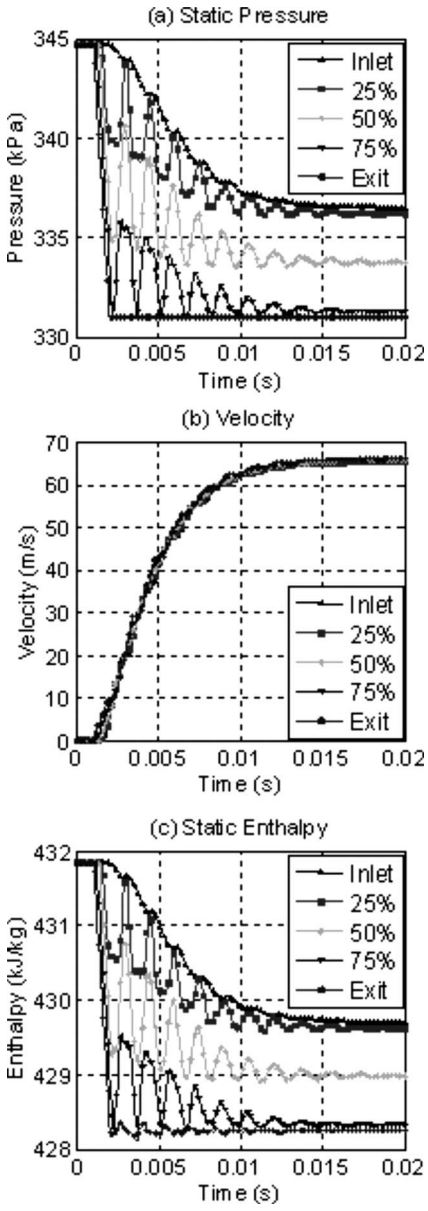

Fig. 3 Nitrogen transient pipe flow

compares transient pressure predictions of the model at the midpoint of the pipe using four different SIMULINK® solvers. The solvers, based on the NDF equations (ode15s), trapezoidal rule (ode23t), and TR-BDF2 solver (ode23tb), give very similar results to the implicit solver (ode23s). However, these solvers run in about 4% of the computational time required for the implicit solver (7443 s for the 0.02 s simulation), making them attractive for quick turn-around analyses. The NDF solver only slightly underpredicts the pressure oscillation frequency after three cycles, while the other solvers show better agreement to frequency and amplitude of the implicit solver results. Finally, Fig. 5(*b*) compares the pressure solution obtained with the implicit solver (ode23s) with the solution obtained using the explicit version of the FORTRAN code discussed in Ref. [9]. The two solvers produce very similar results with only small differences between pressure wave amplitude and frequency. The 0.02 s FORTRAN simulation runs in about 135 s using the explicit solver or in about half the time of the faster SIMULINK® solvers.

A hand calculation [9] for the steady-state case assuming incompressible flow yields a static pressure drop of 5.4095 kPa

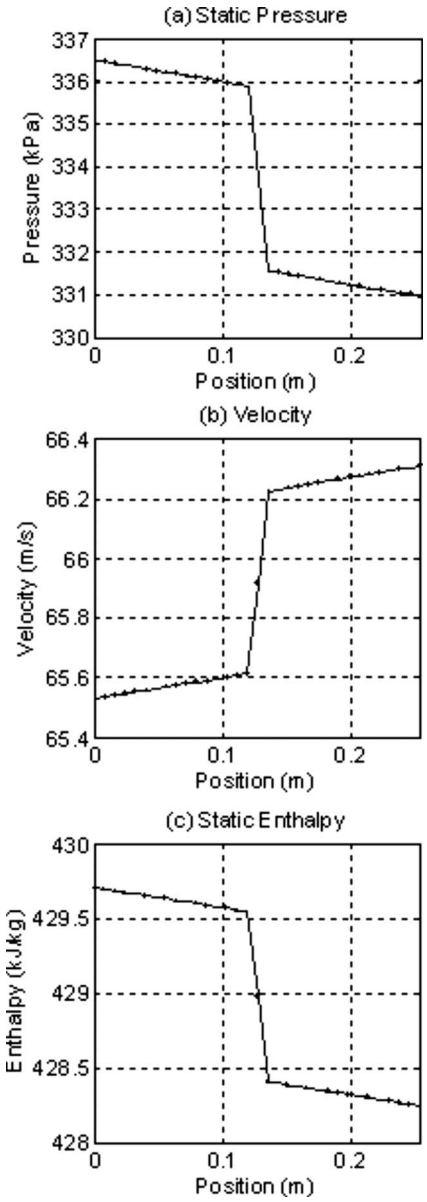

Fig. 4 Nitrogen pipe flow at steady-state

(0.7846 psi (differential)) and a flowrate of 0.1275 kg/s (0.2810 lbm/s). The simulation yields a steady-state static pressure drop of 5.5480 kPa (0.8047 psi (differential)) and a flowrate of 0.1264 kg/s (0.2788 lbm/s). Thus, the simulation results differ from the hand calculations by 2.6% in pressure and 0.8% in flow. However, the hand calculation is expected to have some error due to the incompressibility assumption. Thus, the steady-state simulation results are verified by independent hand calculations.

The period of pressure oscillations can be compared with the period expected for frictionless flow (e.g., organ pipe modes) as a check of the transient response of the computational solution. The pressure waves inside the pipe travel at slightly less than the speed of sound, where the difference is a result of friction losses. Thus, pressure oscillations should occur close to the natural frequency of the pipe (c/2L) or 696 Hz for this case. The oscillation frequency of the first wave in the simulation is 680 Hz, which is slightly lower than the natural frequency of the pipe. The frequency of subsequent waves is lower due to the increasing effects of friction losses as the flow velocity increases. A series of inviscid simulations was also run in which the exit static pressure was dropped over the 0.001 s time interval by 3.4 kPa (0.5 psi (differential)), 13.8 kPa (2 psi (differential)), the same as viscous simulation) and 41.4 kPa (6 psi (differential)) to determine the effects of friction and compressibility. The frequencies of the first wave for these simulations were 685 Hz, 676 Hz, and 649 Hz, respectively. These results, along with the viscous results, show that the frequency of the traveling wave is a function of both the viscous effects and compressibility of the flow. As the exit static pressure drop increases from 3.4 kPa to 41.4 kPa, the velocity of the flow increased, thereby increasing the compressibility of the nitrogen. Steady-state velocities for these cases ranged from 42.2 m/s (138.4 ft/s) to 149.4 m/s (490.2 ft/s). As the compressibility increased, the wave frequency decreased somewhat. The best agreement with the theoretical natural frequency was when the compressibility was minimal. Thus, the method produces transient results in keeping with physical expectations.

5.2 Incompressible Flow in a Pipe. The same configuration described above in Fig. 2 was used for water flow simulation to demonstrate the capability to predict transient flows in essentially incompressible fluids. The critical difference for incompressible fluids is that wave speeds are much larger than in compressible fluids, resulting in smaller time steps for numerical stability. The same time-dependent boundary conditions as discussed above are imposed on the inlet and outlet planes of the pipe. Figures 6 and 7 show the transient and steady-state solutions for the water flow simulation computed using solver ode23tb (the TR-BDF2 solver) with a maximum time step of 1×10^{-5} s. Small amplitude pressure oscillations are evident throughout the duration of the simulation, and the flow relaxes gradually to its equilibrium state. The

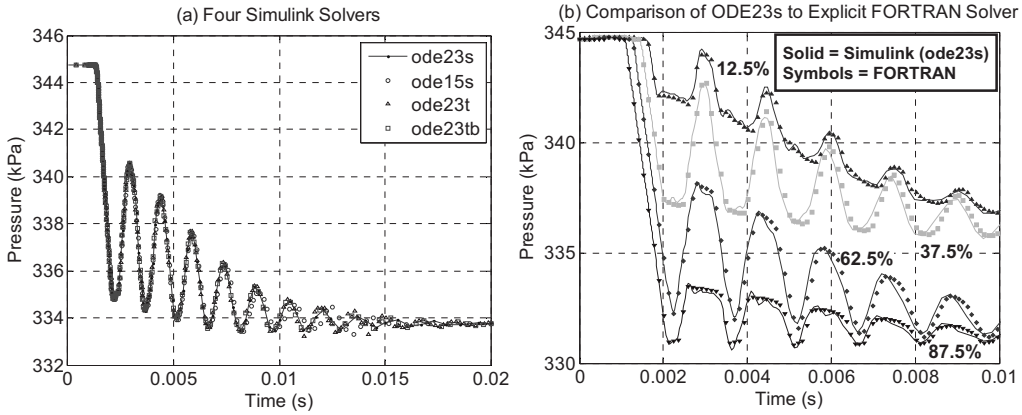

Fig. 5 Transient solution with various solvers

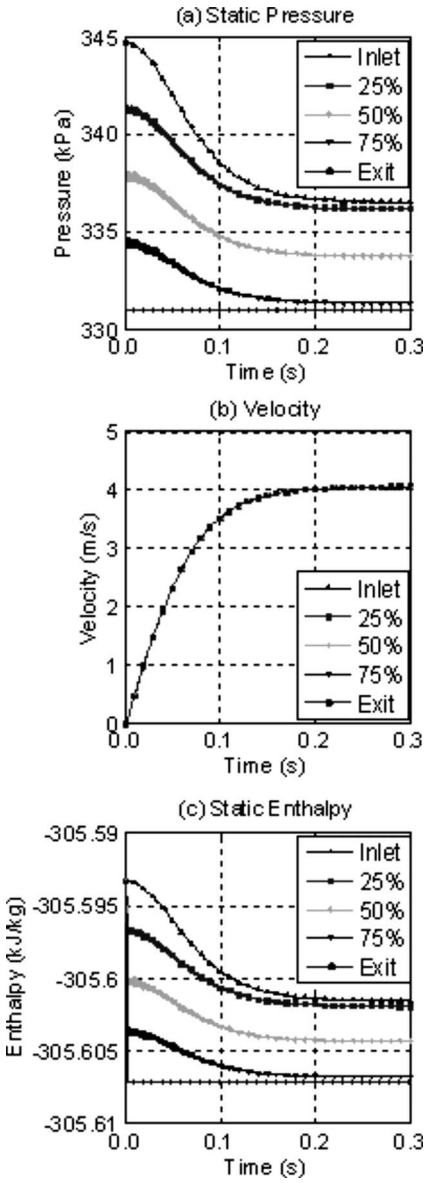

Fig. 6 Water transient pipe flow

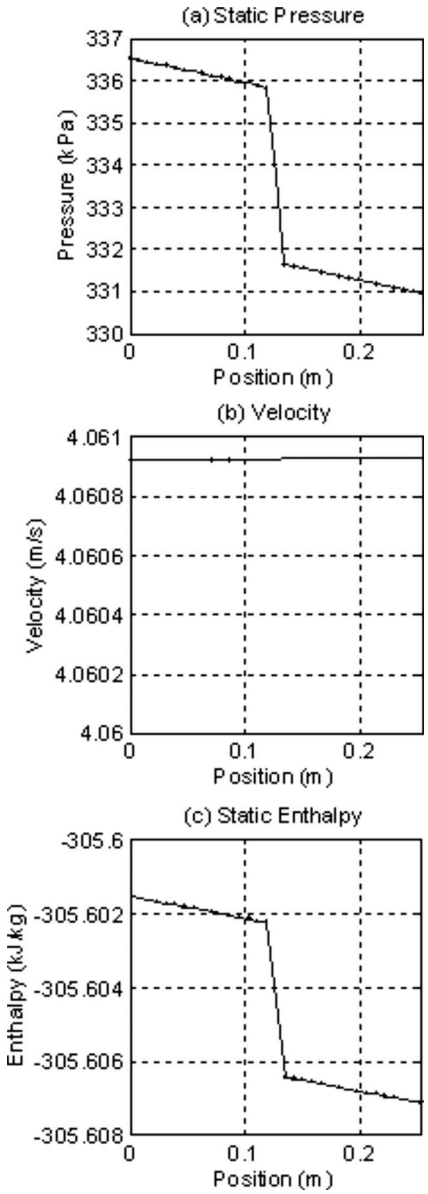

Fig. 7 Water pipe flow at steady-state

time to reach steady-state for water is much longer than that required for nitrogen due to the incompressibility of the fluid. At steady-state, the flow velocity is nearly constant, as expected for a nearly incompressible fluid. Figure 8 shows the first 0.004 s of static pressure and enthalpy variation (velocity variation is initially negligible) and demonstrates good agreement of the SIMULINK® results to the explicit version of the FORTRAN code for oscillation frequency and magnitude.

As with the nitrogen case, the steady-state water solution can be compared with a hand calculation for the same conditions. Both the hand calculation and simulation yield flowrates of 2.0508 kg/s (4.5213 lbm/s) and static pressure drops of 5.5762 kPa (0.8088 psi (differential)). The agreement between the hand calculation and simulation is better for water since the assumption of incompressible flow is more correct for water compared with gaseous nitrogen.

5.3 Cryogenic Fluids With Heat Transfer. The current procedure can also be used to solve for transient behavior of cryogenic fluids, including heat transfer between fluid and pipe. A simple case similar to the one described above was modeled with liquid parahydrogen to demonstrate this capability. A 0.6096 m (24 in.) long straight pipe with an inner diameter of 0.0254 m (1 in.) and a surface roughness of 2.54×10^{-6} m (0.0001 in.) was used. The initial fluid temperature was set at 22.22 K (40 R) and the initial pressure was 345 kPa (50 psi (absolute)). The inlet total pressure was held at 345 kPa (50 psi (absolute)) and the inlet total temperature was held at 22.22 K (40 R). Thus, the initial flow velocity in the pipe was zero. The copper pipe had a 0.003175 m (0.125 in.) thick wall, which was initially set to the same temperature as the fluid. At 0.001 s, the exit static pressure was reduced to 331 kPa (48 psi (absolute)) over 0.001 s (linear ramp). The pipe wall was subjected to zero heat transfer at the inlet and outlet boundaries. The conditions for this problem were chosen to avoid the two-phase flow since this capability is currently not implemented. The problem was modeled using the TR-BDF2 solver (ode23tb) with a maximum time step of 1×10^{-5} s and 32 computational cells along the domain. While the temperature change of the wall is expected to be small for this case, it demonstrates the capability to model conjugate heat transfer using this procedure.

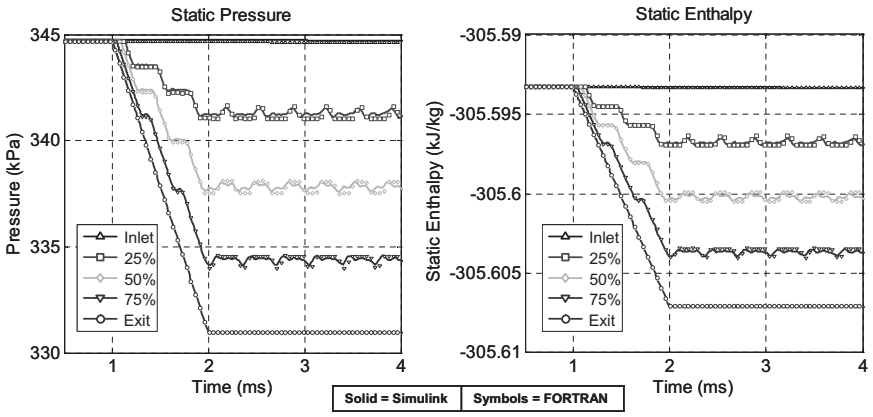

Fig. 8 Comparison of water transient results with FORTRAN code

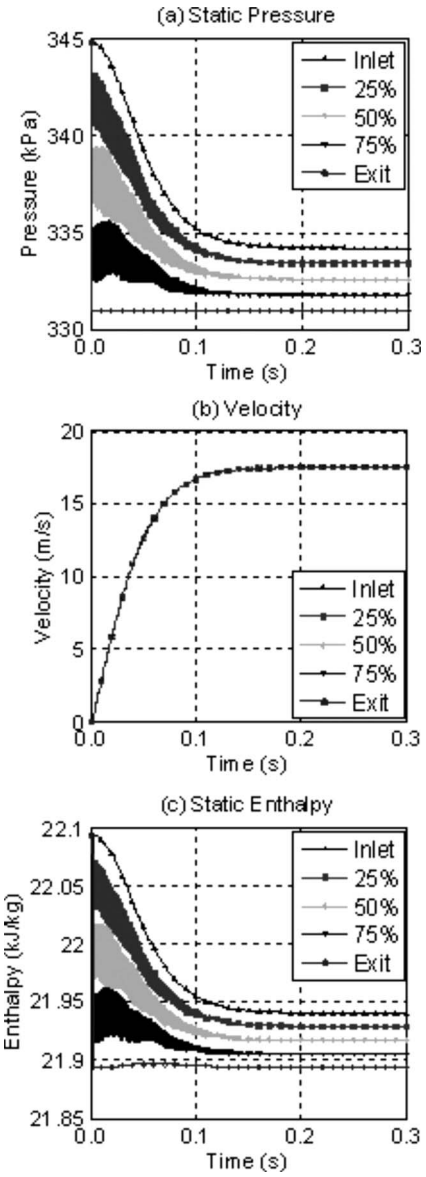

Fig. 9 Liquid hydrogen transient pipe flow

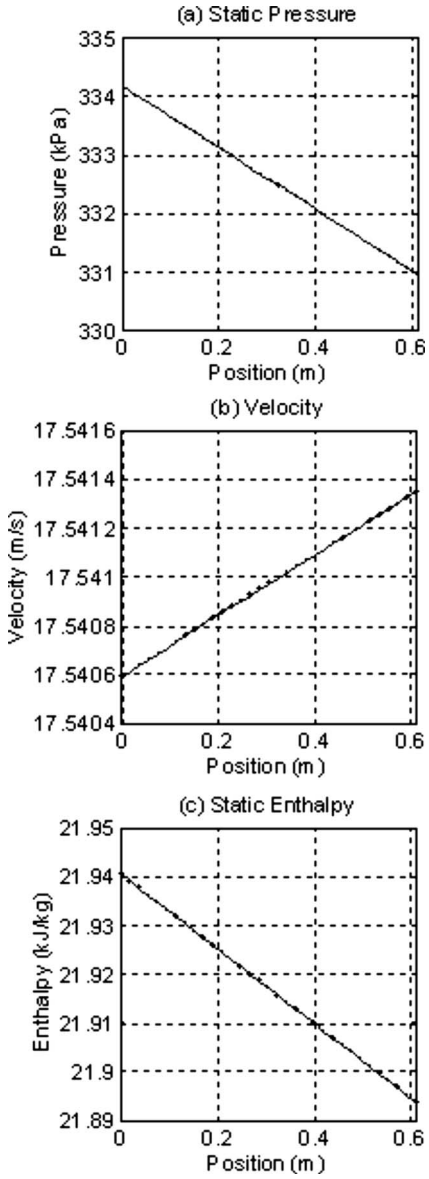

Fig. 10 Liquid hydrogen pipe flow at steady-state

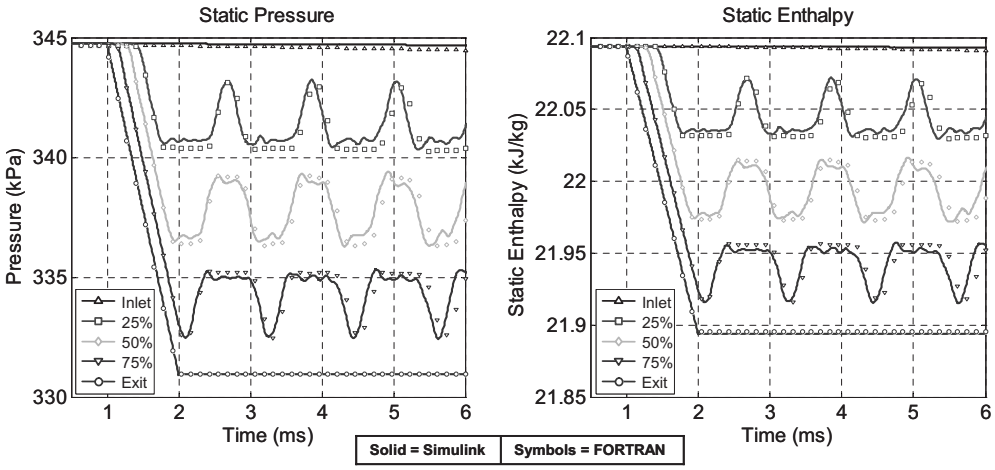

Fig. 11 Comparison of hydrogen transient results with FORTRAN code

Figures 9 and 10 show the transient and steady-state fluid solutions for the liquid hydrogen flow simulation. Pressure oscillations of moderate amplitude are evident throughout the duration of the simulation, and the flow relaxes gradually to its equilibrium state. Since liquid hydrogen compressibility is lower than gaseous nitrogen and higher than liquid water, its behavior is between the previous cases. The time to reach steady-state is similar to the water case. At steady-state, the flow velocity is nearly constant, as expected for a fluid with low compressibility. Figure 11 shows the first 0.006 s of static pressure and enthalpy variation (velocity variation is initially negligible) and demonstrates good agreement of the SIMULINK® results to the explicit version of the FORTRAN code for oscillation frequency and magnitude.

Figures 12 and 13 show the pipe wall temperature history and distribution during the simulation. As shown in Fig. 12, the wall temperature decays as the flow accelerates and the static temperature of the liquid hydrogen is reduced. The wall temperature begins to change first at the pipe outlet since the fluid velocity increases there first. The wall temperature reaches a steady-state distribution within 0.3 s. Figure 13 shows the wall temperature distribution along the length of the pipe at several times during the simulation. Initially ($t=0$), the pipe wall is at a constant temperature. As the flow is established at the exit of the pipe, the wall temperature drops due to forced convection heat transfer. As the flow velocity increases during the simulation, the wall temperature continues to drop. At the end of the simulation ($t=0.3$ s), the pipe wall has reached a temperature distribution in equilibrium with the fluid static temperature distribution, which is shown as circular symbols in the plot.

As with the previous cases, the steady-state solution can be compared with a hand calculation for the same conditions. The hand calculation yields a flowrate of 0.6109 kg/s (1.3467 lbm/s) and a static pressure drop of 3.2222 kPa (0.4673 psi (differential)). At steady-state, the simulation indicates a flowrate of 0.6108 kg/s (1.3467 lbm/s) and a static pressure drop of 3.2230 kPa (0.4675 psi (differential)), or percent differences of 0.004 and 0.02, respectively. The agreement between the incompressible hand calculation and simulation is better for liquid hydrogen compared with gaseous nitrogen, but not as good as water since the compressibility of liquid hydrogen falls between liquid water and gaseous nitrogen.

6 Conclusion

A procedure has been developed for the numerical solution of transient quasi-1D flow in lines and volumes including the effects of friction, minor losses, real-fluid properties, and heat transfer between the fluid and bounding wall. The unique new features and results described include (1) the first-time use of MATLAB/SIMULINK® for detailed transient conjugate real-fluid network flows, (2) the implementation of multiple algorithms that enable the fastest solution turn-around for the desired resolution of unsteady flow physics, (3) the documentation of three fundamental test cases of nitrogen, water, and cryogenic parahydrogen including unsteady pressure, velocity, enthalpy, and wall temperature that can be used by other researchers, and (4) back-to-back com-

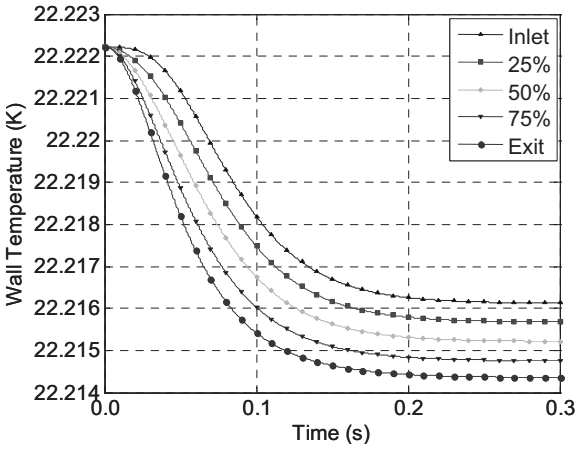

Fig. 12 Wall temperature transient

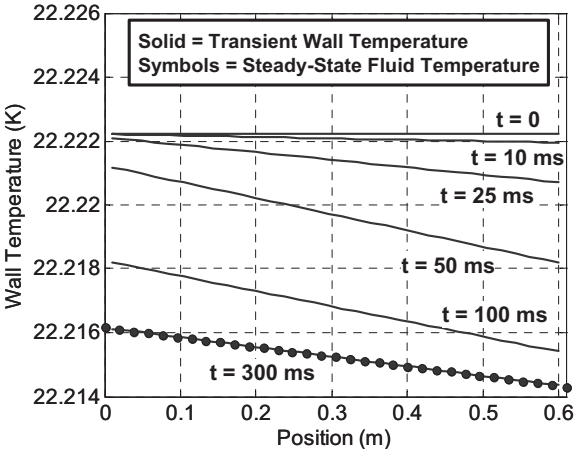

Fig. 13 Wall temperature distribution

parison of fundamental test cases between the SIMULINK® and FORTAN95 solvers and analytical theory. Real-fluid properties are obtained from a NIST fluid property database, allowing both compressible and incompressible flow problems to be treated using the same procedure. For cases with wall heat transfer, the heat conduction equation is solved simultaneously with the fluid equations to provide conjugate solutions. Various compressible and incompressible unsteady flow test cases are presented for verification.

Acknowledgment

The authors wish to acknowledge the U.S. Air Force Research Laboratory for funding this program under Contract No. FA9300-04C-0008, and Mr. Sean Kenny, AFRL program manager, for the Upper Stage Engine Technology (USET) program.

Nomenclature

- A = cross-sectional area
- A_p = perimeter
- a_r = relative acceleration between inertial and absolute frames of reference
- c = fluid speed of sound
- c_w = wall material specific heat
- D = flow passage hydraulic diameter
- E = fluid total energy $=\rho(e+u^2/2)$
- e = fluid internal energy
- f = fluid friction coefficient
- F = vector of fluid mass, momentum, and energy fluxes
- h = forced convection heat transfer coefficient
- H = fluid static enthalpy referenced to fluid normal boiling point at 1atm
- H_{total} = fluid stagnation enthalpy referenced to fluid normal boiling point at 1atm
- i = cell index
- K = minor loss coefficient
- k = fluid thermal conductivity
- k_w = wall material thermal conductivity
- L = domain length
- Nu_D = Nusselt number based on hydraulic diameter ($\text{Nu}_D=hD/k$)
- p = fluid static pressure
- p_{total} = fluid stagnation pressure
- Pr_f = fluid Prandtl number evaluated at film temperature ($\text{Pr}=c_p\mu/k$)
- q_w = heat flux from the wall to the fluid
- Re_D = local flow Reynolds number based on hydraulic diameter ($\text{Re}_D=\rho uD/\mu$)
- Re_f = local flow Reynolds number based on hydraulic diameter evaluated at film temperature
- s = fluid entropy
- S = source vector
- t = time
- T_B = fluid bulk static temperature
- $T_{B,\text{total}}$ = fluid bulk stagnation temperature
- T_f = film temperature ($T_f=(T_w+T_B)/2$)
- T_w = wall temperature
- U = fluid-state vector
- u = fluid absolute velocity
- u_r = relative velocity of moving frame of reference
- V = fluid cell volume
- x = distance along the solution domain
- Δx_i = length of computational cell i
- ε = wall roughness height
- ρ = fluid density
- ρ_w = wall material density
- τ_w = shear force between wall and fluid (friction)
- μ = fluid molecular viscosity

References

[1] Majumdar, A. K., and Flachbart, R. H., 2003, "Numerical Modeling of Fluid Transients by a Finite Volume Procedure for Rocket Propulsion Systems," Proceedings of the Fourth ASME/JSME Joint Fluids Engineering Conference, Honolulu, HI, Paper No. FEDSM2003-45275.

[2] Mason, J. R., and Southwick, R. D., 1991, "Large Liquid Rocket Engine Transient Performance Simulation System," NASA Report No. CR-184099.

[3] Veres, J. P., and Lavelle, T. M., 2000, "Mean Line Pump Flow Model in Rocket Engine System Simulation," NASA Report No. TM-2000-210574.

[4] Wallis, G., 1969, *One-Dimensional Two-Phase Flow*, McGraw-Hill, New York, Chap. 6.

[5] Potter, M. C., and Somerton, C. W., 1993, *Thermodynamics for Engineers* (Schaum's Outline Series), McGraw-Hill, New York.

[6] Wiley, E. B., 1997, *Fluid Transients in Systems*, Prentice-Hall, Englewood Cliffs, NJ.

[7] Machmoum, A., and Seaïd, M., 2003, "A Highly Accurate Modified Method of Characteristics for Convection-Dominated Flow Problems," Computational Methods in Applied Mathematics, **3**(4), pp. 623–646.

[8] Mäkinen, J., Piché, R., and Ellman, A., 2000, "Fluid Transmission Line Modeling Using a Variational Method," ASME J. Dyn. Syst., Meas., Control, **122**, pp. 153–162.

[9] Davis, R. L., and Campbell, B. T., 2007, "Quasi-1D Unsteady Flow Procedure for Real Fluids," AIAA J., **45**(10), pp. 2422–2428.

[10] NIST Database 23: NIST REFPROP, "Reference Fluid Properties," Software Package, Version 7.0, National Institute of Standards and Technology, Boulder, CO.

[11] Anderson, D. A., Tannehill, J. C., and Pletcher, R. H., 1984, *Computational Fluid Mechanics and Heat Transfer*, Hemisphere, New York, Chap. 9.

[12] Patankar, S. V., 1980, *Numerical Heat Transfer and Fluid Flow*, Hemisphere, New York, Chap. 4.

[13] Churchill, S. W., 1977, "Friction-Factor Equation Spans All Fluid-Flow Regimes," Chem. Eng. (New York, NY), **84**(24), pp. 91–92.

[14] Pitts, D. R., and Sissom, L. E., 1977, *Schaum's Outline of Theory and Problems of Heat Transfer*, McGraw-Hill, New York.

[15] Flow of Fluids Through Valves, Fittings, and Pipe, 1969, Crane Co. Technical Paper No. 410, New York.

[16] Using Simulink, 2006, Version 6.4, The MathWorks.

[17] Shampine, L. F., and Reichelt, M. W., 1997, "The Matlab ODE Suite," SIAM J. Sci. Comput. (USA), **18**(1), pp. 1–22.

[18] Shampine, L. F., and Hosea, M. E., 1996, "Analysis and Implementation of TR-BDF2," Appl. Numer. Math., **20**, pp. 21–37.

Motion of a Single Newtonian Liquid Drop Through Quiescent Immiscible Visco-Elastic Liquid: Shape and Eccentricity

Ritu Gupta

R. K. Wanchoo[1]
e-mail: wanchoo@pu.ac.in
e-mail: ravinderwanchoo@gmail.com

Department of Chemical Engineering and Technology,
Panjab University,
Chandigarh 160014, India

The shape of a single Newtonian liquid drop moving freely under gravity in quiescent non-Newtonian liquid (visco-inelastic and visco-elastic) has been studied. Strong effect of fluid elasticity on the shape of Newtonian liquid drop has been observed. Based on experimental observations, a shape regime graph has been suitably modified for elastic fluids. Correlations have also been proposed for the prediction of eccentricity of the Newtonian liquid drop moving through a non-Newtonian visco-elastic liquid.
[DOI: 10.1115/1.3054284]

Keywords: drop shape, eccentricity, Newtonian–non-Newtonian liquid, visco-elastic fluid

1 Introduction

The process of fluid droplets moving through an immiscible continuous phase liquid due to the difference in density is a common phenomenon in any chemical process industry. Since dispersing one phase in the other facilitates the heat and mass transfer rates between the phases, it is important to study the hydrodynamics involved in the motion of single fluid particles through quiescent immiscible fluids. In chemical engineering practice, the phenomenon of bubble and drop motion through rheologically complex fluids occurs in fermenters, mixing, separation, and heat and mass transfer equipment.

Knowledge of the fundamentals of the bubble or drop motion behavior, particularly bubble or drop shape, and terminal velocity are of great importance for understanding the characteristics of such processes. The change in fluid particle shape affects the interfacial area that in turn affects the transfer coefficients in heat and mass transfer equipment.

Considerable work has been reported on the rise or fall of liquid drops in Newtonian media, as may be seen from the several reviews given by Astarita and Appuzzo [1], Calderbank et al. [2], Grace et al. [3], Clift et al. [4], and Wanchoo et al. [5]. However, reported data on the rise or fall of drops in non-Newtonian medium are limited.

Acharya et al. [6] and Acharya and Mashelkar [7] studied the influence of viscoelasticity and shear dependent viscosity of ambient liquids on the motion of the liquid drops and bubbles. For a low Reynolds number range ($\mathrm{Re}<1$), these authors observed that the influence of viscoelasticity on the motion of liquid drop was insignificant. For $\mathrm{Re}>1$, these authors reported that the influence of viscoelasticity was significant for visco-elastic fluids (polyacrylamide (PAM) and polyethylene oxide (PEO)) and the drag was higher than visco-inelastic fluids (carboxy methylcellulose (CMC)), due to the large size of wake formed in such fluids.

Drop distortion and oscillation will change the shape of a moving drop and hence will change the drag coefficient and the terminal velocity. Distortion and oscillation tend to increase the drag and reduce the terminal velocity over that for a rigid sphere of equal volume. Hughes and Gilliland [8] and Garner and Hammerton [9] made some efforts to correlate the shape and amount of distortion as a function of drop or bubble size and other measurable system properties.

If D_X is the largest horizontal dimension of the drop and D_Y is the largest vertical dimension of the drop, then drop eccentricity E, $E=D_x/D_y$, has been used as a parameter by a large number of investigators to report their data by correlating E with other dimensionless groups, such as the Reynolds number ($\mathrm{Re}=DU\rho_C/\mu_C$ for Newtonian liquids and $\mathrm{Re}=D^nU^{2-n}\rho_C/K$ for non-Newtonian liquids, where K is the flow consistency index and n is the flow behavior index of the non-Newtonian continuous phase liquid; ρ_c is the density of the continuous phase liquid and μ_c is the viscosity of the Newtonian continuous phase liquid; and U is the terminal velocity of drop with spherical equivalent diameter, D), Eotvos number ($\mathrm{Eo}=(g(\rho_d-\rho_c)D^2/\sigma)$, where σ is the interfacial tension, ρ_d is the density of dispersed phase liquid, and g is the acceleration due to gravity), Weber number ($\mathrm{We}=DU^2\rho_c/\sigma$), and Morton number ($\mathrm{Mo}=(g(\rho_d-\rho_c)\mu_C^4/\rho_c^2\sigma^3)$ for Newtonian liquids and $(g(\rho_d-\rho_c)K^4/\rho_c^2\sigma^3)(U/D)^{4n-4}$ for non-Newtonian liquids).

Reinhart [10] correlated his data on nonoscillating drops of various liquids in gases in terms of drop eccentricity, E, and expressed as

$$E=1+0.13\ \mathrm{Eo}\quad \text{for}\quad 1<\mathrm{Eo}<8.2 \tag{1}$$

Wellek et al. [11] correlated the data on drop eccentricity, E, of their own and others for 45 liquid-liquid pairs in terms of Weber (We) and Eotvos (Eo) numbers as

$$E=1+0.091\ \mathrm{We}^{0.95}\quad \text{for}\quad 0.194\le \mathrm{We}\le 12.6 \tag{2}$$

$$E=1+0.091\ \mathrm{We}^{0.98}(\mu_c/\mu_d)^{0.07} \tag{3}$$

and almost as well by

$$E=1+0.129\ \mathrm{Eo}\quad \text{for}\quad 0.144\le \mathrm{Eo}\le 9.59 \tag{4}$$

$$E=1+0.163\ \mathrm{Eo}^{0.757} \tag{5}$$

Takahashi et al. [12] developed the graphical representation for E as a function of product of Reynolds and Morton number, $\mathrm{ReMo}^{0.23}$, for bubbles of air in various aqueous Newtonian solutions. They represented the behavior segmentally with empirical relations given below

$$E=1\quad \text{for}\quad \mathrm{ReMo}^{0.23}<2 \tag{6}$$

[1]Corresponding author.

Contributed by the Fluids Engineering Division of ASME for publication in the JOURNAL OF FLUIDS ENGINEERING. Manuscript received January 5, 2008; final manuscript received October 22, 2008; published online January 9, 2009. Assoc. Editor: James A. Liburdy.

$$E = \frac{1.14}{(\mathrm{ReMo}^{0.23})^{0.176}} \quad \text{for} \quad 2 \le \mathrm{ReMo}^{0.23} \le 6 \tag{7}$$

$$E = \frac{1.36}{(\mathrm{ReMo}^{0.23})^{0.28}} \quad \text{for} \quad 6 \le \mathrm{ReMo}^{0.23} \le 16.5 \tag{8}$$

$$E = 0.62 \quad \text{for} \quad \mathrm{ReMo}^{0.23} > 16.5 \tag{9}$$

However, these authors report that no such correlation could be obtained for prolate drops.

Acharya et al. [6] reported the shape of bubbles in visco-elastic fluids. The bubbles were of a tear shape at a small Reynolds number, and with an increased Reynolds number the shape changed from spherical to oblate spheroidal and then to spherical cap. These authors further reported the bubble shape in terms of eccentricity expressed as

$$E = 0.616[G_1]^{-0.168} \quad \text{for} \quad 0.68 < E < 1 \tag{10}$$

$$E = 1 + 0.00083[G_2]^{-0.87} \quad \text{for} \quad 1 < E < 1.5 \tag{11}$$

where $G_1 = K_1(U/R)^m/(\sigma/R)$ is the ratio of elastic stress to surface tension stress, and $G_2 = (\mathrm{Wi}/\mathrm{ReWe})$. Wi is the Weissenberg number defined as $\lambda_t(U/2R)$, with λ_t as the characteristic time of the continuous fluid, and R is the radius of the drop.

Mohan et al. [13] reported the shape of the drop moving in non-Newtonian fluids and concluded that the small sized drop is spherical, but with the increase in drop diameter the drop assumes the shape of an oblate spheroid. A further increase in drop diameter causes oblate→prolate oscillation, which finally results in the distortion of the drop. Addition of polymer to the continuous phase medium causes the drop to tend to a spherical shape and reduces the terminal velocity of the smaller drops. However, the terminal velocity of larger ones remains unaffected.

Motion of Newtonian liquid drop in Newtonian liquid media has been studied by many authors and expressions are available for predicting the terminal velocity and shape of the drop formed, based on the physical properties of the dispersed and continuous phases. For bubbles or drops rising or falling in infinite media, a classical generalized graphical correlation in terms of the Eotvos number, Eo; Morton number, Mo; and Reynolds number, Re, has been proposed by Clift et al. [4] and Grace et al. [3]. This shape regime graph has been successfully used to predict the terminal velocity and the shape of a drop/bubble moving in an immiscible Newtonian liquid. However, for the motion of a Newtonian drop in non-Newtonian liquids, scant information is available for the prediction of terminal velocity and drop shape. Furthermore, from the available data, it was observed that the rheological parameters (K and n) and interfacial tension (σ) could have a strong effect on the shape of the drop moving through the non-Newtonian liquids. Elasticity of the non-Newtonian liquid could also have strong effect on the shape and hence on the dynamics of the drop. In the case of the motion of bubbles through visco-elastic fluids, Acharya et al. [6] observed the formation of prolate shaped bubbles under low Reynolds number flow conditions. With an increase in Reynolds number, the bubble assumes an oblate shape. However, the effect of "negative wake," present in the case of bubble motion through visco-elastic fluids, is still not clear. In the case of the motion of droplets through visco-elastic fluids, the formation of a negative wake has not been reported.

Wanchoo et al. [14] proposed a shape regime graph for the prediction of the shape and terminal velocity of drops moving freely under gravity in visco-inelastic liquids. These authors have also correlated their drop eccentricity data in terms of Eo number and proposed the following correlations:

$$E = 1 + 0.146\ \mathrm{Eo}^{0.437} \quad \text{for} \quad \text{oblate drops}(E > 1) \tag{12}$$

$$E = 1 - 0.086\ \mathrm{Eo}^{0.338} \quad \text{for} \quad \text{prolate drops}(E < 1) \tag{13}$$

Ohta et al. [15] reported their experimental observations on the motion of a Newtonian spherical drop rising freely through inelastic shear thinning fluids represented by the Cross–Carreau model. Numerical evaluation of their results has indicated that the effect of shear thinning on drop motion could be significant.

While reporting the numerical evaluation results on the motion of a Newtonian deformed drop rising through a quiescent shear thinning fluid represented by the Carreau–Yasuda model, Ohta et al. [16,17] observed that the extent of local viscosity change depends on the drop shape, and the remarkable feature of the deformed drop was that a much higher viscosity region at the rear of the drop was formed due to the effect of stagnant flow field behind the drop. Furthermore, their experimental results reveal that the shape of a Newtonian drop moving through a quiescent visco-inelastic fluid changes from spherical to oblate (ellipsoidal) with increase in the Eo number. These results can be safely obtained from the shape regime graph proposed earlier by Wanchoo et al. [14]. Most of the important results related to the motion and shape of fluid particles in non-Newtonian media have been well summarized and reviewed by Chhabra [18].

It is well accepted that the dynamics of fluid particles in non-Newtonian media is influenced by a large number of process, physical, and kinematic variables. In recent years, considerable research efforts have been directed toward carrying out the parametric studies that in turn have helped in elucidating the role of non-Newtonian fluid characteristics on fluid particle dynamics. Nevertheless, in comparison to the study of the motion of fluid particles in Newtonian fluids, a number of unanswered questions still remain to be addressed while considering the motion of fluid particles in non-Newtonian fluid systems including visco-elastic fluids. Available literature indicate that during the free rise/fall of fluid particles in stagnant liquids, entirely different shapes are observed in non-Newtonian systems depending on the degree of shear thinning and viscoelasticity of continuous phase liquid in comparison to Newtonian continuous phase liquid. Likewise the literature on terminal velocity and drag coefficient–Reynolds number relationships also abounds with contradictions and conflicting inferences [18]. In conclusion, our understanding of the behavior of fluid particles in rheologically complex fluids is far from being satisfactory.

The aim of the present investigation is to elucidate experimentally the effect of the elastic nature of non-Newtonian continuous phase (visco-elastic fluid) on the shape of a moving Newtonian fluid drop and based on experimental results, to correlate the drop shape in terms system dimensionless groups. Observed experimental data shall also be used to generate a shape regime graph in terms of characteristic dimensionless groups for a Newtonian drop moving through a quiescent non-Newtonian continuous phase liquid.

2 Materials and Methods

The present study was conducted with the sole aim of studying the effect of density (ρ), viscosity (μ), interfacial tension (σ), rheological parameters (flow consistency index K and flow behavior index n), and fluid elasticity (λ_t) of the continuous phase on the shape of the Newtonian liquid drop formed during its descent in an immiscible non-Newtonian (visco-inelastic/visco-elastic) liquid.

It was necessary to select various combinations of Newtonian dispersed phase and non-Newtonian (visco-inelastic/visco-elastic) continuous phase, so that the effect of physical properties, such as density, viscosity, interfacial tension, rheological parameters (K and n), and the fluid relaxation time (λ_t) could be well elucidated.

In order to accomplish the objectives; the experimental study was divided into the following two sections:

(1) evaluation of the rheological parameters, physical properties of the continuous and dispersed phases, and the inter-

Table 1 Properties of dispersed and continuous phase liquids

Property	Range
Density of continuous phase, ρ_c	996.86–1037.4 kg/m^3
Density of dispersed phase, ρ_d	1106.3–1592 kg/m^3
Viscosity of dispersed phase, μ_d	0.782–2.066 cP
Flow consistency index, K	0.000982–1.486 Pa s^n
Flow behavior index, n	0.431–1
Fluid characteristic time, λ_t	0.106–15.371, s
Interfacial tension, σ	5.87–47.23, mN/m

facial tension between the dispersed phase and the continuous phase
(2) determination of the terminal velocity and the shape of the drop falling through an immiscible quiescent continuous phase

To have a wider range of process variables, it was decided to use the following combinations of the continuous and the dispersed phases.

(a) Continuous phases

(1) distilled water
(2) glycerol in distilled water (20 wt/vol %)
(3) CMC in distilled water (0.2 wt/vol %, 0.5 wt/vol %, and 1.0 wt/vol %)
(4) polyvinyl pyrrolidone (PVP) in distilled water (0.5 wt/vol %, 0.75 wt/vol %, and 1.0 wt/vol %)
(5) PEO in distilled water (0.8 wt/vol % and 1.6 wt/vol %)
(6) PAM (low viscous) in distilled water (0.01 wt/vol %, 0.1 wt/vol %, and 0.5 wt/vol %)
(7) PAM (high viscous) in distilled water (0.05 wt/vol % and 0.1 wt/vol %)

(b) Dispersed phases

(1) carbon tetrachloride (CCl_4)
(2) bromobenzene (BB)
(3) chlorobenzene (CB)
(4) nitrobenzene (NB)
(5) nitrotoluene (NT)
(6) ethyl chloroacetate (ECA)

The various combinations of these continuous and dispersed phases gave a large variation in the physical properties, including rheological parameters (K, n, and λ_t), continuous phase density, dispersed phase density, viscosity, and interfacial tension (σ). The values are reported in Tables 1 and 2.

Interfacial tension was determined using the standard drop weight method given by Harkins and Brown [19], and the rheological behavior of the test fluids was determined using a cone and plate rheometer (Rotovisco, RT-20, HAAKE, Germany; Sensor: Type C60/1 Ti). The data (τ versus $\dot{\gamma}$) and (η versus $\dot{\gamma}$) indicated that all the fluids were pseudoplastics, and a shear thinning behavior was observed for all the fluids. The data were further subjected to different models, and the model parameters corresponding to best fit were noted. The shear stress versus shear rate data were well described by the Ostwald–de Waele power law model as

$$\tau = K\dot{\gamma}^n \tag{14a}$$

where τ is the shear stress (Pa), $\dot{\gamma}$ is the shear rate (s^{-1}), and K (Pa s^n) and n are the rheological parameters called the flow consistency and flow behavior indices, respectively. Likewise the first normal stress N_1 can also be described by a two parameter model as

$$N_1 = K_1\dot{\gamma}^m \tag{14b}$$

where K_1 and m are model parameters. Based on steady shear $\dot{\gamma}$ data, N_1 was evaluated using the method developed by Abdel-Khalik et al. [20]. Similar to Chhabra et al. [21], the fluid characteristic time, λ_t, characterizing the fluid elasticity was evaluated using K, K_1, n, and m, defined as

$$\lambda_t = \left[\frac{K_1}{2K}\right]^{1/m-n} \tag{15}$$

The shear rate, $\dot{\gamma}_w$, evaluated at wall conditions of the column is related to the apparent shear rate, U/D, at the same wall shear stress [7] as

$$\dot{\gamma}_w = \frac{U}{D} \tag{16}$$

where D is the diameter of the drop.

Viscoelasticity of the continuous liquid phase was defined in terms of the Weissenberg number, Wi, [21] as

$$\mathrm{Wi} = \lambda_t\dot{\gamma}_w \tag{17}$$

The values of physical and rheological parameters of fluids used in the present study are reported in Table 3.

For the measurement of terminal velocity and drop shape, the continuous phase was taken in a glass column of 78 mm inside diameter and 110 cm in height fitted inside a rectangular thermo-

Table 2 Values of interfacial tension, σ (mN/m) at 20°C

Continuous phase	Concentration (wt/vol %)	Dispersed phase					
		CCl_4	CB	BB	NB	NT	ECA
Distilled water	-	47.23	36.81	40.67	28.41	27.41	22.91
Glycerol	20.0	46.56	35.82	39.27	27.14	26.84	22.21
PVP	0.50	47.12	28.45	39.94	28.15	27.04	19.48
	0.75	39.43	25.65	38.72	26.13	26.87	19.39
	1.00	33.94	13.54	29.13	23.06	21.68	16.84
PEO	0.80	38.15	31.04	35.85	24.31	23.31	18.94
	1.60	38.02	30.47	32.52	22.58	23.78	14.60
CMC	0.20	33.52	22.85	32.16	25.65	22.35	19.23
	0.50	32.71	21.84	29.06	21.58	21.23	18.84
	1.00	28.52	20.40	25.06	18.55	19.61	16.44
PAM (LV)	0.01	32.10	27.40	40.06	27.65	20.60	20.49
	0.10	39.35	26.80	21.40	16.52	21.24	8.00
	0.50	14.52	6.85	14.35	8.75	12.71	9.09
PAM (HV)	0.05	35.94	19.69	20.12	12.77	14.24	8.99
	0.10	18.41	7.62	14.37	9.95	7.76	5.87

Table 3 Physical and rheological parameters of the continuous phase at 20°C

Continuous phase	Concentration (wt/vol %)	ρ_c (kg/m^3)	Power law constants K (Pa s^n)	n	λ_t (s)	K_1 (Pa s^m)	m
DW	-	997.9	0.0010	1	-	-	-
Glycerol	20	1037.4	0.0019	1	-	-	-
PVP	0.5	999.0	0.0011	1	-	-	-
	0.75	999.5	0.0011	1	-	-	-
	1	1000.3	0.0012	1	-	-	-
PEO	0.8	998.5	0.0041	1	-	-	-
	1.6	1000	0.0140	1	-	-	-
CMC	0.2	999.4	0.0569	0.80	-	-	-
	0.5	999.85	0.3300	0.72	-	-	-
	1.0	1001.9	1.4860	0.64	-	-	-
PAM (LV)	0.01	999.8	0.0009	1	-	-	-
	0.1	998.1	0.0076	0.87	0.106	0.329	0.932
	0.5	1020	0.4245	0.54	0.334	0.693	0.724
PAM (HV)	0.05	996.86	0.0639	0.62	1.590	0.166	0.621
	0.1	1000.73	0.2752	0.43	15.371	1.004	0.651

static water bath made of an acrylic sheet ($250\times250\times900$ mm^3). With this arrangement, distortion in drop was not observed. Temperature inside the column was maintained at 20 ± 0.1°C using Julabo F-30 water circulator.

The dispersed phase was fed from the micropipette to a special nozzle-cup assembly attached at the top of the glass column for the formation of larger drops. A 50 cc constant head burette fitted at the bottom with a joint, designed for use with a wide range of nozzle sizes ranging from 0.5 mm to 5.0 mm, thus enabling the formation of smaller drop sizes, was also used. The nozzles were made of thin walled glass with grounded tips so that the plane of the tip was at the right angle to the axis of the nozzle.

The dispersed phase liquid was released slowly from the nozzle attached to the burette to form a drop, which then grew to a sufficient size, to break away from the nozzle owing to its weight. To avoid any drop interactions, a time difference of at least 20 min was maintained for the formation of two successive drops, thereby ensuring that the trajectory of one drop does not affect the following drop. The volume of the drop produced at the nozzle was determined by counting the number of drops produced by a given volume of the dispersed phase liquid, as measured by the change in volume of the dispersed phase liquid in the burette. The volume of the drop formed by cup assembly was based on the volume of the dispersed phase liquid taken from the micropipette, assuming that no amount of dispersed phase was retained either in the micropipette or in the cup.

Before starting the experiment, the whole column was divided into three sections 25 cm in length, and drop velocities were measured in the middle and last sections of the column. Drop terminal velocity was observed to remain constant in these two sections within experimental error. For rest of the experiments, terminal velocity was measured in the middle section of the column by noting the time of descent of the liquid drop in the column for a fixed distance of 25 cm in the middle section of the column using an electronic stopwatch (least count=1/100 s). This was repeated four to six times and then an average of three concordant time readings was used for further calculations. A wall correction factor was applied wherever applicable [4,18].

The droplets were photographed during free fall through a custom made central viewing section of optically plane acrylic rectangular outer column to eliminate optical distortion effects of the cylindrical column. A Minolta, X-370S, SLR camera equipped with varying film speeds, lens apertures, and an adjustable focus was used for taking photographs of the drops. Zoom lenses were used whenever needed. The camera was mounted on one side of the droplet viewing section and was focused on a standard glass sphere held in the center of the column before taking the picture of the drop. A Kodak 400 film was used in the camera. To illuminate the drop, two 40 W fluorescent tubes were placed adjacent to each other on a stand and placed at about 15 cm behind the column assembly. All photographs were taken in the middle section of the column at a distance of 35 cm from the nozzle tip.

The image of the glass spherical particle with a diameter of 14 mm used as a reference is given in Fig. 1.

The shape of the drops was represented in terms of eccentricity (E) of the drop (Fig. 1) defined as the ratio of its largest horizontal dimension (D_x) to the largest vertical dimension (D_y). After measuring the respective dimensions, D_x and D_y from the photographs, the drops were then characterized as [4]

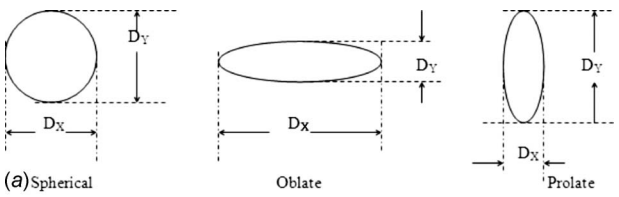

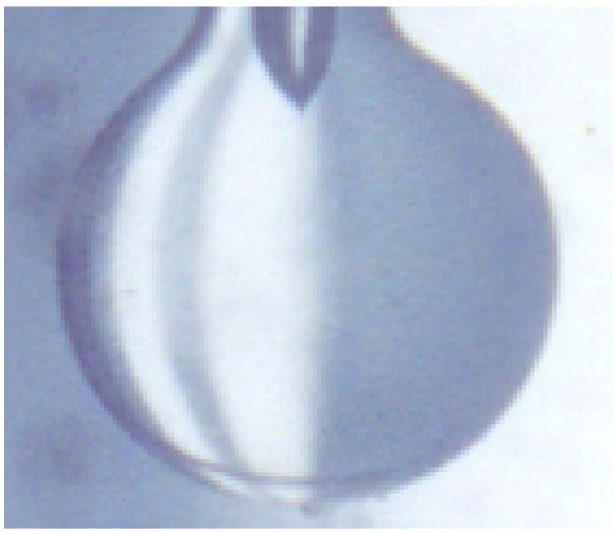

(b)

Fig. 1 Reference glass particle: (*a*) characterization of the drop shape

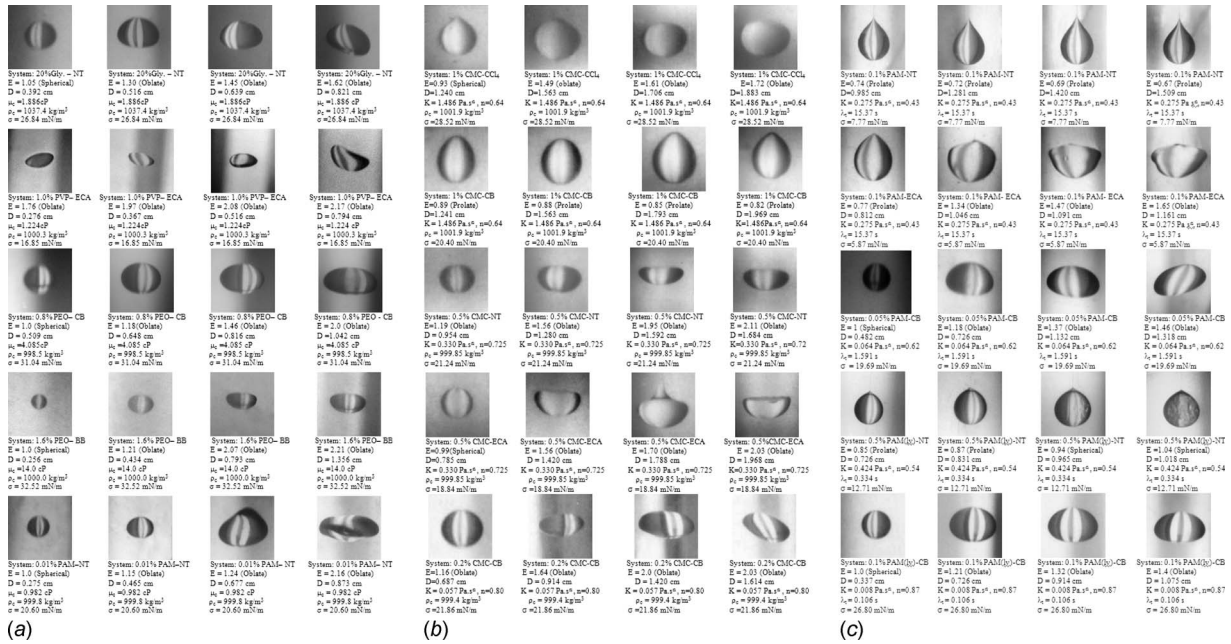

Fig. 2 (*a*) Representative photographs of Newtonian drops in Newtonian liquids, (*b*) representative photographs of Newtonian drops in non-Newtonian (visco-inelastic) liquids, and (*c*) representative photographs of Newtonian drops in non-Newtonian (visco-elastic) liquids

$$0.9 \le E \le 1.1 \quad \text{drop is spherical and } D_V = \frac{D_x + D_y}{2}$$

$$E > 1.1 \quad \text{drop is oblate and } D_V = (D_x)^{2/3}(D_y)^{1/3}$$

$$E < 0.9 \quad \text{drop is prolate and } D_V = (D_x)^{1/3}(D_y)^{2/3}$$

where drop eccentricity $E = D_x / D_y$ and D_v is the equivalent spherical diameter. Representative photographs of a Newtonian drop in various Newtonian and non-Newtonian liquids are shown in Fig. 2(*a*) (Newtonian fluids), Fig. 2(*b*) (visco-inelastic fluids), and Fig. 2(*c*) (visco-elastic fluids).

3 Results and Discussions

3.1 Effect of Physical Properties and System Parameters on Drop Eccentricity (Visual Observations). Drop eccentricity, E, depends on parameters such as D (drop volume equivalent diameter), ρ_d (density of the dispersed phase), μ_d (viscosity of the dispersed phase), μ_c (viscosity of the continuous phase), σ (interfacial tension), K (flow consistency index), n (flow index), and λ_t (fluid characteristic time) in the case of non-Newtonian fluids.

In Newtonian fluids, when all physical properties, such as continuous phase density, dispersed phase density, interfacial tension, and viscosity, were kept constant, the smaller drops (<2 mm in diameter) were spherical in shape, and the shape changed from spherical → oblate as the drop diameter increases. These observations are in confirmation with the earlier observations on the Newtonian-Newtonian system, as reported by other investigators (Refs. [4,3])

In visco-inelastic non-Newtonian fluids, for any pair of dispersed-continuous phase liquids with a specific concentration, smaller drops (<2 mm in diameter) were spherical in shape, and the shape changed from spherical → prolate → oblate with the increase in drop diameter.

In visco-elastic non-Newtonian fluids, keeping the continuous phase density, dispersed phase density, interfacial tension, and apparent viscosity $= K(U/D)^{n-1}$ constant, smaller drops (<2 mm in diameter) were spherical in shape and as the drop diameter increased, the shape changed from spherical → prolate for high values of λ_t (>1.6 s), and from spherical → prolate → oblate for low values of λ_t (≤1.6 s).

As shown in Figs. 3–7, in the case of Newtonian fluids the following were observed.

(i) At constant μ_c, ρ_c, and σ, the drop eccentricity, E, increases with increase in the drop diameter D (Fig. 3).
(ii) At constant μ_c, ρ_c, and D, the drop eccentricity, E, increases with increase in interfacial tension σ (Fig. 4).
(iii) At constant D, μ_c, and ρ_c, the drop eccentricity, E, increases with increase in the drop density ρ_d (Fig. 5).
(iv) For the same values of μ_c, ρ_c, and D, the drop eccentricity, E, decreases with increase in the drop liquid viscosity μ_d (Fig. 6).
(v) The drop eccentricity, E, decreases with increase in continuous phase viscosity μ_c (Fig. 7).

In the case of non-Newtonian visco-inelastic fluids (Figs. 8–10), the following were observed.

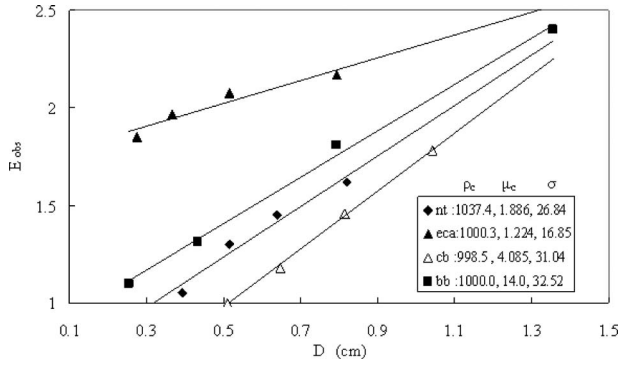

Fig. 3 Effect of drop diameter on drop eccentricity for Newtonian liquids

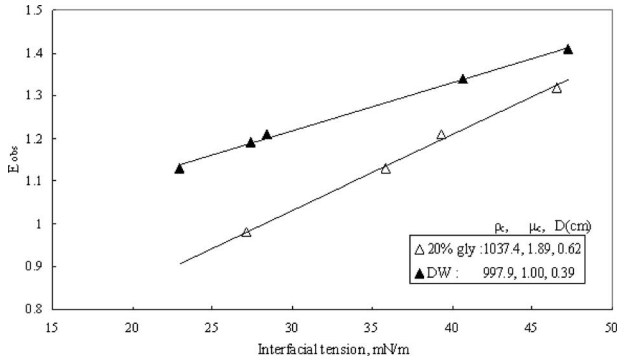

Fig. 4 Effect of interfacial tension on drop eccentricity for Newtonian liquids

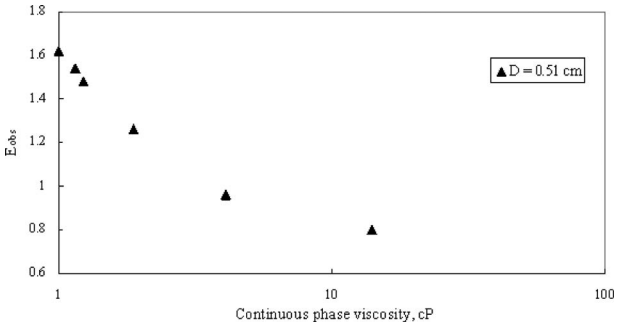

Fig. 7 Effect of continuous liquid viscosity on drop eccentricity for Newtonian liquids

(i) At constant K, n, and σ, the drop eccentricity, E, increases with increase in drop diameter D (Fig. 8).
(ii) At constant K, n, and D, the drop eccentricity, E, increases with increase in interfacial tension σ (Fig. 9).
(iii) For the same value of σ and D, the drop eccentricity, E, decreases with increase in flow consistency index K and decrease in flow behavior index n (Fig. 10).

In the case of non-Newtonian visco-elastic fluids (Figs. 11–13), the following were observed.

(i) At constant K, n, λ_t, and σ, the drop eccentricity, E, increases with increase in drop diameter, D, for $\lambda_t < 1.6$ s, and E decreases with increase in drop diameter, D, for $\lambda_t > 1.6$ s (Fig. 11).
(ii) At constant K, n, λ_t, and D, the drop eccentricity, E, decreases with increase in interfacial tension, σ, at higher values of λ_t (>1.6 s). Also, as can be seen in Fig. 12, at lower values of λ_t (<1.6 s), E first decreases and then increases.
(iii) For the same values of σ and D, the drop eccentricity, E, decreases with increase in λ_t (Fig. 13).

3.2 Terminal Velocity and Drop Shape. Using the observed terminal velocity, rheological parameters, interfacial tension, and physical properties of the dispersed-continuous phases; three dimensionless groups, Re, Mo, and Eo numbers, were calculated. Using these dimensionless groups, the observed data were plotted on the drop shape regime graph proposed by Grace et al. [3] and Clift et al. [4] for Newtonian systems and Wanchoo et al. [14] for non-Newtonian continuous phase fluids (Fig. 14). The following observations were made.

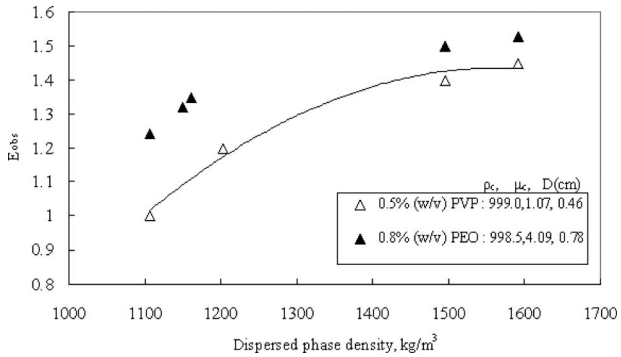

Fig. 5 Effect of dispersed phase density on drop eccentricity for Newtonian liquids

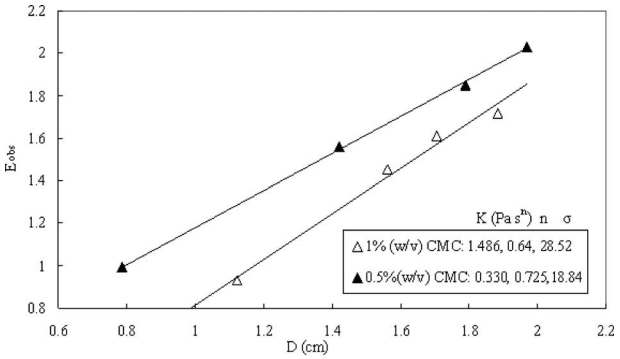

Fig. 8 Effect of drop diameter on drop eccentricity for non-Newtonian (visco-inelastic) liquids

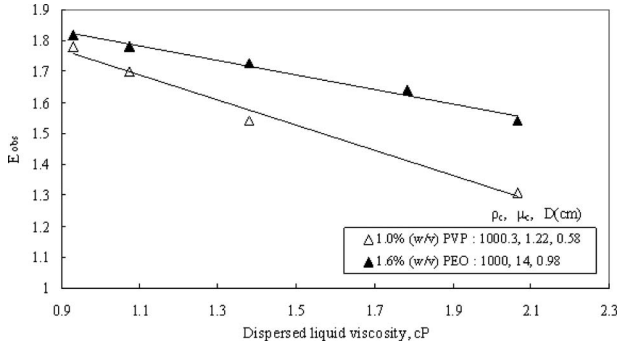

Fig. 6 Effect of dispersed liquid viscosity on drop eccentricity for Newtonian liquids

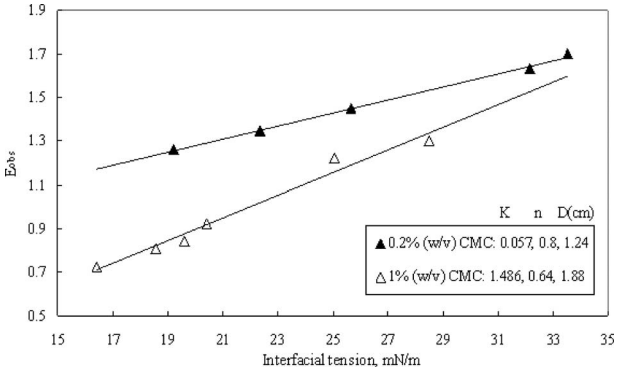

Fig. 9 Effect of interfacial tension on drop eccentricity for non-Newtonian (visco-inelastic) liquids

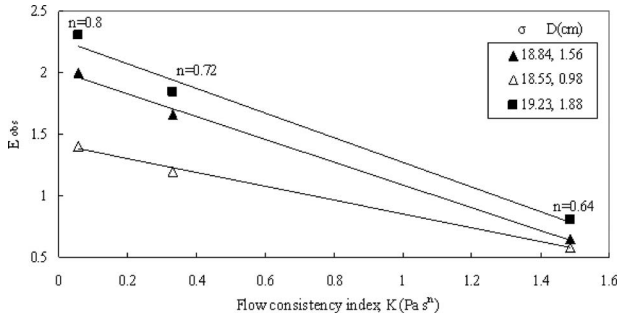

Fig. 10 Effect of flow consistency index (*K*) on drop eccentricity for non-Newtonian (visco-inelastic) liquids

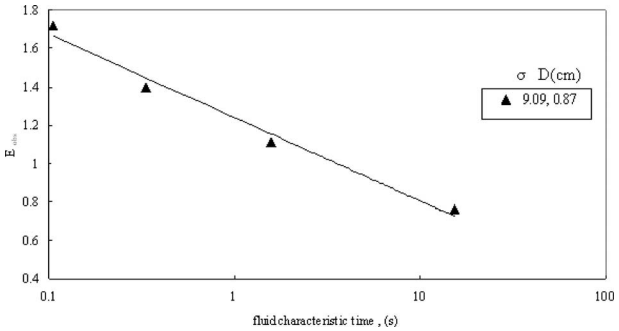

Fig. 13 Effect of fluid characteristic time on drop eccentricity for non-Newtonian (visco-elastic) liquids

(i) From Fig. 14, it was observed that the existing drop shape regime graph given by Grace et al. [3] and Clift et al. [4] explains the behavior of drop eccentricity for drops moving in Newtonian fluids.

(ii) In the case of non-Newtonian visco-inelastic fluids (Fig. 14), the shape of the drop is spherical for $Eo \leq 0.1$ and for all Reynolds numbers. Similar shapes have been reported by Grace et al. [3]. For the present systems, it is also observed that for $0.1 < Eo \leq 1$ and $Re \leq 20$, the shape of the drop is spherical. But for $Re > 20$, the shape of the drop changes from spherical to oblate as $Eo \rightarrow 1$. For $1 \leq Eo \leq 10$ and $Re < 1$, the shape changes from spherical to prolate and for $Re > 1$, the drops assume an oblate shape. For $1 \leq Eo \leq 40$, prolate drops were formed at a lower Reynolds number ($Re < 1$) in the case of fluids with higher K and lower n ($K = 1.486$ Pa s^n, $n = 0.64$), whereas only an oblate shape was observed at $Re > 1$ for systems with lower K and higher n ($K < 0.33$ Pa s^n, $n > 0.72$). For $Eo > 40$, the drops usually assumed a prolate shape for all Reynolds numbers.

(iii) For non-Newtonian visco-elastic fluids (Fig. 14), the shape of the drop was found to have a strong dependence on fluid characteristic time, λ_t, in addition to the parameters such as K, n and the Re, Mo, and Eo numbers. For fluids having $\lambda_t < 1.6$ s, the drop shape was similar to that in visco-inelastic fluids. However, in the case of elastic fluids with higher fluid characteristic time, $\lambda_t > 1.6$ s, for $1 \leq Eo \leq 40$ and $Re > 1$, drops assumed a prolate shape, whereas the shape graph proposed for visco-inelastic fluids predicted the oblate shape, clearly indicating the strong effect of fluid elasticity on the drop shape in this region. Since the Weissenberg number, Wi, has been taken as the representative of the fluid elasticity (defined in Eq. (17)), it was thought worthwhile to remove the ambiguity in the drop shape regime graph by modifying the abscissa of the drop shape regime by replacing Eo by Eo* (i.e., modified

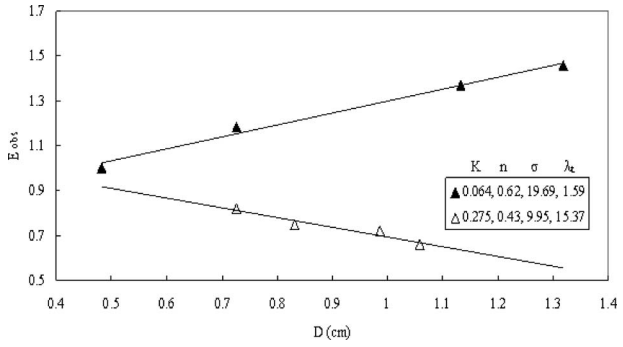

Fig. 11 Effect of drop diameter on drop eccentricity for non-Newtonian (visco-elastic) liquids

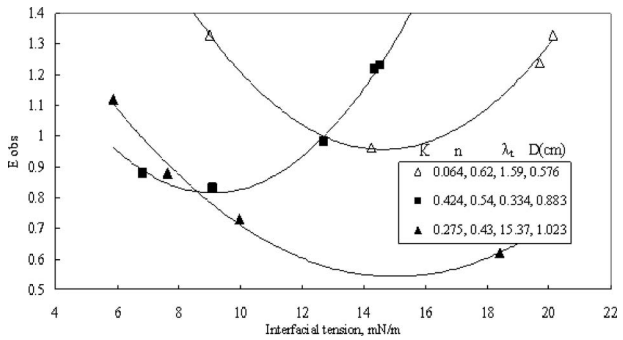

Fig. 12 Effect of interfacial tension on drop eccentricity for non-Newtonian (visco-elastic) liquids

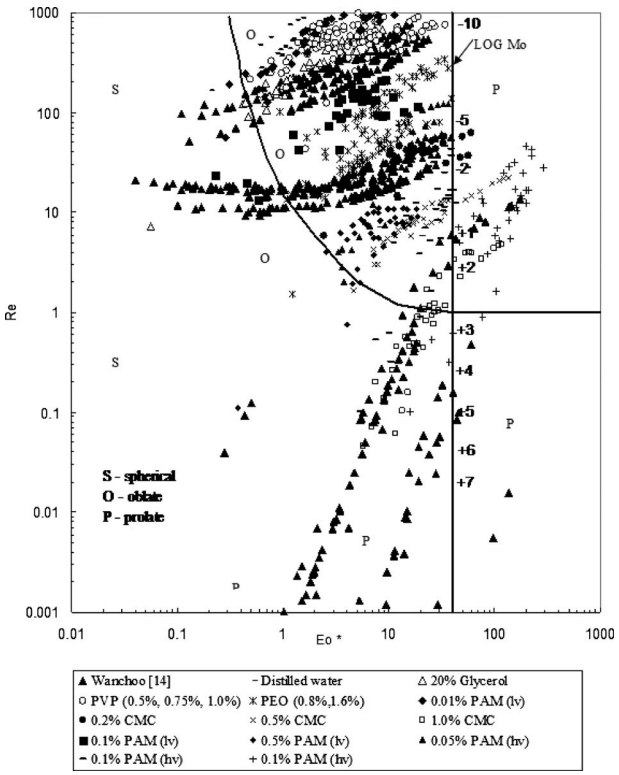

Fig. 14 Shape regimes for Newtonian liquid drop in Newtonian and non-Newtonian (visco-inelastic and visco-elastic) liquids

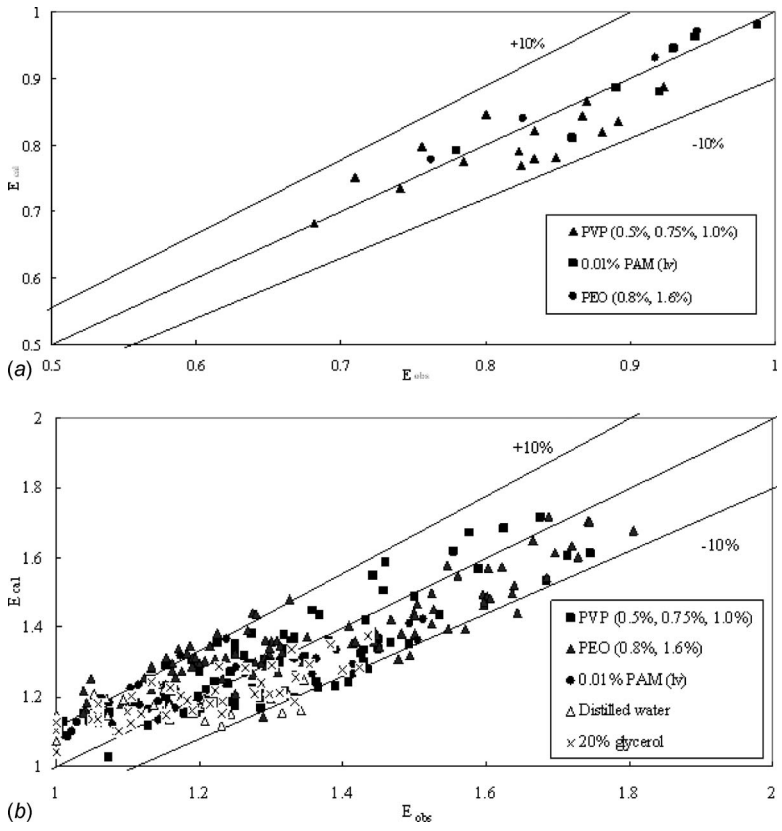

Fig. 15 (*a*) Parity between E_{calc} (Eq. (13)) and E_{obs} for viscous Newtonian systems (prolate) and (*b*) parity between E_{calc} (Eq. (12)) and E_{obs} for viscous Newtonian systems (oblate)

Eotvos number defined as $Eo(1+\sqrt[4]{Wi})$ for visco-elastic fluids). Since for visco-inelastic fluids $Wi \to 0$, the abscissa of the drop shape regime graph for Newtonian fluids is restored. By introducing this modification, drops formed in visco-elastic fluids with a high fluid characteristic time, ($\lambda_t > 1.6$ s), occupy the prolate region of the drop shape graph for $Re > 1$, which is in conformation with the observed drop shape for visco-elastic systems.

3.3 Eccentricity. Eccentricity data on Newtonian fluids and non-Newtonian visco-inelastic fluids were well predicted by the empirical model (Eqs. (12) and (13)) earlier proposed by Wanchoo et al. [14] to within $\pm 10\%$. The parity plots are shown in Figs. 15(*a*), 15(*b*), and 16, respectively.

Eccentricity data on visco-elastic systems are plotted against the Eo number in Fig. 17. A large scatter could be observed for $Eo > 1$. For Eo number less than 1, the drop shape is spherical ($0.9 \leq E \leq 1.1$), as can be observed in Fig. 17 as well. However, no single correlation can explain the whole data, as has been observed by Wellek et al. [11]. In the present study, the method developed by Acharya et al. [6] for the representation of eccentricity data of bubbles was used for the development of correlation in the case of drops moving through visco-elastic fluids. On using

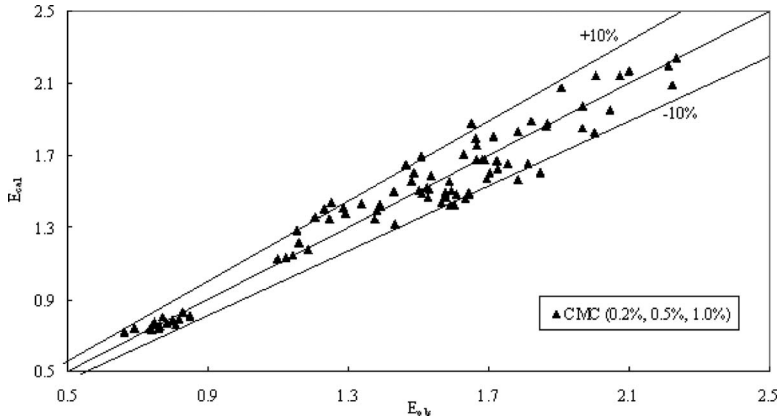

Fig. 16 Parity between E_{calc} (Eqs. (12) and (13)) and E_{obs} for non-Newtonian visco-inelastic systems

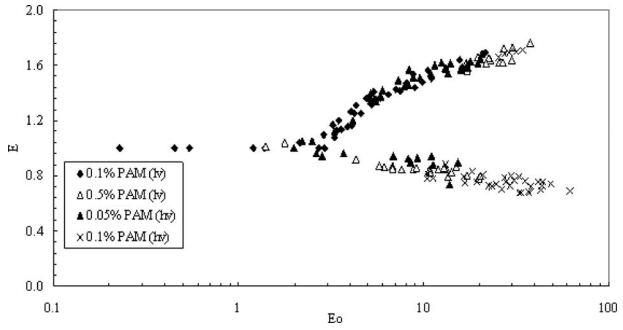

Fig. 17 Observed drop eccentricity data for non-Newtonian visco-elastic liquids

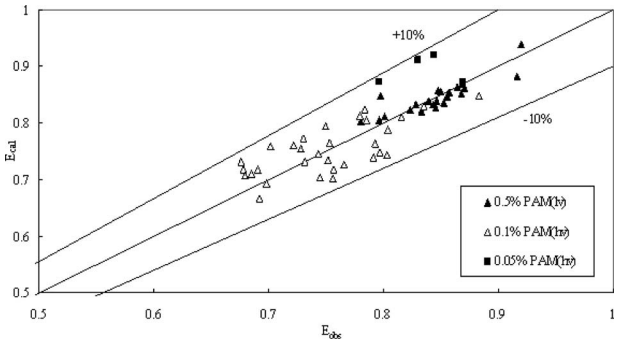

Fig. 18 Parity between E_{calc} (Eq. (18)) and E_{obs} for non-Newtonian visco-elastic systems (prolate)

the correlation proposed by Acharya et al. [6], we observed that their correlation for bubble eccentricity (Eqs. (10) and (11)) underpredicted the present data on drop eccentricity by over 25%.

Attempt was however, made to represent the present eccentricity data by using their coordinates in the form

$$E = c(1/G_1)^d \quad \text{for} \quad E < 1 \text{ (prolate drop)} \tag{18}$$

$$E = 1 + c(G_2)^d \quad \text{for} \quad E > 1 \text{(oblate drop)} \tag{19}$$

where $G_1 = (K_1(U/R)^m/\sigma/R)$ and $G_2 = (\mathrm{Wi}/\mathrm{ReWe})$ are two fluid elastic parameters. c and d are two constants.

Using the nonlinear regression technique, the eccentricity data for oblate and prolate drops moving through quiescent visco-elastic fluids were separately fitted to the model equations. The model parameters, c and d, thus obtained are

Model parameter	Drop shape		95% confidence limits		R^2		Rmsd		Variance	
	Prolate	Oblate	Prolate	Oblate	Prolate	Oblate	Prolate	Oblate	Prolate	Oblate
c	0.772	0.050	±0.007	±0.003						
d	0.125	–0.330	±0.008	±0.013	0.94	0.81	0.004	0.007	0.001	0.003

Respective parity plots for drop eccentricity are given in Figs. 18 and 19. The predicted values of eccentricity, E, agree reasonably well with the experimental data to within ±10%.

Present observed data on drop eccentricity have been compared with the correlations available in literature. Statistical comparison in terms of the parameter mean relative quadratic error (MRQE $= \sqrt{((E_{\exp} - E_{\mathrm{pred}})/E_{\exp})^2/N - 1}$, N is the number of data points) is given in Table 4. From this table, it is observed that our correlations (Eqs. (12) and (13)) explain the present data on drop eccentricity involving Newtonian and non-Newtonian visco-inelastic continuous fluids to a reasonable accuracy as compared with other correlations. Correlations proposed for drop eccentricity involving visco-elastic systems represent the present data very well compared with the correlations proposed by Acharya et al. [6]. Drop eccentricity data on Newtonian–Newtonian and Newtonian–non-Newtonian visco-elastic fluid systems available in the literature were also compared with the predictions of Eqs. (12), (13), (18), and (19). Statistical comparison in terms of the parameter, MRQE, is given in Table 5. Our predictions are also quite reasonable for viscous non-Newtonian fluid systems. Figure 20 shows a parity plot between the literature data and the predicted eccentricity using the present correlation. The data fits reasonably well within ±15%.

4 Conclusions

From the present study the following conclusions can be made.

(1) Drop eccentricity of a fluid particle moving through an immiscible viscous, visco-inelastic, and visco-elastic fluid is influenced by the various stresses operating at the interface due to inertial force, viscous/shear force, and elastic force.
(2) The drop shape regime graph generated for the motion of the Newtonian liquid drops through an immiscible non-Newtonian liquid (visco-inelastic) has shown some discrepancy when compared with the drop shape regime graph for Newtonian-Newtonian system of Grace et al. [3] and Clift et al. [4]. This discrepancy obtained could be due to the shear dependent viscosity of the non-Newtonian fluids. In the case of visco-elastic fluids, the magnitude of fluid elasticity has appreciable effect on drop shape ($\lambda_t > 1.6$ s). There seems to be some justification for the generation/

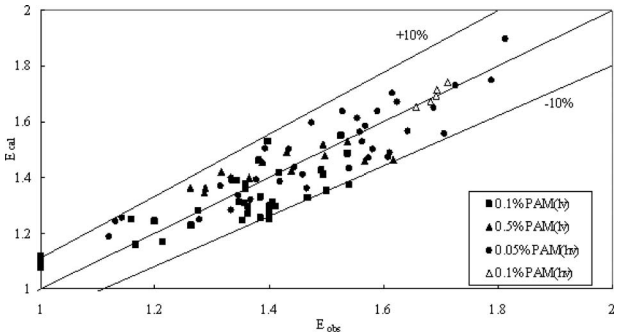

Fig. 19 Parity between E_{calc} (Eq. (19)) and E_{obs} for non-Newtonian visco-elastic systems (oblate)

Table 4 Statistical comparison of different correlations for the prediction of eccentricity *E* with the present data

	MRQE							
System	Reinhart [10], Eq. (1)	Wellek et al. [11], Eq. (2)	Wellek et al. [11], Eq. (3)	Wellek et al. [11], Eq. (4)	Wellek et al. [11], Eq. (5)	Takahashi et al. [12], Eqs. (6) and (9)	Acharya et al. [6], Eqs. (10) and (11)	Present model, Eqs. (12) and (13) or Eqs. (18) and (19)
Distilled water	0.106	0.162	0.106	0.113	0.117	0.205	-	0.088
20% glycerol	0.266	0.152	0.263	0.222	0.132	0.236	-	0.064
PVP	0.731	0.238	0.724	0.358	0.146	0.394	-	0.07
PEO	0.867	3.394	0.858	0.394	0.143	0.461	-	0.1
CMC	3.251	0.463	3.225	0.312	1.573	0.462	-	0.191
PAM (LV) 0.01%	0.421	0.294	0.417	0.156	0.321	0.287	-	0.082
PAM (LV) 0.1% 0.5%	0.855	0.399	0.848	0.316	0.609	0.284	0.263	0.109
PAM (HV)	3.566	1.013	3.529	1.308	2.009	0.381	0.332	0.085

Table 5 Statistical comparison of present model with literature data on viscous Newtonian and non-Newtonian visco-elastic fluids

	MRQE			
Data	Model of Wellek et al. [11], Eqs. (2) and (3)	Model of Wellek et al. [11], Eqs. (4) and (5)	Model of Acharya et al. [6], Eqs. (10) and (11)	Present correlations, Eqs. (12), (13), (18), and (19)
Keith and Hixson [22]	0.368	0.357	-	0.093
Klee and Treybal [23]	0.199	0.208	-	0.137
Wellek et al. [11]	0.228	0.136	-	0.103
Yeheskel and Kehat [24]	0.268	0.189	-	0.094
Acharya et al. [6]	0.364	0.382	0.211	0.073

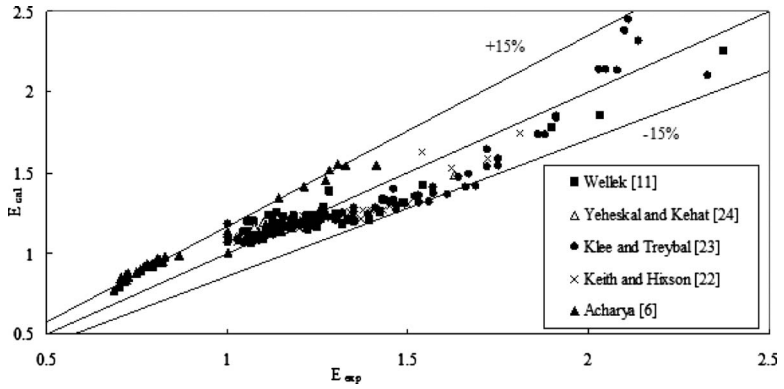

Fig. 20 Parity between eccentricity from literature data and calculated eccentricity using the present model (Eqs. (12) and (13) and Eqs. (18) and (19))

modification of the drop shape regime graph for the Newtonian–non-Newtonian visco-elastic systems.

(3) The shape of a Newtonian liquid drop, expressed in terms of drop eccentricity, *E*, moving through a Newtonian fluid and visco-inelastic continuous liquid phase is well represented by the correlations (Eqs. (12) and (13)) developed by Wanchoo et al. [14]. In the case of visco-elastic fluids, drop eccentricity data are well represented by the proposed correlations (Eqs. (18) and (19)).

(4) As is shown in Table 5, our correlations (Eqs. (12), (13), (18), and (19)) do predict the experimental data of other investigators (those by Keith and Hixson [22], Klee and Treybal [23], Wellek et al. [11], Yeheskal and Kehat [24], and Acharya et al. [6]) within a reasonable accuracy with a minimum mean relative quadratic error of 0.073 in comparison to models available in the literature (Refs. [11,6]).

References

[1] Astarita, G., and Appuzzo, G., 1965, "Motion of Gas Bubbles in Non-Newtonian Liquids," AIChE J., **11**, pp. 815–820.

[2] Calderbank, P. H., Johnson, D. S. L., and Loudon, J., 1970, "Mechanics and Mass-Transfer of Single Bubbles in Free Rise Through Some Newtonian and Non-Newtonian Liquids," Chem. Eng. Sci., **25**, pp. 235–256.

[3] Grace, J. R., Wairegi, T., and Nguyen, T. H., 1976, "Shapes and Velocities of Single Drops and Bubbles Moving Freely Through Immiscible Liquids," Trans. Inst. Chem. Eng., **54**, pp. 167–173.

[4] Clift, R., Grace, J. R., and Weber, M. E., 1978, *Bubbles, Drops and Particles*, Academic, New York.
[5] Wanchoo, R. K., Sharma, S. K., and Gupta, R., 1999, "Motion of Single Liquid Drops in an Immiscible Liquid: Correlation for Drag Coefficient and Terminal Velocity," Indian Chem. Eng., Sect. B, **41**(2), pp. 285–297.
[6] Acharya, A., Mashelkar, R. A., and Ulbrecht, J., 1977, "Mechanics of Bubble Motion and Deformation in Non-Newtonian Media," Chem. Eng. Sci., **32**, pp. 863–872.
[7] Acharya, A., and Mashelkar, R. A., 1978, "Motion of Liquid Drops in Rheologically Complex Fluids," Can. J. Chem. Eng., **56**, pp. 19–25.
[8] Hughes, G. R. R., and Gilliland, E. R., 1952, "The Mechanics of Drops," Chem. Eng. Prog., **48**, pp. 497–504.
[9] Garner, F. H., and Hammerton, D., 1954, "Circulation Inside Gas Bubbles," Chem. Eng. Sci., **3**, pp. 1–11.
[10] Reinhart, A., 1964, "Das Verhalten Fallender Tropfen," Chem. Ing. Tech., **36**, pp. 740–744.
[11] Wellek, R. M., Agrawal, A. K., and Skelland, A. H. P., 1966, "Shape of Liquid Drops Moving in Liquid Media," AIChE J., **12**, pp. 854–862.
[12] Takahashi, T., Miyahara, T., and Izawa, H., 1976, "Drag Coefficient and Wake Volume of Single Bubbles Rising Through Quiescent Liquid," Kagaku Kogaku Ronbunshu, **2**, pp. 480–487.
[13] Mohan, V., Nagarajan, R., and Venkateswarlu, D., 1972, "Fall of Drops in Non-Newtonian Media," Can. J. Chem. Eng., **50**, pp. 37–40.
[14] Wanchoo, R. K., Sharma, S. K., and Gupta, R., 2003, "Shape of a Newtonian Liquid Drop Moving Through an Immiscible Quiescent Non-Newtonian Liquid," Chem. Eng. Process., **42**, pp. 387–393.
[15] Ohta, M., Iwasaki, E., Obata, E., and Yoshida, Y., 2003, "A Numerical Study of the Motion of a Spherical Drop Rising in Shear-Thinning Fluid Systems," J. Non-Newtonian Fluid Mech., **116**, pp. 95–111.
[16] Ohta, M., Iwasaki, E., Obata, E., and Yoshida, Y., 2005, "Dynamic Processes in a Deformed Drop Rising Through Shear-Thinning Fluids," J. Non-Newtonian Fluid Mech., **132**, pp. 100–107.
[17] Ohta, M., Yoshida, Y., and Sussman, M., 2006, "Three-Dimensional Computations of the Motion of a Newtonian Drop Rising Through Immiscible Quiescent Shear-Thinning Liquids," J. Chem. Eng. Jpn., **39**(4), pp. 394–400.
[18] Chhabra, R. P., 2006, *Bubbles, Drops and Particles in Non-Newtonian Fluids*, 2nd ed., CRC, Boca Raton, FL.
[19] Harkins, W. D., and Brown, F. E., 1919, "The Determinations of Surface Tension and the Weight of Falling Drops," J. Am. Chem. Soc., **41**, pp. 499–524.
[20] Abdel-Khalik, S. I., Hassager, O., and Bird, R. B., 1974, "Prediction of Melt Elasticity From Viscosity Data," Polym. Eng. Sci., **14**, pp. 859–867.
[21] Chhabra, R. P., Tiu, C., and Ulherr, P. H. T., 1981, "A Study of Wall Effects on the Motion of a Sphere in Viscoelastic Fluids," Can. J. Chem. Eng., **59**, pp. 771–775.
[22] Keith, F. W., Jr., and Hixson, A. N., 1955, "Liquid-Liquid Extraction Spray Columns," Ind. Eng. Chem., **47**, pp. 258–267.
[23] Klee, A. J., and Treybal, R. E., 1956, "Rate of Rise or Fall of Liquid Drops," AIChE J., **2**, pp. 444–447.
[24] Yeheskel, J., and Kehat, E., 1971, "The Size and Rate of Shedding of Wakes of Single Drops in a Continuous Medium," Chem. Eng. Sci., **26**, pp. 1223–1233.

J. Enrique Julia
Departamento de Ingeniería Mecánica y Construcción,
Campus de Riu Sec,
Universitat Jaume I,
Castellon 12071, Spain
e-mail: bolivar@emc.uji.es

Basar Ozar

Abhinav Dixit

School of Nuclear Engineering,
Purdue University,
400 Central Drive,
West Lafayette, IN 47907-2017

Jae-Jun Jeong
Korea Atomic Energy Research Institute,
150 Dukjin, Yuseong,
Daejeon 305-353, Republic of Korea

Takashi Hibiki

Mamoru Ishii[1]

School of Nuclear Engineering,
Purdue University,
400 Central Drive,
West Lafayette, IN 47907-2017

Axial Development of Flow Regime in Adiabatic Upward Two-Phase Flow in a Vertical Annulus

This study has investigated the axial development of flow regime of adiabatic upward air-water two-phase flow in a vertical annulus. The inner and outer diameters of the annulus are 19.1 mm and 38.1 mm, respectively. The hydraulic diameter of the flow channel, D_H, is 19.0 mm and the total length is 4.37 m. The flow regime map includes 72 flow conditions within a range of 0.01 m/s $<\langle j_g \rangle <$ 30 m/s and 0.2 m/s $<\langle j_f \rangle <$ 3.5 m/s, where $\langle j_g \rangle$ and $\langle j_f \rangle$ are, respectively, superficial gas and liquid velocities. The flow regime has been classified into four categories: bubbly, cap-slug, churn, and annular flows. In order to study the axial development of flow regime, area-averaged void fraction measurements have been performed using impedance void meters at three axial positions corresponding to $z/D_H = 52$, 149, and 230 simultaneously, where z represents the axial position. The flow regime indicator has been chosen to be statistical parameters from the probability distribution function of the area-averaged void fraction signals from the impedance meters, and self-organized neural networks have been used as the mapping system. This information has been used to analyze the axial development of flow regime as well as to check the predictions given by the existing flow regime transition models. The axial development of flow regime is quantified using the superficial gas velocity and void fraction values where the flow regime transition takes place. The predictions of the models are compared for each flow regime transition. In the current test conditions, the axial development of flow regime occurs in the bubbly to cap-slug (low superficial liquid velocities) and cap-slug to churn (high superficial liquid velocities) flow regime transition zones. [DOI: 10.1115/1.3059701]

Keywords: two-phase flow, flow regime, flow pattern, annulus, neural network

1 Introduction

Multiphase flows are encountered in a wide range of important industrial applications. In particular, gas-liquid two-phase flows can be observed in boilers, the core or steam generators in nuclear reactors, petroleum transportation, electronic cooling, and various types of chemical reactors. The two phases can flow in several topological configurations called flow patterns or flow regimes, which are determined by the dynamic interfacial structure between the phases. The flow regime depends on a variety of parameters such as gas and liquid flow velocities, physical properties of the phases, and flow channel size and geometry. Correct identification of the flow regimes and prediction of the transition boundaries are particularly indispensable because they have a profound influence on all two-phase transport processes. Various models have been developed to predict the transition criteria between the flow regimes. The majority of the studies in this field have been confined to circular flow geometry [1,2] and the transition criteria have been extended to minichannel systems [3,4]. In all the cases, reliable experimental flow regime maps are needed to understand the physical phenomena involved in the flow regime transitions as well as to validate the models.

Many researchers have been working on developing objective flow regime identification methodologies. Most flow regime identification approaches have two steps in common: the first step consists of developing an experimental methodology for measuring certain parameters that are intrinsic to the flow and are also suitable flow regime indicators (usually void fraction fluctuations) [5–10]. In the second step, a nonlinear mapping is performed to obtain an objective identification of the flow regimes in accordance with these indicators.

A significant advance in the objective flow regime identification was achieved by Mi et al. [11,12]. Using statistical parameters from the PDF of the signal collected by nonintrusive impedance void meters and Kohonen self-organizing neural networks (SONNs), they were able to identify the flow regimes more objectively. Subsequently, some improvements in the methodology developed by Mi et al. have been made. Lee et al. [13] used the cumulative probability distribution function (CPDF) of the impedance void meter signals as the flow regime indicator. The CPDF is a more stable parameter than the PDF because it is an integral parameter. Also, it has a smaller input data requirement that makes faster flow regime identification possible. Hernandez et al. [14] developed different neural network strategies to improve the flow regime identification results. Different types of neural networks, training strategies, and flow regime indicators based on the CPDF were tested in their work. In order to minimize the effect of the fuzzy flow regime transition boundaries on the identification results, a committee of neural networks was assembled. Then the identification result was obtained by averaging the results provided by all the neural networks that made up the committee. In particular, the flow regime prediction capabilities of the probabilistic neural networks (PNNs) were verified by Sharma et al. [15] in round pipes. In their work, a large set of experimental data

[1]Corresponding author.

Contributed by the Fluids Engineering Division of ASME for publication in the JOURNAL OF FLUIDS ENGINEERING. Manuscript received June 25, 2008; final manuscript received November 24, 2008; published online January 12, 2009. Assoc. Editor: Theodore Heindel.

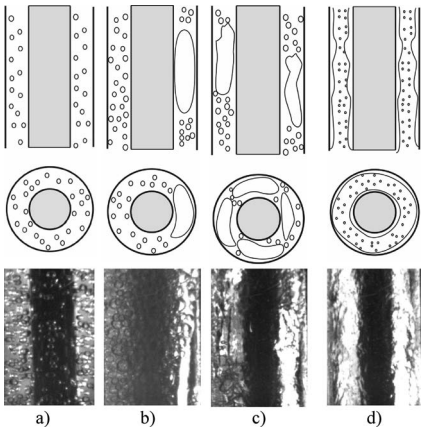

Fig. 1 Flow regime definitions: (*a*) bubbly flow, (*b*) cap-slug flow, (*c*) churn flow, and (*d*) annular flow

obtained in round pipes was used for training a PNN using the superficial velocities, pipe diameter, and inclination angle as inputs. The results given by the PNN show good agreement even in the flow regime boundaries. Finally, it has to be mentioned that the neural networks have been successfully used not only for two-phase but also for three-phase flows [16].

Most of the studies on flow regime identification have concentrated on gas-liquid two-phase flows in tubes due to the simple geometry and many practical applications; however, in many chemical and nuclear systems more complex geometries exist. The annulus channel is often utilized to simulate phenomena encountered in complex geometries such as the subchannel of a rod bundle in a nuclear reactor core, yet it is simple enough to perform fundamental studies. Sadatomi and Sato [17] and Furukawa and Sekoguchi [18] studied the flow regimes of gas-liquid two-phase flows in noncircular flow ducts, including a concentric annulus. Kelessidis and Dukler [19] and Das et al. [20,21] investigated the flow patterns in vertical upward flow for concentric and eccentric annulus channels. They also developed flow regime transition criteria based on phenomenological models and compared the models with their experimental findings. Sun et al. [22] investigated the cap bubbly-to-slug flow regime transition criteria in an annulus and suggested a model for the transition criteria by modifying the study of Mishima and Ishii [2]. In the past, the axial development of the two-phase flow interfacial structures in a vertical annulus has been studied by several researchers [23,24]; however, it has focused on void fraction and interfacial area concentration development. Only the work of Jeong et al. [24] provides observation about the axial development of flow regime in an annulus. In their work, the flow regime map was obtained from visual information and few flow conditions were studied.

This work studies the axial development of gas-liquid two-phase flow regimes in adiabatic upward vertical flow in an annular channel. The flow regime indicator has been obtained from the area-averaged void fraction signals measured by impedance meters at three axial locations, and artificial neural networks have been used as a mapping system. The information obtained has been used to analyze the axial development of flow regime as well as to compare the predictions given by the existing flow regime transition models.

2 Flow Regime Definitions and Transition Boundary Modeling

2.1 Flow Regime Definitions in Annulus. Figure 1 shows the typical flow patterns observed in the annular test section with inner and outer diameters of 19.1 and 38.1 mm, respectively. Vertical upward two-phase flows in a vertical annulus are usually classified into four basic flow regimes [19,20]. In what follows, the characteristics of each flow regime are described.

2.1.1 Bubbly Flow (Designated as B in Secs. 3–5). The liquid phase is continuous and small dispersed bubbles flow in the liquid. No major difference from the bubbly flow in round tubes can be found (Fig. 1(*a*)).

2.1.2 Cap-Slug Flow (Designated as CS in Secs. 3–5). The number density of small bubbles increases and bigger bubbles are formed due to the bubble coalescence. Cap bubbles observed in round tubes cannot exist in the annulus if the annulus gap size is smaller than the distorted bubble limit (or minimum cap bubble limit), e.g., 10.9 mm for air-water flow under atmospheric pressure at 25°C [25]. Thus, a growing bubble is radially confined by the inner and outer walls before it reaches the maximum distorted bubble limit. If the bubble grows further, it becomes a cap bubble squeezed between the inner and outer walls. Typical large bullet-shaped bubbles (slug or Taylor bubbles), which have diameters close to the pipe diameter and occupy almost the whole cross section, are not present in the annulus. In most cases, slug bubbles in the annulus are wrapped around the inner tube but cannot cover it completely due to the long periphery in this flow channel. As a result, cap and slug bubbles are not distinguishable in this test section and an intermediate flow regime between cap bubbly and slug flows, which are usually observed in round pipes, exists in the annulus as verified by Jeong et al. [24]. Therefore, the "cap-slug flow" expression has been chosen for this flow regime (Fig. 1(*b*)). It should be noted that in previously published works, the expression "slug flow" is commonly used for this flow regime.

2.1.3 Churn Flow (Designated as C in Secs. 3–5). By increasing the gas flow rate, a breakdown in the slug bubbles leads to an unstable flow regime, and the continuity of the liquid slug is repeatedly destroyed. This liquid accumulates, forms a bridge, and is again lifted by the gas. This oscillatory or alternating direction of the liquid motion is typical of churn flow. No major difference between churn flow in a round pipe and an annulus is observed (Fig. 1(*c*)).

2.1.4 Annular Flow (Designated as A in Secs. 3–5). The gas phase flows in the center of the gap and the liquid phase flows along the walls as a film. Generally, part of the liquid phase is entrained as small droplets in the gas core. No major difference between annular flow in a round pipe and an annulus is observed (Fig. 1(*d*)).

2.2 Existing Models of Flow Regime Transition Criteria in an Annulus Channel. Three models of flow regime transition criteria have been chosen and compared with the experimental data obtained in this work. Two of the models, Kelessidis and Dukler [19] and Das et al. [21], were developed for air-water adiabatic upward flows in a vertical annulus. In addition, the model developed by Mishima and Ishii [2] for vertical upward two-phase flow in round tubes has been selected, since it has been successfully applied to several flow configurations. The three models are summarized in Secs. 2.2.1–2.2.3.

2.2.1 Kelessidis and Dukler Model. Kelessidis and Dukler investigated the vertical upward gas-liquid flow in concentric and eccentric annuli with inner and outer diameters of 5.08 cm and 7.62 cm, respectively [19]. The flow regime indicator was a set of some characteristic parameters of the PDF obtained from the voltage signal of two conductivity probes. The flow regime mapping was performed by applying some rules to the flow regime indicator measurements following the methodology developed by Barnea et al. [10]. The flow regime maps were obtained for two axial locations (z/D_H=160 and 200 approximately) and 85 flow conditions within a range of 0.05 m/s$<\langle j_g\rangle<$20 m/s and 0.01 m/s $<\langle j_f\rangle<$2 m/s, where $\langle j_g\rangle$ and $\langle j_f\rangle$ are the superficial gas and liquid velocities, respectively.

Kelessidis and Dukler proposed a flow regime map based on the phenomenological model of Taitel et al. [1] and on their experimental observations. The assumed flow regime transition criteria in the model are summarized as follows.

(1) Transition from bubbly to slug flow is governed by bubble packing. For low liquid velocity, the transition occurs when the area-averaged void fraction, $\langle\alpha\rangle$, reaches 0.25. For high liquid velocity, the flow regime remains bubbly flow due to the bubble breakup caused by the strong turbulence force even at $\langle\alpha\rangle \geq 0.25$ and the void fraction at the finely dispersed bubbly to slug flow transition is set at $\langle\alpha\rangle = 0.52$. The transition from bubbly to dispersed bubbly is given by a maximum stable bubble diameter criterion derived from a force balance between the surface tension and turbulent fluctuations.
(2) Slug to churn flow transition is governed by stable liquid slug length criteria similar to that proposed by Taitel et al. [1] in round pipes. It is proposed that the stability of the liquid slug in an annulus is associated with the liquid falling as a film around the slug bubble. It is postulated that the liquid slug is stable if it is long enough that the liquid jet around the slug bubble is absorbed by the liquid slug and the velocity of the liquid jet slows down to that of the surrounding. The fact that the Taylor bubbles in the annulus cannot cover the flow channel completely is not considered in the model. It should be noted here that axial coordinate dependence is considered in the flow regime transition boundary criterion.
(3) Churn to annular flow transition occurs when the void fractions of churn flow and the void fraction for annular flow are equal. The void fraction for the annular flow can be obtained based on geometric considerations and a force balance between interfacial shear, gravity, and axial pressure drop. The void fraction of churn flow is estimated based on the ratio of superficial gas velocity and bubble rise velocity.

2.2.2 Model of Das et al.. Das et al. [21] carried out experiments on air-water upward flow through three concentric annulus geometries with inner and outer diameters of 2.54 cm, 1.27 cm, 1.27 cm and 5.08 cm, 3.81 cm, 2.54 cm respectively. The flow regime indicator was a set of characteristic parameters of the PDF obtained from the voltage signal of two parallel conductivity probes. Flow regime mapping was performed by applying some rules to the flow regime indicator set. The flow regime maps were obtained for two axial locations, entrance and developed flow regions, but no quantitative information about its location was available. More than 150 flow conditions within a range of $0.04\ \text{m/s} < \langle j_g \rangle < 9\ \text{m/s}$ and $0.08\ \text{m/s} < \langle j_f \rangle < 2.8\ \text{m/s}$ were obtained.

They developed a phenomenological model of the flow regime boundaries as functions of the annulus dimensions, physical properties, and the velocities of the two phases. The assumed flow regime transition criteria in the model are summarized as follows.

(1) The transition from bubbly to slug flow is postulated to occur due to an onset of asymmetric phase distribution from the symmetry prevailing in bubbly flow. This asymmetry persists in the entire range of slug flow and occurs due to the typical shape of cap and Taylor bubbles. Experimental observation [20] revealed that the coalescence of cap bubbles rather than the spherical ones played a major role in this flow regime transition. Consequently, it is assumed that the slug flow appears when the elongated bubbles formed from the coalescence of cap bubbles have attained the nose dimensions of the Taylor bubble. This approach provides a transition void fraction, $\langle\alpha\rangle = 0.2$, lower than the maximum bubble packing criterion followed by several authors [1,2]. However, for high liquid flow rate (dispersed bubbly flow) this criterion is replaced by the one given by Kelessidis and Dukler [19].
(2) The slug to churn flow regime transition results from the collapse of the Taylor bubbles. Experimental results showed that flooding in the Taylor bubble region would be the main mechanism underlying the flow regime transition. The flooding correlation proposed by Wallis is used as the basis of the governing equation for this phenomenon [26]. The fact that the Taylor bubbles in the annulus cannot cover the flow channel completely is not considered in the model.
(3) No criterion is given for the transition from churn-to-annular flow.

2.2.3 Mishima and Ishii Model. Mishima and Ishii [2] considered different mechanisms for the flow regime transition criteria between bubbly-to-slug, slug-to-churn, and churn-to-annular flows. These criteria were compared with experimental data under steady-state and fully developed flow conditions by using relative velocity correlations and can be summarized as follows.

(1) The transition criteria between bubbly to slug flow are based on the maximum bubble packing before significant coalescence occurs, which is estimated as $\langle\alpha\rangle = 0.3$. No finely dispersed bubbly flow regime is considered.
(2) Slug to churn flow transition occurs when the mean void fraction over the entire flow channel exceeds that over the Taylor bubble section. Under this condition, the liquid slug becomes unstable to sustain its individual identity due to strong wake effects.
(3) The criteria for the churn-to-annular flow transition are modeled by postulating two different mechanisms: flow reversal in the liquid film section along large bubbles and destruction of liquid slugs or large waves by entrainment or deformation. The second criterion from the onset of entrainment is applicable to predict the occurrence of annular-mist flow or to predict the churn-to-annular flow transition in a large diameter tube.

3 Experimental Methodology

3.1 Two-Phase Flow Loop. Figure 2 shows the schematic of the experimental facility. The main components of the facility were the test section, the separator tank, and the circulation pump. The air-water separation tank was open to the atmosphere.

In the primary loop, water was held in the separator tank with an internal volume of approximately 0.2 m^3. A stainless steel vertical centrifugal pump circulated the water in the loop. The pump speed was controlled by a frequency inverter. A globe valve was installed upstream of the inlet piping, which was utilized with the pump controller to control the flow rate. Flow rate measurement was performed by using a magnetic flow meter with an uncertainty of about 1% and least counts of $2 \times 10^{-5}\ \text{m}^3/\text{s}$. Finally, the water entered the test section through a header where the water flow was evenly divided into four separate lines. In order to maintain the constant pressure boundary conditions, the bypass section was designed so that it carried five to ten times the flow rate through the test section. In this way, the pressure head given by the centrifugal pump is almost constant for all the flow conditions. Filtered and chemically treated water with a conductivity of 60 μS, pH=8.5, and a surface tension of 0.073 N/m was used in the experiments. More details about these procedures can be found in Ref. [24].

Air was supplied from an air compressor. The air flow rate was controlled by four rotameters with different maximum ranges of volumetric flow. The measurement accuracy of each rotameter was $\pm 3\%$ when the flow rate was greater than 50% of the full scale. The air line was divided into four separate lines in the header. Figure 3(*a*) shows the schematic of the air-water mixing unit in the header, which was composed of a tee, a sparger with a

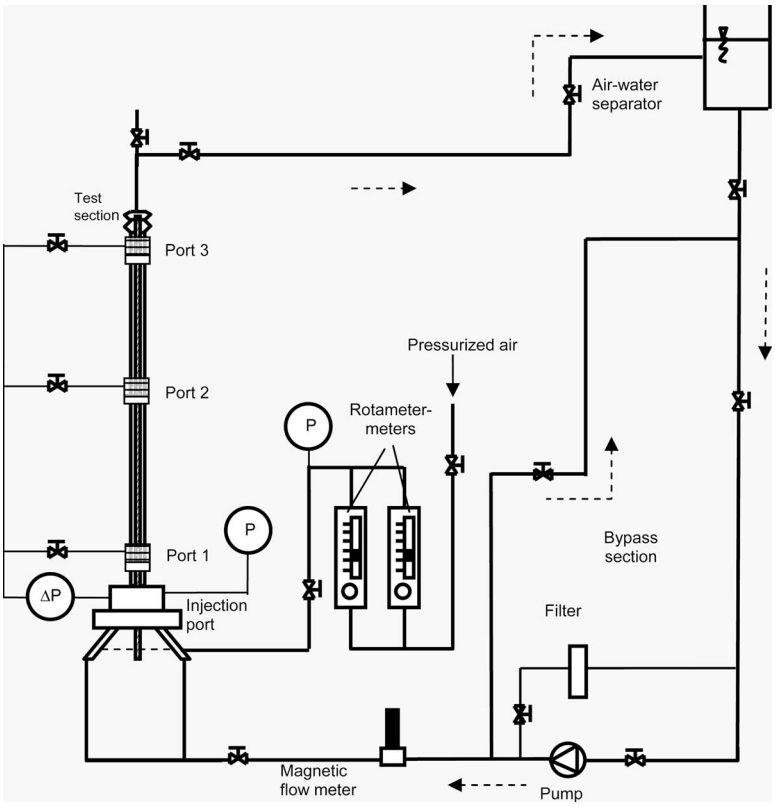

Fig. 2 Two-phase flow loop

mean pore size of 10 μm, and a nipple. In this unit, air bubbles were sheared off from the spargers by the water in the nipple. The bubble sizes at the mixing unit were about 2–3 mm.

The test section was about 4.37 m high and composed of an injection port, an annulus section, and three measurement ports. The annulus consisted of an inner rod with a diameter of 19.1 mm and a transparent Pyrex glass tube with the inner diameter of 38.1 mm. The measurement ports were located at z/D_H=52, 149, and 230. Figure 3(*b*) shows the schematic of one measurement port unit. Pressure and temperature were measured at each measurement port as well as at the injection port. The temperature measurements were performed by using T-type thermocouples with an uncertainty of $\pm 0.7\,^{\circ}$C and least counts of $0.1\,^{\circ}$C. The local pressure at each port was measured by using a differential pressure transducer. A pressure tap located at each port was connected to one sensing line of a differential pressure transducer. The other sensing line of the transducer was connected to the injection port. An absolute pressure transducer was used to measure the pressure at the injection port. Thus, pressure was measured at each measurement port in reference to the injection port. The pressure transducers have an uncertainty of 0.5% of the measured value. The averaged combined error for the local pressure in the measurement ports is 3.9%. The least count of the pressure transducers is 20 Pa. The local pressure is used for calculating the superficial gas velocity at each measurement port. The superficial velocity is defined as the volumetric flow rate divided by the flow channel section. Since the test section presents a pressure loss, the volumetric air flow rate measured at the inlet section by the rotameters needs to be corrected by the local pressure at each measurement section. The error in the superficial velocity measurements is less than 1% for the liquid and between 3% and 6% for the air.

3.2 Impedance Meter. The area-averaged void fraction was measured by an impedance void meter at each measurement port simultaneously with a sampling rate of 1 kHz and an acquisition time of 60 s. An impedance void meter is a nonintrusive conductance type probe that utilizes the difference in electrical conductivity between the air and water. For a test section with annulus geometry, a ringwise impedance meter is utilized. A stainless steel ring, which is located at the bottom section, acts as one of the electrodes of the impedance meter. The second electrode is the sheath of the heater. The stainless steel ring is cushioned from three sides by a Teflon sleeve and two Teflon rings. These Teflon pieces act as electrical insulators and electrically isolate the electrode from the instrumentation port. An alternating current is supplied to the electrodes and the electrodes are connected to the electronic circuit, which is especially designed so that the output voltage of the circuit is proportional to the measured admittance, which is the inverse of impedance, between the electrodes. The measured admittance is normalized by the following equation:

$$G^* = \frac{G_m - G_1}{G_0 - G_1} \tag{1}$$

where G_m is the instantaneous two-phase mixture admittance, G_0 is the admittance when void fraction is zero (i.e., single phase water), and G_1 is the impedance when the void fraction is unity (i.e., single phase air). Finally, the volume averaged void fraction can be obtained from the measured admittance. The void fraction is almost a linear function of the nondimensional admittance. Thus, the void fraction measured by the void meter is an instantaneous area averaged void fraction. The uncertainty of the impedance meter can be estimated as 3% and the least count of 1% (void fraction).

3.3 Flow Regime Identification Methodology. The flow regime identification procedure used in this study is based on the methodology developed by Mi et al. [12] and used by Sun et al. [22] in an annulus. However, some significant improvements have been made. In this study, the area-averaged void fraction CPDF distribution is used as a flow regime indicator. The flow regime

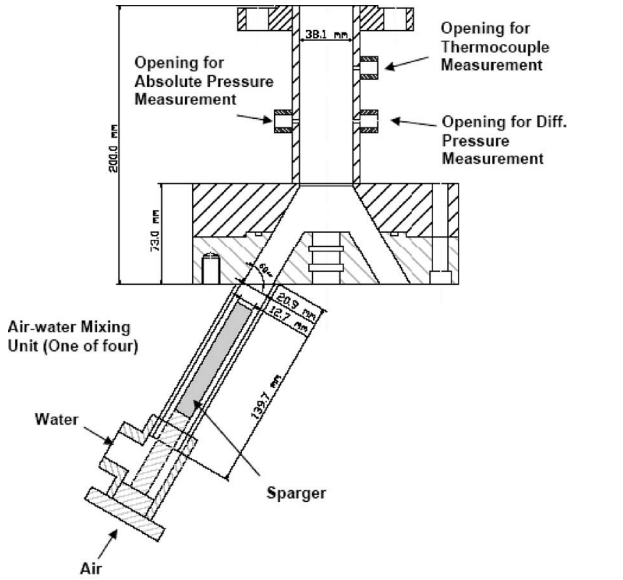

a)

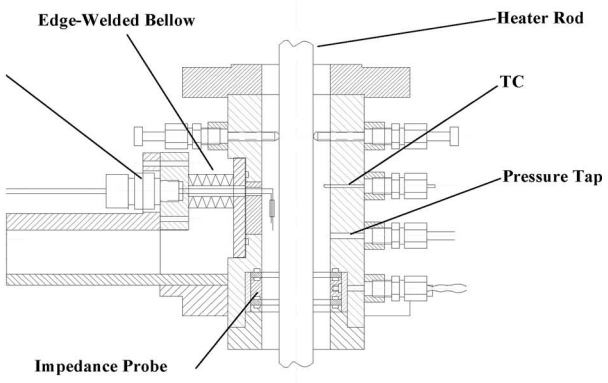

b)

Fig. 3 (*a*) Air-water mixing unit and (*b*) measurement port unit

mapping was performed by a SONN. This neural network architecture was trained without supervision but the number of flow regime categories was specified. In this study, flow regime is classified into four categories.

The steps followed in the flow regime identification methodology are depicted in Fig. 4. This figure is interpreted from left to right. The first column provides examples of images of the typical four flow regimes considered in this study (B, CS, C, and A). The first step in the identification procedure consists of obtaining the nondimensional admittance signal, G^*, defined in Eq. (1).

It should be noted here that the selected flow conditions to be utilized for neural network training must contain all the considered flow regimes with a sufficient number of conditions from each flow regime. If this condition is not satisfied, biased identification results are obtained [14]. In order to meet this requirement, a sensitivity analysis to identify the effect of data points and their flow conditions on flow regime identification was performed by changing the number of data points and their flow conditions for a certain flow regime. It was concluded that the number of data points and their flow conditions determined in this study was sufficiently large. The second column of Fig. 4 shows examples of typical G^* time series for the flow regimes considered in the present study. The PDF of the signals are also plotted in the third column of the figure. From the plots, one may realize that the nondimensional admittance signals possess some characteristics of the flow regimes that can be used as flow regime indicators and the characteristics may be represented by the statistical parameters of the signals.

The next step in the identification procedure consists of selecting the set of statistical parameters of the G^* statistical distributions that will be used as flow regime indicators. Usually the mean, standard deviation, and skewness of the PDF have been used for this purpose [12,22]. However, the CPDF is a more stable integral parameter than the PDF with a smaller input data requirement [14]. In this study, the distribution has been characterized by the G^* values where the CPDF values are 0.25, 0.5, 0.75, and 1 (four index method), see the solid squares in the fourth column of the figure. A set composed of a four-index vector for each flow condition and axial location is used as a flow regime indicator. This method represents a simple and fast procedure to characterize a CPDF and has been successfully tested in two-phase flow regime identification procedures [14], providing similar results to those obtained using more sophisticated flow regime indicators [27].

Once the set of flow regime indicator vectors is obtained, a blind training process is applied to the SONN. The set of flow regime indicator vectors are divided into two separated groups used for training the neural network (training group) and for obtaining the identification results (identification group). The blind training process assures unbiased identification results and increased objectivity of the final result. The vectors are selected randomly, but a minimum amount of flow conditions for every flow regime is needed in the training group in order to avoid biased results [14]. The amount of flow conditions needed in the training group is constrained by the flow regime with the smallest number of conditions and the minimum amount of flow conditions needed to avoid biased results. In the present work, the training group contains the 90% of the vectors and the identification group has the other 10% of the vectors (right hand side of Fig. 4). The training and identification processes are applied ten times until all the flow regime indicator vectors, i.e., flow conditions, have been identified. It is imposed that any flow condition can be identified twice. The outputs of the SONN are ordinal numeric values between 1 and 4 having a natural ordering based on the observed typical sequence of regime transitions.

In addition, in order to minimize the effect of the fuzzy flow regime boundaries on the flow regime identification results, a committee of 50 neural networks is assembled. If a single neural network is used, some of the flow regime identification results are unstable, mainly in the flow regime transition zones. If a committee of 50 neural networks is used, flow regime map repeatability higher than 95% can be achieved. The same training and identification groups are used for all the neural networks that integrate the committee. Finally, the identification result is obtained by averaging the results provided by all the neural networks that compose the committee. More details about the neural network methodology used in this work can be found in Ref. [14].

4 Flow Regime Identification Results and Axial Development

Since the pressure drop by gravity and friction was not negligible in the present test conditions, an averaged increase in the superficial gas velocity between $z/D_H=52$ and 230 was 28% for all flow conditions. This entailed the expansion of air resulting in a continuous flow development along the test section. In the present study, the axial development of a flow regime map within a range of $0.01\ \text{m/s}<\langle j_g\rangle<30\ \text{m/s}$ and $0.2\ \text{m/s}<\langle j_f\rangle<3.5\ \text{m/s}$ have been investigated based on the neutral network flow regime identifications for 216 conditions (72 flow conditions times three axial locations at $z/D_H=52$, 149, and 230). Figure 5 shows the axial development of flow regime obtained with the

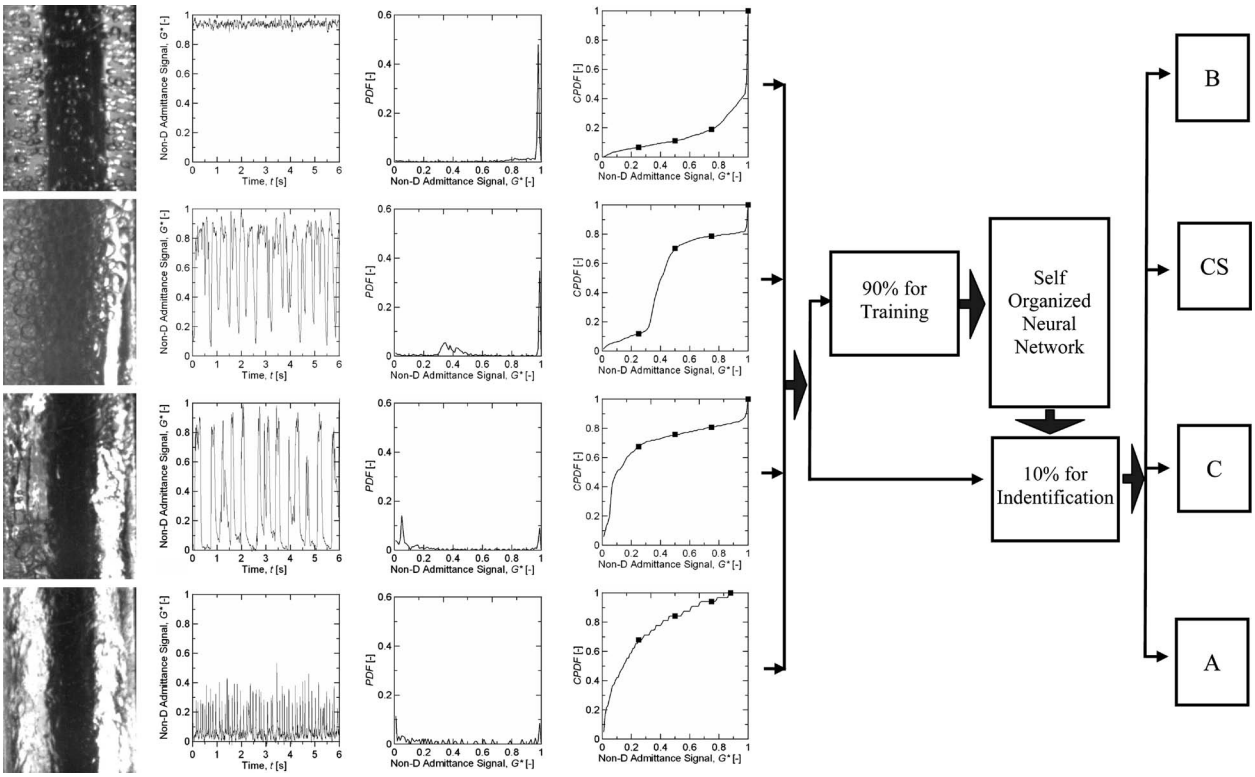

Fig. 4 Flow regime identification methodology

identification methodology presented in Sec. 3.3. In order to make the information more compact, only one flow regime map is used for the three axial locations and the superficial gas velocity in the map represents the value measured at $z/D_H=52$. Each symbol in the map displays the information of the flow regimes identified at the three axial locations. For example, B-CS-C means bubbly flow regime at $z/D_H=52$, cap-slug flow regime at $z/D_H=149$, and churn flow regime at $z/D_H=230$. The black and gray symbols represent the flow conditions where the flow regime does not and does present axial change, respectively. The flow conditions where axial development took place were located in the boundaries between two flow regimes. Most of the flow conditions with axial development of flow regime occurred in the B to CS transition zone. Axial development in the CS and C transition zones was observed at high superficial liquid velocity conditions. Axial development in the C to A flow regime transition zone occurred in only two flow conditions. Table 1 provides the complete information of the identification results including the superficial gas velocity at each axial location.

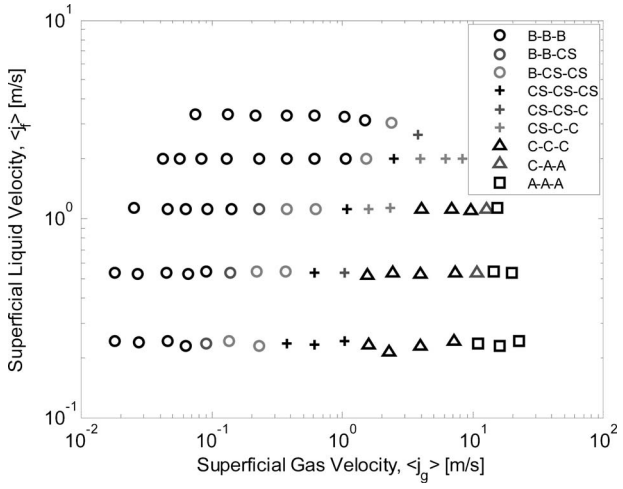

Fig. 5 Flow regime identification results

In order to analyze the results in detail, quantitative information of the axial development of the flow regime is presented in Fig. 6. Figures 6(*a*)–6(*c*) show the flow regime transition boundaries at the three axial locations for the B to CS, CS to C, and C to A transitions, respectively. Figures 6(*d*)–6(*f*) show the critical void fraction, $\langle\alpha_c\rangle$, at the flow regime transitions corresponding to Figs. 6(*a*)–6(*c*), respectively. In all the cases, the flow regime transition boundaries have been defined by utilizing the averaged gas phase related quantities, $\langle j_g\rangle$ or $\langle\alpha_c\rangle$, between the two neighboring flow regimes at a given $\langle j_f\rangle$ and z/D_H values.

The axial development of the flow regime represents a decrease in the critical superficial gas velocity along the axial distance. Axial development at the B to CS flow regime transition is observed for superficial liquid velocities lower than 2 m/s (Fig. 6(*a*)). For higher $\langle j_f\rangle$ conditions, no noticeable change in the critical superficial gas velocity or critical void fraction is observed. This effect was also observed by Kelessidis and Dukler [19] in their experiments. Although no quantitative information was given in their work, it is inferred that the effect of the axial development of flow regime on the critical superficial gas velocity is not as important as that observed in the present study and they did not include it in their model. In addition, Jeong et al. [24] confirmed B to CS axial development using conductivity probes in the same annulus two-phase flow loop and similar experimental conditions. However, their study was limited to a small number of flow conditions and the flow regime identification was done using the visual information. Hibiki and Ishii [28] pointed out the axial development of flow regime based on the adiabatic vertical upward two-phase flow experiment performed in a 10.2 cm inner diameter pipe. Their study focused on the bubbly to slug flow regime transition at three axial positions: $z/D_H=12.8$, 26.6, and 41.8.

For low z/D_H and $\langle j_f\rangle$ conditions, the critical void fraction at

Table 1 Experimental conditions and flow regime identification results

Superficial velocities (m/s)				Flow identification results		
			Air			
Water	z/D_H=52	z/D_H=149	z/D_H=230	z/D_H=52	z/D_H=149	z/D_H=230
0.244	0.016	0.018	0.020	B	B	B
0.240	0.024	0.027	0.030	B	B	B
0.244	0.041	0.046	0.051	B	B	B
0.229	0.057	0.063	0.070	B	B	B
0.234	0.080	0.090	0.100	B	B	CS
0.244	0.12	0.14	0.15	B	CS	CS
0.230	0.21	0.23	0.25	B	CS	CS
0.236	0.34	0.37	0.41	CS	CS	CS
0.233	0.56	0.61	0.67	CS	CS	CS
0.241	0.96	1.03	1.15	CS	CS	CS
0.233	1.51	1.59	1.61	C	C	C
0.214	2.13	2.25	2.54	C	C	C
0.229	3.75	3.95	4.49	C	C	C
0.241	6.99	7.18	7.31	C	C	C
0.236	10.43	10.79	10.97	A	A	A
0.229	14.91	16.02	16.56	A	A	A
0.244	19.72	22.33	24.83	A	A	A
0.536	0.016	0.018	0.020	B	B	B
0.525	0.024	0.027	0.031	B	B	B
0.537	0.040	0.045	0.051	B	B	B
0.530	0.058	0.065	0.074	B	B	B
0.539	0.080	0.090	0.10	B	B	B
0.531	0.12	0.14	0.15	B	B	CS
0.542	0.20	0.22	0.24	B	CS	CS
0.544	0.33	0.37	0.41	B	CS	CS
0.535	0.55	0.61	0.67	CS	CS	CS
0.536	0.94	1.03	1.13	CS	CS	C
0.517	1.45	1.56	1.67	C	C	C
0.531	2.23	2.42	2.66	C	C	C
0.528	3.65	3.96	4.33	C	C	C
0.531	6.45	7.22	7.77	C	C	C
0.531	9.37	10.69	12.05	C	A	A
0.539	12.45	14.32	16.47	A	A	A
0.534	16.61	19.59	23.22	A	A	A
1.133	0.022	0.025	0.029	B	B	B
1.114	0.040	0.045	0.051	B	B	B
1.120	0.054	0.063	0.072	B	B	B
1.118	0.080	0.091	0.10	B	B	B
1.118	0.12	0.14	0.16	B	B	B
1.122	0.20	0.23	0.26	B	B	CS
1.114	0.33	0.38	0.43	B	CS	CS
1.122	0.54	0.62	0.70	B	CS	CS
1.122	0.95	1.09	1.18	CS	CS	CS
1.122	1.37	1.58	1.81	CS	C	C
1.129	2.04	2.31	2.60	CS	C	C
1.114	3.50	3.99	4.53	C	C	C
1.122	5.78	6.83	8.10	C	C	C
1.107	7.95	9.53	11.54	C	C	C
1.114	10.18	12.50	15.37	C	A	A
1.129	12.39	15.29	19.51	A	A	A
2.004	0.036	0.042	0.048	B	B	B
2.007	0.048	0.056	0.065	B	B	B
2.000	0.071	0.082	0.095	B	B	B
2.007	0.17	0.21	0.26	B	B	B
2.007	0.20	0.23	0.26	B	B	B
2.000	0.32	0.37	0.43	B	B	B
2.007	0.52	0.61	0.71	B	B	B
2.000	0.88	1.05	1.23	B	B	B
2.007	1.28	1.51	1.81	B	CS	CS
2.000	2.05	2.45	2.95	CS	CS	CS
1.992	3.26	3.96	4.92	CS	C	C
1.992	4.99	6.17	7.98	CS	C	C
1.992	6.62	8.24	11.66	CS	C	C
3.336	0.061	0.075	0.092	B	B	B
3.343	0.11	0.13	0.16	B	B	B
3.328	0.18	0.22	0.27	B	B	B
3.328	0.31	0.37	0.46	B	B	B
3.306	0.50	0.61	0.75	B	B	B

Table 1 (***Continued.***)

Superficial velocities (m/s)				Flow identification results		
			Air			
Water	$z/D_H=52$	$z/D_H=149$	$z/D_H=230$	$z/D_H=52$	$z/D_H=149$	$z/D_H=230$
3.247	0.84	1.03	1.29	B	B	B
3.122	1.22	1.47	1.84	B	B	B
3.026	1.91	2.38	3.08	B	CS	CS
2.657	3.01	3.79	5.86	CS	CS	C

the boundary of B to CS (Fig. 6(*d*)) is between 0.25 and 0.3 as suggested by the maximum bubble packing criteria [1,2]. However, the critical void fraction is reduced to 0.2 at further downstream. This value is closer to the one predicted by the asymmetric phase distribution hypothesis proposed by Das et al. [21]. Similar results were obtained by Hibiki and Ishii [28] with critical void fraction values of 0.3 and 0.16 at axial positions of $z/D_H=12.8$ and 41.8, respectively. A weaker effect of the axial position on the critical void fraction can be observed when the $\langle j_f \rangle$ is increased. The critical void fraction values are about 0.4, which is lower than the one at the finely dispersed bubbly flow to S or C flow regime transition modeled by Taitel et al. [1] ($\langle \alpha_c \rangle = 0.52$) and adopted by the models of Kelessides and Dukler [19] and Das et al. [21].

The reduction in $\langle \alpha_c \rangle$ along the axial position observed for low liquid velocity conditions can be explained by the increased bubble coalescence rate due to the increased bubble residence time inside the flow channel. This explanation seems feasible since the B to CS transition is generally associated with coalescence phenomena. Thus for low liquid velocity conditions, the bubble interaction time, namely, axial length from the inlet, is important for flow regime transition and thus the history of the inlet flow regime is sustained even at a long distance from the inlet. Hibiki and Ishii [29] discussed the inlet history effect on the interfacial structure using the interfacial area transport equation. For $\langle j_f \rangle$ higher than 2 m/s, the axial development is not observed because sufficient bubble interaction is attained even within a short distance from the inlet. The critical $\langle j_f \rangle$ observed in this study coincides with the liquid velocity at the flow regime transition boundary between bubbly and finely dispersed bubbly flows, which is predicted to be $\langle j_f \rangle \sim 1.8$ m/s in an annulus by Kelessidis and Dukler [19].

The CS to C flow regime transition also represents axial development (Fig. 6(*b*)) for $\langle j_f \rangle > 0.5$ m/s. Kelessidis and Dukler [19] considered the axial development in the slug to churn turbulent

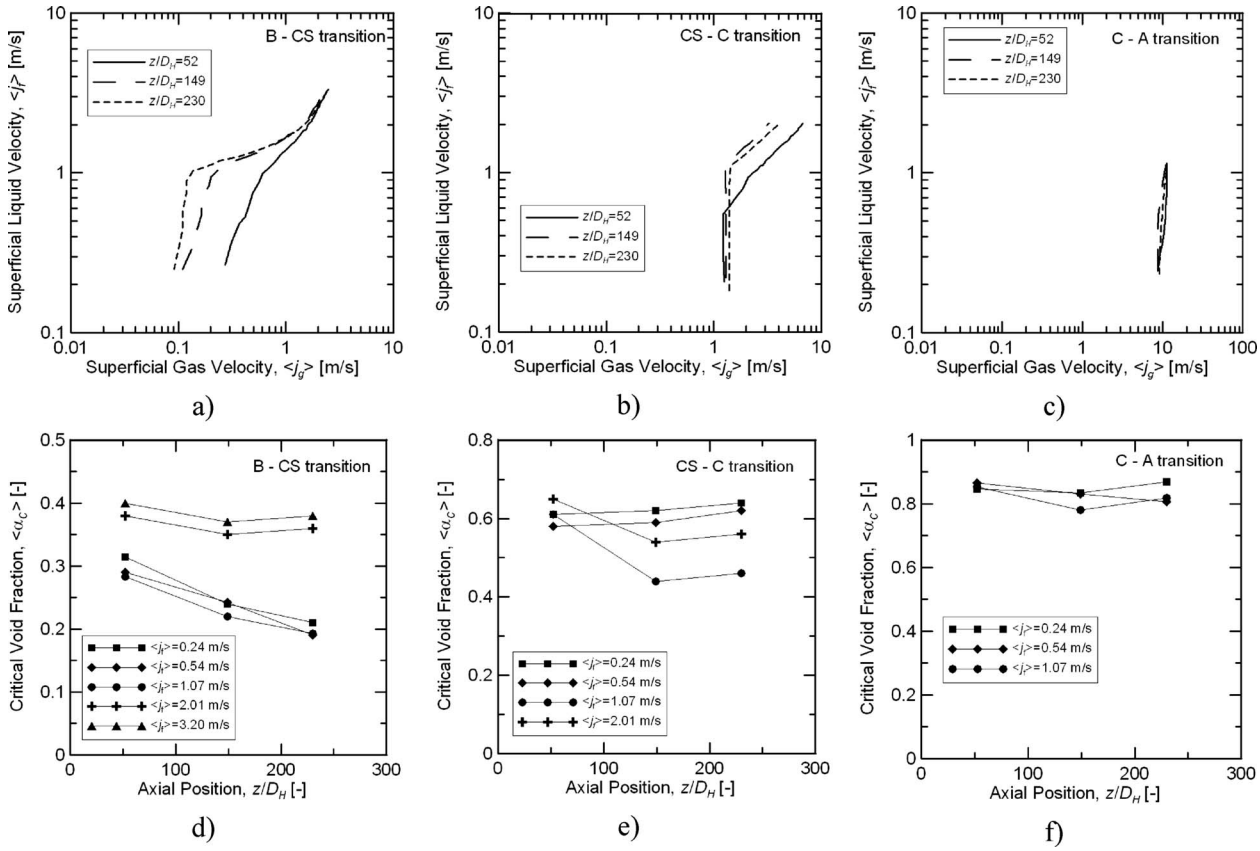

Fig. 6 Flow regime transitions and critical void fraction dependences with the axial distance: ((*a*) and (*d*)) bubbly-to-cap-slug, ((*b*) and (*e*)) cap-slug-to-churn, and ((*c*) and (*f*)) churn-to-annular flow transitions

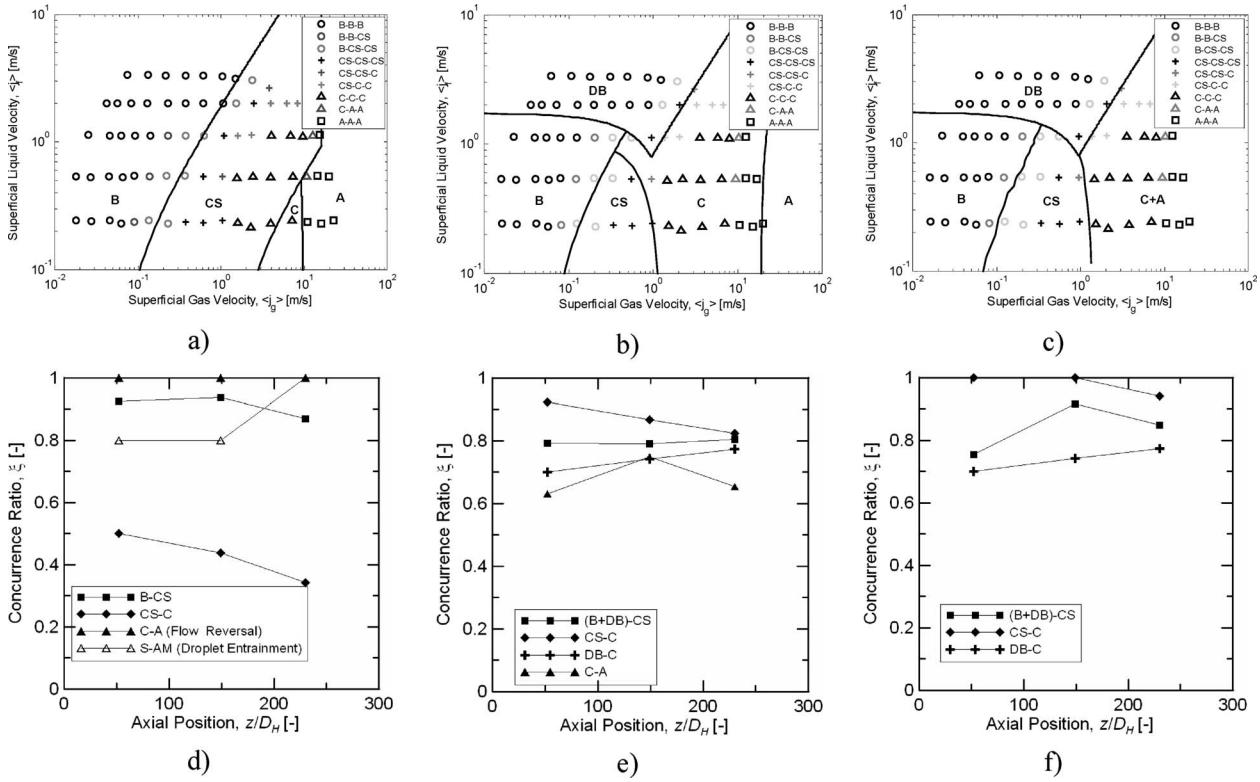

Fig. 7 Comparison of flow regime identification results with published flow regime transition models and flow regime concurrence ratio dependence with z/D_H: ((*a*) and (*d*)) Mishima–Ishii, ((*b*) and (*e*)) Kelessidis and Dukler, and ((*c*) and (*f*)) Das et al.

flow regime transition, but it indicated that an increase in critical $\langle j_g \rangle$ along the axial location occurred only $\langle j_f \rangle < 1$ m/s, differing from the experimental evidence obtained in the present study. For high $\langle j_f \rangle$ conditions, the finely dispersed bubbly to churn flow regime transition was proposed with no consideration of axial development in their model. The decrement observed in the critical void fraction was up to 20% (Fig. 6(*e*)), and it usually occurred near the test section inlet. Only the model proposed by Mishima and Ishii [2] can explain the decrement observed in the critical void fraction. In their model, the critical void fraction is decreased with increased mixture volumetric flux, $\langle j \rangle$. Due to the pressure drop along the flow direction, the gas velocity is increased and, thus, the mixture volumetric flux is increased with the axial coordinate. The pressure drop is more important for high $\langle j_f \rangle$ conditions, so a larger decrement of the critical void fraction is expected for this flow regime map as experimentally observed.

Finally, the C to A flow regime transition zone does not present appreciable axial development (Fig. 6(*c*)) and the critical void fraction is almost constant (Fig. 6(*f*)).

5 Comparison of Flow Regime Identification Results With Existing Models

In this section, the existing models for the flow regime transition criteria summarized in Sec. 2.2 are compared with the flow regime identification results obtained in this study. Figures 7(*a*)–7(*c*) compare the flow regime map with the transition boundaries modeled by Mishima and Ishii [2], Kelessidis and Dukler [19], and Das et al. [21], respectively. In the computation of the B to CS transition boundary by Mishima and Ishii's model, a distribution parameter is set at 1.1 as obtained for a vertical annulus [30]. In the Kelessidis and Dukler map, CS to C flow regime transition boundary at $z/D_H = 149$ is shown.

In order to quantify the model applicability, we propose a concurrence ratio, ξ, defined as the number of flow conditions correctly predicted by the boundary divided by the total number of flow conditions identified in the two flow regimes considered. High concurrence ratio indicates higher prediction accuracy. The concurrence ratio is utilized only for comparative purposes between the existing models and it is not intended to provide the exact prediction accuracy of them. Figures 7(*d*)–7(*f*) show the dependence of the concurrence ratio on the axial position for the models proposed by Mishima and Ishii [2], Kelessidis and Dukler [19], and Das et al. [21], respectively. In the last two models, the dispersed bubbly flow regime is considered as bubbly flow.

All the models show a high concurrence ratio for the B to CS flow regime transition. The best prediction results are obtained for the Mishima and Ishii [2] model, $\xi > 0.9$ for all z/D_H conditions. A weak dependence of ξ on the axial location is observed and the ξ value becomes lower at $z/D_H = 230$. The opposite result is obtained for the model of Das et al. [21], $\xi > 0.8$ for all z/D_H conditions, and the concurrence ratio is improved at higher z/D_H values. The concurrence ratio of Kelessidis and Dukler [19] model is about 0.8 with almost no dependence on the axial location. These results are in concordance with the critical void fractions measured in Fig. 6(*d*), since the models of Mishima and Ishii, Kelessidis and Dukler, and Das et al. predict critical void fractions of 0.3, 0.25, and 0.2, respectively. This result implies that the channel geometry does not play a major role in this flow regime transition boundary. A decrement of the critical void fraction along the flow direction should be modeled by considering the bubble contact time or developing length.

The concurrence ratio for the CS to C flow transition computed by the Mishima and Ishii model [2] is below 0.5 and many flow conditions identified as C are located in the computed CS region. This indicates that the flow regime transition criteria provided by Mishima and Ishii [2] cannot predict the geometry effect observed

in this study since it was developed for pipe flows. If partial Taylor bubbles are considered, a considerable decrement of the superficial gas velocity at the CS to C flow regime transition in the Mishima and Ishii model may be obtained and the concurrence ratio given by Mishima and Ishii may be significantly improved. A similar approach was used by Sun et al. [22] to model the B to CS flow regime transition in an annulus. Although the models of Kelessidis and Dukler [19] and Das et al. [21] do not consider the fact that the Taylor bubbles in the annulus cannot cover the flow channel completely, they can predict the CS to C flow regime transition reasonably well for $\langle j_f \rangle$ values lower than 1 m/s. The Kelessidis and Dukler model provides an average concurrence ratio of 0.87 showing better results for low z/D_H values. The best prediction results are obtained by Das et al. [21] with $\xi > 0.98$. This result may validate the destruction of the Taylor bubbles by flooding in the Taylor bubble region as assumed by the model of Das et al. [21].

The flow regime transition between CS to C flow for $\langle j_f \rangle$ values higher than 1 m/s presents an important axial development. If the dispersed bubbly flow regime is considered [19,21], this flow regime transition is modeled as dispersed bubbly to churn flow. The models of Kelessidis and Dukler [19] and Das et al. [21] share the transition criteria developed by Taitel et al. [1] with a maximum $\langle \alpha \rangle = 0.52$ as transition boundary. This simple condition cannot predict the axial development observed in the results. In addition, no direct transition from dispersed bubbly to churn is observed in the experimental results. In contrast, a continuous development between B to CS and C is identified similar to the one observed for low $\langle j_f \rangle$ values. In this way, only the Mishima and Ishii [2] model can predict the CS flow regimes for flow conditions with high $\langle j_f \rangle$ values. However, this model was developed for round pipes and it assumes symmetric Taylor bubbles and additional work is needed to adapt it to partial length Taylor bubbles. Consequently, the best averaged concurrence ratio for this flow regime transition, given by Kelessidis and Dukler [19] and Das et al. [21], is only 0.73, which is the lowest found in the flow map.

For the C to A transition, only the Mishima and Ishii [2] and Kelessidis and Dukler [19] models are available. Mishima and Ishii model suggests that in the current flow channel the C to A transition occurs due to flow reversal for low $\langle j_f \rangle$ conditions. For $\langle j_f \rangle$ higher than 1 m/s, the transition is governed by droplet entrainment and the slug to annular-mist flow regime transition takes place. When the flow regime transition occurs due to flow reversal, the concurrence ratio is 1 for all the axial positions. The concurrence ratio for high $\langle j_f \rangle$ conditions (droplet entrainment) is also high with $\xi > 0.8$ for all the axial locations. It should be noted that in the latter case, flow conditions identified as CS and C have been used to compute the concurrence ratio. If only CS flow conditions are considered, the concurrence ratio values are almost zero. This fact is supported by Mishima and Ishii's work [2] since they pointed out that the flow behavior in the slug to annular flow regime transition is similar to that for churn flow. The Kelessidis and Dukler criterion only provides an averaged concurrence ratio of 0.64 showing a clear overestimation of the critical $\langle j_g \rangle$.

6 Conclusions

The axial development of a flow regime map in a vertical annulus within a range of 0.01 m/s $< \langle j_g \rangle <$ 30 m/s and 0.2 m/s $< \langle j_f \rangle <$ 3.5 m/s has been investigated based on neutral network flow regime identifications for 216 conditions (72 flow conditions times three axial locations at $z/D_H = 52$, 149, and 230). The flow regime indicator has been chosen to be area-averaged void fraction signals from the admittance void meter and a neural network has been used as mapping system. Flow conditions comprised of bubbly (B), cap-slug (CS), churn (C), and annular (A) flow regimes have been identified. This information has been used to analyze the axial development of flow regime and to compare the existing models of flow regime transition criteria proposed by Mishima and Ishii [2], Kelessidis and Dukler [19], and Das et al. [21]. The main conclusions obtained in this study are summarized as follows.

1. *Bubbly-to-cap-slug flow transition*. Although this flow regime transition presented an important axial development for $\langle j_f \rangle$ lower than 2 m/s, the prediction accuracies of the considered models provided reasonable results. The critical void fraction measurements showed that the maximum bubble packing criteria might be used as transition criteria and modeled by considering the bubble contact time or developing length. For $\langle j_f \rangle$ higher than 2 m/s, the dependence of the critical void fraction on the axial length was not observed.
2. *Cap-slug-to-churn flow transition*. This flow regime transition did not present the axial development for $\langle j_f \rangle$ conditions lower than 1 m/s. From the three models considered, the best prediction results were obtained by the model of Das et al. [19] that assumed the destruction of Taylor bubbles by flooding as the governing phenomena in this transition.
3. *Dispersed bubbly cap-slug to churn for* $\langle j_f \rangle > 1$ *m/s*. This flow regime transition presented a significant axial development. The models of Kelessides and Dukler [19] and Das et al. [21] could not predict this flow regime transition properly since they used a constant void fraction criterion $\langle \alpha \rangle = 0.52$. In addition, these models predict the direct transition from dispersed bubbly to churn flow regime differing from the experimental results. Only the Mishima and Ishii [2] model could predict the gradual flow regime transition between DB-CS-C, but it was pointed out that the model should be reconsidered including the consideration of the flow channel geometry.
4. *Churn-to-annular flow transition*. The axial development of the flow regime transition was not observed in this regime and Mishima and Ishii [2] model gave the best prediction results for the transition boundary.

Acknowledgment

This work was performed under the auspices of the U.S. Nuclear Regulatory Commission (USNRC). The authors would like to express their sincere appreciation for the encouragement, support, and technical comments on this program from Dr. Kelly and Mr. Ireland of USNRC. The authors would like to express their appreciation to Mr. Joshua P. Schelegel (School of Nuclear Engineering, Purdue University) for reviewing this paper

Nomenclature

D_H = hydraulic diameter (m)
G = admittance (Ω^{-1})
G^* = dimensionless admittance
j = superficial velocity (m s^{-1})
v = velocity (m s^{-1})
z = axial position in the flow direction (m)

Greek Symbols

α = void fraction
ξ = concurrence ratio

Subscripts

crit = critical
f = liquid phase
g = gas phase
m = mixture

Mathematical Symbols

$<>$ = area average

References

[1] Taitel, Y., Barnea, D., and Dukler, A. E., 1980, "Modeling Flow Pattern Transitions for Steady Upward Gas-Liquid Flow in Vertical Tubes," AIChE J., **26**, pp. 345–354.

[2] Mishima, K., and Ishii, M., 1984, "Flow Regime Transition Criteria for Upward Two-Phase Flow in Vertical Tubes," Int. J. Heat Mass Transfer, **27**(5), pp. 723–737.

[3] Mishima, K., and Hibiki, T., 1996, "Some Characteristics of Air-Water Two-Phase Flow in Small Diameter Vertical Tubes," Int. J. Multiphase Flow, **22**, pp. 703–712.

[4] Hibiki, T., and Mishima, K., 2001, "Flow Regime Transition Criteria for Upward Two-Phase Flow in Vertical Narrow Rectangular Channels," Nucl. Eng. Des., **203**, pp. 117–131.

[5] Jones, O. C., and Zuber, N., 1975, "The Interrelation Between Void Fraction Fluctuations and Flow Patterns in Two-Phase Flow," Int. J. Multiphase Flow, **2**, pp. 273–306.

[6] Hubbard, N. G., and Dukler, A. E., 1966, "The Characterization of Flow Regimes for Horizontal Two-Phase Flow," *Proceedings of the 1996 Heat Transfer and Fluid*, Mechanics Institute, Stanford University Press, Stanford, pp. 100–121.

[7] Tutu, N. K., 1982, "Pressure Fluctuations and Flow Pattern Recognition in Vertical Two-Phase Gas-Liquid Flows," Int. J. Multiphase Flow, **8**, pp. 443–447.

[8] Matsui, G., 1984, "Identification of Flow Regimes in Vertical Gas-Liquid Two-Phase Flow Using Differential Pressure Fluctuations," Int. J. Multiphase Flow, **10**, pp. 711–720.

[9] Cai, S., Toral, H., Qiu, J., and Archer, J. S., 1994, "Neural Network-Based Objective Flow Regime Identification in Air-Water Two-Phase Flow," Can. J. Chem. Eng., **72**, pp. 440–445.

[10] Barnea, D., Shoham, O., and Taitel, Y., 1980, "Flow Pattern Characterization in 2-Phase Flow by Electrical Conductance Probe," Int. J. Multiphase Flow, **6**, pp. 387–397.

[11] Mi, Y., Ishii, M., and Tsoukalas, L. H., 1998, "Vertical Two-Phase Flow Identification Using Advanced Instrumentation and Neural Networks," Nucl. Eng. Des., **184**, pp. 409–420.

[12] Mi, Y., Ishii, M., and Tsoukalas, L. H., 2001, "Flowregime Identification Methodology With Neural Networks and Two-Phase Flow Models," Nucl. Eng. Des., **204**, pp. 87–100.

[13] Lee, J. Y., Ishii, M., and Kim, N. S., 2008, "Instantaneous and Objective Flow Regime Identification Method for the Vertical Upward and Downward Co-Current Two-Phase Flow," Int. J. Heat Mass Transfer, **51**, pp. 3442–3459.

[14] Hernandez, L., Julia, J. E., Chiva, S., Paranjape, S., and Ishii, M., 2006, "Fast Classification of Two-Phase Flow Regimes Based on Conductivity Signals and Artificial Neural Networks," Meas. Sci. Technol., **17**, pp. 1511–1521.

[15] Sharma, H., Das, G., and Samanta, A. N., 2006, "ANN-Based Prediction of Two Phase Gas-Liquid Flow Patterns in a Circular Conduit," AIChE J., **52**, pp. 3018–3028.

[16] Xie, T., Ghiaasiaan, S. M., and Karrila, S., 2003, "Flow Regime Identification in Gas-Liquid-Pulp Fiber Slurry Flows Based on Pressure Fluctuations Using Artificial Neural Networks," Ind. Eng. Chem. Res., **42**, pp. 7017–7024.

[17] Sadatomi, M., and Sato, Y., 1982, "Two-Phase Flow in Vertical Noncircular Channels," Int. J. Multiphase Flow, **8**, pp. 641–655.

[18] Furukawa, T., and Sekoguchi, K., 1986, "Phase Distribution for Air-Water Two-Phase Flow in Annuli," Bull. JSME, **29**, pp. 3007–3014.

[19] Kelessidis, V. C., and Dukler, A. E., 1989, "Modeling Flow Pattern Transitions for Upward Gas-Liquid Flow in Vertical Concentric and Eccentric Annuli," Int. J. Multiphase Flow, **15**, pp. 173–191.

[20] Das, G., Das, P. K., Purohit, N. K., and Mitra, A. K., 1999, "Flow Pattern Transition During Gas Liquid Upflow Through Vertical Concentric Annuli. I. Experimental Investigations," ASME Trans. J. Fluids Eng., **121**, pp. 895–901.

[21] Das, G., Das, P. K., Purohit, N. K., and Mitra, A. K., 1999, "Flow Pattern Transition During Gas Liquid Upflow Through Vertical Concentric Annuli—Part II: Mechanistic Models," ASME Trans. J. Fluids Eng., **121**, pp. 902–907.

[22] Sun, X., Kuran, S., and Ishii, M., 2004, "Cap Bubbly-to-Slug Flow Regime Transition in a Vertical Annulus," Exp. Fluids, **37**, pp. 458–464.

[23] Hibiki, T., Situ, R., Mi, Y., and Ishii, M., 2003, "Experimental Study on Interfacial Area Transport in Vertical Upward Bubbly Two-Phase Flow in an Annulus," Int. J. Heat Mass Transfer, **46**, pp. 427–441.

[24] Jeong, J. J., Ozar, B., Dixit, A., Julia, J. E., Hibiki, T. M., and Ishii, M., 2008, "Interfacial Area Transport of Vertical Upward Air-Water Two-Phase Flow in an Annulus Channel," Int. J. Heat Fluid Flow, **29**, pp. 178–193.

[25] Ishii, M., and Zuber, N., 1979, "Drag Coefficient and Relative Velocity in Bubbly, Droplet or Particulate Flows," AIChE J., **25**, pp. 843–855.

[26] Wallis, G. B., 1969, *One-Dimensional Two-Phase Flow*, McGraw-Hill, New York, pp. 243–374.

[27] Juliá, J. E., Hernández, L., Paranjape, S., and Ishii, M., 2007, "On the Use of Area-Averaged Void Fraction and Local Bubble Chord Length Entropies as Two-Phase Flow Regime Indicators," Sixth International Conference on Multiphase Flow, Germany.

[28] Hibiki, T., and Ishii, M., 2000, "Experimental Study on Hot-Leg U-Bend Two-Phase Natural Circulation in a Loop With a Large Diameter Pipe," Nucl. Eng. Des., **195**, pp. 69–84.

[29] Hibiki, T., and Ishii, M., 2002, "Development of One-Group Interfacial Area Transport Equation in Bubbly Flow Systems," Int. J. Heat Mass Transfer, **45**, pp. 2351–2372.

[30] Ozar, B., Jeong, J. J., Dixit, A., Juliá, J. E., Hibiki, T., and Ishii, M., 2008, "Flow Structure of Gas-Liquid Two-Phase Flow in an Annulus," Chem. Eng. Sci., **63**, pp. 3998–4011.

Incubation Time and Cavitation Erosion Rate of Work-Hardening Materials

Jean-Pierre Franc
LEGI,
BP 53,
38041 Grenoble Cedex 9, France
e-mail: jean-pierre.franc@hmg.inpg.fr

A phenomenological analysis of the cavitation erosion process of ductile materials is proposed. On the material side, the main parameters are the thickness of the hardened layer together with the conventional yield strength and ultimate strength. On the fluid side, the erosive potential of the cavitating flow is described in a simplified way using three integral parameters: rate, mean amplitude, and mean size of hydrodynamic impact loads. Explicit equations are derived for the computation of the incubation time and the steady-state erosion rate. They point out two characteristic scales. The time scale, which is relevant to the erosion phenomenon, is the covering time—the time necessary for the impacts to cover the material surface—whereas the pertinent length scale for ductile materials is the thickness of the hardened layer. The incubation time is proportional to the covering time with a multiplicative factor, which strongly depends on flow aggressiveness in terms of the mean amplitude of impact loads. As for the erosion rate under steady-state conditions, it is scaled by the ratio of the thickness of hardened layers to the covering time with an additional dependence on flow aggressiveness, too. The approach is supported by erosion tests conducted in a cavitation tunnel at a velocity of 65 m/s on stainless steel 316 L. Flow aggressiveness is inferred from pitting tests. The same model of material response that was used for mass loss prediction is applied to derive the original hydrodynamic impact loads due to bubble collapses from the geometric features of the pits. Long duration tests are performed in order to determine experimentally the incubation time and the mean depth of penetration rate and to validate the theoretical approach. [DOI: 10.1115/1.3063646]

1 Introduction

Cavitating flows are characterized by the development of relatively large vapor structures, which usually break up into smaller ones. For instance, a sheet cavity attached to the leading edge of a blade generally splits into many tiny bubbles in its closure region. It may also shed more or less regularly large clouds made of a myriad of small bubbles. If the overall features of the flow depend mainly on the global extent of cavitation, erosion is essentially caused by the individual collapses of small scale vapor structures.

The rate of production of such structures has been the subject of several investigations. Pereira et al. [1] using a tomographic technique could measure the rate of production of small scale vapor structures by a leading edge cavity together with their volume. They showed that the production rate is ruled by a Strouhal-like law, i.e., that the shedding frequency of small scale structures is inversely proportional to their size. The smaller the structures, the larger the production rate. Such a relationship is qualitatively confirmed by pitting tests that show that pit density generally increases when pit size decreases (see, e.g., Fig. 12 of the present work). This comparison assumes that pit size is correlated with bubble size, which seems physically reasonable although still open to discussion. A Strouhal similarity law for the prediction of the production rate of small scale structures was also proposed by Lecoffre et al. [2] following the work of Kato [3] as the basis for analyzing the effects of velocity and length scale on cavitation damage. In the scenario they propose for a quantitative prediction of cavitation erosion, Kato et al. [4] also addressed the problem of the breakup of a sheet cavity into small vapor structures. To quantify the number of bubbles generated by a leading edge cavity, they propose a two-step procedure. The flow rate of vapor shed by a cavity is first estimated from ventilation tests, assuming that the rate of air necessary to sustain an artificial cavity is the same as the vaporization rate for a natural cavity of equal length. Then, using measurements of bubble population in the wake of a sheet cavity [5] and assuming that the vaporization rate in the cavity is equal to the flow rate of vapor bubbles shed by it, they could get an estimate of the number and size of small scale vapor structures, which are all potential sources of erosion. In spite of such investigations, the detailed mechanism producing small scale structures from a macroscopic cavitation is not yet entirely understood, and it remains very difficult to predict the production rate of small scale vapor structures responsible for cavitation erosion together with their typical size and real nature, bubbles or vortices.

The damage potential of each of these individual structures is also very difficult to predict. Many studies have been conducted on single bubbles in order to investigate the detailed mechanisms of impulsive pressure generation by bubble collapse and associated damage (see, e.g., Refs. 6–8). Bubble dynamics near solid boundaries involves complex phenomena such as the formation of jets, counterjets, ring vortices, etc., whose influence on the cavitation erosion process is not always fully recognized. Several parameters are, however, known to have a major influence on the erosive potential, such as the distance of the bubble to the wall, its maximum size prior to collapse, the adverse pressure gradient to which the bubble is subjected, and which causes its collapse. Collective effects may also affect the violence of the collapse and the associated erosive potential. Reisman et al. [9] showed that the collapse of a cloud of bubbles may enhance the erosive potential of individual bubbles because of the focusing effect of shock waves near the cloud center. In spite many years of fundamental research on this topic, the quantification of the erosive potential of collapsing vapor structures remains a challenge in real cavitating flows.

Energy considerations are often used to approach this problem

Contributed by the Fluids Engineering Division of ASME for publication in the JOURNAL OF FLUIDS ENGINEERING. Manuscript received October 19, 2007; final manuscript received August 28, 2008; published online January 15, 2009. Assoc. Editor: Steven Ceccio.

from a global viewpoint in order to predict cavitation damage, disregarding local detailed collapse mechanisms. This type of approach is also the one that is adopted in the present paper. From the classical Rayleigh analysis of the dynamics of a spherical cavity in an inviscid incompressible liquid at rest at infinity, it is well known that the energy discharged as kinetic energy in the fluid by a cavity of volume V collapsing under a pressure difference Δp (relative to the pressure inside the bubble) is given by the work of the pressure forces, i.e., $V \times \Delta p$ [10]. According to Stinebring et al. [11], this total cavitation bubble collapse energy is the sum of the energy absorbed by the material, the elastic energy due to the recovery of the surface after the collapse, which produces an acoustic wave propagating through the fluid, and the energy remaining in the bubble after the initial collapse, i.e., the energy of the rebunding bubble(s). The residual plastic energy remaining in material after impact is generally assumed to be proportional to the volume of the resulting pit [10,12]. Hammitt [13] introduced the cavitation erosion efficiency, i.e., the ratio between this residual plastic energy and the energy actually applied to the surface by shock waves and microjet impacts. He suggests to estimate the latter from pulse height spectra measured in the collapse region using piezoelectric microtransducers. On the basis of linear acoustic theory, Hammitt [13] proposed to estimate the energy emitted by cavitation bubble collapse from the quantity $p^2 \times \Delta t/(\rho c)$ calculated using the measured amplitude p of each detected pressure pulse, its duration Δt, and the acoustic impedance ρc of the liquid. By considering all pressure pulses detected by the transducer during a given lapse of time and computing the summation of individual collapse energies as defined above, a total energy can be introduced, which is expected to represent the cumulative impact energy of all the vapor structures that have collapsed on the sensitive surface of the transducer during the measuring time. Several investigations concluded on a linear relationship between measured erosion and the total impact energy deduced from pulse height spectra analysis [13–16]. This relation depends on the material but proves to be independent of test conditions including Venturi and vibratory erosion tests. This technique appears then as a valuable method to quantify the erosive potential of a cavitating flow.

Another way to measure the flow aggressiveness is to use pitting tests as proposed 50 years ago by Knapp [17,18]. This is the technique that is used in the present work for reasons developed in Sec. 3.2. Since this pioneering work, techniques of analysis of pitted surfaces have been improved [12,19], and the detailed shape of erosion pits is now available. Information on pit size and pit depth allow an improved quantification of the erosive potential in comparison with the only pit density used originally. Using pitting tests as a basis for the determination of flow aggressiveness implies that the material itself is considered as a special transducer whose response to bubble collapses is precisely made of surface pits. A quantitative approach requires us to model the material behavior in order to convert data on pit geometry into data on hydrodynamic loads. This is one of the objectives of the present work.

Another objective is to predict long term damage using the same model of material response. The evolution of cavitation erosion with the exposure time shows different periods. Three main stages are generally distinguished (see, e.g., Refs. 13 and 20). At the very beginning, the erosion damage is made of isolated pits, which progressively overlap as the exposure time increases. Usually, negligible mass loss occurs during this incubation period. Then, mass loss actually begins, and an acceleration period is observed, with a damage rate gradually increasing up to a maximum. A steady-state period with a constant erosion rate is then expected as long as the flow pattern remains unchanged. Secondary effects may affect this schematic behavior, and more complicated evolutions are found in the literature depending, in particular, on the test facility [21]. For example, the steady-state period may be almost inexistent, or the maximum may be followed by a deceleration or even oscillations of the erosion rate [22]. These effects are generally due to an interaction between the cavitating flow and the walls via, for instance, changes in roughness or wall shape induced by the wear itself. They are ignored in the present paper, which focuses on the three basic stages described above. In addition, all erosion tests were started from a highly polished surface, and the effect of the initial surface roughness, which may substantially affect the incubation period [23], was not considered. Corrosion effects were also ignored, and the deterioration of the surface is supposed to result only from the mechanical attack of collapsing bubbles.

This paper is based on an analysis proposed in 1987 by Karimi and Leo [24] and adapted in 2002 by Berchiche et al. [25]. The method is applicable to ductile materials (such as stainless steel 316 L considered here), which undergo work hardening when exposed to cavitation. Work hardening is characterized by a change in microhardness, dislocation density, and strain with depth below the worn surface [26]. In this paper, it is represented by the shape of the microhardness profile in cross sections of eroded specimens and, in particular, by the thickness of the hardened layer. The starting point of the prediction procedure is made of pitting tests from which the erosive potential of the cavitating flow is characterized in terms of impact loads, as mentioned previously. Berchiche et al. [25] characterized the erosive potential of the cavitating flow by a distribution in size and amplitude of impact loads. They reproduced it numerically a large number of times and could compute mass loss as a function of the exposure time. Because of the wide spectrum of pits, they were obliged to use a numerical procedure that gives realistic evolutions in time and space of the damage but makes difficult a phenomenological analysis. In order to point out the basic parameters of the model and their influence mainly on the incubation time and the steady-state erosion rate, the approach has been reformulated in a simplified way in this paper. The simplification consists in representing the whole spectrum by a limited number of integral parameters. Analytical relationships can then be derived, from which it is much easier to draw general trends and, in particular, to point out the relevant length scale and time scale of the erosion phenomenon for ductile materials.

2 Phenomenological Analysis

2.1 Erosive Potential. The real cavitating flow comprises a large variety of vapor structures. When collapsing, each structure is supposed to generate a load on the wall. A large variety of impact loads of various sizes and amplitudes are then generated. The simplification that is made here consists in characterizing the whole impact load spectrum by a mean value $\bar{\sigma}$ of the amplitude and a mean value $\bar{S}$ of the impacted area. A third major parameter with respect to flow aggressiveness is the number N per unit time and unit surface area of these impacts. In summary, the erosive potential of the cavitating flow is characterized here by a set of three parameters, $\bar{\sigma}$, $\bar{S}$, and N. The averaging procedure to represent a complex spectrum by a unique set of values $(\bar{\sigma}, \bar{S}, N)$ is presented in more detail in Sec. 4.1. The general idea is to preserve the total energy impacting the wall.

The present model of an individual impact is the simplest one that can be imagined since the radial distribution of stress is considered as uniform: stress is equal to $\bar{\sigma}$ over the surface $\bar{S}$ and zero outside. Moreover, no indication is given on the time evolution of the applied stress. This means, in particular, that the strain rate, which is known to be very high in cavitating flows, is ignored at this step. The introduction of strain rate in the present analysis would require further developments.

From a purely dimensional viewpoint, a characteristic time can be built on the basis of two of these parameters. It is defined by $\tau = 1/N\bar{S}$. From a physical viewpoint, this time can be interpreted as the *covering time*. i.e., the time necessary for the surface to be

fully covered exactly once by the cavitation impacts. This characteristic time plays a fundamental role in the erosion process, as will be shown later.

2.2 Material Thresholds. To estimate damage caused to the wall, it is necessary to compare the amplitude of impact loads to specific material characteristics used as thresholds. In the present paper and following the initial analysis of Karimi and Leo [24], we systematically refer to tensile tests to define these thresholds using the ordinary yield strength σ_Y and ultimate tensile strength σ_U. More appropriate material tests should probably be used to better account for the very specific type of loading due to bubble collapse. One limitation among others is that ordinary tensile tests are conducted at a strain rate several orders of magnitude smaller than that of cavitation. However, within the same simplified approach, the high strain rate encountered in cavitation erosion can be taken into account, to some extent, by artificially increasing σ_Y and σ_U with respect to the values given by a classical tensile test at much smaller strain rate.

In the present paper, a Ludwik-type consolidation relationship between stress σ and strain ε is chosen,

$$\sigma = \sigma_Y + K\varepsilon^n \tag{1}$$

Let us observe that although Eq. (1) is, strictly speaking, valid only up to the ultimate strength, it will be extrapolated beyond σ_U. This is the basis for the computation of mass loss rate.

Throughout this paper, we shall take the example of stainless steel 316 L, which has been used for the experimental part of this work. Typical values for SS 316 L are [25]

$$\sigma_Y = 400 \text{ MPa}$$

$$\sigma_U = 1020 \text{ MPa}$$

$$K = 900 \text{ MPa}$$

$$n = 0.5 \tag{2}$$

The erosion damage depends primarily on the mean amplitude $\bar{\sigma}$ of the impact loads relative to the two previous thresholds. Three cases can happen.

(i) If $\bar{\sigma} < \sigma_Y$, the impacts are supposed to cause no damage at all, whatever their size and rate may be. The elastic behavior dominates.
(ii) If $\bar{\sigma}$ lies between σ_Y and σ_U, successive impacts cause first the progressive hardening of the initially virgin material without any mass loss and then its rupture, and the penetration of the damage after the work-hardening process is completed. This fatigue-type mechanism is the way the incubation time is accounted for in the present model.
(iii) Finally, if $\bar{\sigma} > \sigma_U$, mass loss appears from the very beginning of exposure to cavitation.

2.3 Work Hardening. For a virgin material, strain is zero everywhere inside the material. As it is exposed to bubble collapses, the successive hydrodynamic impacts lead to a progressive superficial hardening. The strain profile inside an eroded sample can be determined from microhardness measurements on a cross section [25]. A classical representation of the strain profile inside the material is

$$\varepsilon(x) = \varepsilon_0 \left[1 - \frac{x}{\ell} \right]^\theta \tag{3}$$

where ε_0 is the strain on the surface, x is the distance below the surface, ℓ is the thickness of the hardened layers, and θ is a shape factor for the strain profile.

The thickness ℓ of the hardened layer progressively increases with exposure time and reaches a maximum (denoted as L) when the work-hardening process is completed. The surface strain is then ε_U corresponding to σ_U: the material is then ready to rupture at its surface. Typical values of L and θ for stainless steel 316 L are [25]

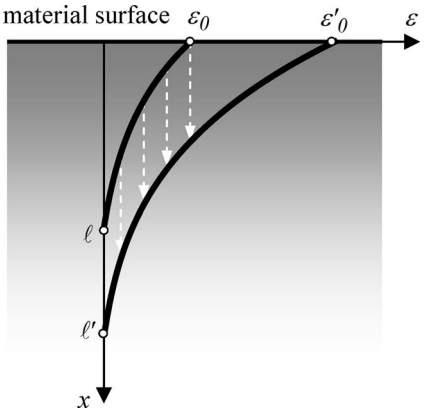

Fig. 1 Work-hardening progress

$$L = 200 \ \mu\text{m}$$

$$\theta = 5 \tag{4}$$

To predict the evolution of ℓ with ε_0, it is observed that the strain profile can be considered as simply translated inside the material as work hardening proceeds. This is a property of the power law chosen to describe the strain profile. In other words, if ε_0 increases up to ε'_0 whereas ℓ increases up to ℓ' (Fig. 1), the new strain profile is

$$\varepsilon(x) = \varepsilon'_0 \left[1 - \frac{x}{\ell'} \right]^\theta \tag{5}$$

and we have $\varepsilon(x) = \varepsilon_0$ for $x = \ell' - \ell$, i.e.,

$$\frac{\varepsilon_0}{\varepsilon'_0} = \left[\frac{\ell}{\ell'} \right]^\theta \tag{6}$$

Equation (6) shows that the thickness ℓ of the hardened layer increases as $\varepsilon^{1/\theta}$. In particular, ℓ is connected to the maximum value L by

$$\frac{\varepsilon_0}{\varepsilon_U} = \left[\frac{\ell}{L} \right]^\theta \tag{7}$$

2.4 Single Impact. As already mentioned in Sec. 1, the present approach is based on energy considerations. A key concept is the energy absorbed by the material when submitted to a single hydrodynamic impact $(\bar{\sigma}, \bar{S})$. This energy is assumed to be independent of the degree of hardening of the material and is evaluated on the basis of a virgin material. It is also assumed to be independent of surface roughness.

Let us denote by ε_1 the strain on the material surface resulting from an impact of amplitude $\bar{\sigma}$ on the virgin material. There is a unique correspondence between $\bar{\sigma}$ and ε_1 via the material stress/strain relationship (1). The ε_1-variable can then be used instead of $\bar{\sigma}$. In case $\bar{\sigma} > \sigma_U$, the approach remains valid provided the stress/strain relationship is extrapolated beyond σ_U.

After a single impact, the material surface behaves as indicated schematically in Fig. 2(*a*). The surface strain is ε_1 corresponding to impact load $\bar{\sigma}$. The energy absorbed per unit volume by the most superficial layer is the area below the stress/strain curve. As for internal layers, strain $\varepsilon(x)$ decreases with distance x from the surface according to Eq. (3), and the energy absorbed (which is still the area below the stress/strain curve) is smaller for inner layers than for the most superficial ones (Fig. 2(*b*)).

The total energy absorbed by the material can be computed as

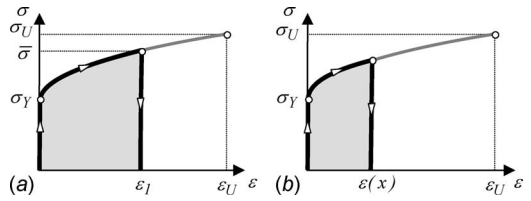

Fig. 2 Behavior of a virgin material after being loaded by a hydrodynamic impact of amplitude $\bar{\sigma}$. (*a*) Case of the superficial layer. (*b*) Case of a layer at depth *x*.

$$W(\varepsilon_1) = \int_{x=0}^{\ell} \left[\int_{\varepsilon=0}^{\varepsilon(x)} \sigma d\varepsilon \right] \bar{S} dx \tag{8}$$

It is given by

$$W(\varepsilon_1) = \varepsilon_1 \bar{S} L \left(\frac{\varepsilon_1}{\varepsilon_U} \right)^{1/\theta} \frac{\sigma_Y + \beta K \varepsilon_1^n}{1+\theta} \tag{9}$$

with

$$\beta = \frac{1+\theta}{(1+n)(1+\theta+n\theta)} \tag{10}$$

L is the maximum thickness of the hardened layers when work hardening is complete, whereas the quantity

$$L \left(\frac{\varepsilon_1}{\varepsilon_U} \right)^{1/\theta} \tag{11}$$

is the thickness of the hardened layers for a partial hardening due to the only considered impact $\bar{\sigma}$ (see Eq. (7)).

2.5 Incubation Period. As exposure time increases, the material is hardened and surface strain progressively increases. After the first covering of the initially virgin material (i.e., after time τ), surface strain is uniformly equal to ε_1. After the second covering (time 2τ), surface strain is increased from ε_1 up to a value of ε_2, which is deduced from the conservation of energy. Since there has been two coverings, the flow has discharged into the material the energy $2W(\varepsilon_1)$. Moreover, if surface strain is ε_2, the total energy absorbed by the material is actually $W(\varepsilon_2)$. The energy balance writes $W(\varepsilon_2)=2W(\varepsilon_1)$. This equation allows the determination of the ε_2-value. The work-hardening process is continued between the second covering (instant 2τ) and the third one (instant 3τ). Surface strain increases up to a ε_3-value given by $W(\varepsilon_3)=3W(\varepsilon_1)$, and so on (see Fig. 3).

No mass loss is expected until surface strain reaches the ultimate strain ε_U corresponding to the ultimate tensile strength σ_U. The number of coverings necessary to reach this critical point is $n=W(\varepsilon_U)/W(\varepsilon_1)$, and the corresponding time is $n\tau$. This time is

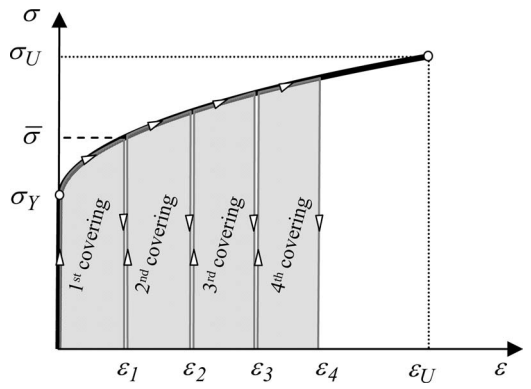

Fig. 3 Material response during the incubation period

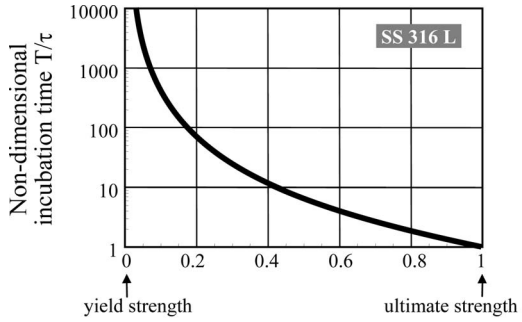

Fig. 4 Typical example of the variation of the incubation period with the amplitude of impact loads $\bar{\sigma}$. Case of stainless steel 316 L. The values of the material constants are given in Eqs. (2) and (4). The abscissa represents the nondimensional amplitude of impact loads defined by $(\bar{\sigma}-\sigma_Y)/(\sigma_U-\sigma_Y)$, whereas the ordinate is the incubation time *T* made nondimensional using the covering time τ.

precisely the incubation period T beyond which mass loss is expected. Using Eq. (9), together with the stress/strain relationship (1), the incubation time is given in a nondimensional form by

$$\frac{T}{\tau} = \left[\frac{\sigma_U - \sigma_Y}{\bar{\sigma} - \sigma_Y} \right]^{(1+\theta)/n\theta} \frac{\sigma_Y + \beta(\sigma_U - \sigma_Y)}{\sigma_Y + \beta(\bar{\sigma} - \sigma_Y)} \tag{12}$$

Equation (12) accounts for both the influence of the erosive potential of the cavitating flow and that of the material properties. The incubation period depends on the material properties σ_Y, σ_U, n, and θ (but not on the thickness L of the hardened layers) and on the flow aggressiveness $\bar{\sigma}$, $\bar{S}$, and N. Concerning the last two parameters, the incubation period appears to be simply proportional to the covering time $\tau=1/N\bar{S}$. The dependence with respect to the amplitude of impact loads $\bar{\sigma}$ is more complex. When $\bar{\sigma}$ approaches σ_Y, the incubation time tends to infinity. This is consistent with the assumption that no damage will occur if the amplitude of impacts is smaller than the yield strength. On the other hand, for $\bar{\sigma}=\sigma_U$, one has $T=\tau$. This means that mass loss is expected to happen after the material surface has been covered only once. This is quite understandable from a physical viewpoint. Beyond σ_U, the incubation time takes no sense since erosion occurs from the very beginning of exposure. Between σ_Y and σ_U, the incubation period progressively decreases as flow aggressiveness (here $\bar{\sigma}$) increases. As an example, the evolution of the incubation period with the mean amplitude of impact loads is presented in Fig. 4 for stainless steel 316 L using the numerical values given in Eqs. (2) and (4). In case the mean amplitude of impact loads is only a little higher than the yield strength, i.e., for flows of relatively small erosive potential, the number of coverings necessary before mass loss happens may be quite large, and the incubation time may be several orders of magnitude larger than the covering time.

2.6 Steady-State Mass Loss Rate. After the incubation period, surface strain is maximum and equal to ε_U. Any further impact will cause material removal. After a new complete covering of the material surface, strain at surface reaches a value of ε' greater than ε_U (see Fig. 5). This ε'-value is extrapolated beyond the ultimate tensile strength on the stress/strain relationship. It can be considered as virtual in so far as all the layers of the material with a strain greater than ε_U are indeed assumed to be ruptured and eroded. This ε'-value is computed, as previously, from an energy balance, which is written as

$$W(\varepsilon') = W(\varepsilon_U) + W(\varepsilon_1) \tag{13}$$

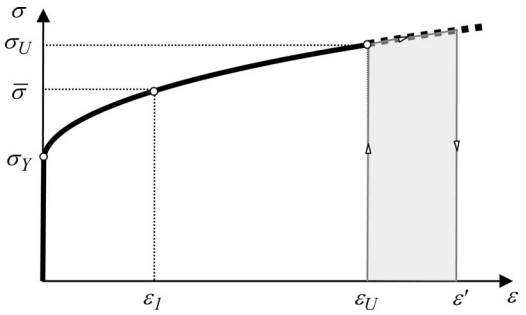

Fig. 5 Material behavior after the incubation period during steady-state erosion

Once the new surface strain ε' is known, the new strain profile inside the material can be computed. Both profiles, just after the incubation period and after an additional covering, are compared in Fig. 6. They are simply translated with a length ΔL given by

$$\frac{\Delta L}{L} = \left[\frac{\varepsilon'}{\varepsilon_U}\right]^{1/\theta} - 1 \tag{14}$$

as explained in Sec. 2.3. The previous equation is a direct consequence of Eq. (7).

Mass loss is computed by assuming that the material cannot sustain a strain greater than the ultimate strain ε_U so that the thickness ΔL is actually eroded and removed during the interval of time τ. The mean depth of penetration rate (MDPR) is then

$$\text{MDPR} = \frac{\Delta L}{\tau} = \frac{L}{\tau}\left[\left(\frac{\varepsilon'}{\varepsilon_U}\right)^{1/\theta} - 1\right] \tag{15}$$

A major outcome of this equation is that the steady-state erosion rate MDPR is proportional to L/τ. In other words, from a dimensional viewpoint, it appears that the characteristic length, which is pertinent for the computation of MDPR is the thickness L of the hardened layers (which is a feature of the material), whereas the characteristic time to be considered is the covering time τ (which is a feature of the fluid flow). The term in brackets is a multiplicative factor, which depends primarily on flow aggressiveness. It is estimated below in the case of stainless steel 316 L.

A practical way to compute MDPR is as follows. From the mean value of the impact load $\bar{\sigma}$, strain ε_1 is computed using the stress/strain relationship, and the corresponding energy $W(\varepsilon_1)$ is computed using Eq. (9). The energy conservation equation (Eq. (13)) is then solved in order to determine ε'. Since this equation cannot be solved analytically, we cannot get a fully analytical equation for MDPR. The mean depth of penetration rate can then be computed using Eq. (15).

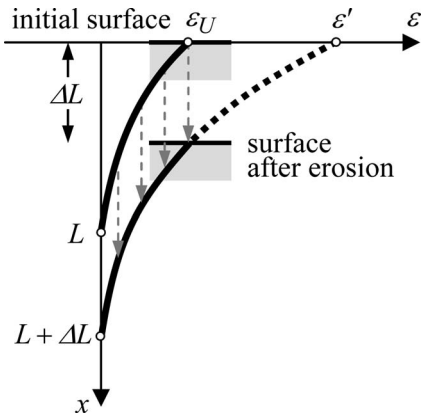

Fig. 6 Principle of the computation of mass loss

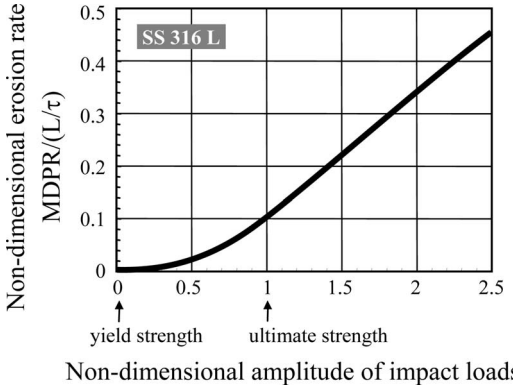

Fig. 7 Typical example of the variation in the MDPR with the mean amplitude of impact loads. Case of stainless steel 316 L (see Eqs. (2) and (4) for values of constants). MDPR is made nondimensional using the characteristic erosion rate L/τ, whereas the nondimensional amplitude of impact loads is defined as in Fig. 4.

A typical evolution of the erosion rate with flow aggressiveness is presented in Fig. 7, still in the case of stainless steel 316 L. In the limit case $\bar{\sigma}=\sigma_Y$, one has $W(\varepsilon_1)=0$, $\varepsilon'=\varepsilon_U$, and then MDPR=0, as expected. Figure 7 shows that MDPR increases first slowly with $\bar{\sigma}$ around the yield strength and tends to be more or less linear with $\bar{\sigma}$ beyond the ultimate strength. For $\bar{\sigma}<\sigma_U$, damage is due to fatigue associated with the accumulation of energy in the material. The present approach remains valid for severe cavitation erosion ($\bar{\sigma}>\sigma_U$).

3 Experiments

3.1 Experimental Facility. To support the previous phenomenological analysis, erosion tests were conducted in a cavitation tunnel (Fig. 8). The facility is designed for a maximum operating pressure of 40 bars. This relatively high pressure provides high velocities and, consequently, high erosive potential for the cavitating flow. This is an essential condition to obtain significant mass loss within reasonable exposure times and to make possible the investigation of the advanced stages of erosion. The pump is a centrifugal pump driven by an electric motor of 80 kW in power. The maximum flow rate is 11 l/s. The facility includes a downstream tank of about 1 m^3. Pressurization is achieved by means of a bottle connected to the tank by a pipe of small diameter in order to limit the diffusion of nitrogen used for pressurization. Liquid is tap water without any special control of dissolved gas. Water temperature is kept constant by means of a heat exchanger. It is a countercurrent exchanger made of 85 tubes of 11 mm in diameter with a nominal power of 80 kW. Tests are conducted at ambient temperature. The rise in temperature after a run of 5 h is typically of the order of 0.5°C. The tunnel is equipped with several transducers to determine the operating conditions: an electromagnetic flowmeter, a pressure transducer to measure the absolute pressure upstream of the test section p_u, a differential pressure transducer to measure the pressure drop through the test section, and a temperature probe.

The test section is about 6 m above the pump in order to avoid any cavitation of the pump. It is axisymmetric and made of a nozzle of 16 mm in diameter followed by a radial divergent of 2.5 mm in thickness (Fig. 9). Under cavitating conditions, a cavity is attached to the nozzle exit whose length can be adjusted by changing the cavitation number, which is obtained in practice by changing the downstream pressure p_d. Cavitation number is defined by

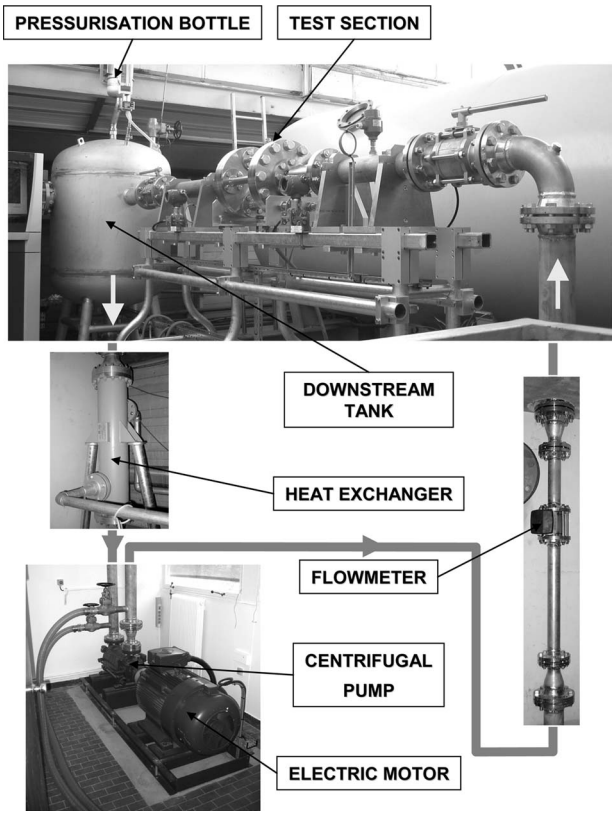

Fig. 8 View of the cavitation erosion tunnel

$$\sigma = \frac{p_d - p_v}{p_u - p_d} \tag{16}$$

The σ-value is chosen to be equal to 0.9, which leads to a cavity of about 25 mm in mean length. This ensures that the zone of maximum erosion, which corresponds to cavity closure lies in an appropriate region of the target for the subsequent analysis. The tests presented in this paper were conducted at a flow rate of 6.25 l/s. The upstream pressure is 21.3 bars, and the pressure drop through the test section given by

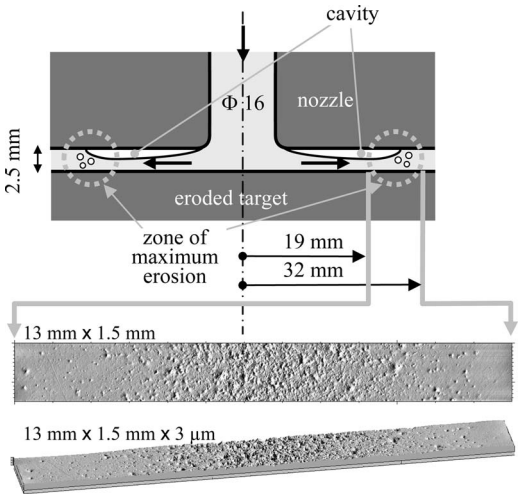

Fig. 9 Schematic view of the test section together with an eroded target. The size of the eroded surface shown is 13 $\times$1.5 mm^2. The operating conditions are V_c=65.3 m/s, p_u =21.3 bars, p_d=10.1 bars, and σ=0.9. Test duration: 30 min.

$$p_u - p_d \cong \frac{1}{1+\sigma} p_u \tag{17}$$

is 11.2 bars at σ=0.9. The mean velocity in the 16 mm nozzle is 31 m/s. The reference velocity on the cavity where pressure is assumed to be equal to the vapor pressure p_v can be estimated from the Bernoulli equation in which the vapor pressure is neglected compared with the upstream pressure,

$$V_c \cong \sqrt{\frac{2p_u}{\rho}} \tag{18}$$

For present tests, the reference velocity on the cavity is V_c =65.3 m/s.

The target to be eroded faces the nozzle exit. Erosion appears in the form of a ring centered on cavity closure where erosive potential is maximum (see Fig. 15). Both sides of the channel are expected to be eroded, but the nozzle is made of a highly resistant material so that no significant erosion is observed on the nozzle itself. Erosion tests are conducted on stainless steel 316 L, free of any corrosion effect in water. Prior to exposure to cavitation, a metallurgical polishing of the specimen surface is carried out with successive diamond pastes down to 0.25 μm, which ensures a mirror-type polish. The effect of roughness on cavitation erosion damage is not considered in the present investigation.

3.2 Pitting Tests. Pitting tests are used here to characterize the erosive potential of the cavitating flow. The idea of using the material itself as a kind of transducer to reveal the flow aggressiveness is classical [10]. It consists in considering that each indentation is the signature of the collapse of a bubble. In a first approach, it can reasonably be assumed that pit depth is representative of maximum load and pit size of the extent of the loaded area. This is the assumption made in Sec. 4.1 below.

As mentioned in Sec. 1, an alternative for characterizing flow aggressiveness is to use pressure transducers. Li et al. [27] showed that the temporal pressure fluctuations given by a transducer flush mounted in the cavitating region is made of several components. In addition to basic flow noise and low-frequency fluctuations associated with the global behavior of the two-phase region, they observed high-frequency pulses due to cavitation bubble collapse. Several investigators (see, e.g., Refs. 15, 28, and 29) have shown that a good correlation exists between erosion damage and the number of pulses above a suitable threshold. However, the quantitative evaluation of pressure load due to bubble collapse by pressure transducers raises a few basic difficulties. The very high characteristic frequency of cavitation pulses requires transducers of small rise time in order to follow reliably the fast pressure rise. Very significant progress has been made in this field by the development of special transducers [15,30]. But a major difficulty remains concerning the size of the sensitive surface, which, although miniaturized, is much bigger than that of indentations. Even though realistic estimates can be obtained by dividing the measured load in terms of force by the area of the indentation [30], pressure transducers cannot directly supply pressure load. This problem leads us to prefer pitting tests to evaluate flow aggressiveness. Nevertheless, the estimate of pressure load from indentation characteristics is not straightforward as well, and a special procedure (see Sec. 4.1) based on a modeling of the material response is needed.

Figure 10 presents a typical view of a pitted surface (see also top of Fig. 22). A pitting test can be considered as acceptable if the degree of pit overlapping is low enough. It is clear that the response of a ductile material is not the same whether the impact falls on a virgin part of its surface or an already pitted area. This is because of the increase in superficial hardness due to pitting. Since the analysis of the pitting test presented in Sec. 4.1 is based on the assumption that each pit falls on a virgin area, it is of major importance to limit overlapping in order to obtain an unbiased estimate of the erosive potential. The degree of overlapping is

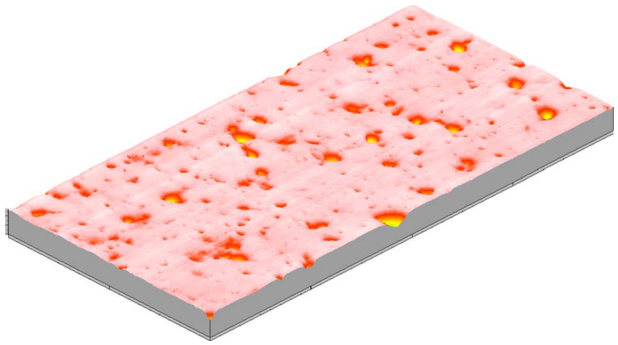

Fig. 10 Typical 3D view of the surface after a pitting test. The size of the volume shown is 2 mm×4 mm×2.8 μm. Same operating conditions as in Fig. 9. Exposure time: 5 min.

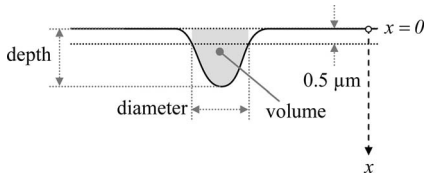

Fig. 11 Sketch showing the definition of pit depth, diameter, and volume

controlled by the exposure time, and, statistically speaking, it can be reasonably assumed that it is negligible if the exposure time is small enough. In practice, it has to be compared with the covering time introduced in Sec. 2.1. In the case of Fig. 10, the covering time is estimated to 88 min, whereas the exposure time is only 5 min. It can then be concluded that overlapping is negligible. The photograph in Fig. 10 confirms that, at least qualitatively, overlapping is only occasional. Provided the exposure time is much smaller than the covering time, it can be expected that the analysis of a pitting test to evaluate flow aggressiveness is independent of exposure time. The smaller the exposure time, the smaller the pit number and the less accurate the estimate. Conversely, the larger the exposure time, the larger the degree of overlapping and the less accurate the estimate as well. It is then necessary to find a compromise. A possibility can be to make several pitting tests of rather short duration and to cumulate the data to get a representative sample from a statistical viewpoint, as will be done later. Furthermore, it is essential that the exposure time be sufficiently short so that large portions of the original virgin surface remain easily detectable between indentations. This is important for the analysis technique since the original surface is used as a reference for the determination of pit depth.

Several techniques are available to analyze a pitted surface. Belahadji et al. [19] used an interferometric technique, and Fortes Patella et al. [12] used a laser profilometer. In the present work, a contact-type profilometer has been used with a stylus of tip radius of 2 μm and a vertical maximum resolution of 3.2 nm. The surface is scanned along parallel lines distanced 1 μm apart with a resolution of 0.5 μm between two successive points. For most tests, a surface of 2×4 mm^2 was scanned. Treatment of the data starts by subtracting a polynomial obtained by the least mean square technique. After several tests, a polynomial of degree 5 was considered. It proved to satisfactorily remove the mean shape of the surface often due to large scale machining or polishing defects without altering the shape of pits at a much smaller scale. The next step consists in applying a threshold to the surface in order to define the pit border. For all the analyses presented here, the threshold was fixed at 0.5 μm below the reference surface corresponding to the original material surface. All pits whose depth is smaller than 0.5 μm are then ignored. This threshold is constant and independent of the indentation. Its influence on the subsequent prediction of incubation time and mass loss rate is discussed in Sec. 4.2. The chosen value of 0.5 μm proved to give a correct description of the pits (see Fig. 22). Other investigators [12,19] consider a pit dependent threshold often taken as a fraction (typically 10%) of maximum pit depth. The influence of the analysis technique on the estimate of the erosive potential of the flow and the subsequent estimate of long term damage has not been investigated.

By this technique, each pit is identified, and its main characteristics (surface, volume, maximum depth, and mean diameter) are computed. Pit size is defined as the equivalent diameter of the section of the pit by the plane $x=0.5$ μm. Pit depth is counted from the original material surface $x=0$, and volume is defined as shown in Fig. 11.

Figure 12 gives a representation of a sample of almost 800 pits analyzed here in a diagram whose coordinates are pit depth and pit diameter. No correlation is noticeable between pit depth and pit diameter so that both parameters can be considered as independent. In other words, large pits are not necessarily deeper, and no definite geometric similarity is observed on pit profiles.

The distribution of pits as a function of diameter is shown in Fig. 13. The smaller the pits, the higher the pitting rate. As for the contribution of each class of size to the damage, it can be estimated by considering the eroded surface defined here as the total surface of pits belonging to each class of size. The corresponding cumulative and probability density functions (PDFs) are shown in Fig. 14. PDF exhibits a maximum for pit diameters around 100 μm. Small pits are many but do not contribute significantly to the eroded surface because of their small size. The contribution of large pits is also negligible, but because of their small probability. The existence of a maximum is then quite understandable. It has also been observed by Belahadji et al. [19] for pitting tests in a cavitating Venturi. The conclusion is the same when considering the eroded volume defined as the total volume of pits belonging to each class of size. In particular, the PDF of the eroded volume exhibits a maximum in the same range of size, around 100 μm, as shown in Fig. 15. For the prediction of incubation time and mass loss rate, it is essential that the technique of analysis of pitting tests focuses on the range of pit diameters, which contribute most to the damage. In the present case, the contribution of pits smaller than 20 μm was ignored, whereas the largest observed pit was 220 μm in diameter (see Fig. 12).

Note that pitting tests are conducted here on the same material as the one used for mass loss experiments. This obviously simpli-

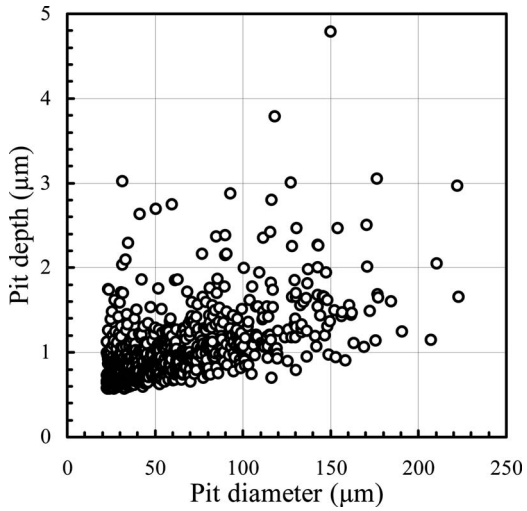

Fig. 12 Pit depth versus pit diameter. Each point represents a pit. The total number of pits is 797.

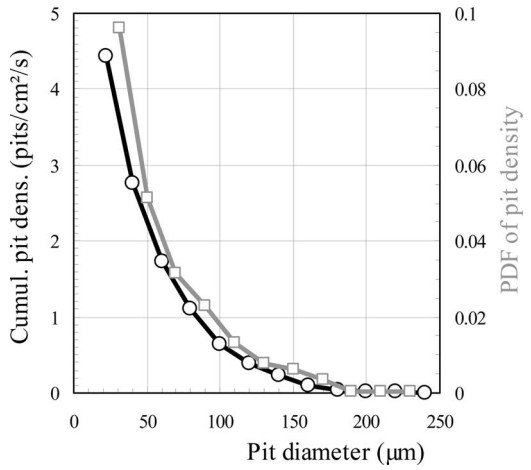

Fig. 13 Cumulative distribution and probability density functions of pit density per unit time and unit surface area. Same operating conditions as in Fig. 9. Total number of pits: 797. Analyzed surface: 59.9 mm².

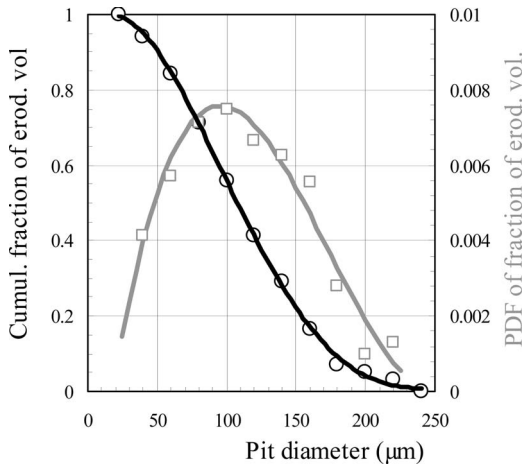

Fig. 15 Cumulative distribution and probability density functions of the fraction of eroded volume. Same conditions as in Fig. 12.

fies the approach in comparison with pitting tests conducted on another material, for instance, a softer one as it is often done in order to reduce test duration. The problem of the dependency of the estimated flow aggressiveness on the material used for pitting tests as well as the question of transposition from a material to another are not addressed in the present paper.

3.3 Mass Loss Experiments. A series of mass loss experiments with increasing exposure times has been conducted on a SS 316 L target for the same operating conditions as the pitting tests presented in Sec. 3.2. Figure 16 presents a view of the material surface after the maximum exposure time of 104 h. Damage is concentrated on a ring corresponding to the closure region of the cavity with almost no damage inside the cavity. On the whole, damage appears axisymmetric enough despite a few undulations in the upper left quarter, which may be due to erosion of the nozzle even though very limited. The measurements were then concentrated on the three other quarters free of defects.

The mass loss test was bracketed by two pitting tests in order to detect any possible alteration in flow aggressiveness during the long duration test. No significant variation was observed between both pitting tests so that it can be considered that flow aggressiveness has remained invariable all along the mass loss test. This results from (i) a negligible change in wall geometry since the maximum depth of penetration was 70 μm after 104 h, which is negligible in comparison with the 2.5 mm gap (Fig. 9), and (ii) a precise control of the operating conditions, which prevent any shift during operation.

Radial profiles of erosion are presented in Fig. 17 for an increasing exposure time. During about the first 30 h of exposure to cavitation, there is no measurable penetration of damage, which is essentially characterized by an increase in roughness. After this incubation period, some material is removed and the depth of penetration regularly increases. Raw profiles shown in Fig. 17 reveal the strong roughness of the eroded surface; they need to be smoothed for further analysis. An averaging technique on a 1 mm wide moving window was systematically applied before estimating the depth of penetration. Let us observe that because of the massive feature and large weight of the sample, mass loss could not be measured with a sufficient accuracy by a weighting technique. Strictly speaking, present estimates are then volume loss

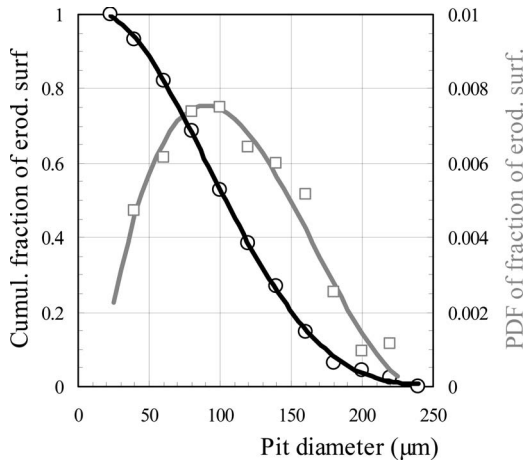

Fig. 14 Cumulative distribution and probability density functions of the fraction of eroded surface. Same conditions as in Fig. 12.

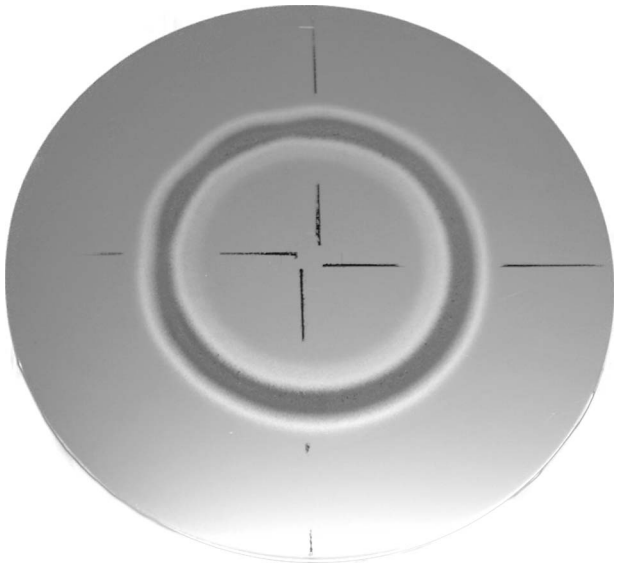

Fig. 16 Photograph of an eroded sample after an exposure time of 104 h. The external diameter of the sample is 100 mm. Operating conditions: V_c=65.3 m/s, p_u=21.3 bars, p_d =10.1 bars, and σ=0.9.

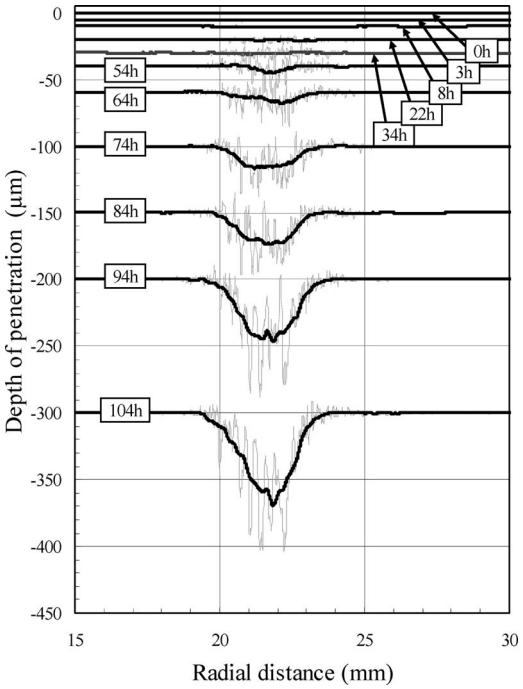

Fig. 17 Influence of the exposure time on radial profiles of erosion for the sample presented in Fig. 19. For each time, two profiles are presented: (i) light gray: raw data with a step of 10 μm; (ii) thick black: moving average data on 100 points or 1 mm. (The origins of horizontal and vertical scales are arbitrary.)

and not mass loss measurements.

The comparison of three different radial profiles (not shown here) confirms a satisfactory axisymmetry of the erosion pattern, as already concluded from the photograph of Fig. 16. Data on MDPR presented below are relative to the average of three smoothed profiles. Two quantities are considered: (i) the maximum depth of penetration and (ii) a mean depth of penetration defined over a radial distance of 2 mm centered on the point of maximum erosion. This last procedure presents the advantage of smoothing the data and reducing the dispersion since the damage is defined on a more global basis. Both estimates of depth of penetration are shown in Fig. 18. The smooth one is favored for future comparisons with theory.

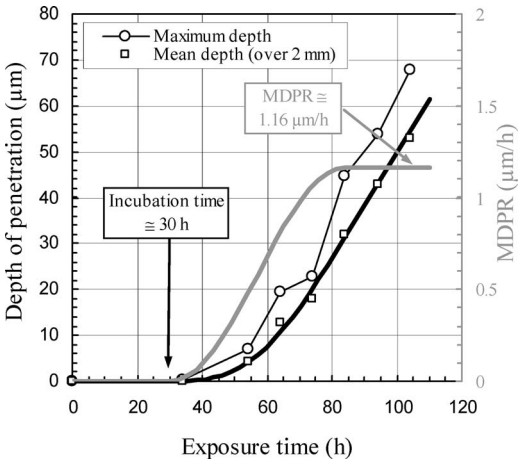

Fig. 18 Mean depth of penetration (in black, left scale) and mean depth of penetration rate (in gray, right scale) versus exposure time. The gray curve is the time derivative of the thick black curve.

The evolution of the mean depth of penetration with exposure time presented in Fig. 18 is quite conventional. After an incubation period during which the depth of penetration remains zero, an acceleration period is observed, followed by a quasilinear increase in the depth of penetration with exposure time. The MDPR was obtained by derivation with respect to time. For further validation, special attention is paid to the constant value of MDPR during the steady-state regime of erosion. The existence of a steady-state regime characterized by a linear increase in depth of penetration with time is a good indicator of the invariance of the erosive potential of the cavitating flow, confirmed by pitting tests. The duration of this steady-state period and the evolution of mass loss beyond 104 h were not investigated.

4 Analysis of Experimental Results

4.1 Estimation of Erosive Potential. The first step in the prediction procedure is the estimation of the erosive potential of the cavitating flow in terms of the three integral parameters considered in the present work: mean impact load $\bar{\sigma}$, mean area of impact load $\bar{S}$ (or equivalent mean diameter $\bar{D}$), and pitting rate N. For each pit, the impact load responsible for it is deduced from the measurement of its maximum depth. Let us first consider the case of an impact load σ smaller than the ultimate strength σ_U of the material. Plastic deformation occurs without any material removal, and the depth of the resulting indentation is

$$H = \int_{x=0}^{\ell} \varepsilon(x)dx \tag{19}$$

Using Eq. (3) for the strain profile $\varepsilon(x)$ inside the material, we obtain

$$H = \frac{\varepsilon_0 \ell}{1+\theta} \tag{20}$$

and finally, by means of Eq. (7),

$$H = \frac{\varepsilon_U L}{1+\theta}\left(\frac{\sigma - \sigma_Y}{\sigma_U - \sigma_Y}\right)^{(1+\theta)/n\theta} \tag{21}$$

This equation is used to estimate the impact load σ from the measured depth H of the indentation. It is valid for flows of moderate aggressiveness, i.e., for $\sigma < \sigma_U$. In the limit case of an impact load equal to the material ultimate strength $\sigma = \sigma_U$, the depth of the indentation is

$$H = \frac{\varepsilon_U L}{1+\theta} \tag{22}$$

In the case of highly erosive potential defined by $\sigma > \sigma_U$ (which is not the case in the present experiment), some material is removed and the depth of the removed material given by Eq. (14) has to be added to the previous depth (Eq. (22)) to obtain the actual pit depth,

$$H = \frac{\varepsilon_U L}{1+\theta} + L\left[\left(\frac{\sigma - \sigma_Y}{\sigma_U - \sigma_Y}\right)^{1/n\theta} - 1\right] \tag{23}$$

Previous Eq. (23) is valid only for $\sigma > \sigma_U$.

Equations (21) and (23) are represented in Fig. 19 for stainless steel 316 L. The limit value (22) estimated using material characteristics (2) and (4) is 15.8 μm. Since the maximum measured pit depth on the sample of 800 pits considered here is 4.8 μm (see Fig. 12), it is concluded that all impact loads are below the material ultimate strength. The maximum load corresponding to the maximum pit depth is 777 MPa. In other words, the present cavitating flow with a velocity of 65.3 m/s can be considered as a cavitating flow of moderate aggressiveness. The influence of flow velocity was not investigated here. It is generally reported that erosion damage increases with a relatively high power of the flow

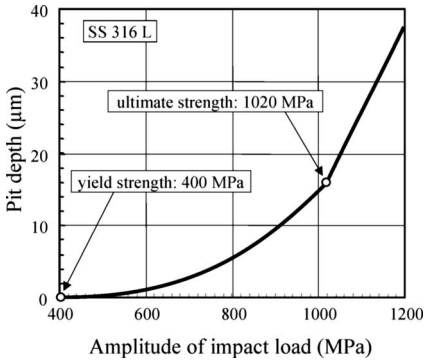

Fig. 19 Pit depth versus amplitude of impact load for stainless steel 316 L. The two branches correspond to Eq. (21) if $\sigma < \sigma_U$ and Eq. (23) if $\sigma > \sigma_U$.

velocity of the order of 6 [31].

The previous correspondence between pit depth and impact load is systematically applied to each pit. A distribution of hydrodynamic impact loads is then obtained. In order to define a mean value representative of the whole spectrum, an averaging procedure is used based on energy arguments. From a dimensional viewpoint, the product of pit volume V and impact load σ has the units of energy. Hence, it was decided to define the mean impact load $\bar{\sigma}$ by the following averaging procedure:

$$\bar{\sigma} = \frac{\sum V_i \sigma_i}{\sum V_i} \tag{24}$$

where the summation is relative to all identified pits. The previous definition of mean impact load is based on the principle of conservation of energy discharged in the material. In the present case, the mean impact load determined by Eq. (24) on the sample of 797 indentations is equal to 621 MPa. This value lies between yield strength and ultimate strength, which confirms that the erosive potential of the present cavitating flow is moderate and that fatigue and work-hardening processes prevail. The mean surface of impact load $\bar{S}$ is defined by a classical averaging procedure,

$$\bar{S} = \frac{1}{\nu} \sum S_i \tag{25}$$

where ν is the total number of pits analyzed. As for the pitting rate N, it is simply the number of pits per unit time and unit surface area.

The influence of the number of pits used for the determination of flow aggressiveness was investigated for each of the three variables $\bar{\sigma}$, $\bar{D}$, and N. The analysis showed that flow aggressiveness can be considered as correctly defined by a sample of typically a few hundreds of pits (see Fig. 20 for the influence of the number of pits on MDPR and incubation time). In practice, 797 pits were considered here. For the present cavitating flow, the mean diameter of impact loads is 72 μm. This value is near the characteristic value of pit diameter, leading to maximum damage as deduced from Figs. 14 and 15.

4.2 Incubation Time and MDPR. Once flow aggressiveness defined by the quantities $\bar{\sigma}$, $\bar{S}$, and N has been computed, it is possible to apply the predictive method developed in Secs. 2.5 and 2.6 and, particularly, Eqs. (12) and (15) to predict the incubation period and mass loss rate. Flow aggressiveness has been estimated from eight different surfaces similar to the one presented in Fig. 10 relative to the same pitting test but to eight different angular positions on the target at the same radius corresponding to maximum damage.

There is a non-negligible dependence of the predicted values of

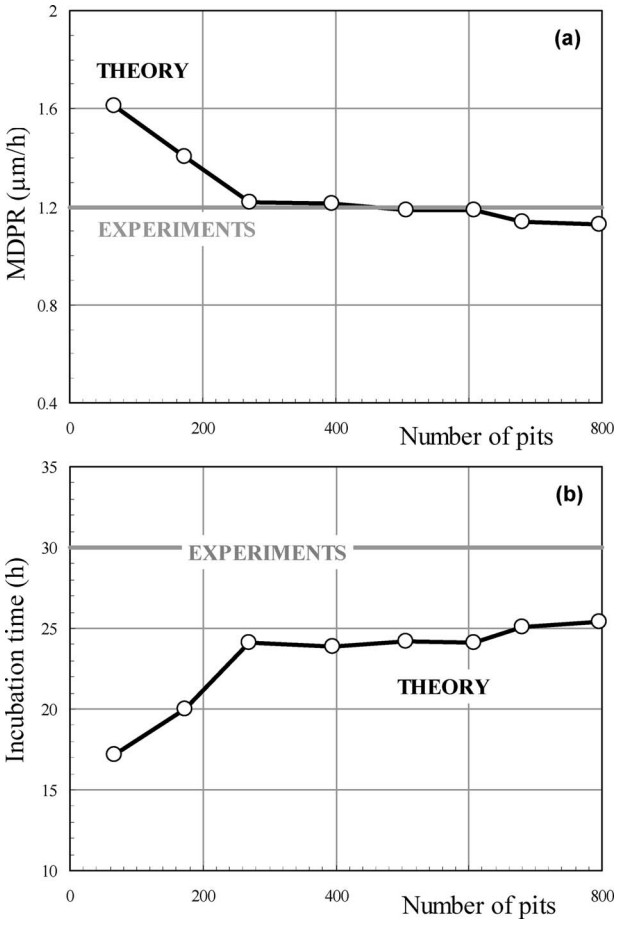

Fig. 20 Comparison between theory and experiments for (*a*) MDPR and (*b*) incubation time. The theoretical prediction depends on the number of pits used to estimate the erosive potential of the cavitating flow. Prediction can be considered as stabilized above a few hundred pits.

MDPR and incubation period on the pitted surface considered to evaluate the erosive potential. Following the previous discussion on the influence of the size of the sample on the evaluation of the erosive potential of the cavitating flow, it can be expected that the values corresponding to the total number of pits analyzed here are actually good estimates of the long term damage and are suitable for a comparison with experiments. Figure 20 shows that the predicted values of MDPR (1.1 μm/h) and incubation time (25.4 h) based on the total number of pits (797 pits) are in reasonable agreement with the experimental measurements deduced from Fig. 18 (1.16 μm/h and 30 h).

A careful examination of the values of MDPR and incubation time predicted from the eight pitting surfaces mentioned above showed that both variables are strongly correlated. A small MDPR is associated with a long exposure time, both being the consequence of a relatively small aggressiveness. The product of the incubation time T by MDPR proved to be almost constant. Using Eqs. (12) and (15) for incubation time T and MDPR, respectively, and multiplying them together in order to compute the product MDPR$\times T$, it appears that the covering time τ vanishes. The only hydrodynamic parameter remaining in the product is the amplitude of impact loads $\bar{\sigma}$ (which also appears through ε'), all other parameters being material properties, which remain unchanged for a given material. In the present case, it has been observed that the value of $\bar{\sigma}$ for the various computations is nearly constant. This explains the almost constant value of the product MDPR$\times T$ in the present case.

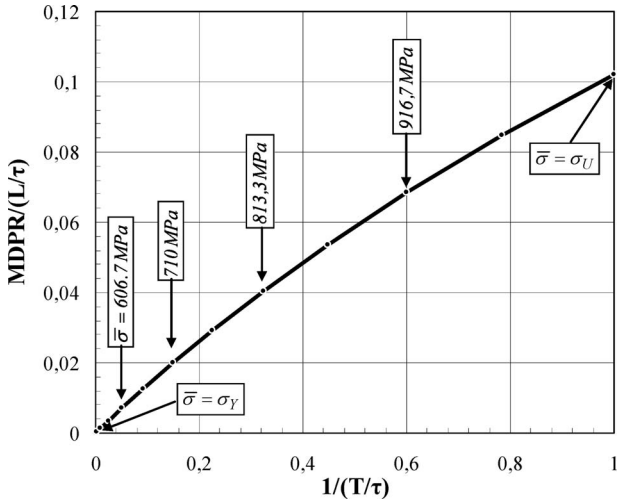

Fig. 21 Relation between nondimensional MDPR and inverse of nondimensional incubation time for stainless steel 316 L. The curve has been obtained by varying the flow aggressiveness in terms of mean amplitude of impact load $\bar{\sigma}$.

More generally, several works have attempted to derive a relation between incubation time and MDPR. Soyama and Futakawa [32], for instance, recently showed that the incubation time can be estimated by evaluating the amount of erosion at a postincubation point. Hammitt [13] and Zhou and Hammitt [23] suggested the following form for this correlation:

$$\frac{1}{\text{MDPR}} = kT^{\alpha} \tag{26}$$

where parameter k should remain constant for a given material and type of test. Available estimates of exponent α from both cavitation and liquid impact data indicate $0.6 < \alpha < 1$ [13]. Using the present model, nondimensional MDPR was plotted in Fig. 21 for SS 316 L versus the inverse of the nondimensional incubation time to further analyze the relation between both parameters. Each point on the curve corresponds to a given value of flow aggressiveness in terms of impact load $\bar{\sigma}$. The whole curve was obtained by varying $\bar{\sigma}$ between the material yield strength and its ultimate strength, the latter being the maximum value for which the incubation time still has meaning. It then refers to a quite large range in flow aggressiveness. From the examination of Fig. 21, it can be concluded that the present model predicts an almost linear dependence between MDPR and the inverse of the incubation period in the whole range of variation in flow aggressiveness.

Let us observe that the present simplified model fails at predicting the acceleration period clearly visible in Fig. 18. This is due to the noninclusion in the model of the statistical nature of impact loads in terms of amplitude, size, and space distribution. As a consequence, strain is assumed uniform on the material surface at any time, and ultimate strain and subsequent mass loss are reached at the same time at any point of the material surface. Then, there is no distinction between the end of the incubation period and the beginning of the steady-state erosion period so that a steplike behavior for MDPR versus exposure time is found. As shown by Berchiche et al. [25], a more realistic variation with an acceleration period would be obtained by considering the whole spectrum of impact loads (and not only average values) and assuming that impact loads are randomly distributed in space. If so, ultimate strain progressively gains the whole material surface depending on the amplitude of successive impact loads and their possible partial overlapping. This results in a transitional regime between incubation and steady-state erosion characterized by a gradual increase in the erosion rate, as shown experimentally. However, in the present paper, we have deliberately chosen to ignore the random distribution in space, size, and amplitude of impact loads in order to be able to derive analytical relationships and more easily point out the key parameters of the damage process, which was our primary objective.[1]

A final remark concerns the evaluation of the influence of the threshold chosen for the analysis of pitting tests on the prediction of the incubation period and erosion rate. An excessive value of the threshold obviously tends to underestimate the number and size of pits, whereas a too small value will overestimate them and even lead neighboring pits to merge. It is difficult to derive an objective criterion for the choice of this threshold. Here, the choice is made on the basis of a qualitative comparison of the original image to the binary one obtained after applying the threshold. From Fig. 22, it is clear that the two extreme thresholds 0.8 μm and 0.3 μm considered here are not acceptable, whereas the threshold 0.5 μm can be considered to give a relatively satisfactory description of the pitted surface. It is of major concern to observe that if the number and size of pits depend on the threshold, pit depths, which are measured from the original virgin surface and not from the threshold level (see Fig. 11), are unchanged, as well as the subsequent amplitudes of impact loads. The influence of the threshold on the predicted incubation time and erosion rate is presented in Fig. 23, together with the experimental measurements. The higher the threshold, the higher the incubation time and the smaller the erosion rate. Although the predicted values depend on the precise value of the threshold, Fig. 23 shows that in the range of 0.4–0.6 μm, which is considered acceptable from visualizations of Fig. 22, they remain of the same order of magnitude as in experiments.

5 Concluding Remarks

The present paper focuses on the prediction of incubation time and erosion rate of ductile materials exposed to a cavitating flow. From a dimensional viewpoint, the erosion rate measured in terms of the MDPR has the units of a characteristic length divided by a characteristic time. The present work suggests that

(i) The relevant time scale is the covering time τ, i.e., the time necessary for the surface to be exactly covered by the hydrodynamic impacts. This time depends on the impact rate and the size of the loaded areas. It is a feature of the cavitating flow in so far as it depends mainly on hydrodynamic aspects (such as bubble production rate and bubble size).

(ii) The relevant length scale for ductile materials is the thickness of the hardened layer L. It can be determined from microhardness measurements on cross sections of eroded specimens. This is essentially a material characteristic, although it probably integrates to some extent the very specific type of loading due to bubble collapses since it is determined on specimens actually eroded by cavitation.

MDPR can be estimated by the ratio L/τ with a multiplicative factor, which depends principally on flow aggressiveness in terms of the mean amplitude of the hydrodynamic impact loads. It is zero in the limit case of impact loads equal to the yield strength and progressively increases with flow aggressiveness. An explicit formulation is proposed to estimate this dependency.

As for the incubation time, the present approach shows that it is proportional to the covering time and that the ratio is strongly dependent on the flow aggressiveness. For impact loads close to the material ultimate strength, the incubation time matches the covering time. When the impact load approaches the material yield strength, i.e., for flows of relatively small aggressiveness, the incubation time increases considerably and can be several or-

[1]This difference in shape between the theoretical and experimental evolutions of MDPR with exposure time may be the reason for a poorer comparison between theory and experiment for the incubation period compared with MDPR (see Fig. 19).

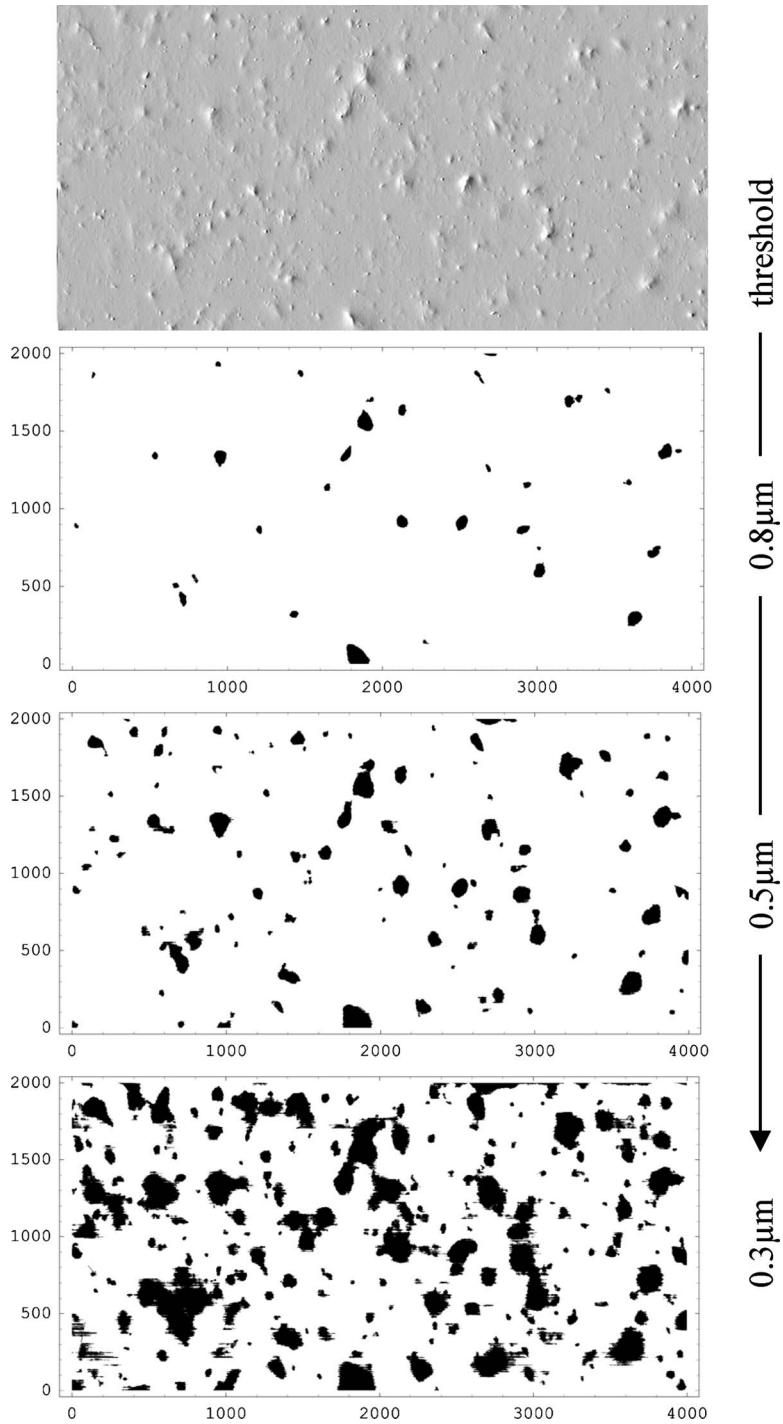

Fig. 22 Influence of depth threshold on the treatment of a pitting test (same surface as in Fig. 10)

ders of magnitude larger than the covering time. The model proposed here accounts for this variation. It also allows us to predict the relationship between MDPR and the inverse of incubation time, which appears to be almost linear in the whole range of flow aggressiveness.

The model is supported by an experimental investigation in which erosion is produced by a cavitating flow in a radial divergent. In the absence of any reliable method of estimation of flow aggressiveness from global hydrodynamic parameters (such as cavitation number and flow rate), pitting tests are used to quantify the erosive potential of the cavitating flow. Hydrodynamic impact loads are deduced from the measurement of the maximum pit depth by means of the same model of response of the material as the one used for mass loss prediction. As for the rate and surface area of the impact loads, they are deduced from the pitting rate and pit size. By introducing such an estimate of the erosive potential of the cavitating flow into the model, it has been possible to predict the incubation period and mass loss rate under steady-state conditions. Predictions are compared with experimental values obtained from mass loss experiments. The tested material is stainless steel 316 L, which is known to exhibit high work hardening.

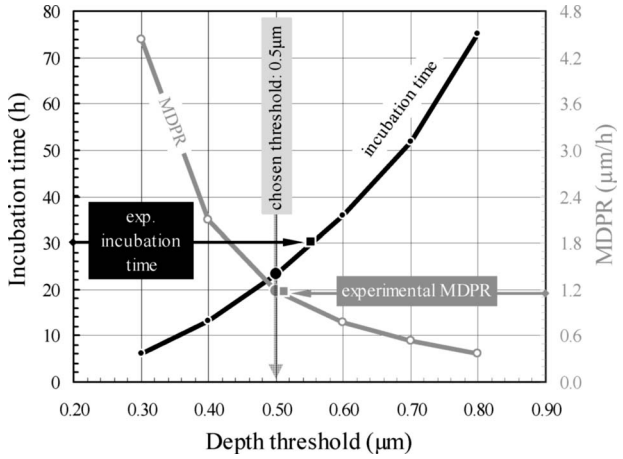

Fig. 23 Influence of depth threshold on predicted incubation period and erosion rate

On the whole, the agreement between predicted and measured values of the incubation time and MDPR is satisfactory.

The present approach is based on an elementary modeling of the flow aggressiveness. It consists in approximating the whole impact load spectrum by mean values of both the impact loads and the impacted areas. This results in a steplike variation in the erosion rate versus the exposure time with no mass loss before the incubation time and a constant steady-state erosion beyond. To account for the acceleration period, which actually exists between the incubation and the steady-state periods, as shown by experiments, it is necessary to take into account the whole distribution of impact loads in size and amplitude and also the spatially random nature of the hydrodynamic impacts. This can easily be done in the framework of the same phenomenological analysis but requires the development of a numerical procedure. The objective of the present work based on a simplified characterization of the erosive potential of a cavitating flow was essentially to contribute to elucidating the erosion mechanism of ductile materials, point out the major parameters that control damage, and propose a deterministic approach of the erosion process. Although it is still under development, such a technique of prediction of cavitation erosion can be considered as a future alternative to more conventional techniques based on correlations with material properties such as Vickers hardness, ultimate resilience, and fatigue tests (see, e.g., Refs. 13 and 33–35).

Acknowledgment

The present research has been conducted in the framework of the European project "PREVERO" under Contract No. ENK6-CT-2002-00605. The author is particularly grateful to AVL, coordinator of the project, and all other partners of the consortium for fruitful discussions. The author would also like to acknowledge the essential help provided by J.C. Jay, Y. Lecoffre, J.M. Michel, and M. Riondet for the design of facility and experiments.

Nomenclature

H = maximum pit depth (m)
K = constant in stress/strain relationship (1) (Pa)
ℓ = thickness of the hardened layer for partial hardening (m)
L = thickness of the hardened layer for complete hardening (m)
MDPR = mean depth of penetration rate (m/s)
n = exponent in stress/strain relationship (1)
N = impact rate per unit surface area (impacts/m^2/s)
p_d = downstream pressure in test section (Pa)
p_u = upstream pressure in test section (Pa)
p_v = vapor pressure (Pa)
$\bar{S}$ = mean size of impacted area (m^2)
T = incubation time (s)
V = pit volume (m^3)
V_c = reference velocity on cavity (Eq. (18)) (m/s)
W = energy absorbed by the material (Eq. (8)) (J)
x = distance inside the material from the surface (m)
β = parameter defined by Eq. (10)
ε_U = ultimate strain
ε = strain
ε' = virtual surface strain during the steady-state erosion period (see Sec. 2.6)
θ = metallurgical shape factor (Eq. (3))
σ = cavitation number (Eq. (16)) or stress (Pa)
$\bar{\sigma}$ = mean amplitude of impact loads (Pa)
σ_U = material ultimate tensile strength (Pa)
σ_Y = material yield strength (Pa)
τ = covering time $1/N\bar{S}$ (s)

References

[1] Pereira, F., Avellan, F., and Dupont, Ph., 1998, "Prediction of Cavitation Erosion: An Energy Approach," ASME J. Fluids Eng., **120**, pp. 719–727.
[2] Lecoffre, Y., Marcoz, J., Franc, J. P., and Michel, J. M., 1985, "Tentative Procedure for Scaling Cavitation Damage," Proceedings of the Joint ASCE/ASME Mechanics Conference on "Cavitation in Hydraulic Structures and Turbomachinery," Albuquerque, NM, Jun. 24–26, R. E. A. Arndt and D. R. Webb, eds., FED-Vol. 25, pp. 1–11.
[3] Kato, H., 1975, "A Consideration on Scaling Laws of Cavitation Erosion," Int. Shipbuild. Prog., **22**(253), pp. 305–327.
[4] Kato, H., Konno, A., Maeda, M., and Yamaguchi, H., 1996, "Possibility of Quantitative Prediction of Cavitation Erosion Without Model Test," ASME J. Fluids Eng., **118**, pp. 582–588.
[5] Maeda, M., Yamaguchi, H., and Kato, H., 1991, "Laser Holography Measurement of Bubble Population in Cavitation Cloud on a Foil Section" First ASME-JSME Fluids Engineering Conference, Portland, OR, Jun. 23–27, H. Kato and O. Furuya, eds., FED-Vol. 116, pp. 67–75.
[6] Tomita, Y., and Shima, A., 1986, "Mechanism of Impulsive Pressure Generation and Damage Pit Formation by Bubble Collapse," J. Fluid Mech., **169**, pp. 535–564.
[7] Vogel, A., Lauterborn, W., and Timm, R., 1989, "Optical and Acoustic Investigations of the Dynamics of Laser-Produced Cavitation Bubbles Near a Solid Boundary," J. Fluid Mech., **206**, pp. 299–338.
[8] Philipp, A., and Lauterborn, W., 1998, "Cavitation Erosion by Single Laser-Produced Bubbles," J. Fluid Mech., **361**, pp. 75–116.
[9] Reisman, G. E., Wang, Y.-C., and Brennen, C. E., 1998, "Observation of Shock Waves in Cloud Cavitation," J. Fluid Mech., **355**, pp. 255–283.
[10] Knapp, R. T., Daily, J. W., and Hammitt, F. G., 1970, *Cavitation*, McGraw-Hill, New York.
[11] Stinebring, D. R., Holl, J. W., and Arndt, R. E. A., 1980, "Two Aspects of Cavitation Damage in the Incubation Zone: Scaling by Energy Considerations and Leading Edge Damage," ASME J. Fluids Eng., **102**, pp. 481–485.
[12] Fortes Patella, R., Reboud, J. L., and Archer, A., 2000, "Cavitation Damage Measurement by 3D Laser Profilometry," Wear, **246**, pp. 59–67.
[13] Hammitt, F. G., 1979, "Cavitation Erosion: The State of the Art and Predicting Capability," Appl. Mech. Rev., **32**(6), pp. 665–675.
[14] Hattori, S., Sun, B.-H., Hammitt, F. G., and Okada, T., 1985, "An Application of Bubble Collapse Pulse Height Spectra to Venturi Cavitation Erosion of 1100-O Aluminium," Wear, **103**, pp. 119–131.
[15] Okada, T., Iwai, Y., Hattori, S., and Tanimura, N., 1995, "Relation Between Impact Load and the Damage Produced by Cavitation Bubble Collapse," Wear, **184**, pp. 231–239.
[16] Hattori, S., Mori, H., and Okada, T., 1998, "Quantitative Evaluation of Cavitation Erosion," ASME J. Fluids Eng., **120**, pp. 179–185.
[17] Knapp, R. T., 1955, "Recent Investigations of the Mechanics of Cavitation and Cavitation Damage," Trans. ASME, October, pp. 1045–1054.
[18] Knapp, R. T., 1958, "Accelerated Field Tests of Cavitation Intensity," Trans. ASME, January, pp. 91–102.
[19] Belahadji, B., Franc, J. P., and Michel, J. M., 1991, "A Statistical Analysis of Cavitation Erosion Pits," ASME J. Fluids Eng., **113**, pp. 700–706.
[20] Thiruvengadam, A., 1974, "Handbook of Cavitation Erosion," Hydronautics Inc., Technical Report No. 7301-1.
[21] Karimi, A., and Martin, J. L., 1986, "Cavitation Erosion of Materials," Int. Met. Rev., **31**(1), pp. 1–26.
[22] Pallabazzer, R., and Mancuso, G., 1998, "Erosive Cavitation Tests in Water Tunnel," XIX Symposium AIRH, pp. 500–509.
[23] Zhou, Y. K., and Hammitt, F. G., 1983, "Cavitation Erosion Incubation Period," Wear, **86**, pp. 299–313.

[24] Karimi, A., and Leo, W. R., 1987, "Phenomenological Model for Cavitation Rate Computation," Mater. Sci. Eng., **95**, pp. 1–14.
[25] Berchiche, N., Franc, J. P., and Michel, J. M., 2002, "A Cavitation Erosion Model for Ductile Materials," ASME J. Fluids Eng., **124**, pp. 601–606.
[26] Ball, A., 1983, "On the Importance of Work Hardening in the Design of Wear-Resistant Materials," Wear, **91**, pp. 201–207.
[27] Li, S., Zhang, Y., and Hammitt, F. G., 1986, "Characteristics of Cavitation Bubble Collapse Pulses, Associated Pressure Fluctuations, and Flow Noise," J. Hydraul. Res., **24**(2), pp. 109–122.
[28] Nguyen, M., Franc, J. P., and Michel, J. M., 1987, "On Correlating Pitting Rate and Pressure Peak Measurements in Cavitating Flows," J. W. Holl and M. L. Billet, eds., Proceedings of the ASME International Symposium on Cavitation Research Facilities and Techniques, ASME, Boston, Dec. 13–18, FED-Vol. 57, pp. 207–216.
[29] Fry, S. A., 1989, "The Damage Capacity of Cavitating Flow From Pulse Height Analysis," ASME J. Fluids Eng., **111**, pp. 502–509.
[30] Momma, T., and Lichtarowicz, A., 1995, "A Study of Pressures and Erosion Produced by Collapsing Cavitation," Wear, **186–187**, pp. 425–436.
[31] Franc, J. P., and Michel, J. M., 2004, *Fundamentals of Cavitation*, Kluwer Academic, Dordrecht.
[32] Soyama, Y., and Futakawa, M., 2004, "Estimation of Incubation Time of Cavitation Erosion for Various Cavitating Conditions," Tribol. Lett., **17**(1), pp. 27–30.
[33] Hattori, S., Ishikura, R., and Zhang, Q., 2004, "Construction of Database on Cavitation Erosion and Analyses of Carbon Steel Data," Wear, **257**(9–10), pp. 1022–1029.
[34] Hattori, S., Maeda, K., and Zhang, Q., 2004, "Formulation of Cavitation Erosion Behavior Based on Logistic Analysis," Wear, **257**(9–10), pp. 1064–1070.
[35] Bedkowski, W., Gasiak, G., Lachowicz, C., Lichtarowicz, A., Lagoda, T., and Macha, E., 1999, "Relations Between Cavitation Erosion Resistance of Materials and Their Fatigue Strength Under Random Loading," Wear, **230**, pp. 201–209.

Thermal Effect at the Incipient Stage of Cavitation Erosion on a Stainless Steel in Ultrasonic Vibration Cavitation

Chen Haosheng
State Key Laboratory of Tribology,
Tsinghua University,
Beijing 100084, China
e-mail: chenhs@mail.tsinghua.edu.cn

Li Jiang
Mechanical Engineering School,
University of Science and Technology Beijing,
Beijing 100083, China

Liu Shihan
State Key Laboratory of Tribology,
Tsinghua University,
Beijing 100084, China

An ultrasonic vibration cavitation erosion experiment was performed to study the thermal effect during the erosion process. The ring affected zone was observed on the sample surface around the erosion pit at the incipient stage of the cavitation erosion. The results of the surface testing on roughness, hardness, and chemical composition proved that the zone was caused by thermal effect, and that the zone surface experienced a tempering process with the temperature higher than 300°C. Numerical simulation results show that the high temperature domain in the bubble directly contacting the solid wall is a necessary condition for the occurrence of the tempering process on the zone surface, or the heat in the bubble can hardly be transferred to the solid wall under the effects of the great temperature gradient in the bubble and the quick cooling process in the water.
[DOI: 10.1115/1.3054282]

Keywords: cavitation erosion, bubble dynamics, thermal effect, ultrasonic vibration cavitation

1 Introduction

It has been acknowledged that the collapse of a bubble close to a solid wall is the main reason for the cavitation erosion, and thermal effect may appear during the bubble compress and collapse processes [1]. The experimental phenomenon observed by Nowotny [2] and Gavranek et al. [3] showed that high temperature was reached in the bubble at the end stage of the bubble collapse. In the experiment, the temperature was so high that the metal strength was reduced and the metal surface even melted. On the other hand, numerical results formally reviewed by Knapp et al. [4] and recently provided by Wu and Robert [5] and Ying and An [6] showed that the temperature in the bubble can reach 10,000°C at the moment of collapse. However, in many cavitation erosion experiments, it is difficult to find the evidence of thermal effect on the damaged surface. As Knapp et al. [4] pointed out, although the temperature was very high in the bubble, the heat was hard to be transferred to the surface efficiently with the existence of water separating the hot bubble and the solid wall. Another important reason was that the surface of some materials, such as steel, cannot reach high temperature because it has good heat conductivity.

According to Knapp's explanation, it seems that the sample surface may not be affected by the thermal effect during the cavitation erosion process. However, at least two questions still need to be answered. First, can every bubble be separated by the water and none of them have the chance to contact the solid wall? Second, it is well known that the collapse process is very quick, for example, a bubble with 1 mm radius will collapse in several microseconds. When a bubble collapses near a solid surface, high temperature will be reached in a very short time, which is like the formation of *flash temperature* [7]. It is proved that the flash temperature can damage the local metal surface before it is decreased by the metal heat conductivity. Hence, the thermal effect may have the chance to take part in the erosion process on a metal surface.

Our undergoing study investigates whether the thermal effect takes part in the formation of the pit. To achieve this goal, samples made of stainless steel (1Cr18Ni9Ti) were installed on a static platform and the bubbles generated by an ultrasonic vibration system rush forward to the sample surface. After the experiment, surface profile, surface hardness, and elemental composition of the erosion pit were tested to look for the evidence of the thermal effect at the incipient stage of the cavitation erosion. Later, numerical analyses are given to explain the experimental results.

2 Vibration Cavitation Experiment

Figure 1 shows an ultrasonic vibration cavitation system. The vibration stick performs an axial vibration with the frequency of 20 kHz and the amplitude of 6 μm. A sample piece was installed on the support arm of a two dimensional table. The testing surface of the sample faced the tip of the vibration stick. The interval between the two surfaces was adjusted by the translation stage, while the pitch angle of the sample surface was adjusted by the rotation stage. The experiment was performed in a beaker filled with de-ionized water, which is provided by a supplier, with the standards of resistivity higher than 10 MΩ/cm, a reactive silica level of generally less than 20 μg/l, and the maximum total dissolved solids less than 10 mg/1. The temperature of the water during the experiment was measured by a mercury thermometer. The original temperature before the experiment was 20°C, while it increased to 23.5°C at the end of a 5 min experiment. The dissolved gas content in the de-ionized water before experiment is 1.78% measured by HI9804 water quality analyzer. Figures 1(*b*) and 1(*c*) show the sample and its surface profile, respectively. The sample was designed according to Chinese standards (GB6383–86) on vibration cavitation erosion system. The sample surface was polished, and the root mean square (Rq) value of the surface roughness was 12.5 nm, which was tested by an atomic force microscope (AFM) CSPM 4000. It should be noted here that there were three measuring regions on the sample surface marked as 1–3 in Fig. 1(*b*). Each region was the size of 5×5 μm^2, and the surface roughness of the sample surface was the mean value of the three regions.

The experiment lasted 5 min. The cavitation phenomena captured by a digital camera was shown in Fig. 1(*d*). A clear cavitation domain was found near the vibration stick's tip, and some bubbles were seen rushing toward the sample surface. Figure 2(*a*) shows the erosion pits on the steel surface observed by an Olympus LEXT OLS3100 confocal laser scanning microscope. It was found that a distinguished ring zone with an iridescent color was formed around some erosion pits. An erosion pit with an obvious ring zone was tested and its surface profile was shown in Fig. 2(*b*). The continuous curve represents the surface profile of the sample surface at the position where the dashed line stands. The erosion pit is narrow and deep, and it is usually called needlelike

Contributed by the Fluids Engineering Division of ASME for publication in the JOURNAL OF FLUIDS ENGINEERING. Manuscript received June 12, 2007; final manuscript received May 3, 2008; published online January 9, 2009. Assoc. Editor: Steven Ceccio.

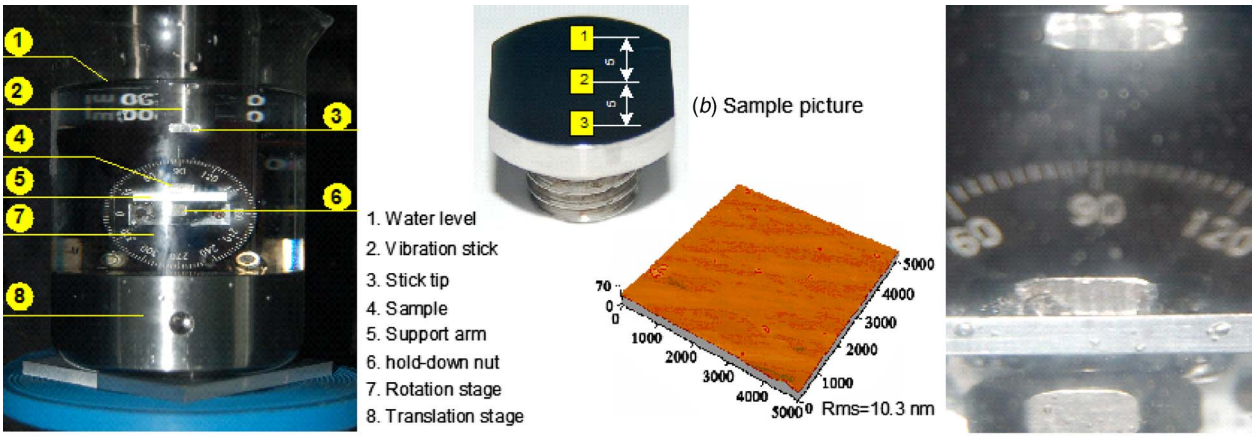

Fig. 1 (*a*) Vibration cavitation system, (*b*) the picture of the sample, (*c*) surface profile of the sample surface, and (*d*) experimental phenomenon

pit [1], which is a characteristic phenomenon that appeared at the incipient stage of cavitation erosion. The ring zone was raised from the base, which copes with the experimental results done by Knapp [8] on the aluminum surface. The ring zone is believed to be the result of the plastic deformation of the material under the effect of the microjet formed at the moment of the bubble collapse [9]. This result proves that the cavitation erosion occurs, and a kind of ring zone appears at the incipient stage of the cavitation erosion.

The hardness of the damaged surface was tested by a Nano Tester (Micro Materials Ltd.). Twelve indents were made on the sample surface shown in Fig. 3(*a*). The interval between the indents was 15 μm, and the maximum load was 50 mN. The hardness of the surface within and outside the ring area is shown in Fig. 3(*b*). It is found that the mean value of the hardness inside the ring is obviously lower than that outside the ring. Also, obvious plastic deformations were seen around the indents inside the ring, while the triangle shape of the indent outside of the ring is clear. Moreover, as shown in Figs. 2 and 3(*a*), the ring is colorful. The appearance of the iridescent color indicates that the temperature on the steel surface may reach 300°C according to the experiment of Wang et al. [10]. On the other hand, it is known that the hardness of the steel decreases when the steel is tempered with the temperature higher than 300°C. Hence, the iridescent color and the decreased surface hardness both indicate that the surface within the ring experienced a high temperature tempering process.

Based on the heat treatment theory [11], the surface hardness reduction during the tempering process is caused by the precipitation of the carbides on the surface. Therefore, the elemental composition of the damaged surface was tested by EPMA-1600 electronic probe with a wavelength dispersive spectrometry (WDS). Six elements, namely, ferro, carbon, oxygen, chrome, nickel, and titanium were detected within the ring. In Fig. 4(*a*), the distribution of the carbon on the damaged surface was tested using an area scan method, where the concentration was represented by the color. It is found that the carbon distribution also has a ring shape. The quantitative concentrations of the six elements are shown in Figs. 4(*b*) and 4(*c*) using line scan along the horizontal diametric line, as shown in Fig. 4(*a*). The *y*-axis represents the percentage of each element counts compared with its maximum atom counts, except for oxygen whose value is the percentage of counts compared with 100. The numbers marked in the figure are the tested maximum and minimum atom counts for each element. Each curve is the mean result of three scanned results at the same position, the uncertainty of each curve is calculated according to the standard error calculation method. The uncertainties of concentrations with respect to different elements are ±3.5%

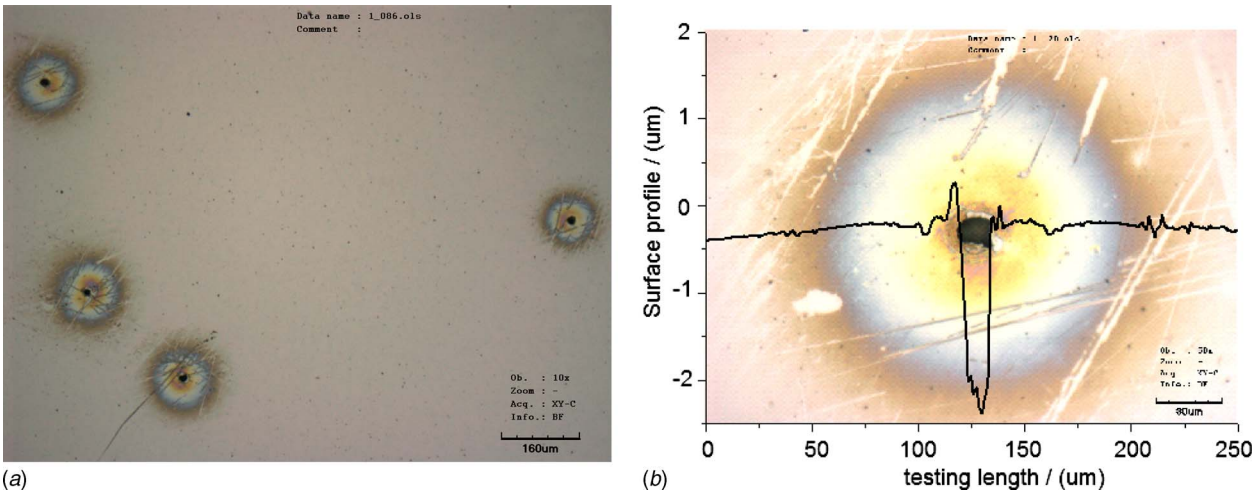

Fig. 2 (*a*) Pits scattered on the surface and (*b*) surface profile of the erosion pit tested by confocal laser scanning microscope; the uncertainty of the measured data is 0.01 μm according to the precision of the microscope

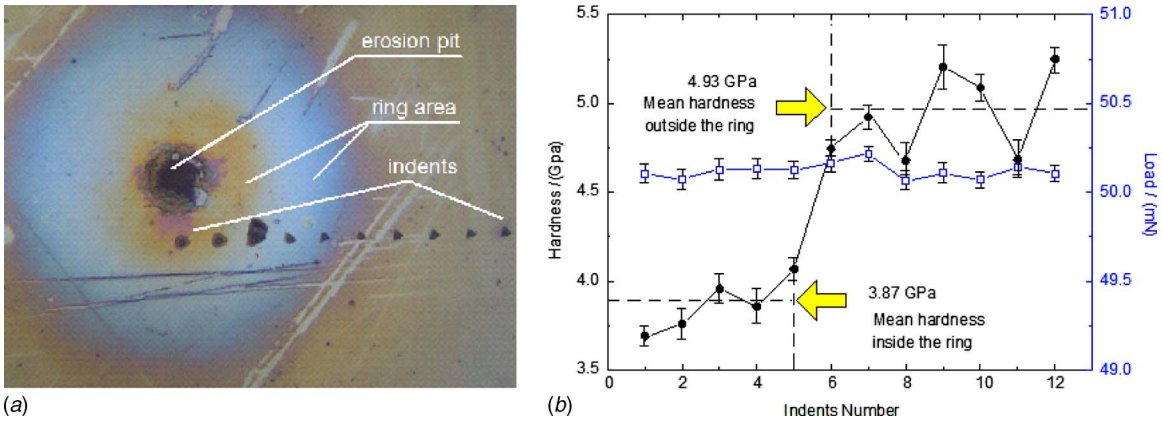

Fig. 3 Surface hardness testing; (*a*) is the pit with indents, and (b) is the hardness in and outside the ring affected zone

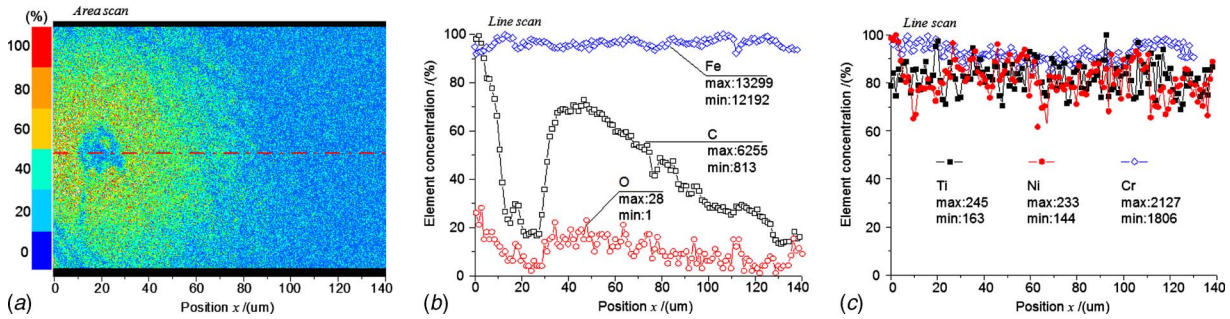

Fig. 4 The elemental composition of surface materials tested by EPMA-1600 electronic probe: (*a*) is the area scan result of carbon; (*b*) is the line scan results of Fe, C, and O; and (*c*) is the line scan results of Cr, Ti, and Ni

(Fe), ±7.5% (C), ±7.0% (O), ±9.5% (Ti), ±12.5% (Ni), and 6.5% (Cr). The carbon concentration increased in the ring while the concentrations of the other five elements did not change much. It proves that the carbon precipitated on the surface, and the ring has experienced a tempering process. The lack of oxygen on the surface indicates that the ring area is not a chemical oxygenized result under a lower temperature.

3 Conclusions

A kind of ring heat-affected zone is observed around the erosion pit on a steel surface in an ultrasonic vibration cavitation erosion system. Surface analyses on roughness, hardness, and chemical composition proves that the zone is caused by the thermal effect, and that the zone surface is considered to experience a tempering process with temperature higher than 300°C.

Acknowledgment

Project (No. 50505020) supported by the NSFC and project (No. 2007CB707702) supported by the National Basic Research Program of China are thanked.

References

[1] Hammitt, F. G., 1980, *Cavitation and Multiphase Flow Phenomena*, McGraw-Hill, New York, p. 241.
[2] Nowotny, H., 1942, *Destruction of Materials by Cavitation*, VDI-Verlag, Berlin.
[3] Gavranek, V. V., Bol'shutkin, D. N., and Zel'dovich, V. I., 1960, "Thermal and Mechanical Action of a Cavitation Zone on the Surface of a Metal," Fiz. Met. Metalloved., **10**, pp. 262–268.
[4] Knapp, R. T., Daily, J. W., and Hammit, F. G., 1970, *Cavitation*, McGraw-Hill, New York.
[5] Wu, C. C., and Robert, P. H., 1993, "Shock-Wave Propagation in a Sono-Luminescence Gas Bubble," Phys. Rev. Lett., **70**(22), pp. 3424–3427.
[6] Ying, C. F., and An, L., 2002, "High Temperature and High Pressure Distribution in Gas Bubbles Generated by Sound Cavitation," Sci. China, Ser. A: Math., Phys., Astron., **32**(4), pp. 305–313.
[7] Nishi, T., Shibata, H., Tsutsumi, K., Ohta, H., and Waseda, Y., 2002, "Measurement of Thermal Diffusivity of Steels at Elevated Temperature by a Laser Flash Method," ISIJ Int., **42**(5), pp. 498–503.
[8] Knapp, R. T., 1955, "Recent Investigations of Cavitation and Cavitation Damage," Trans. ASME, **77**, pp. 1045–1054.
[9] Plesset, M. S., and Ellis, A. T., 1955, "On Mechanism of Cavitation Damage," Trans. ASME, **77**, pp. 1055–1064.
[10] Wang, Z. C., Zhang, Y., and Zhang, X. Q., 2001, "Thermal Effect of Cavitation Erosion," Chinese Journal of Materials Research, **15**(6), pp. 287–290.
[11] Gregory, E., and Simons, N., 1958, *The Heat-Treatment of Steel*, Pitman & Sons, London.